Enhanced Next Generation Alternator

by

Leandro Manalac Lorilla

S. B., Massachusetts Institute of Technology (2000)
M. Eng., Massachusetts Institute of Technology (2000)

Submitted to the Department of Electrical Engineering and Computer Science
in partial fulfillment of the requirements for the degree of
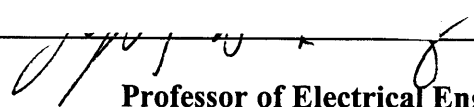
Doctor of Philosophy
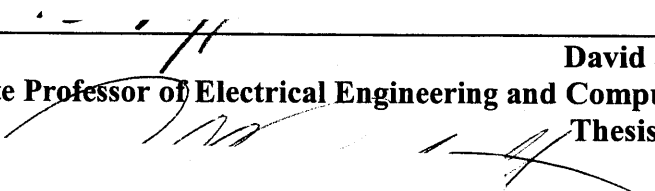
at the

Massachusetts Institute of Technology

September, 2005

Signature of Author:_____
                    Department of Electrical Engineering and Computer Science

Certified by:_____
   Thomas A. Keim
                Principal Research Engineer and LEES Assistant Director
                                                Thesis Supervisor

Certified by:_____
                                                Jeffrey H. Lang
                Professor of Electrical Engineering and Computer Science
                                                Thesis Supervisor

Certified by:_____
                                                David J. Perreault
                Associate Professor of Electrical Engineering and Computer Science
                                                Thesis Supervisor

Accepted By:_____
                Chair, Department Committee on Graduate Students
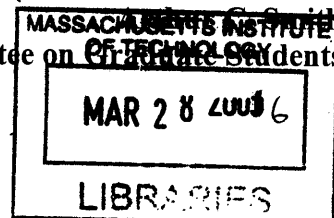
Enhanced Next Generation Alternator

By

Leandro M. Lorilla

Submitted to the Department of Electrical Engineering and Computer Science
On September 12, 2005 in Partial Fulfillment of the Requirements
for the Degree of Doctor of Philosophy in Electrical Engineering

Abstract

The power requirements of automotive alternators are increasing significantly due to the introduction of new vehicle electrical loads. Moreover, the possible transition to a 42 V electrical system is introducing new concerns regarding the load dump overvoltage transient of alternators. This thesis makes several contributions to the power density, efficiency, and transient performance of future alternators.

A comparison and design optimization of four alternator types is conducted to identify the least cost alternator that meets the challenging requirements of future automobiles. Alternator designs with conventional diode rectifiers and switched-mode rectifiers are investigated. It is found that optimized Lundell alternators are capable of meeting the demands of future systems, and that wound field synchronous machines may also be competitive. It is also found that incorporation of a simple switched-mode rectifier enables substantial improvements in designs optimized for their use.

The behavior of the Lundell alternator under load dump transient conditions is studied. It is found that rotor eddy currents limit the rate at which the machine can be de-excited to terminate the transient overvoltage. Models for the de-excitation process are developed based on experimental measurements, and new field control circuits are proposed that provide fast field de-excitation.

The use of foil field windings in Lundell alternators to improve alternator power density is also explored. Foil field windings are shown to provide higher conductor packing factors than conventional wire wound fields (e.g. 73% as opposed to 64% for a typical wire wound design) and offer improved thermal transfer properties. These advantages are demonstrated to enable significant increases in field ampere turns and achievable alternator output power. However, realizing these advantages requires new field excitation circuits that can deliver high field currents at low voltages, without exceeding the limited current ratings of alternator brushes.

Two new field excitation circuits capable of meeting the needs of foil field windings are developed and experimentally demonstrated. The first field excitation circuit is based on the use of a coreless printed circuit board transformer with a rotating secondary for contactless transfer of power to the rotor. A stationary inverter delivers high frequency ac to the transformer primary, and the power received by the transformer secondary is

rectified and delivered to the field. This approach eliminates the need for brushes, and their associated wear and current limitations. This rotating transformer topology is designed, built and tested at standstill with a foil wound bobbin. Experimental results demonstrate that a 51% increase in ampere turns on the rotor can be delivered with this approach, which is more than sufficienct for practical applications.

The second class of field excitation circuits developed in this thesis uses a DC/DC converter on the rotating side to provide a step down in voltage and a step up in current for the foil field. Control information is communicated to the rotating converter to regulate the field. An experimental alternator implementing a foil field winding and this excitation circuit is developed and experimentally validated. Tests at idle speed demonstrate an improvement of 15% in alternator output power, and an approximate increase of 30% in field ampere turns for similar temperature limits. It is anticipated that significantly larger power improvements could be achieved if the alternator stator were redesigned to take advantage of this improved field capability.

Thesis Co-Supervisor: Dr. Thomas A. Keim

Title: Principal Research Engineer and LEES Assistant Director

Thesis Co-Supervisor: Prof. Jeffrey H. Lang

Title: Professor of Electrical Engineering and Computer Science

Thesis Co-Supervisor: Prof. David J. Perreault

Title: Associate Professor of Electrical Engineering and Computer Science

Acknowledgements

This thesis would not have been possible if it were not for the help and guidance from several people. I would like to thank Wayne Ryan, who helped me with my experimental setups and prototype. Thank you very much, especially during those times you came in to help me despite being on vacation.

I would like to thank my advisors for their guidance and tutelage. Thank you Prof. Dave Perreault, Prof. Jeff Lang, and Dr. Tom Keim for all the advice and mentoring. I've learned a lot from them.

I would like to acknowledge the support I have received from the Automotive Consortium on Electrical/Electronic Systems. Thanks to the Sheila and Emanuel Landsman foundation for partially funding my work. I would also like to thank OE Plus for providing us with the alternators parts, and Dave Piccirilli for always being willing to help.

I would like to thank my friends in my lab for their friendship and support, including those whom I've learned from: Tim Neugebauer, Vahe Caliskan, and Ivan Celanovic. I also want to thank Fergus Hurley for his help with the photographs used in my thesis.

Finally, I would like to thank my family, for supporting me throughout the years. And Pia, thank you for always being there for me.

Contents

9

F. Matlab Code   **225**

List of Figures

13

17

List of Tables

Chapter 1

Introduction

The electrical power requirements in automobiles are increasing significantly. Average electrical power levels in automobiles at the time of this writing are around 1 kW with peaks above 2 kW. However, electrical demand may increase to as much as 12 kW within 5 years [1]. The shift from mechanically to electrically controlled functions is contributing to such an increase in power demand. The electrification of functions such as engine valves, water pumps, engine cooling fans and power steering, as well as new functions such as heated windshield, catalytic converter pre-heat, active suspension, communication, navigation, and entertainment accessories all contribute to the increase in power requirements. To have more electrical power available, the automobile must generate more power. This thesis will address this challenge by focusing on the source of electrical power, namely the alternator.

The main goal of this thesis is to increase both the power capability and power density so as to get more power out of automotive alternators. More power is desired without having to increase the size of the alternator due to the limited space allowed for the alternator. Improving the alternator's efficiency and transient performance are other goals of the work described here. To achieve these goals, this thesis considers alternative types of electrical generators, addresses the incorporation of switched-mode power electronics into the alternator, and explores the use of computer-aided optimization of the generator system. This thesis makes significant contributions to the design of alternators, and elucidates new means to enhance power output, efficiency, and transient performance of the alternator at minimal cost. Increased power output and efficiency are vital due to the increased number of loads in future automobiles. In addition, a cost effective solution to the load dump overvoltage is introduced in order to allow for a transition to the new 42 V bus.

1.1 Transient Considerations

The existing automobile uses a 14 V bus. Substantial currents at the relatively low voltage of 14 V result in increased size, weight, and cost of the wiring harnesses. Higher ohmic losses result in increased variation of the voltages at the loads and reduced efficiency. Higher temperatures resulting from the higher currents increase the need for cooling. A move towards a higher voltage (42 V) electrical system is presently being pursued [2]. A shift from the existing 14 V bus to a 42 V bus is likely to result in a decrease in size of the semiconductors used for control, with an associated decrease in cost [1]. Wiring harnesses are also expected to decrease in size and some loads are more efficient at the higher voltage. Although there are advantages to using the higher voltage bus of 42 V, there is also a downside. Transient performance of the alternator at the higher voltage is a concern. This thesis will address this problem to facilitate the transition to 42 V.

The overvoltages that can occur on a 42 V bus with a conventional alternator design would have much more harmful effects than those occurring on the present 14 V bus and would not be acceptable in practice. One situation where an overvoltage occurs is during a load dump. The disconnection of a load, such as the battery, from the alternator, can cause a large voltage rise. When the battery is disconnected, the alternator current cannot change instantaneously. The stored energy in the armature winding results in an impulse in the output voltage, followed by the open-circuit back voltage of the alternator being impressed upon the system until the field current is reduced [3]. The transient voltage takes around 5 to 10 ms to rise to its peak and then takes around 40 to 400 ms to decay. Energy that can easily exceed 100 Joules is forced onto the rest of the electrical system [3]. The voltage surge can be close to the open circuit voltage of the alternator which is much higher than the DC bus voltage. The transient may be limited to around 40V and last for around 100ms if there is some protection, such as with the use of avalanche diodes [4]. Without transient suppression, the transient could last for 400 ms and reach 120 V. For the 42 V system, the overvoltage could be much worse. This could damage electrical components including semiconductors. A standards working group has recommended that the maximum allowable transient overvoltage in the bus be 58V [5] to

avert the risk of electric shock. An important requirement of future alternators is to limit the amplitude and duration of the overvoltage. One of the challenges addressed in this thesis is developing methods for overvoltage suppression given the higher voltage bus of 42V.

Improving on transient performance is a major goal. One way to quickly reduce the load dump is to employ fast-field de-excitation, or sudden removal of current from the field winding. Such de-excitation is less expensive and involves smaller components than de-excitation by clamping at the stator side. Field de-excitation can be achieved by the application of a reverse voltage across the field winding, and can be made even more effective with current reversal. A reverse current through the field winding would create flux that opposes the flux created by eddy currents, which serve to limit the de-excitation rate. Means to achieve transient improvement through fast field de-excitation are explored as part of this thesis.

1.2 Power Improvement

This thesis aims to improve power output of the alternator at all speeds, but most especially at idle speed, where the power capabilities are lowest. At the idle speed point, more field ampere turns is desired, but thermal constraints limit the extent to which a designer can meet this desire. Insufficient power generation at idle leads to discharging of the battery [7]. Obviously, output power can be increased by increasing alternator size. However, the space allowed for the alternator is not increasing [8]. The goal of this thesis is to develop the least expensive alternator, within size constraints, that generates the required amount of power. In other words, the alternator with the highest power density must be determined. Typically, the smaller the alternator, the lower the cost. So the desire for lowest cost is nearly equivalent to the desire for highest power density. This design direction also maximizes the probability of meeting space constraints. In addition, the alternator must meet certain efficiency and transient performance requirements.

Several alternator types are studied in this thesis with the goal of finding the highest power density, highest efficiency alternator that meets automotive requirements. We have optimized four alternator types using the conventional alternator rectifier circuit

shown in Figure 1.1: the non-salient and salient wound field alternators, the Lundell or claw-pole alternator, and the homopolar inductor alternator.

Several years ago, Perreault and Caliskan introduced an invention based on switched-mode power electronic controls that enables increased power output and efficiency at high speeds [9, 30]. They replaced the diode rectifier in Figure 1.1 with a switched-mode rectifier and introduced a load-matching control strategy that maximizes achievable output power. The new system is shown in Figure 1.2. The three low side diodes are replaced with controllable switches creating a switched-mode rectifier, which allows for optimal power transmission via load matching. The improvements in power output and efficiency were obtained using an existing over-the-counter alternator. This thesis also presents the results of a reoptimization of alternator design, taking into account the availability of the switched-mode rectifier. A reoptimization achieves further improvements in power density and efficiency.
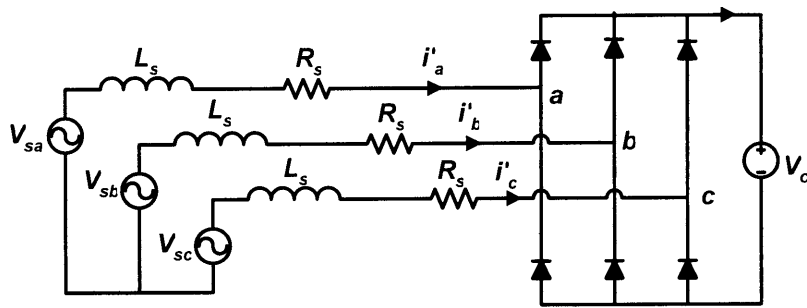
Figure 1.1: Alternator with a diode bridge rectifier with constant voltage load.
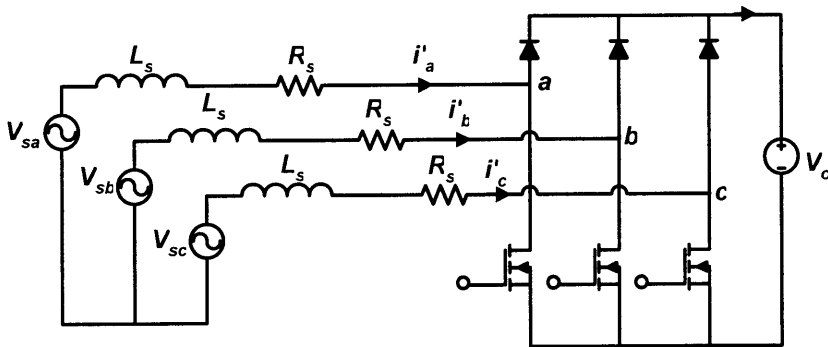
Figure 1.2: Alternator with a semi-bridge switched-mode rectifier with constant voltage load.

The thesis also explores the improvement of output power and efficiency by replacing the existing round wire field winding with a foil winding. The foil winding can have better packing and thermal properties, allowing for more field ampere turns. More field ampere turns generates more power. Saturation, however, must be taken into account. In addition, fewer turns must be used while allowing for more current since the foil winding packing factor is higher at a fewer turns count.

In order to allow for the use of a foil winding and fast field de-excitation, a new field excitation circuit is required. Such a circuit must be capable of providing the larger currents needed by the foil field winding to the rotor of the machine. In addition, the circuit must be able to apply a large negative voltage across the field winding for fast de-excitation. Allowing for current reversal is another goal. This thesis explores two possible circuit solutions. The first employs a DC/DC converter on the rotor to allow for larger currents at the (rotating) field winding without having to transfer higher currents across the brushes and slip rings of the alternator. Several variants of the circuit allow for voltage or both voltage and current reversal. A second circuit solution that is explored incorporates a rotating transformer to transfer power from the stationary to the rotating side, eliminating the brushes that limit the current that can be supplied to the field winding. This strategy also permits the use of a foil winding and fast de-excitation. These design strategies are validated through analysis, simulation and experiments, including the development of a prototype alternator with a foil winding and electronic controls.

1.3 Preview of Results

The alternator comparison and optimization results reveal that the Lundell alternator is still the most cost effective alternator while meeting the challenging requirements of future automobiles. The switched-mode rectifier results in significant cost savings of at least 10% for the optimal machines.

The field de-excitation experiments show that eddy currents limit the rate of decay of the overvoltage transient. Fast field de-excitation employing voltage reversal is used to de-excite the field winding. Voltage reversal together with current reversal further decreases the overvoltage transient duration.

27

Several circuit topologies are designed to enable a higher field ampere turn excitation of the foil winding and fast-field de-excitation of the rotor. The first topology is a rotating DC/DC converter that creates a step up in current to the field winding while maintaining the brush currents. The second topology utilizes a rotating transformer that enables contactless power transfer from the stationary side to the rotating field winding. Both topologies are implemented and achieve significant increases in ampere turns exceeding 40%. The rotating DC/DC converter is embedded into a foil wound alternator and a 15% increase in output power is achieved at a similar field winding temperature rise as a stock alternator.

1.4. Thesis Organization

This thesis consists of 8 chapters, including this introductory chapter. Chapter 2 covers the optimization and comparison of four types of alternators given the higher power and efficiency requirements of future automobiles. Analytical comparisons of the output power and efficiencies of these four alternator types are made using lumped parameter models for each of them. Operation with both diode and switched-mode rectifiers are considered. To verify the analytical results, a grid-search optimization of each of the alternators is presented with and without the switched mode rectifier. The minimum cost alternators meeting all the constraints are selected and mechanical finite element analyses are conducted to ensure that the optimal alternators meet the stress requirements. A recommendation is made on the alternator of choice for future automobiles. The benefits of the switched-mode rectifier in terms of reduced cost and size of the optimal machines are also presented.

Chapter 3 addresses the issue of load dump protection for future alternators at higher power and/or higher voltage. The load dump overvoltage is examined and the limitations in the decay rate of the overvoltage due to the presence of eddy currents in the rotor poles are investigated through experiments. Fast field de-excitation via applied voltage reversal is explored as a means of mitigating the overvoltage. A rotor model is obtained to account for the effects of the eddy currents in the rotor poles. Simulations using the model are performed to determine the necessary voltage reversal and/or current reversal required to achieve an acceptable overvoltage duration.

Chapter 4 explores the use of copper foil as a replacement for the existing round wire field winding. A foil winding is advantageous by virtue of its higher packing factor, which allows for a higher ampere turn excitation and therefore an increase in output power. Since the packing factor of copper foil is higher at fewer turns, a field winding implemented with copper foil is most effectively designed for more amperes and fewer turns.

Chapter 5 introduces circuit topologies that allow for an increased current supply to the field winding given the limitations of the existing brushes. A rotating transformer with a stationary primary and a rotating secondary is proposed that enables power transfer to the rotor field winding without the use of brushes. The use of a DC/DC converter on the rotor that will create a step up in current to the field winding and a step down in voltage is also proposed. Modifications of these two topologies will be presented that will enable the fast de-excitation of the field winding via voltage reversal across the field winding, or both voltage and current reversal.

Chapter 6 presents the results of an implementation of the rotating transformer topology. A circuit design based on an air-core printed circuit board (PCB) transformer is presented along with the experimental results that show an increase in ampere turns.

Chapter 7 presents the design implementation, and results of the rotating DC/DC converter approach. The design of the DC/DC converter is covered as well as the communications technique used to communicate the control information from the stationary side to the rotating side. An increase in ampere turns is again demonstrated and results from a prototype alternator incorporating the design are presented. Chapter 8 provides conclusions and recommendations for future work in the area.

Chapter 2

Alternator Cost Optimization

2.1 Introduction

It is commonly asserted that the Lundell (or claw pole) alternator construction that is universally used on modern automobiles must be replaced to meet the increased power demands of future vehicles. Nevertheless, a design strategy has been introduced that uses switched-mode rectification to substantially enhance the Lundell alternator/rectifier system [9, 30]. This approach allows the effective voltage seen by the bridge rectifier to be varied in what is effectively a load-impedance matching technique to enable optimum transmission of power. The use of this technique with an over-the-counter automotive alternator has shown substantial increases in power output and efficiency. One goal of the study described here is to determine how much more performance can be obtained if the Lundell alternator is optimized for use with the switched mode rectifier. In other words, how much more cost effective will the alternator be having been reoptimized for the new duty. Conclusions are also offered concerning the feasibility of building belt-driven automotive alternators for future high-electric-demand automobiles.

In addition to the Lundell alternator, alternative alternator designs are investigated and compared, including the wound-field synchronous alternator and homopolar inductor alternator [31,32,33,34,35,36]. All candidate alternators are required to produce a minimum specified power at each of two speeds, and to operate at and achieve a minimum efficiency at a third combination of speed and load. The machines are constrained to obey heat flux limitations based on heat flux levels obtained in today's automotive alternators. Magnetic parts are sized to avoid magnetic saturation. The resulting rotor inertias and rotational stresses are evaluated and compared.

2. 2 Alternator Types

Figures 2.1 through 2.4 present the alternative alternator constructions under consideration. These diagrams are somewhat stylized representations which can be

useful for comparing specific machines. These figures are generated by a drawing program (included in appendix F) from a few specific parameters. The diagrams to the left reasonably portray a section view in the axial direction, assuming that the section is taken at the boundary between the motor stack and the end turns. Many of the dimensions of the drawing represent values determined during the course of the cost optimization. (Figures 2.1 through 2.4 merely introduce the machine types; the dimensions in these figures do not represent optimized machines.) In later drawings of optimized machines, produced by the same drawing program, the rotor outside diameter, stator inside and outside diameter are to scale. So are the stator and (if applicable) the rotor slot depth and slot fraction. The inner circle does not represent an optimized value. The diagrams to the right of each motor axial section represent another rotor section, this time a vertical section taken through the diameter. In the representation of an optimized machine, all the axial dimensions represent values selected by the optimization process. The small blocks extending from the blocks representing the stator (and possibly rotor) stack(s) are approximations of the volume occupied by winding end turns.

The first class of alternators is the wound-field synchronous alternator, of which we have the non-salient [10] and salient-pole types [10, 36] shown in Figures 2.1 and 2.2, respectively. The non-salient-pole wound-field alternator has the field winding wound in slots such that the resulting flux density is approximately sinusoidal. The salient-pole wound-field alternator has the field winding wound around poles. Consecutive poles are wound to have opposite polarities.

The third machine is the Lundell or claw-pole alternator which is currently used in automobiles (Figure 2.3). The Lundell alternator has cantilevered poles. All north poles are attached to a disk on one side, and all south poles are attached to a disk on the opposite side. The poles alternate polarities as one traverses the air gap in the circumferential direction. The field winding is a single coil wound concentric with the axis of rotation.

The fourth type of machine is the homopolar inductor alternator shown in Figure 2.4. This machine has a field winding wound on the stator concentric with the axis of rotation. It is wound right next to the armature winding in the stator. The machine has two axially distinct stator stacks, and excitation flux flows in a path that crosses one air

32

gap in a radially outward direction, continues axially through a tubular ferromagnetic path (the outermost member in Figure 2.4) to the other stator stack, crosses the air gap at the second stack in the radially inward direction, and returns axially through the rotor body. The north poles are all formed from the rotor body at the axial location of one of the stacks. The south poles are formed on the same rotor body at a different axial location. All four alternators have conventional three-phase armature windings wound along slots in the stator.
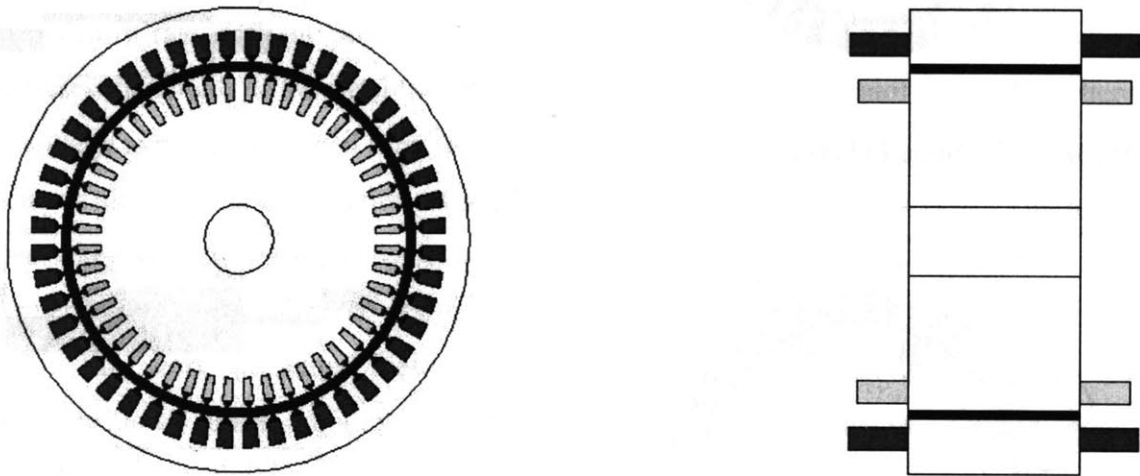
Figure 2.1: Non-salient pole wound-field synchronous alternator.
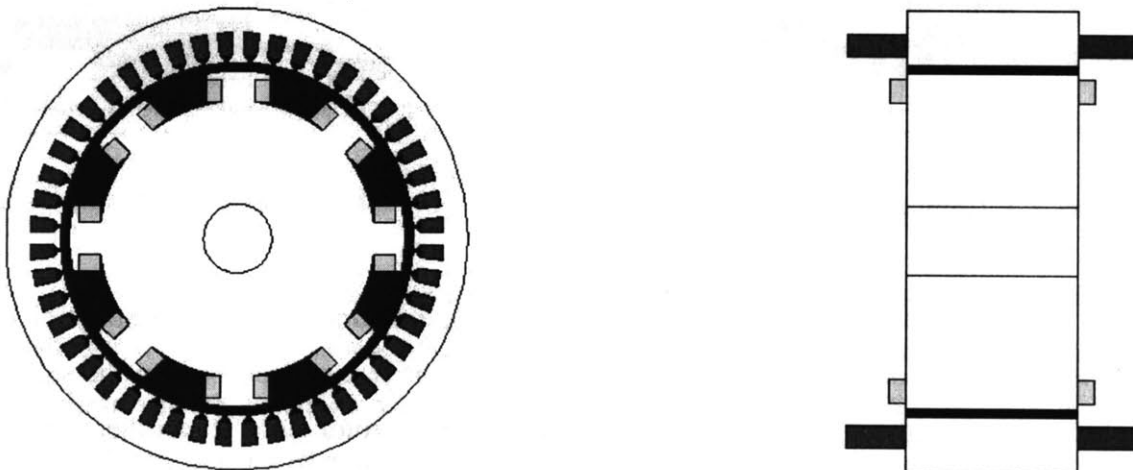
Figure 2.2: Salient-pole wound-field synchronous alternator.
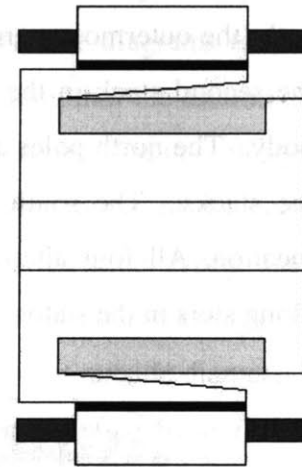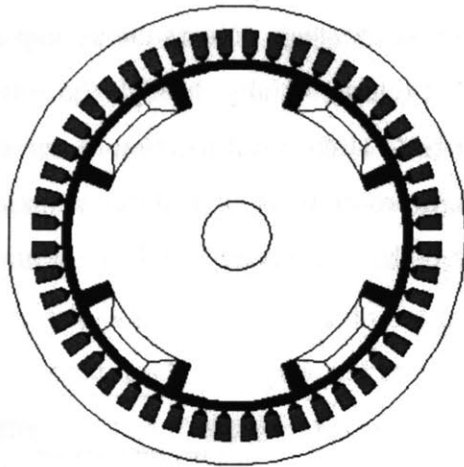
Figure 2.3: Lundell alternator.
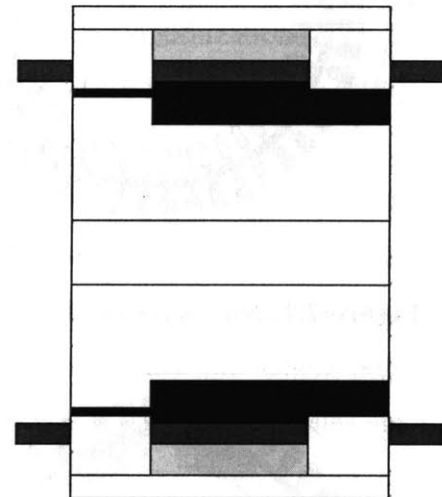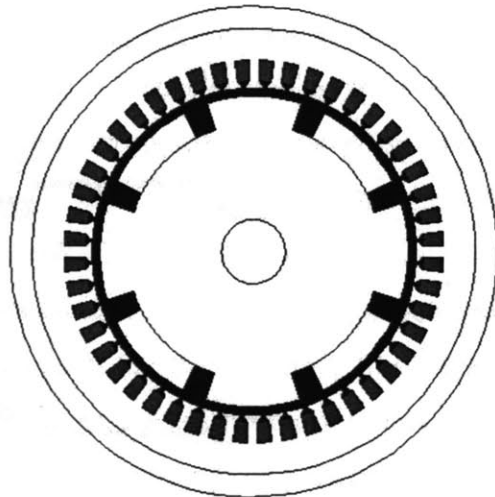
Figure 2.4: Homopolar inductor alternator.

Research has previously been done on all four alternators. The rotor construction of the wound field non-salient pole synchronous alternator is more robust than the salient pole version because its field windings are located in the rotor slots. It can therefore be run at higher speeds than the salient-pole rotor . The salient pole synchronous generator has the highest electrical output per pound per rpm among all generators according to a NASA study published in 1965 [10]. It also has the lowest reactances and therefore its regulation and transient performance are the best. Its speed limitations are due to the high

stresses that result from centrifugal loading of the field coils. For extreme environments, the Lundell and homopolar inductor alternator are more likely to be used than the wound-field alternators. The Lundell is typically smaller and lighter than the homopolar inductor alternator [11]. The Lundell, however, is more stress limited because of its cantilevered poles [12]. On the other hand, due to its robust rotor structure, the homopolar inductor alternator can be run at the highest speeds among all four alternators [11]. The flux per pole is higher for the homopolar inductor alternator than that of a salient pole alternator because of the DC flux that it has to carry. This DC flux makes it larger than the equivalently rated salient pole alternator [12]. Also, the field excitation coil location increases the length of the machine. It increases the length of the stator conductor where no voltage is being generated thus resulting in higher copper losses [12]. The homopolar inductor alternator is the heaviest of all the alternators at the same rpm [11]. The many interlocked tradeoffs among these machine types necessitates careful evaluation and comparison to identify suitable designs for future alternators.

The work presented here involves optimizing these alternators given the requirements of future automobiles and evaluating their performances and limitations. The first set of optimizations will be done assuming these alternators are utilized with a diode bridge. The second set of optimizations will assume that these alternators are connected to a switched-mode rectifier. We will then assess how much smaller and less expensive these alternators could be made given the availability of the switched-mode rectifier. This has not been done previously.

2.3 Equivalent Circuit Model

In order to determine alternator output power, an equivalent electrical circuit model is derived, taking saliency into account. This circuit as seen from the terminals of each phase will be a voltage source in series with an inductor and resistor. This circuit successfully models all four alternators.

The flux linkage equations for each alternator can be expressed as

$$\begin{bmatrix} \lambda_a \\ \lambda_b \\ \lambda_c \\ \lambda_f \end{bmatrix} = \begin{bmatrix} L_{s0} + L_{s2}\cos(2p\theta) & -L_{ss} + L_{s2}\cos(2p\theta - 2\pi/3) & -L_{ss} + L_{s2}\cos(2p\theta + 2\pi/3) & M\cos(p\theta) \\ -L_{ss} + L_{s2}\cos(2p\theta - 2\pi/3) & L_{s0} + L_{s2}\cos(2p\theta + 2\pi/3) & -L_{ss} + L_{s2}\cos(2p\theta) & M\cos(p\theta - 2\pi/3) \\ -L_{ss} + L_{s2}\cos(2p\theta + 2\pi/3) & -L_{ss} + L_{s2}\cos(2p\theta) & L_{s0} + L_{s2}\cos(2p\theta - 2\pi/3) & M\cos(p\theta + 2\pi/3) \\ M\cos(p\theta) & M\cos(p\theta - 2\pi/3) & M\cos(p\theta + 2\pi/3) & L_r \end{bmatrix} \begin{bmatrix} i_a \\ i_b \\ i_c \\ i_f \end{bmatrix}$$

$$(2.1)$$

where $p\theta = \omega t + \delta$ is in electrical degrees, L_r is the field winding self inductance, M is the magnitude of the field and armature mutual inductance, L_{s0} corresponds to the armature winding self inductance if the machine were non-salient, and the L_{s2} term reflects saliency. The flux linked by phase a of the armature winding due to the field excitation is

$$\lambda_{af} = M\cos(p\theta)i_f \qquad (2.2)$$

The generated back voltage is

$$\frac{d\lambda_{af}}{dt} = -\omega M \sin(p\theta) i_f \qquad (2.3)$$

The three-phase armature currents (motor convention) may be expressed as

$$i_a = I_s \sin(p\theta - \phi) \qquad (2.4)$$

$$i_b = I_s \sin(p\theta - \phi - 2\pi/3) \qquad (2.5)$$

$$i_c = I_s \sin(p\theta - \phi + 2\pi/3) \qquad (2.6)$$

where ϕ is the internal power factor angle or the angle between the back-emf and the armature phase current. The flux linked by phase a due to all three armature phases (with i_f equal to zero) is

$$\begin{aligned} \lambda_{as} &= (L_{s0} + L_{s2}\cos(2p\theta))I_s \sin(p\theta - \phi) \\ &\quad + (-L_{ss} + L_{s2}\cos(2p\theta - 2\pi/3))I_s \sin(p\theta - \phi - 2\pi/3) \\ &\quad + (-L_{ss} + L_{s2}\cos(2p\theta + 2\pi/3))I_s \sin(p\theta - \phi + 2\pi/3) \\ &= (L_{s0} + L_{ss})I_s \sin(p\theta - \phi) - \frac{3}{2}L_{s2}I_s \sin((p\theta - \phi) + 2\phi) \\ &= (L_{s0} + L_{ss} - \frac{3}{2}L_{s2}\cos(2\phi))I_s \sin(p\theta - \phi) \\ &\quad - \frac{3}{2}L_{s2}\sin(2\phi)I_s \cos(p\theta - \phi) \end{aligned}$$

$$(2.7)$$

The non-ohmic voltage drop across phase a due to balanced currents in the three phases is

$$\frac{d\lambda_{as}}{dt} = (L_{s0} + L_{ss} - \frac{3}{2}L_{s2}\ \cos(2\phi))\frac{di_a}{dt} + \frac{3}{2}\omega L_{s2}\ \sin(2\phi)i_a \tag{2.8}$$

from which expressions for the equivalent inductance and resistance are

$$L_s = L_{s0} + L_{ss} - \frac{3}{2}L_{s2}\cos(2\phi) \tag{2.9}$$

$$R_s = r_a + \frac{3}{2}\omega L_{s2}\sin(2\phi) \tag{2.10}$$

where r_a is the ohmic resistance of the armature winding.

The equivalent circuit representing equations 2.3 and 2.8 to 2.10 is shown in Figure 2.5. Here V_{sa}, V_{sb}, and V_{sc} are the back-emf excitation voltages, $d\lambda_{af}/dt$, $d\lambda_{bf}/dt$, and $d\lambda_{cf}/dt$.
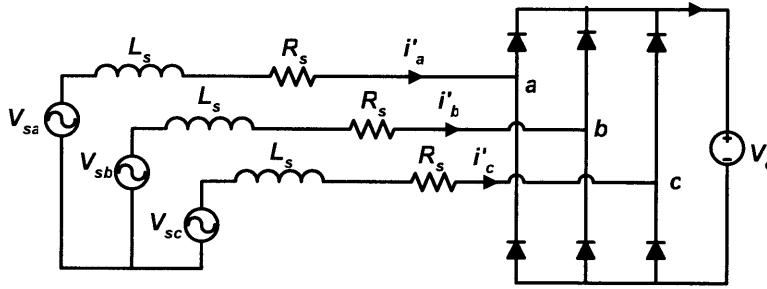
Figure 2.5: Alternator, rectifier and constant voltage load circuit.

In [9], it is shown that the use of a boost rectifier circuit can be understood as affecting the operation of the machine in essentially the same manner as the diode rectifier affects the machine in Figure 2.5, with the additional feature that varying the duty ratio on the boost switch gives the flexibility to vary the effective dc voltage seen at the rectifier output over a range from zero to the physical limit of the dc source. This boost rectifier (switched-mode rectifier) circuit is shown in Figure 2.6.
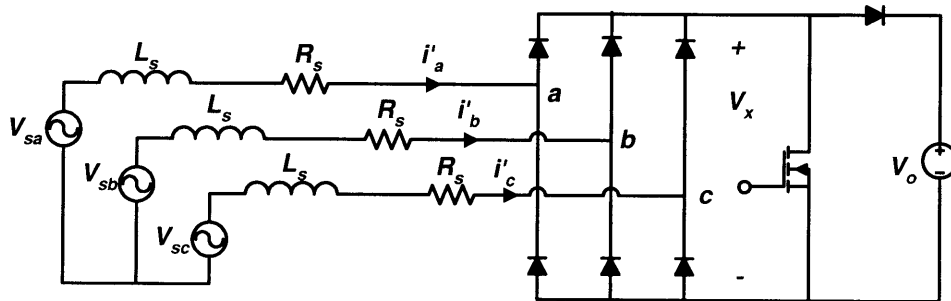
Figure 2.6: Alternator, switched-mode rectifier, and constant voltage load circuit.

The work above shows how we can conveniently include the effect of rotor saliency in our analysis, but the rectifier in Figure 2.5 (or 2.6) still presents a non-linear element which precludes a fast, analytic solution. Reference [13] provides a convenient approximation which permits a simple solution. Based on [13], the circuit in Figure 2.5 (or 2.6) can be approximated by the circuit shown in Figure 2.7 with balanced resistive loads.
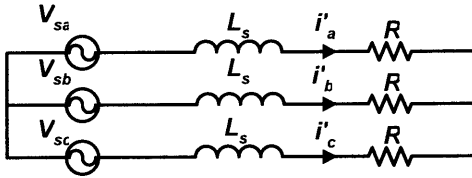
Figure 2.7: Equivalent circuit with balanced resistive loads.

Following [13], each resistive load has the value

$$R = R_s + \frac{V_{o1}^2 R_s + V_{o1}\sqrt{(\omega L_s)^2 (V_s^2 - V_{o1}^2) + R_s^2 V_s^2}}{V_s^2 - V_{o1}^2}$$

$$R = \frac{V_s^2 R_s + V_{o1}\sqrt{(\omega L_s)^2 (V_s^2 - V_{o1}^2) + R_s^2 V_s^2}}{V_s^2 - V_{o1}^2}$$

(2.11)

where V_s is the back-emf voltage and where

$$V_{o1} = \frac{4}{\pi}\left(\frac{V_0}{2} + V_d\right)$$

(2.12)

where V_d is a diode drop. The power angle can be obtained using

$$\tan(\phi) = \frac{\omega L_s}{R}$$

(2.13)

The output power is then

$$P = \frac{3}{\pi} I_s V_o = \frac{3}{\pi}\left(\frac{V_s}{\sqrt{(\omega L_s)^2 + R^2}}\right) V_o$$

(2.14)

2.4 Lumped Parameter Model Derivations

Having completed the circuit model, the appropriate inductances and resistances must then be determined. The procedure is to first determine the flux density in the air gap due to the field winding and the armature windings and then to determine the flux linked by the stator windings from the various sources. The flux linked by each armature winding due to the field excitation will give the back electromotive force while the flux linked by each armature winding due to all three armature phase currents yields the synchronous reactance and equivalent resistance due to armature reaction. The flux density in the air gap is found by multiplying the magnetomotive force (MMF) across the air gap by the permeance per unit area. The MMF drop across the air gap is obtained assuming that the permeability of steel is infinite which implies that flux lines are assumed to terminate perpendicularly to the steel. The details of the process are instructive and straightforward, but also tedious. They are presented in Appendix A.

2.5 Simplified Analytical Evaluation and Calculation

The comparative evaluation is conducted in several ways and at several different levels of analytical and computational sophistication. The most extensive comparison is the result of a cost optimization study. This study, which is presented in Section 2.6, compares machines of different constructions, each of which is capable of operating over a specified area in power-speed space and meeting certain other constraints. The lowest cost machine of each type meeting all the constraints is selected. The results of that comparison will be presented later in Section 2.7. In this section we present simplified analytical results which provide some level of insight about how fundamental differences among the machine types give rise to substantial differences in performance, as observed in Section 2.7.

Consider the approximate equivalent circuit of Figure 2.7. It is readily shown that for fixed values of machine parameters, maximum power is delivered to the load at the load-matched condition (when the synchronous reactance equals the effective resistance). The main goal is to obtain the lowest cost machine meeting all the requirements. A comparison of machines loaded to maximum power may nevertheless be

39

relevant, because least cost machines may be expected to be loaded to maximum power at one or more design points. As an aside, there is one more consideration to make before accepting that impedance-matched (maximum power) operation is relevant to the pursuit of least-cost machines. If the power rating of the machine is a continuous, as opposed to a momentary, rating, impedance-matched operation is relevant only if the machine is well enough cooled to operate at this loading. As a rule, the inductive contribution to machine reactance is dominant over the resistive component, so armature resistive losses tend to be small compared to load power. In practice, it often is possible to design machines which are adequately cooled when operated at the impedance-matched load.

The power delivered to an impedance-matched load can be written approximately as

$$P_{\max} = \frac{3}{\pi} I_s V_x \tag{2.15}$$

where I_s is the armature phase current and V_x is the effective voltage seen at the armature terminals which varies depending on the duty ratio of the switched mode rectifier. Based on [13], the armature phase current is obtained as

$$I_s = \frac{\sqrt{V_s^2 - \left(\frac{2V_x}{\pi}\right)^2}}{\omega L_s} \tag{2.16}$$

Substituting I_s from equation 2.16 into equation 2.15 and taking the derivative with respect to V_x, the output power is maximum at

$$V_{xopt} = \frac{\pi}{\sqrt{8}} V_s \tag{2.17}$$

Substituting V_{xopt} back into equation 2.15 will give the maximum power equal to

$$P_{\max} = \frac{3}{4} \frac{V_s^2}{\omega L_s} \tag{2.18}$$

Since the magnitude of the back emf is

$$V_s = \omega L_{afm} I_f \tag{2.19}$$

the gross output power at the load-matched condition can be found to be

40

$$P_{\max} = \frac{3}{4}\omega \frac{\left(L_{afm}\Big/N_f\right)^2}{L_s}\left(N_f I_f\right)^2 \qquad (2.20)$$

where N_f is the number of field turns and I_f is the field current. This is obtained having ignored the armature resistance, diode drop, the larger air gap in the case of the homopolar inductor alternator, saliency, and the leakage inductances. Following (2.20) and Appendix A.6, the maximum power capability (at the impedance-matched load) for each of the the four machines is

$$P_{\max} \cong 8k_{wf}^2\left(\frac{\omega\mu_o RL}{\pi g}\right)\left(\frac{N_f I_f}{2p}\right)^2 \qquad (2.21)$$

for the non-salient wound-field alternator,

$$P_{\max} \cong 8\left(\frac{\omega\mu_o RL}{\pi g}\right)\left(\frac{N_f I_f}{2p}\right)^2 \qquad (2.22)$$

for the salient wound-field alternator,

$$P_{\max} \cong 8\left(\frac{\omega\mu_o RL}{\pi g}\right)\left(\frac{N_f I_f}{2}\right)^2 \qquad (2.23)$$

for the Lundell alternator, and

$$P_{\max} \cong 4\left(\frac{\omega\mu_o RL}{\pi g}\right)\left(\frac{N_f I_f}{2}\right)^2 \qquad (2.24)$$

for the homopolar inductor alternator.

The symbols R, L, and g in (2.21)-(2.24) correspond to the air gap radius, axial length, and air gap radial dimension respectively. The ratios of output powers among the machines can be found in Table 2.1.

Table 2.1: Approximate ratios of output power (column over row)

	Non-salient WFSM	Salient WFSM	Lundell	Homopolar
Non-salient WFSM	1	$1/k_{wf}^2$	p^2/k_{wf}^2	$p^2/(2k_{wf}^2)$
Salient WFSM		1	p^2	$p^2/2$
Lundell			1	½
Homopolar				1

It is evident that the Lundell alternator produces the most power in this comparison, followed by the homopolar inductor alternator, the salient-pole wound field alternator, and lastly, the non-salient pole wound field alternator. The factor of p^2 results from the Lundell and inductor alternators having their field windings exciting all the poles. For these two machines, the required number of field ampere turns is independent of the pole count.

Output power comparisons given the same number of field ampere turns are shown below in Figure 2.8. The ordinate is terminal voltage operating with a resistive load, normalized to the no-load voltage. This shows that at the same number of field ampere turns, the Lundell outperforms the rest by a large margin. Figure 2.8 is prepared for the case of four pole pairs. The machines being compared in Figure 2.8 all operate at the same speed and all correspond to R = 0.1 m, L = 0.1 m, and g = 0.005 m.

The comparison which gives rise to Figure 2.8 required many choices to be able to reduce the mathematical expressions for the capabilities of each machine type to simple expressions with many common terms. Many of these choices were of necessity arbitrary, but we tried in every case to be reasonable. The single most important feature giving rise to the striking comparison in Figure 2.8 is the fact that in the Lundell and homopolar machines, each ampere turn of field excitation excites field flux in every pole, while in the wound-field machines, each ampere turn excites flux in only one pole. This difference is made evident by requiring all machine types to have the same number of poles. The output power at each of the peaks corresponds directly to equations 2.21-2.24.

It can further be argued that comparison at a constant number of field ampere turns is also unreasonable. It is quite credible that the cost of a field ampere turn for a Lundell alternator as measured by most reasonable means is higher than the cost of a field ampere turn for a wound field machine. However, the fundamental message of Figure 2.8 does not depend on the comparison being accurate to 5% or even to 50%. Rather, the principal conclusion from Figure 2.8 is that the favorable field excitation path of the Lundell alternator (and to a strong extent, the homopolar inductor alternator) is a powerful advantage over other machine types, in terms of power deliverable from a machine of a given size. For other machine types to prevail in an overall comparison, it will be necessary that these other types exhibit strong advantages in other elements of design not considered here.

Figure 2.9 shows a different comparison. Here the machine types are compared at constant field ampere turns per pole. On this basis, the salient pole machine is the equal of the Lundell alternator. In practice, it may not be possible to put so many field ampere turns on a salient-pole structure.
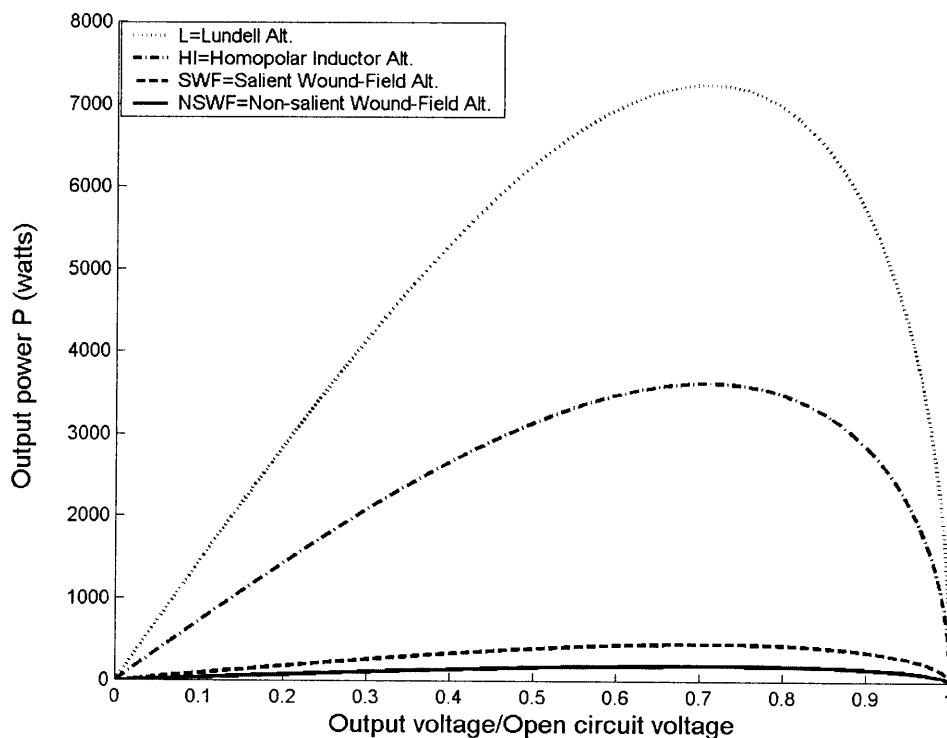
Figure 2.8: Output power curves vs. voltage at same number of field ampere turns.
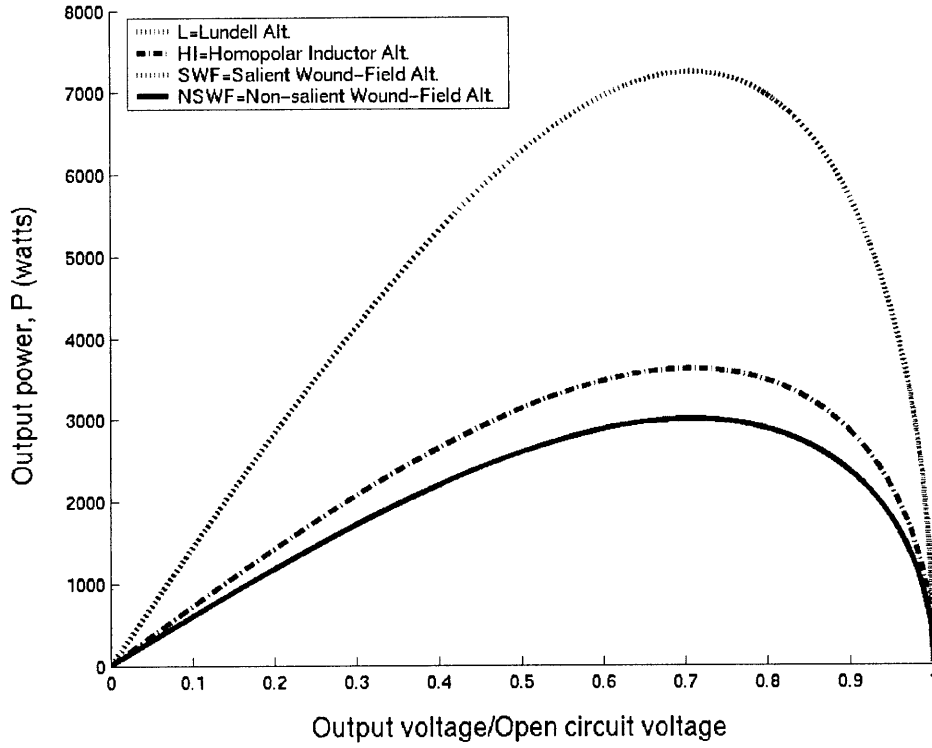
Figure 2.9: Output power curves vs. voltage at the same number of field ampere turns per pole

The electrical efficiency can also be solved for at the load-matched condition. Electrical efficiency is defined as

$$\eta = \frac{P_{out}}{P_{out} + P_{field} + P_{arm}}$$

$$\eta = \frac{P_{max} - P_{field}}{P_{max} - P_{field} + P_{field} + P_{arm}} \tag{2.25}$$

$$\eta = \frac{P_{max} - P_{field}}{P_{max} + P_{arm}}$$

where P_{max} is the gross power output, P_{out} is the net power output, P_{field} is the field loss, and P_{arm} is the armature loss.

The field loss is

$$P_{field} = I_f^2 R_f = \left(N_f I_f\right)^2 \left(\frac{R_f}{N_f^2}\right) \tag{2.26}$$

where R_f is the field winding resistance. The armature loss is approximated by

$$P_{arm} = \frac{3}{2} I_s^2 R_a \qquad (2.27)$$

where R_s is the armature resistance. Substituting the optimal V_{xopt} in Equation 2.17 into Equation 2.16 gives the armature phase current I_s at the load matched condition

$$I_{sopt} = \frac{V_s}{\sqrt{2}\omega L_s} \qquad (2.28)$$

Substituting Equation 2.28 into Equation 2.27 and using equation 2.19 for V_s gives

$$P_{arm} = \frac{3}{4} \frac{\left(L_{afm}/N_f \right)^2}{L_s^2} \left(N_f I_f \right)^2 R_a \qquad (2.29)$$

At the load matched condition, the alternator electrical efficiency is therefore

$$\eta = \frac{\omega L_s - \dfrac{4 R_f L_s^2}{3 L_{afm}^2}}{\omega L_s + R_a} \qquad (2.30)$$

with a minimum value of zero which occurs when all the power generated is used to power the field winding, resulting in no net output power. Only the field and armature conduction losses were taken into account for this efficiency calculation. The efficiency is independent of field ampere turns and therefore independent of the net power requirement. This is because at the load matched condition, the field copper losses and armature losses are proportional to the square of the number of field ampere turns as shown in Equations 2.26 and 2.29 which is the same dependence that the gross output power has on field ampere turns as shown in Equation 2.20. The efficiency is also independent of the operating voltage at every load matched point. The efficiency, however, varies with speed. The efficiency increases with larger field armature mutual inductance. Using the same approximations and simplified conditions for the comparison of output power (at idle speed) along with the additional assumption that R_f is independent of machine type, the efficiencies of the non-salient wound field, salient wound field, Lundell, and homopolar inductor alternators are 0.4727, 0.5508, 0.8405, and 0.6231, respectively. These estimates indicate that the Lundell alternator has the highest efficiency. This is primarily due to its large field armature mutual inductance.

.

45

Based on these simple calculations, and considering load–matched operation for maximum power, the Lundell alternator is the most promising of the candidates considered here. In addition to its many simplifications, this analysis ignores several other considerations which may substantially influence the choice of machine type. For example, for a given diameter and speed, the rotor stresses in a Lundell alternator can be expected to be much higher than in other machine types. If the range of diameters and speeds under consideration are such that rotor stresses are comfortably below stress limits for all machine types, then this difference is unimportant. But if rotor stresses in a Lundell rotor are excessive, the application may require use of a different machine type. But in general, in circumstances where maximum power per unit volume is required and, by implication, assuming comparable average mass densities, also in cases where maximum power per unit weight is the objective, the Lundell machine warrants high consideration. Likewise, assuming comparable mass densities among machines, the Lundell machine is expected to be highly effective on a power per mass basis.

2.6 Optimization

2.6.1 Search for Optimal Machines

This section provides a more detailed comparison of the four alternators. Here, the four alternators are cost optimized via numerical methods given several requirements and constraints. First among these are the output power and efficiency requirements, arrived at by a consensus of a group of interested researchers and engineers [14,15], and based on anticipated load and performance requirements. Each machine must provide at least 4 kW at 1200 rpm, and at least 6 kW at 12000 rpm; 12000 rpm is the maximum operating speed. Each must be at least 75% efficient while generating 3250 W and running at 3000 rpm. The power outputs stated here are net; gross power must include net power plus field winding loss, but no allowance is made for field winding power conversion inefficiencies. Maximum limits are set for the heat fluxes as discussed later in Section 2.6.2.1. Saturation of the teeth and pole necks are avoided by requiring the flux densities to be less than 1.8 Tesla. The back iron radial thickness dimension is not a search variable, but is determined based on this same flux density limit.

46

Given these requirements, the machines are optimized for cost by using a grid search over the entire design space. The objective function is a very simple one. The cost of the copper windings is added to the cost of the active magnetic materials to determine a total cost. The volume of the windings is estimated from the geometry, with simple approximations for end turn volumes, and assuming a turns packing density which is assumed constant for all machines. The mass of copper and then the dollar cost of copper is computed. The active magnetic materials included the stator stack and the magnetically active rotor (a stack or a solid object). The volume and mass of these components are computed, using a stacking factor of unity in the case of laminated structures. A constant price per unit mass is applied to the entire (rotor plus stator) iron mass. The specific costs assumed are $5/kg for copper and $1/kg for iron.

The most cost effective machines are further compared based on size, rotor inertia, and mechanical stresses. We want the best alternator to be the most cost effective alternator which should have other desirable properties such as small volume, low rotor inertia, and allowable mechanical stresses.

Unlike previous optimizations done on alternators [14]-[15], the apparent load voltage seen at the output of the rectifier can be varied. This is the fundamental contribution of the switched-mode rectifier. For each of the operating points, the optimizer determines the minimum required number of field ampere turns are determined to generate enough power across effective output voltages less than or equal to 42 V. Thus, the machines are not necessarily operating at the load matched condition or peak of the power vs. voltage curves.

For each geometry and a given set of output voltages, the highest number of armature turns that meets the efficiency and heat flux limits is selected. This is done because the flux densities in the air gap tend to decrease with a higher number of armature turns and so the back iron thicknesses are allowed to decrease as well.

47

2.6.2 Details on Properties Subject to Constraints

2.6.2.1 Heat Transfer Limits

Candidate windings are evaluated on the basis of heat flux density, or heat flow per unit of cooling area. Machines with heat fluxes below the established limit are considered as candidates for the lowest cost machine; machines with heat flux densities above the limit are removed from further consideration.

The total heat flow from a winding is considered to be the ohmic loss within that winding, and all the heat flux is presumed to flow over a specified heat transfer area. In most cases, the area used is an approximation to the area exposed to air in the end turn structure of the machine. In Figures 2.1 through 2.4, for example, the end turns are represented schematically by rectangular figures in the transverse section views. Each of these rectangular figures can be considered to represent the cross section of a ring of rectangular section, coaxial with the machine. One axial face of each ring is considered to abut the stator or rotor, as the case may be. Heat is presumed to enter the ring through this face. The remaining surface area of the ring is presumed to be available for heat transfer.

The radial dimension of the rings representing the end turns are the same as the radial slot dimension for the winding in question, and the axial dimension is determined by a simple approximation. For example, the exposed area of the armature winding for each of the four machines is

$$A_a = 2\left(\pi\left(R_{statslotbot}^2 - R_{statin}^2\right) + 2\pi\left(R_{statslotbot} + R_{statin}\right)W_{endturn}\right) \tag{2.31}$$

where $R_{statslotbot}$ and R_{statin} are the stator slot bottom radius and stator inner radius respectively, and $W_{endturn}$ is the distance that an end turn extends from the edge of the stator. The method for determining the end turn width $W_{endturn}$ can be found in [15].

The field windings of the homopolar and Lundell alternators do not have end turns in the same sense as the other windings considered here. In these cases, the complete winding is approximated as a ring (toroid) of rectangular cross section, and heat transfer is presumed to occur on only one surface with a radial normal, in particular the outer surface in the case of the Lundell alternator and the inner surface for the homopolar alternator.

48

It is acknowledged that the real heat transfer performance of an alternator is far more complicated than the situation depicted by this simple model, but the simplifications offered here are reasonable for the purpose of this study. The dominant cooling path for windings in automotive generators is convection through the end turns, and the temperature drop at the winding-to-air interface is generally dominant over other temperature drops in the cooling path. Other heat sources (iron loss, bearings, windage, etc.) and other heat paths (radial through the core, axial along the shaft, etc.) both exist, but the heat sources and coolant paths considered here are dominant over the others, especially in the performance-limiting conditions.

The thermal model presented here has the benefit that the limiting values for heat flux can be determined by observation of present-day design practice. In an automotive alternator, for example, the dimensions of the armature end-turn ring and of the field winding heat transfer surface can be measured, and the value of winding losses can be calculated from the rated current and the measured winding resistance. These inferred values have been applied directly to the machines in this study. This implies that for a machine in this study to be adequately cooled, it is necessary only that the ratio of actual effective end-winding heat transfer area to the area of its approximating ring be similar between the machine from this study and the alternator from which the measurements were taken, and further that the air flow and heat transfer coefficient be comparable in the two machines. Since both the required area and the required air flow and heat transfer coefficient have already been achieved in one case (the measured machine), it should not be impossible to achieve them in the relatively similar proposed new machines. The heat flux density limits used here are 7.28 x 10^4 W/m^2 for the armature windings of all machines and field winding of the wound-field alternators and 6200 W/m^2 for the field windings of the Lundell and homopolar inductor alternators based on actual measurements.

The heat flux density for the field winding can be expressed as

$$q_f = \frac{\left(\frac{R_f}{N_f^2}\right)\left(N_f I_f\right)^2}{A_f} \qquad (2.32)$$

where R_f is the field resistance and A_f is the exposed area of the field winding. The partitioning of terms in Equation 2.32 is not as capricious as it may first seem. The importance of the grouping $N_f I_f$ is well understood from Section 2.5, and the grouping R_f/N_f^2 makes sense when one recognizes this as the resistance of a one-turn field winding occupying the available winding volume.

The heat flux density equation for the stator winding is

$$q_a = \frac{\frac{3}{2} I_s^2 R_a}{A_a} \qquad (2.33)$$

where I_s is the peak armature phase current, R_a is the armature resistance and A_a is the area of the exposed armature winding.

2.6.2.2 Efficiency

In calculating the efficiencies, only the field and armature winding losses and diode losses are included. The Lundell and homopolar inductor alternators are expected to have higher efficiencies since the number of field ampere turns do not have to increase with an increase in pole count. As indicated in the discussion above, we acknowledge that other losses exist and are important in some cases, but for this study, only the winding losses and diode losses are included.

2.6.2.3 Saturation

In order to compare the alternators in terms of saturation, expressions for the flux densities in the air gap, obtained in Appendix A.7, are used. Only the average and fundamental components are used. The flux density in the air gap is related to the flux density in the stator, and, if relevant, the rotor teeth and also to the flux density in the stator return iron by geometric constants.

2.6.1.4 Inertia

The rotor inertia for each of the four machines is determined using simplified approximations of rotor geometry. All the tooth and pole boundaries with a large radial component are modeled as purely radial. The main factors that contribute to inertia will be the air gap radius and machine length. Optimization of machines will result in machines with different air gap radii and machine length. The machines that create air gap fluxes most effectively are expected to have the smallest radii and lowest inertia. The ordering from best to worst in terms of output from a fixed geometry with a fixed number of field ampere turns is likely to apply as well to rotor inertia.

2.6.3   Results

2.6.3.1 Optimization Results Using Switched-Mode Rectifier

The optimization is performed to obtain the least expensive machines (flowchart is shown in Appendix B and code in Appendix F) that meet the requirements. A satisfactory machine will have a combination of radii, active length, air gap width, and slot depth that allows it to generate enough power while meeting the efficiency, heat flux, and saturation limits.

The four optimal machines are shown in Figures 2.10-2.13. For ease of comparison, the machines are drawn to the same scale. The inductor alternator optimized to the largest dimensions. This is due to saturation limitations since the flux in the air gap in addition to the alternating flux is an average flux. In a machine with no average flux, field ampere turns can be increased without increasing saturation, provided that direct axis armature ampere turns increases a corresponding amount. In the homopolar inductor alternator, direct axis armature ampere turns can cancel the alternating flux, but not the circumferential average flux. Thus, in order to increase the number of field ampere turns to generate the required power, the dimensions of the machine must be increased. The large dimensions cause this machine to be the most expensive.

The non-salient wound-field alternator is the next most expensive machine, followed by the salient-pole wound-field alternator and finally, the Lundell, which is the

least expensive alternator. The salient version of the wound-field alternator performs better than the non-salient type because of the field winding factor which is less than one for the non-salient alternator. This diminishes the output power of the non-salient type machine.

In agreement with the simplified analysis of Section 2.5 is the result that the Lundell alternator is the most effective in generating power. Looking back at the simplified analysis, given the same output power, the Lundell alternator has the largest field-armature mutual inductance which contributes to efficiency. In fact, looking at Table 2.2, the efficiency of the optimal Lundell alternator is around 83%, which is far above the limit of 75%.

The limitations for the Lundell alternator are saturation of the rotor structure and the field heat flux limit. The Lundell alternator rotor structure is limited by saturation since the flux entering all the south poles for example, has to enter the supporting disk (also known here as the flux plate) through the end of the poles and return axially in the steel radially inside the field winding. This requires minimum thicknesses for both pieces of steel. Thus the rotor radius can not be reduced further.

As reported in Section 2.6, the field winding heat flux limit for the Lundell alternator was lower than that used for the wound-field machines, consistent with our observations of an automotive alternator. Table 2.2 shows that the heat flux limit was reached before the efficiency limit. It is plausible that our observation is generally correct, in that it is credible that it will be harder to extract heat from a cylindrical surface, shielded from high velocity air flow by the claw pole structures, than from a finely subdivided end turn structure in the direct path of the flow from a radial fan. Since the field currents are lower for the Lundell and homopolar inductor alternator, the lower heat flux limit does not severely limit their capabilities compared to the wound-field alternator.

The last three rows in Table 2.2 show the effective voltage for each machine at each operating point. The action of the switched-mode rectifier makes it possible for a machine to run at an effective voltage anywhere at or below the nominal bus voltage of 42 volts. It is evident that the optimizer found it beneficial to use switched-mode operation of the controlled rectifier only at the high-torque low-speed design point. The

entries of 42 volts imply no switched-mode action. These operating points could be achieved with a simple diode rectifier. Since active switches are indicated for low-speed operation, it seems probable that they would be used in synchronous rectifier mode, whenever boost mode is not indicated.

0   50 mm
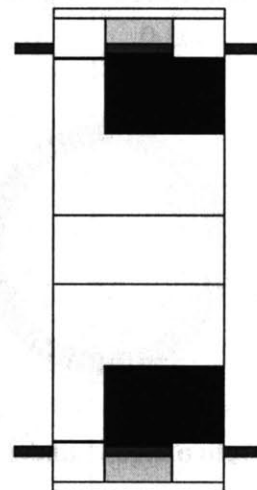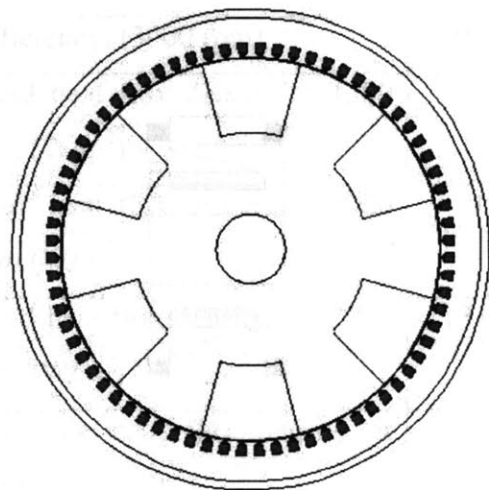
Figure 2.10: Homopolar inductor alternator.
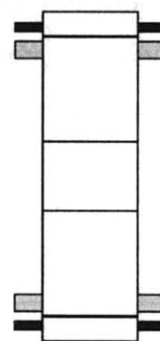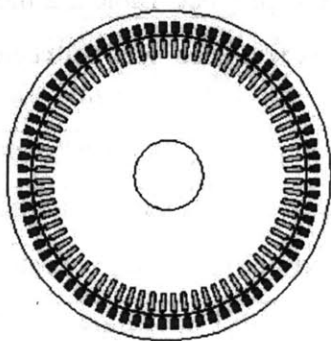
Figure 2.11: Wound-field non-salient pole alternator.
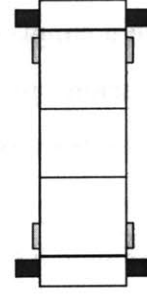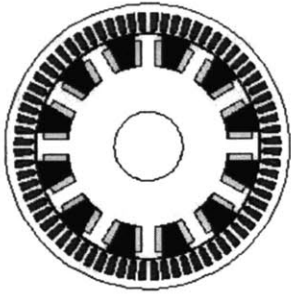
Figure 2.12: Wound-field salient pole alternator.
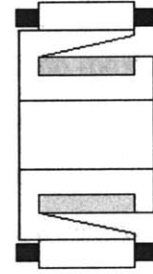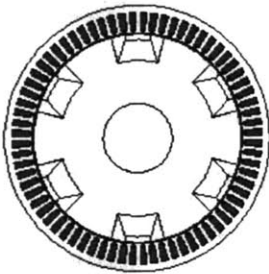
Figure 2.13: Lundell alternator.

Perhaps the most remarkable finding is not that the Lundell alternator was found to be least expensive, but that, given the huge difference seen in Section 2.5, the difference between the Lundell and its closest competitor is as small as it is. Given the many approximations and inaccuracies remaining in the process to produce Table 2.2 the fairest conclusion is probably that the competition for lowest cost is a dead heat between the Lundell alternator and the wound-field salient alternator.

Table 2.2: Comparison of optimal machines.

Feature	WFNS	WFS	Lundell	HIA
Cost ($ steel+$ copper)	16.2	12.0	11.8	40.3
Outer radius (m)	0.0949	0.0832	0.0771	0.1393
Outer length (m)	0.055	0.05	0.0784	0.099
Max Stress (10^8N/m^2)	0.8	0.4	3.45	1.2
Inertia (kg.m^2)	0.0245	0.0072	0.0077	0.0686
Efficiency (3000 rpm)	0.7598	0.7582	0.8267	0.8064
Field heat flux density at 1200 rpm (W/m^2)	53261	41005	6184	6024
Field heat flux density at 3000 rpm (W/m^2)	9512	9698	1721	2090
Field heat flux density at 12000 rpm (W/m^2)	31806	57680	5472	5937
Armature heat flux density at 1200 rpm (W/m^2)	61455	60643	53820	17023
Armature heat flux density at 3000 rpm (W/m^2)	10779	14567	15307	7432
Armature heat flux density at 12000 rpm (W/m^2)	43502	71968	52789	25835
Flux density at 1200 rpm (T)	1.758	1.753	1.788	1.783
Flux density at 3000 rpm (T)	0.777	0.758	0.881	0.776
Flux density at 12000 rpm (T)	0.333	0.293	0.566	0.489
Output voltage at 1200 rpm (V)	30	31	28	35
Output voltage at 3000 rpm (V)	42	42	42	42
Output voltage at 12000 rpm (V)	42	42	42	42

2.6.3.2 Stress Analysis of Optimum Machines

Meeting mechanical stress limits is an important consideration in machine design. Based on finite element analyses, the salient wound-field alternator is the most robust stresswise among all four machines, followed by the non-salient wound-field alternator, the homopolar inductor alternator and the Lundell alternator. This rank order arises at least in part because we have considered stress only in the rotor iron. We are aware that it is common in wound-field machines for the maximum structural stress to occur not in the main rotor steel but rather in wedges or other structures which retain windings in their places. It is also possible that the most limiting effect of rotation and temperature does not occur in any part of the rotor structural material, but rather in the compressive load in the conductor itself. While the conductor is not in the load path, the yield stress of copper, especially at elevated temperature, is so low that this consideration may be more restrictive than the capability of the rotor structure. Although we acknowledge these effects, we do not expect them to render any of the machines analyzed here mechanically unsuitable for their intended duties, so we do not explore these matters further.

The Lundell alternator as expected has the highest stress due to the cantilevered pole structure protruding from the supporting disks. The stresses, though, are within the allowable limits set for steel.

The finite element models for each of the candidate machines are shown in Figures 2.14 through 2.17. The arrow in each figure points to the maximum stress location. In each case, symmetry is exploited to the maximum possible extent. In general we see one half of one pole, but in the case of the non-salient wound-field machine we see one half of one tooth. The models in these figures are not in any case the first model considered, but reflect adjustments made to reduce peak stress where needed.

It is frequently the case that the largest stress in the entire solution domain occurs at a geometric discontinuity. This occurs for two reasons. First, geometric discontinuities do introduce stress concentrations in true (physical) stress fields. Second, finite element methods give rise to mathematical, non-physical, large numbers due to approximation errors at geometric discontinuities. Fillets and larger radii tend to improve the calculated

stress by acting favorably on both effects, and finer grid geometries can be used to control approximation errors.

We have used both techniques, with special emphasis on fillets, to reduce the calculated stresses. We believe the geometries we have chosen represent reasonable approximations to practical solutions, and are not unduly compromised by insensitivity to good mechanical design. This last statement is probably least robust in the case of the Lundell alternator.

The only constraint which we placed on the mechanical stress was a requirement that the peak von Mises stress be less than 4×10^8 N/m^2 (a bit less than 60,000 psi). This may be conservative, relative to the strength obtainable in the parts under consideration. We found that with reasonable fillets we could get all the cost-optimum designs below this limit, so we were not motivated to investigate the credibility of some higher limit.

Note that this study has left many possible investigations unexplored. In particular, in the optimization, we considered only one number of pole pairs and have constrained all machines to operate at the same speeds. This latter condition corresponds to considering only one possible drive ratio between engine and generator. Both limitations seem at least somewhat arbitrary.
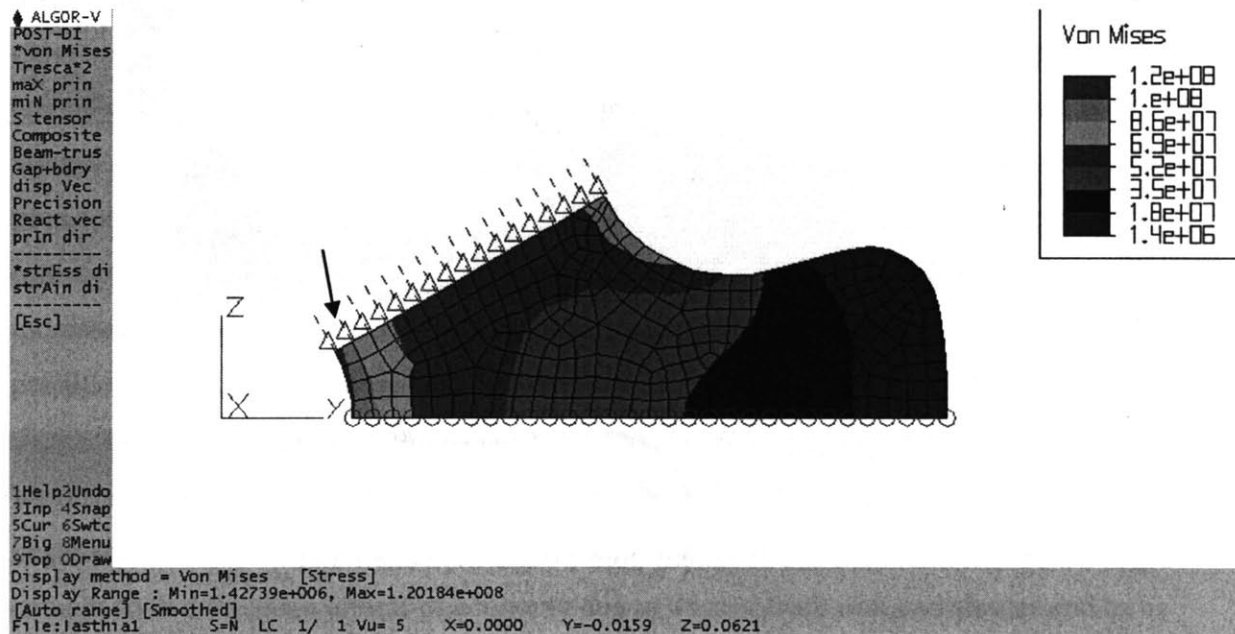
Figure 2.14: Mechanical FEA of homopolar inductor alternator .

57
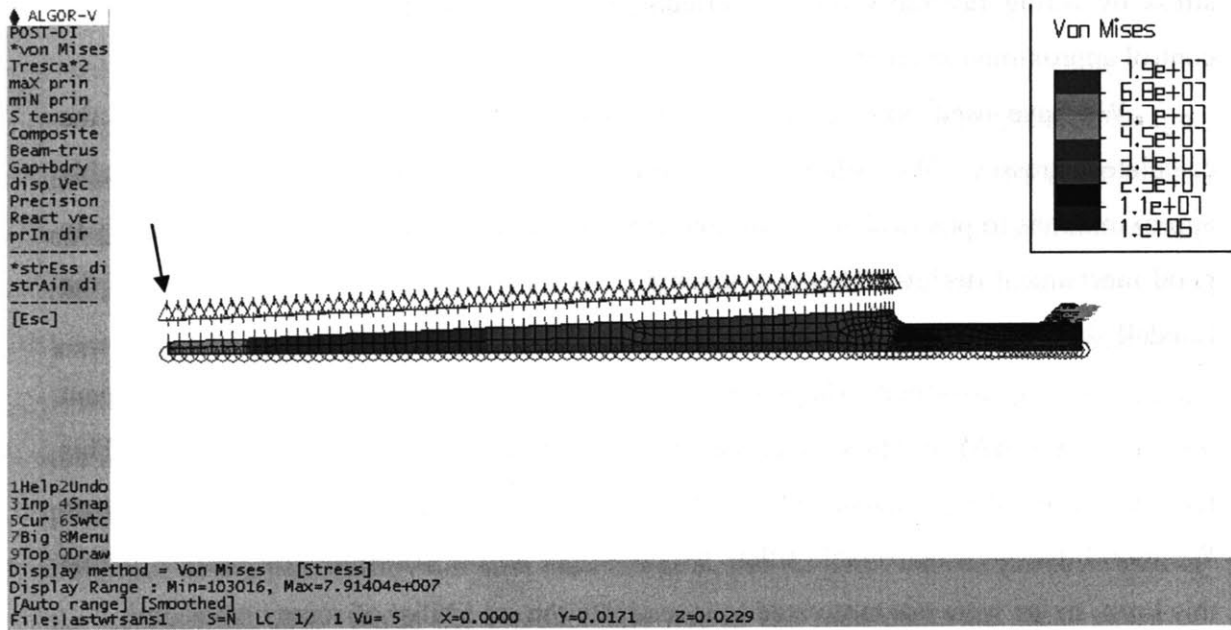
Figure 2.15: Mechanical FEA of non-salient wound-field alternator .
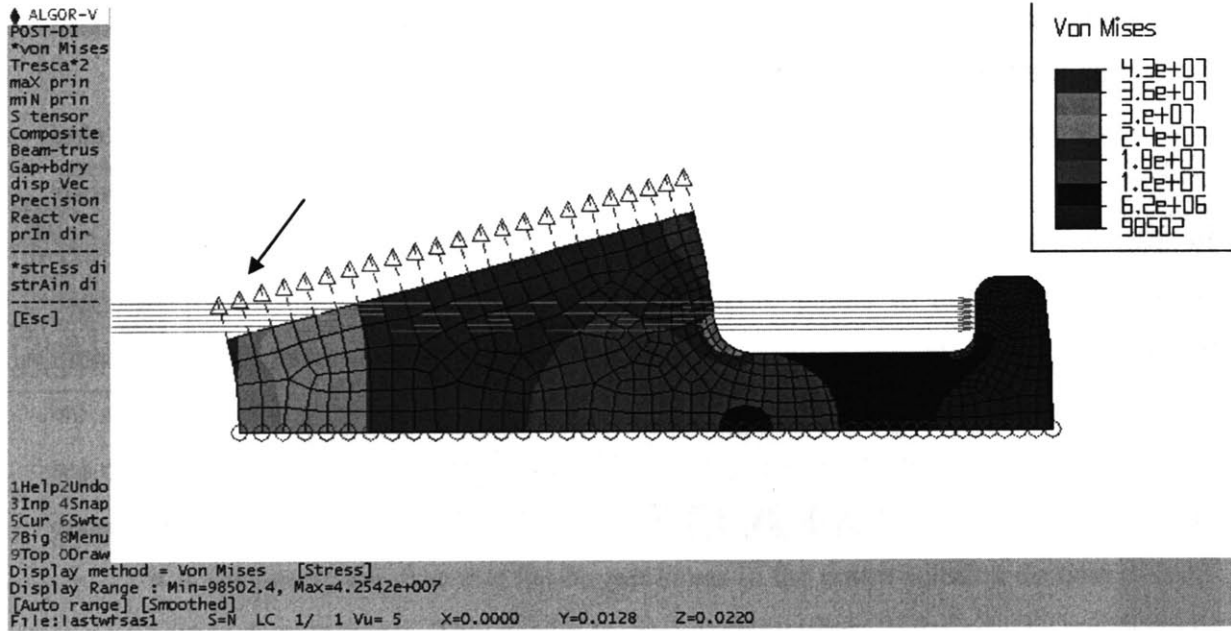
Figure 2.16: Mechanical FEA of salient-pole wound-field alternator .

58
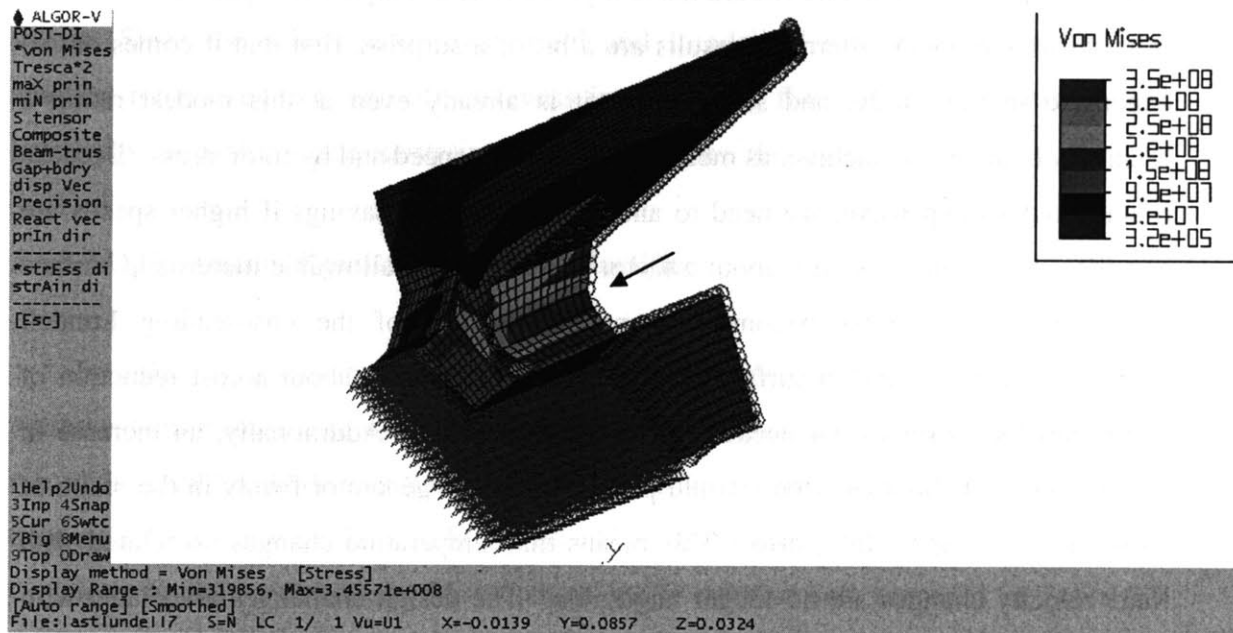
Figure 2.17: Mechanical FEA of Lundell alternator.

There is a fairly strong justification for our choice not to vary pole count. In previous studies [14]-[15] involving similar modeling and the same load requirements and cost function, we included pole count as an optimization variable. There, we almost always observed a cost function which decreases monotonically but asymptotically as pole count increases. We find these results uninteresting. Common sense tells us that the true optimum is not at infinite pole count. Increased time in winding the machine, increased cost per unit for finer wire, the increased lamination expense and other system penalties of higher frequency operation, are real effects which put an upper bound on the practical pole count of a machine. We have chosen not to model these effects. Instead, we observe that at 6 pole pairs, we are still low enough so that the adverse effects of these neglected considerations are not large. But at the same time, the pole count is high enough so that the main effects of economy due to thinner back iron and shorter end turns have been realized.

As for the effect of generator speed on cost, there remains substantial room for further work. The principal reason for considering the homopolar inductor alternator is that its simple rotor structure should make it possible to use high rotor speeds.

The homopolar alternator results are a bit of a surprise, first that it comes out so expensive in this study, and second, that it is already even at this modest rating a relatively high speed machine, as measured by surface speed and by rotor stress. Because it starts out so expensive, we need to anticipate great cost savings if higher speeds are considered. But there is only about a factor of 1.7 or so of allowable increase in surface speed, before the stress becomes comparable to that of the cost-leading Lundell alternator. This change in surface speed is unlikely to bring about a cost reduction of more than the factor of 3.4 needed to match the Lundell. Additionally, an increase in surface speed of this magnitude would put the air in the generator firmly in the realm of transonic, or compressible, flow. This means that temperature changes associated with fluid velocity changes are no longer negligible. The design challenges associated with producing a well cooled design in such a flow regime will be substantial. Additionally, flow noise will assume an increased importance, and the simple crude structure indicated by Figure 2.14 is unlikely to be acceptable without fairing and/or other treatments. In summary, given how far the homopolar inductor alternator has to go, it is not clear that this is a fruitful direction.

The very low stress levels computed for the wound field machines suggest that consideration of these machines at higher speeds may be productive. There are two general concerns about this direction. First, as discussed above, the real rotational speed limit in these machines may not be in the rotor steel, but in parts that have yet to be considered. A detailed mechanical design can give guidance about the possible existence and detailed nature of these limits, but the result will be harder still to include in a cost-optimizing grid search. Second, the compressible flow and flow noise concerns discussed in connection with the inductor alternator remain considerations for wound field machines.

While there may be benefits to considering different machines operating at different speeds, the results are definitely beyond the scope of this study.

In terms of inertia, the salient-pole wound field machine has the least inertia followed by the Lundell machine, the non-salient pole wound-field machine and the homopolar inductor alternator. In general, the smaller the rotor structure, the lower the inertia. Since the salient-pole wound-field and Lundell alternators optimized to the smallest rotor sizes due their effectiveness in generating flux and being relatively less limited by the performance constraints, their inertias are the lowest.

2.6.3.3 Optimization Results Using Diode Rectifier

In order to assess the effect of the switched-mode rectifier on the cost of the optimized alternators, a separate set of runs were performed on all four machines while run with simply a diode rectifier where the effective voltage seen at the output from Section 2.3 can only be 42 V. The set of cheapest machines for the optimization with (previous results) and without the switched- mode rectifier are compared in Table 2.3 below.

The results show that the switched-mode rectifier results in a decrease in cost of the least expensive machines by more than 10% from those obtained without using a switched-mode rectifier. At least part of the cost of implementing the switched-mode rectifier is offset by the savings that it enables.

From Table 2.3, notice that the switched-mode rectifier is used only at the idle point. It is at the idle point where the field-ampere turns required are highest. It is also at the idle point where the air gap flux densities are highest. Therefore, it is at the idle point where back-iron thicknesses are determined which in turn affect cost. If the output voltage is lowered, the result is that the equivalent switched-mode rectifier resistance decreases and the internal power angle increases, the net result of which is a decrease in the flux density in the airgap. In order to meet the output power, the armature current increases and so does the back-emf through the field ampere turns. Despite these increases in currents, the net effect on the flux density is still a decrease. Given the decrease in flux density, there is now more room for cost optimization. The air gap radius can then be decreased which results in an increase in the flux density but a decrease in

cost. Thus, the optimal machine used with the switched-mode rectifier is likely to have a smaller radius.

Table 2.3: Comparison of least expensive machines obtained with and without the switched-mode rectifier

	Diode rectification	Switched-mode recitification	Percent decrease in cost
Non-salient WFSM	$18.46	$16.19	12.3%
Salient WFSM	$14.20	$11.98	15.6%
Lundell	$13.53	$11.45	15.4%
Homopolar	$44.86	$40.30	10.2%

2.7 Conclusion

To summarize, the lumped parameter models for the four alternators are tied together with the circuit model for the switched-mode rectifier in order to derive analytical expressions for machine performance at the load matched condition. To validate the performance of the four machines and make more accurate comparisons, an exhaustive grid search optimization was done to determine which machine is most cost effective while meeting the more demanding requirements of next generation automobiles.

Looking at the optimization results while taking note of the predictions made using the analytical expressions, it is understandable that the Lundell alternator is the most cost effective alternator. What is surprising is that it has mechanical stresses below allowable limits while meeting these challenging power and efficiency requirements. The salient-pole wound-field alternator does perform well and comes in as a close second. To the accuracy of this study, the two machines are virtual equivalents from a cost viewpoint.

We expect that for this application, the industry will continue to select the Lundell alternator because of the vastly larger experience base with such machines. But the results here suggest that for another specification, even one only slightly more challenging to the Lundell machine, a different machine might be preferred.

The optimization runs done on the Lundell alternator using only a diode rectifier show that the switched mode rectifier results in a 15% decrease in the cost of the optimal machine. A switched-mode rectifier is also useful for transient voltage suppression and jump starting thus sparing us the cost of additional components used for these functions.

Chapter 3

Load Dump Protection

3.1 Introduction

A "load dump" in an automotive electrical system is a severe voltage transient associated with the alternator that has a major impact on the design requirements of automotive electronic components [3,5,25,26]. A load dump occurs when there is a sudden disconnection of a high current load (especially the battery) that forces the alternator output current to drop quickly. The reactive drops across the machine inductances are thus reduced, and the large alternator back-emf is imposed on the electrical system until the field control circuit is able to sufficiently reduce it.

The load dump is an important consideration in 14 V electrical systems, since the peak voltage ratings on electrical components may be as high as 60 V [27]. Some form of passive clamp is often used to limit the transient voltage [26], but substantial overvoltage requirements are the norm. It is generally thought that the much tighter overvoltage requirements of proposed 42 V systems will require some form of active clamp in addition to passive clamping [27].

An energy absorbing clamp at the output of the alternator must absorb the alternator output power during a load dump (excepting any power delivered to remaining loads), representing a substantial dissipation requirement. The size of the passive clamp is related to the energy that it has to absorb. Examples of passive clamps are metal oxide varistors (MOV) and zener diodes; the alternator rectifier diodes are designed to avalanche for this purpose. An absorbing active clamp performs similarly, but attains lower voltage overhead through intelligent control circuitry. There are several approaches to active suppression that can reduce the dissipation requirements of absorbing clamps. An example of such is shorting the machine output. For example, if an alternator already has a switched-mode rectifier for load matching (e.g. as shown previously in Figure 1.2), the machine output can be shorted out by simply turning on all the three low side switches [9, 30].

Another method that has been used to reduce clamping requirements for load dump protection is improved field current control. This allows us to limit the overvoltage

transient with components rated at lower power levels, compared with stator side clamping. At present, following a load dump, the voltage supply to the field winding is turned off by the voltage regulator [5]. The field current will then decay exponentially. While present, the field current creates the high voltage at the output. One way of reducing the overvoltage that results from the load dump would be fast field de-excitation, or quickly bringing the field current to zero following a load dump. When used in conjunction with voltage clamping at the output, rapid field de-excitation lowers the duration of the clamping current, so clamp elements are called to absorb or dissipate less energy. Therefore the components are expected to be smaller and less expensive [25]. This chapter explores the use of rapid control of the field current to reduce the clamping requirement. Models and experiments are developed that show the requirements and limits of this general approach, and circuits suitable for achieving maximum performance are introduced.

3.2 Fast Field De-excitation

3.2.1 Eddy Current Limitations

Fast field de-excitation is the quick reduction of current in the field winding. The back-emf is a function of alternator speed and excitation current. Following a load dump, the output voltage could approach the back-emf or open circuit voltage. With no field current, there should be no back-emf. However, in a Lundell alternator, the sudden removal of the field current will induce eddy currents to flow in the solid rotor poles. The output voltage will not immediately disappear due to the presence of these eddy currents. As these eddy currents decay, so will the output voltage. The rate of decay of the output voltage is limited by the rate of decay of the eddy currents.

In order to assess the limitations due to eddy currents, the field winding of a Motorcraft 14V, 140 A automotive alternator was connected to the circuit shown below in Figure 3.1. A more detailed circuit schematic can be found in Figure C.2 of Appendix C. The experiment was conducted with an initial field current of 1 A and an alternator speed of 1840 rpm. After the switch is opened, de-excitation occurs as the field energy is transferred from the field winding (inductor) to a capacitor over a quarter of a cycle of the circuit's natural frequency. The field current and capacitor voltage waveforms are shown

in Figures 3.2 and 3.3. The field current vanishes after a few tenths of a millisecond (0.24 ms). The average reverse voltage is approximately 35 times the initial voltage. Since the de-excitation through the capacitor can be made very fast compared to the duration of the overvoltage, the field current can be assumed to vanish instantaneously, and only the effects of the eddy currents through the solid rotor poles will be reflected in the output voltage waveform. Using this circuit will result in the fastest decay of the output voltage that can be achieved without having a bi-directional field current (which can create flux that opposes the effects of the eddy currents). This open circuit (phase to neutral) stator output voltage exhibits an envelope of the decaying oscillation containing at least two time constants: a faster time constant of around 15 ms and a slower one of around 100 ms. The envelope can be expressed using the following function:

$$V = A_1 e^{-(t-t_L)/\tau_1} + A_2 e^{-(t-t_L)/\tau_2} + A_3 \qquad t \geq t_L$$
$$\tau_1 = 15ms$$
$$\tau_1 = 100ms$$
$$A_1 = 4.33V$$
$$A_2 = 1.44V$$
$$A_3 = 0.52V$$

(3.1)

The positive half of the line-to-neutral output voltage during the transient is shown in Figure 3.4.
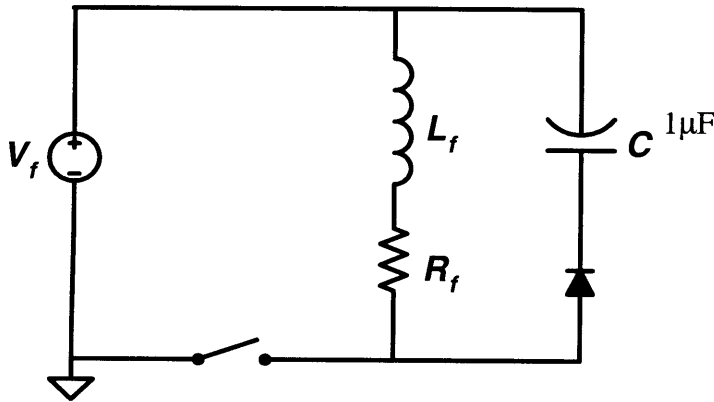
Figure 3.1: Circuit for de-excitation through capacitor.
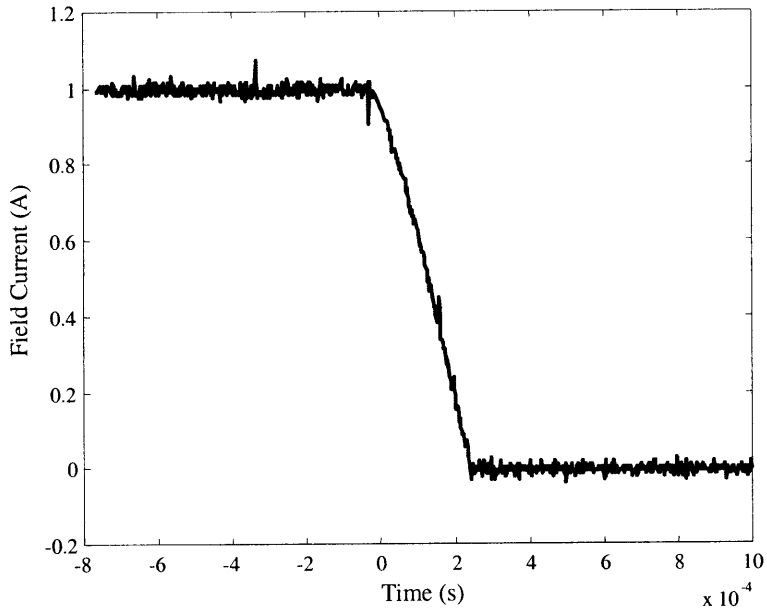
Figure 3.2: Field current during fast de-excitation.
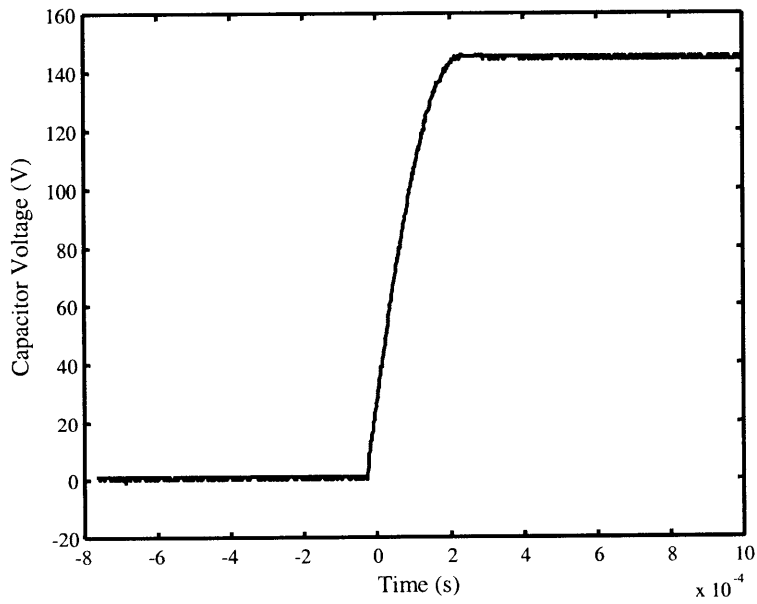
Figure 3.3: Field voltage during fast de-excitation.
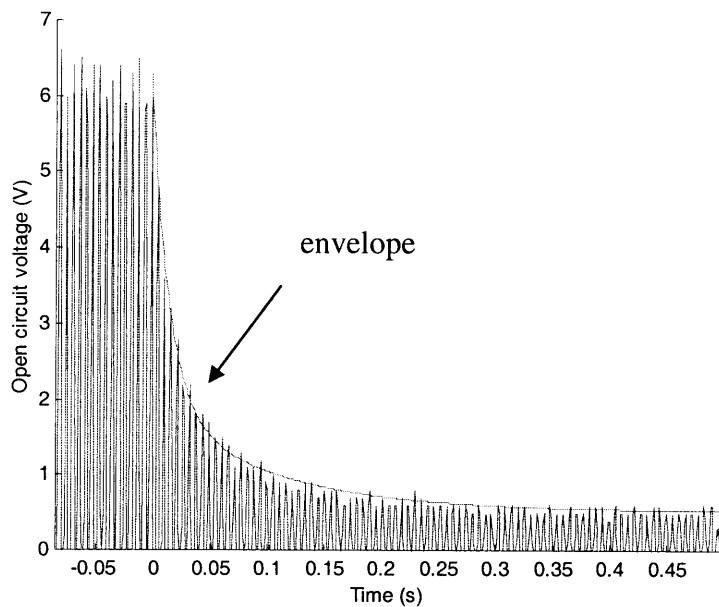
Figure 3.4: Positive half of stator phase open circuit voltage.

We can use information from Figure 3.4 to extrapolate what a load dump transient might look like in a modern 42-Volt automobile. We can extrapolate the pre-event portion of the experimental event to allow us to estimate the voltage which would appear at the machine terminals immediately following an instantaneous loss of full load. The pre-event voltage level can be assumed to be made up of two parts – A voltage which exists as a result of current in the field winding, and a second voltage which exists as a result of residual magnetization of the rotor. From the late post-event portion of the trace, we see a small voltage that does not appear to be declining. This is the voltage due to residual magnetization. Superposition can be assumed to apply in this case, so we expect the voltage due to residual magnetization to be the same at all points in the trace. This means that the voltage due to field current is the difference between the total pre-event voltage and the voltage due to remanent flux. This statement is true independent of the relative phase of the two voltages, but if the two are in phase, then the statement can be applied to the difference of the amplitudes.

To calculate the effect of operating at a different field current, the voltage due to field current may be scaled by the ratio of the new field current to that of the test current

(1 ampere). This is rigorously valid if magnetic saturation is unimportant. To calculate the effect of operating at a different speed, the total voltage (both the field-dependent and remanent flux components) may be scaled by the ratio of speeds.

And finally, if we want to postulate a 42 volt machine, we may scale both components of the voltage by a factor of 3 to account for the expected increase in mutual flux linkage due to a change in the number of stator turns. If we make all these corrections, the result is the step amplitude shown in Figure 3.5. The curve for the remainder of Figure 3.5 is derived by scaling the fraction of the voltage attributable to remanent magnetism by a factor derived from the envelope from Figure 3.4.

Following the load dump, it takes around 50 ms for the voltage to reach an acceptable level (below 58 V) of around 1/5 the peak reached. Any clamp will have to be effective for at least 50 ms. To decrease the overvoltage duration further, as desired, negative field currents would have to be imposed through the field winding to counter the effects of the eddy currents.
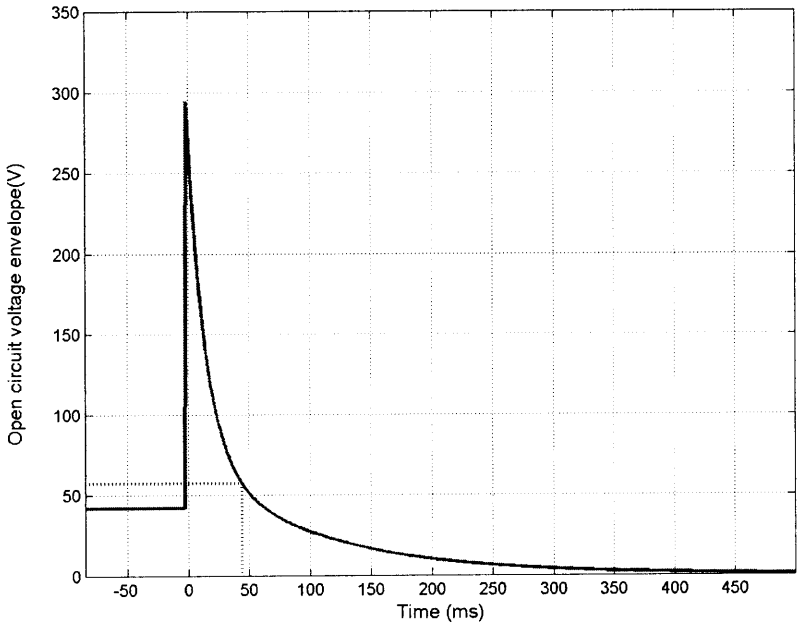
Figure 3.5: Load dump voltage envelope for 42 V system with alternator running at 6000 rpm and having an initial field current of 3A.

3.2.2 Method for Fast Field De-excitation

70

Fast field de-excitation is achieved by applying a negative voltage across the field winding. A simplified diagram illustrating de-excitation of the field winding in this manner is shown in Figure 3.6. The field winding is represented as a series combination of an inductor and resistor; rotor eddy currents are ignored. The field is de-excited by switching the field voltage from its initial positive value to some negative value, as shown in Figure 3.7. Such field de-excitation results in a field current decay time to zero of approximately

$$t_z = \left(\frac{L_f}{R_f}\right) \ln\left(\frac{k+1}{k}\right), \qquad k \geq 0 \qquad (3.2)$$

where k is the ratio of the magnitude of the applied reverse voltage (V_f after load dump) to the voltage originally applied (V_f before load dump). See Appendix C.1 for a derivation. Having a k of zero corresponds to shorting out the field winding. In this case, since the field current decay is exponential, it will take around three time constants for the field current to approach zero, but will take infinitely long to actually reach zero. Even three time constants is much longer than the time we want to achieve in order to minimize clamp losses in future high power-alternators. Having a larger k will result in a shorter period of time for removal of the current. A fast response from a field de-exciter will allow for a smaller and less expensive clamp. The faster the de-excitation current, the more costly it becomes. The objective then is to achieve a fast field de-exciter at lower cost. As mentioned earlier, the model of the field winding in Figure 3.6 is a simplified version of the actual field circuit dynamics. Equation (3.2) formally holds only when the armature is open circuited and when the field decay process is slow enough so that rotor eddy currents are not important. If the armature is loaded, the field current decay can be faster than indicated by (3.2). If rotor eddy currents are important, field current decay will be faster, but the speed voltage in the armature will no longer be proportional to the field current, as the rotor eddy currents induce voltage in the armature.
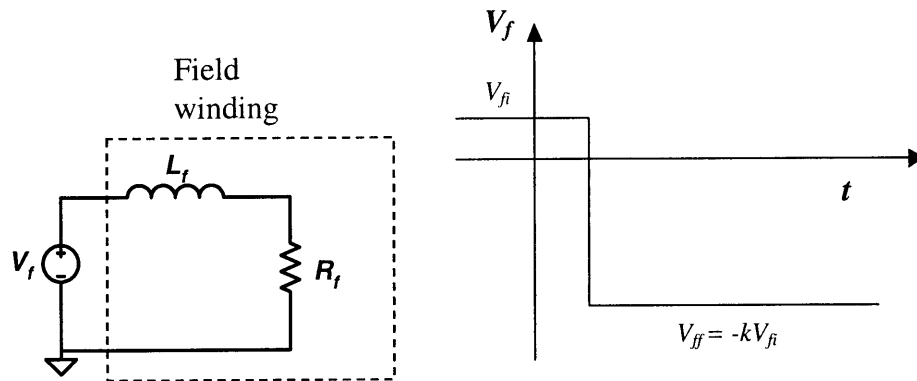
Figure 3.6: De-excitation of the field winding by voltage reversal.

3.2.3 De-excitation Experiment

We have conducted an experiment to evaluate de-excitation by reversing the voltage across the field winding (theoretical k=1). To evaluate the effects of applying a reverse voltage across the field winding, a bridge was constructed using four transistors as shown in Figure 3.7. A more detailed schematic is shown in Figure C.4 of Appendix C. This experiment was conducted with an initial field current of 1 A at idle speed (1800 rpm). The open circuit voltage and the field current were observed following a reversal of the applied field voltage. The experimental results are shown in Figure 3.8. Theoretically, the reversal should be by a factor of $k = 1$. However, the additional reverse voltage is due to the drops across the MOSFET body-diodes and line resistances. The drops across the resistances decrease as the field current decreases to zero. As the field current goes negative, the MOSFET R_{DSon} drops further decrease the magnitude of the reverse voltage. The field current decreased to zero after around 48 ms while the open circuit voltage decreased to 1/5 of its original value after 75 ms. In order to have the field current vanish more quickly, a larger negative voltage must be applied across the field winding.
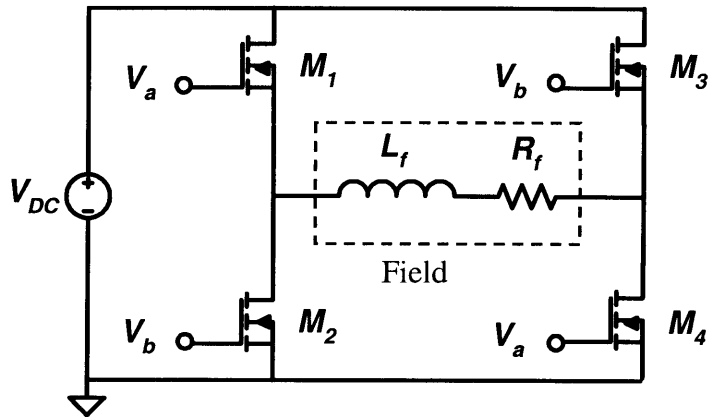
Figure 3.7. Full-bridge circuit used for voltage reversal.
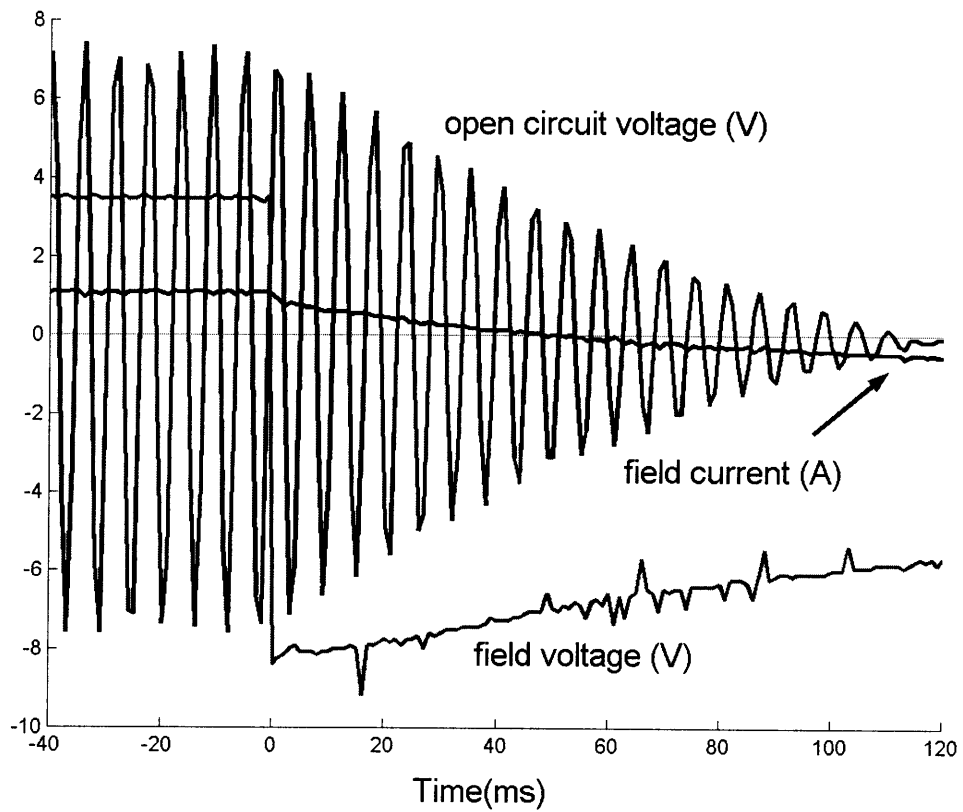
Figure 3.8: De-excitation of field winding by reversal of applied voltage.

3.2.4 Rotor Equivalent Circuit

In order to assess approximately what multiple of the original voltage is required to obtain a decay rate comparable to that obtained using a capacitor (very fast), a rotor equivalent circuit model is developed in this section.
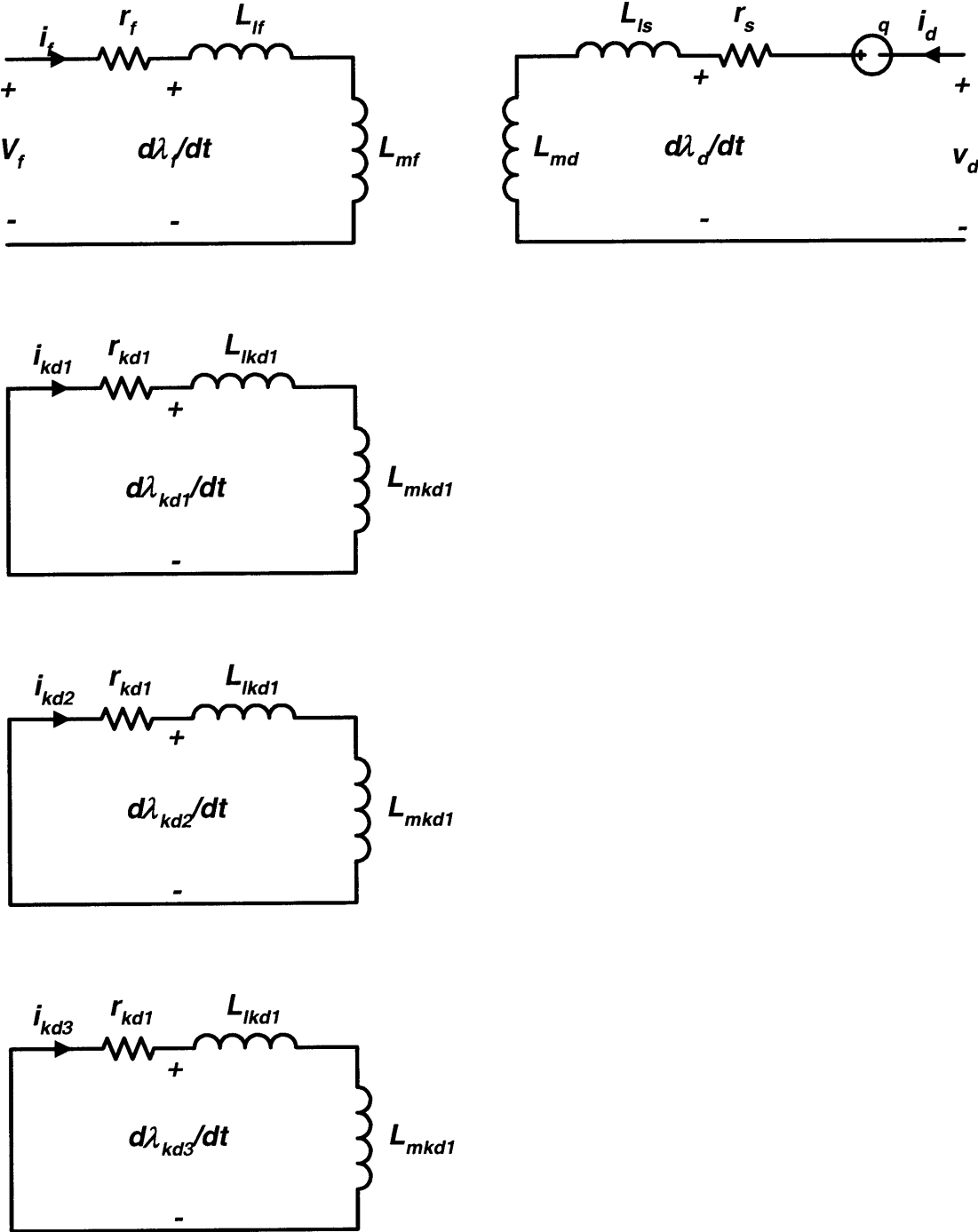
Figure 3.9: Rotor d-axis circuit.

The rotor circuit could be modeled as shown in Figure 3.9, where only the d-axis is considered. It is assumed that the eddy current effects occur in circuits along the d-axis. The model of the rotor has the field winding, three eddy current circuits which are shown to be short circuited. These are coupled to each other and to the d-axis stator winding.

The flux linkage equations (taken from [16]) with the addition of two more damper windings are

$$\lambda_f = \frac{3}{2} L_{sf} i_d + \left(L_{mf} + L_{lf} \right) i_f + L_{fkd1} i_{kd1} + L_{fkd2} i_{kd2} + L_{fkd3} i_{kd3} \tag{3.3}$$

$$\lambda_{kd1} = \frac{3}{2} L_{skd1} i_d + L_{fkd1} i_f + \left(L_{mkd1} + L_{lkd1} \right) i_{kd1} + L_{kd1kd2} i_{kd2} + L_{kd1kd3} i_{kd3} \tag{3.4}$$

$$\lambda_{kd2} = \frac{3}{2} L_{skd2} i_d + L_{fkd2} i_f + L_{kd1kd2} i_{kd1} + \left(L_{mkd2} + L_{lkd2} \right) i_{kd2} + + L_{kd2kd3} i_{kd3} \tag{3.5}$$

$$\lambda_{kd3} = \frac{3}{2} L_{skd3} i_d + L_{fkd3} i_f + L_{kd1kd3} i_{kd1} + L_{kd2kd3} i_{kd2} + \left(L_{mkd3} + L_{lkd3} \right) i_{kd3} \tag{3.6}$$

$$\lambda_d = \left(L_{md} + L_{ls} \right) i_d + L_{sf} i_f + L_{skd1} i_{kd1} + L_{skd2} i_{kd2} + L_{skd3} i_{kd3} \tag{3.7}$$

where the following notation holds:

λ_f = flux linked by field winding

λ_d = flux linked by armature d-axis winding

λ_{kdi} = flux linked by ith eddy current circuit for i=1,2,3

i_f = current through field winding

i_d = current through armature d-axis winding

i_{kdi} = current through ith eddy current circuit for i=1,2,3

L_{mf} = field magnetizing inductance

L_{lf} = field leakage inductance

L_{sf} = field armature mutual inductance

L_{fkdi} = mutual inductance between field winding and ith eddy current circuit for i=1,2,3

L_{skdi} = mutual inductance between stator winding and ith eddy current circuit for i=1,2,3

L_{mkdi} = magnetizing inductance of ith eddy current circuit for i=1,2,3

L_{lkdi} = leakage inductance of ith eddy current circuit for i=1,2,3

L_{kdikdj} = mutual inductance between ith and jth eddy current circuit for i,j=1,2,3

The stator is open circuited so the d-axis stator winding current is zero (i_d=0) and therefore has no effect on the rotor circuit. To simplify the derivations, it is assumed that there is a common permeance (or reluctance) seen by all the windings. Assuming a common permeance, the various inductances can be found to be

$$L_{mf} = N_f^2 P_d \qquad (3.8)$$

$$L_{mkdi} = N_{kdi}^2 P_d \qquad (3.9)$$

where N_{kdi}, N_f are the number of turns corresponding to the damper windings and field winding respectively, and P_d is the permeance function common to all windings. The constant N_{kdi} does not correspond to real turns but instead can be seen as a factor that relates the permeance to the inductance.

Given this common permeance, each of the other rotor windings can be seen as coupled to the field winding through transformers with turns ratios of N_{kdi}/N_f. Therefore, transforming all the eddy current circuits to the side of the field winding involves multiplication of the inductances and resistances by $(N_f/N_{kdi})^2$. The transformed circuit is shown in Figure 3.10 where

$$L_{lri} = \left(\frac{N_f}{N_{kdi}} \right)^2 L_{lkdi} \qquad (3.10)$$

$$R_{ri} = \left(\frac{N_f}{N_{kdi}} \right)^2 r_{kdi} \qquad (3.11)$$

As shown in the final equivalent circuit model of Figure 3.10, there are 3 additional RL sub-circuits representing the effects of the eddy currents. Although the eddy current waveform in Figure 3.4 was approximated earlier with two time constants, three rotor eddy current subcircuits are included in this model for an additional degree of freedom and improved matching. Without the eddy currents, we have the simple field winding circuit. The objective of the above derivations is to show that the circuit in Figure 3.9 can be transformed to the circuit in Figure 3.10 with some approximations. The field circuit in Figure 3.10 simplifies analysis or simulation.

The best-fit values for the circuit elements in Figure 3.10 were then determined iteratively using simulations in Pspice with the goal of replicating the experimental

results shown in Figures 3.2, 3.3, 3.4, and 3.9 (see Appendix C.4). The resulting circuit parameters are enumerated in Table 3.1. The model captures the main characteristics of the actual rotor. The next step then is to predict what the actual performance of the alternator would be under different situations, by running simulations on the model under those conditions. This circuit model assumes that the stator is open circuited. Following a load dump, the output voltage can approach the open circuit voltage. The phase a open circuit voltage will be

$$
\begin{aligned}
V_a &= \omega \lambda_d \cos\theta_r + \frac{d\lambda_d}{dt}\sin\theta_r \\
&= \omega \frac{N_s}{N_f} L_{mf} I_{mf} \cos\theta_r + \frac{N_s}{N_f} L_{mf} \frac{dI_{mf}}{dt}\sin\theta_r \\
&\approx \omega \frac{N_s}{N_f} L_{mf} I_{mf} \cos\theta_r
\end{aligned}
\tag{3.12}
$$

where N_s and N_f are the armature turns per phase and field turns respectively, ω is the electrical frequency, and I_{mf} is the current through the field magnetizing inductance. The envelope of the open circuit voltage is approximately a scaled version of the current through L_{mf} as shown in (3.12). During steady state, there is no current through the three additional rotor circuits representing the eddy current effects. During transient conditions, such as a load dump, currents will flow through these rotor circuits and represent the eddy currents that will flow and oppose the change of flux in the air gap.

3.2.5 Required Voltage Reversal

A simulation of a voltage reversal with $k=1$ applied to the equivalent rotor circuit (with reverse currents allowed) in Figure 3.11 shows that it takes approximately 135 ms for the open circuit voltage to reach 1/5 of its original value. The result appears in Figure 3.11 where the phase voltage is derived using (3.12). This is considerably longer than the 75 ms achieved by de-excitation via a capacitor. Therefore a higher reverse voltage is required. The results shown in Figure 3.11 are different when compared with those in Figure 3.8 since the actual voltage reversal shown in Figure 3.8 is greater than $k=1$ and actually closer to $k=2$.
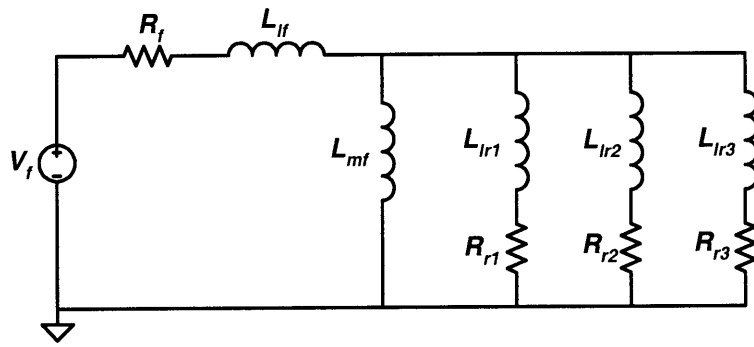
Figure 3.10: Equivalent rotor circuit simulated in PSpice.

Table 3.1: Parameter values for rotor circuit of existing Lundell alternator (Motorcraft 14 V, 140 A alternator).

Parameter	Value
R_f	2.54 Ω
L_{lf}	20mH
L_{mf}	550mH
L_{lr1}	1mH
R_{r1}	30Ω
L_{lr2}	200mH
R_{r2}	25Ω
L_{lr3}	900mH
R_{r3}	90Ω
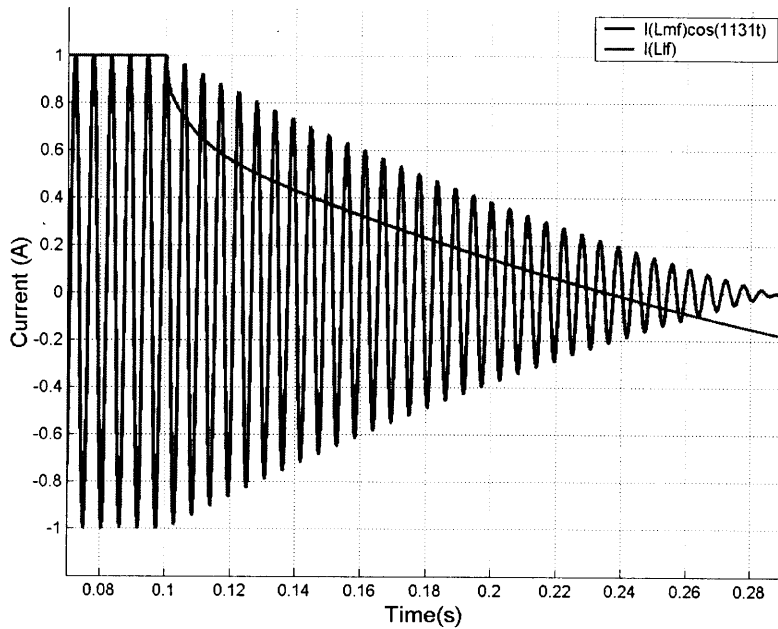
Figure 3.11: Simulation of de-excitation by voltage and current reversal with k=1 (showing normalized field current and phase voltage).

We then determined what field voltage with current reversal could accomplish the same effect on the open circuit voltage as that obtained through de-excitation via a capacitor (with approximately a factor of k=35, allowing for only positive field currents). The circuit in Figure 3.10 is simulated while varying the reversal factor k. The resulting simulated field current and normalized output voltage waveforms (scaled version of current through L_{mf}) are shown in Figure 3.12. The voltage takes approximately 70 ms to reach 1/5 of its value preceding the transient. The simulations show that a voltage reversal by a factor of 2.5 (while allowing for a bi-directional current) has the same effect as a reverse voltage by a factor of 35 (with unidirectional current). It shows that allowing for a reverse current makes a significant contribution to de-excitation. Such performance is approximately as good as that achieved using ultra-fast field de-excitation with the capacitor. Based on the experimental results, we need a field de-excitation circuit with a k of at least 2.5 to match the effect of instant current cut off. However, based on our predictions of the actual open circuit voltage with the alternator running close to full field

(with an overvoltage transient lasting around 50 ms), we need a k of 4 while allowing for a reverse current.
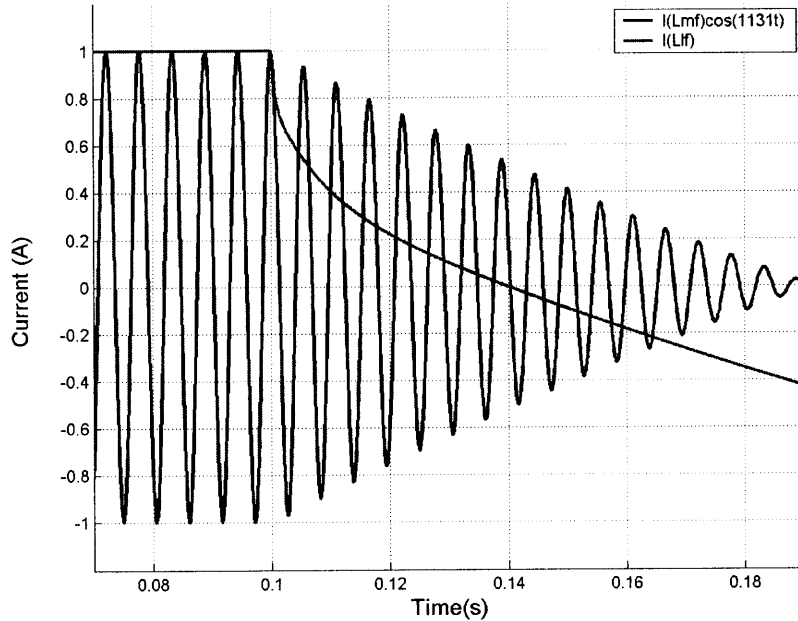
Figure 3.12: Simulation of de-excitation by voltage and current reversal with k=2.5 (showing normalized field current and phase voltage).

3.3 Summary

Fast field de-excitation can be used to reduce the load dump overvoltage transient duration and amplitude with components operating at lower power levels (compared with clamps at the output). If the field winding current is shut off immediately, the load dump overvoltage does not immediately vanish because of the eddy currents that flow in the rotor poles immediately following such de-excitation. One method of de-exciting the field winding is by voltage reversal. It has been demonstrated, however, that current reversal in addition to voltage reversal is necessary such that a reasonable voltage reversal ratio is possible. A voltage reversal of k=4 together with current reversal is sufficient to reduce the duration of the overvoltage at the same rate as reducing the field current to zero instantaneously. A higher voltage reversal results in even better performance.

Chapter 4

Foil Field Winding

From Equation 2.20, the maximum power output for an alternator at the load-matched condition can be expressed as

$$P_{max} = \frac{3}{4}\omega \frac{\left(L_{afm}\!\!\Big/N_f\right)^2}{L_s}\left(N_f I_f\right)^2 \tag{4.1}$$

where ω is the electrical frequency, L_{afm} is the field-armature mutual inductance, L_s is the synchronous inductance, N_f is the number of field turns and I_f is the field current. This shows that the higher the number of field ampere turns (at least at the load matched condition while not saturating the alternator), the higher the output power achieved. Even when a machine is not designed to operate at the load matched condition, higher field ampere-turns can be used by the machine designer to improve performance. To cite just one example, higher field mmf will allow the specification of a larger air gap without loss of rotation induced voltage in the armature. The larger airgap will reduce armature inductance, allowing a higher current for a fixed induced voltage and load voltage, thereby increasing power output.

Our aim is to increase the number of field ampere turns by modifying the alternator field winding. Currently, the field winding of an automotive Lundell alternator consists of round copper wire with a packing factor near 0.6. For the same number of turns and winding area, the higher the packing factor, the larger each wire can be and therefore the lower the resistance of the field winding and the lower the copper losses will be. One way of increasing the packing factor would involve replacing the round wire field winding with a foil coil. There are several advantages to doing this. Foil packs more tightly so the geometric packing factor will be higher, and in addition has better thermal heat transfer (lower thermal resistance than round wire). A plot comparing the round wire and foil packing factor can be found in Figure 4.1 assuming constant insulation thickness. The insulation thickness for the foil winding of 1 mil is currently the minimum available

thickness. The comparisons were made assuming a fixed winding bobbin. The equation used to determine the packing factor of round wire is

$$k_{pf} = \frac{N_f \pi}{A_s} \left(\sqrt{\frac{A_s k_f}{N_f \pi}} - t \right)^2$$ (4.2)

where N_f is the number of field turns, A_s is the area of the slot, t is the insulation thickness, and k_f is a factor representing how tightly the wires (including insulation) pack. For square packing, as assumed below, k_f equals $\pi/4$ (0.785). The packing factor for foil with single sided insulation is

$$k_{pf} = \frac{W_{Cu} \left(H_s - N_f t \right)}{A_s}$$ (4.3)

where W_{Cu} is the width of the copper foil, H_s is the height of the slot, N_f is the number of field turns, A_s is the area of the slot, and t is the insulation thickness.
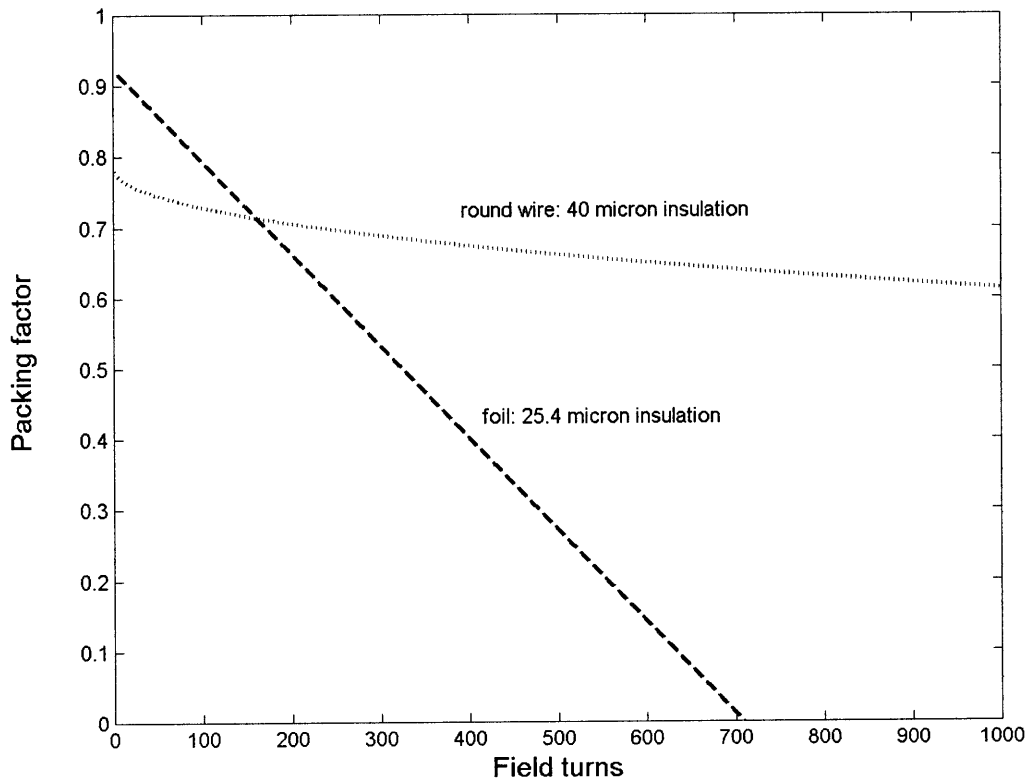
Figure 4.1: Packing factor for foil and round wire versus number of field turns (constant insulation thickness).

This calculation in Figure 4.1 is done for a slot width of W_s=26 mm, a slot height of H_s = 18 mm, square packing of round wire (k_f= π/4) and typical insulation thicknesses t as indicated in the plot.

Below a certain number of turns (depending on bobbin size), the foil packing factor is larger. Decreasing the number of turns further increases the packing factor, as shown by Equation 4.3 and assuming constant insulation thickness. The field resistance is equal to

$$R_f = \frac{N_f^2 \pi (R_i + R_o)}{\sigma A_s k_{pf}}$$ (4.4)

where R_i is the inner radius of the bobbin, R_o is the outer radius, σ is the conductivity of copper, and A_s is the area of the slot. The field copper loss is equal to

$$P_{Cu} = I_f^2 R_f = I_f^2 \frac{N_f^2 \pi (R_i + R_o)}{\sigma A_s k_{pf}} = (N_f I_f)^2 \left(\frac{\pi (R_i + R_o)}{\sigma A_s k_{pf}} \right) = (N_f I_f)^2 R_{f1}$$ (4.5)

where I_f is the field current, R_f is the field resistance, and R_{f1} is the resistance of one turn of the field winding. Winding the field with copper foil will allow us to put in more field ampere turns while maintaining the same field copper losses. This is because, using Equation 4.5, the field resistance per turn R_{f1} decreases with an increase in packing factor achieved by using foil. That implies that the number of field ampere turns $N_f I_f$ can be increased while keeping the copper losses P_{Cu} constant. It is unlikely that winding costs will be higher with foil since there are many other copper foil applications. In addition, the field winding will be easier to cool because of improved heat transfer. This permits a still greater increase in achievable ampere turns for comparable allowed winding temperature (at higher field copper loss).

Plots comparing the number of ampere turns allowed in a foil-wound alternator with that in an existing Lundell alternator for different design conditions can be found in Figure 4.2. These plots were generated assuming the same current density is maintained or the same copper losses are maintained. The fewer the foil field turns, the larger the number of field ampere turns allowed because packing factor increases with fewer turns, given constant insulation thickness.
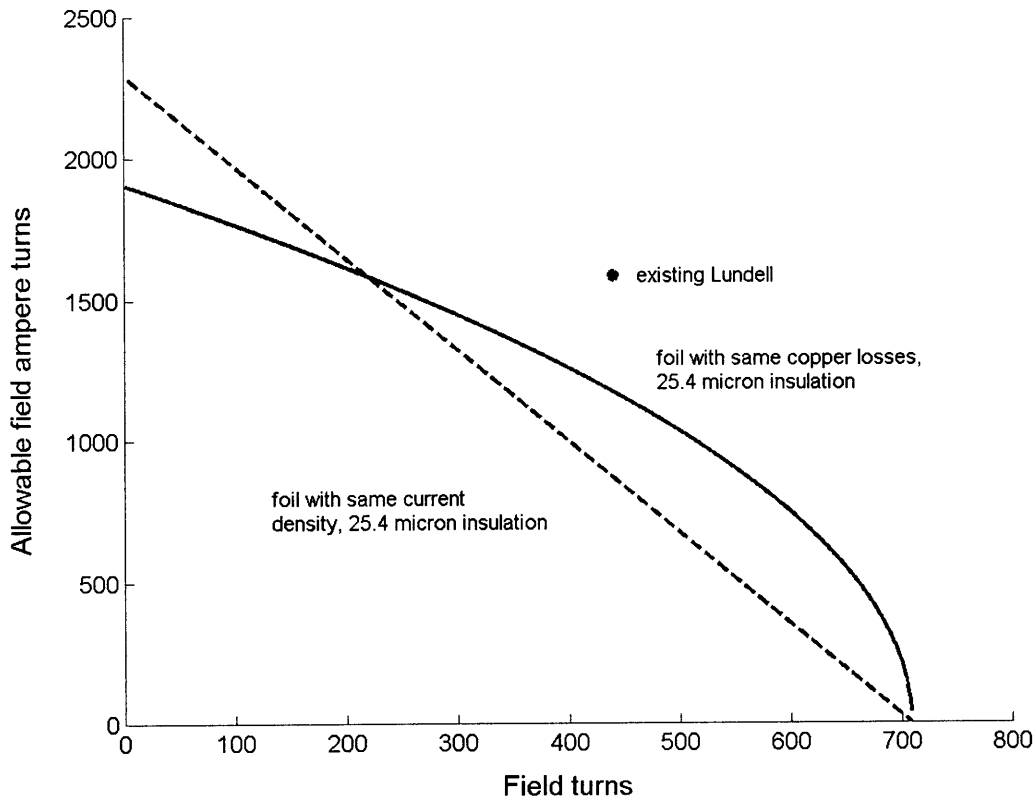
Figure 4.2: Number of field ampere turns allowed for foil winding compared with that in an existing Lundell alternator, for the cases of maintaining the same copper losses, and maintaining the same current density in the copper.

Another great advantage of winding with foil is that it can facilitate faster field de-excitation. Using copper foil for the field winding will require a lower number of turns and a higher field current. Having higher field winding currents by, for example, a factor of 10 (36 A) will allow us to regulate, by using a chopper, the field voltage to 1.4 V (for the 14 V bus voltage). Following a load dump, we can then apply the reverse of the bus voltage (-14 V) across the field winding using simple electronics. This will result in a reversal factor k of 10.

The equivalent field circuit when copper foil is used instead of the round wire winding will have the same form as that shown previously in Figure 3.10, but, with the parameters shown in Table 4.1. To first order, the new inductances will be the old inductances multiplied by the ratio of the new number of field turns to old, squared, since

84

the magnetic path remains approximately the same. The resistance will also vary by the same turns factor and by the change in packing factor. If the rotor eddy currents are ignored, and if the armature windings are open circuited, the field current decay time to zero will depend on the field winding time constant as shown previously in (4.1). The time constant will be larger for the foil wound field due to the smaller resistance relative to inductance (packing factor increase). This must be compensated for by a slightly higher voltage reversal.

Table 4.1: Parameter values for a rotor circuit with copper foil field winding. The bobbin has a slot width of W_s = 24 mm, a height of H_s= 12.9 mm, copper thickness of 6.2 mil, insulation thickness of 1 mil, and 65 turns of foil. The bobbin used is that corresponding to the alternator in which the transient experiments were performed in Chapter 3.

Parameters	Values
R_f	0.0833 Ω
L_{lf}	0.84155mH
L_{mf}	23.1mH
L_{lr1}	42.08μH
R_{r1}	1.2623Ω
L_{lr2}	8.4mH
R_{r2}	1.0519Ω
L_{lr3}	37.9mH
R_{r3}	3.787Ω

In Chapter 7, the development of a foil wound alternator with a rotating DC/DC converter is discussed. The bobbin used in that alternator has a slot width of W_s = 26 mm, and a slot height of H_s = 18 mm (used to generate plot of Figure 4.1). It is wound with 90 turns of copper foil and has an approximate packing factor of 0.73. That is compared with the round wire bobbin with a packing factor of 0.64. This results in 14.8 % increase in packing factor. The foil wound field winding is shown below in Figure 4.3.
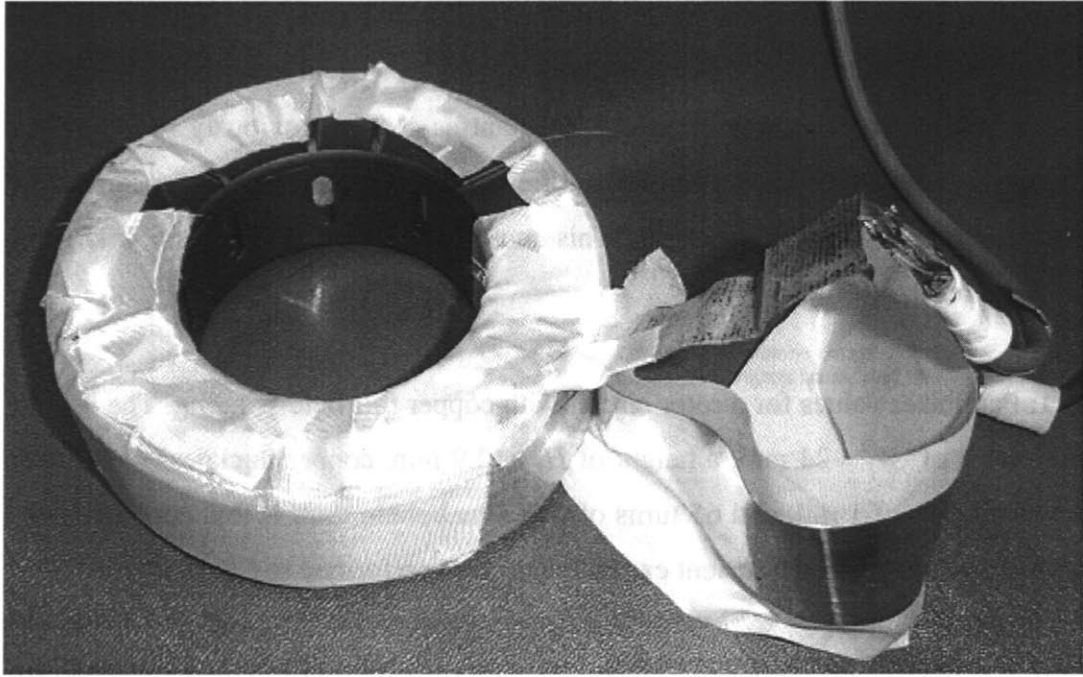
Figure 4.3: Foil wound field winding (outer white tape is insulation to prevent a short circuit with the Lundell alternator claws)

Chapter 5

Field Circuitry

5.1 Objectives

One of the main goals of our research is to develop field circuitry that allows us to use a foil field winding and rapidly de-excite the field winding through the application of a reverse voltage, and possibly, to allow for a reverse current.

The foil winding has a higher packing factor when fewer turns of thicker foil are used. This will require a higher current through the winding to at least maintain the number of field ampere turns. The higher packing factor relative to round wire allows us to increase the number of ampere turns relative to round wire. This will require an even higher current. A higher field current can be achieved in several ways. Since the brushes limit the allowed field current, one way would be to use larger brushes to allow for more current. A second way would be to keep the brushes while having some dc/dc conversion on the rotor to provide larger currents to the field winding. The third way is to eliminate the brushes which limit the field current and replace the existing voltage regulator with a new circuit that functions without the need for brushes. The rotating transformer topology and rotating DC/DC converter circuit will be explored and developed in more detail in Chapters 6 and 7, respectively.

5.2 Circuit Types

5.2.1 DC/DC Converter on Rotor

One method for generating a larger current through the field winding than passes through the brushes is to use a DC/DC converter on the rotor. The converter's function is to create a step down in voltage and an increase in current. Although it is possible to keep the voltage regulator on the primary side and have the converter on the rotating side maintain a constant conversion ratio, it is more efficient (and more elegant) to eliminate the voltage regulator on the stator and have a controllable DC/DC converter on the rotating side that performs both the regulation and conversion functions. One implementation of such a field excitation circuit is shown in Figure 5.1. It is then

necessary to control the active switch on the rotating side based on the alternator output voltage. Controlling the switch on the rotating side will involve some additional circuitry. This could be achieved, for example, by using line carrier transmission to send the control signal encoded in a frequency modulated carrier sinusoid from the stationary side, through the existing brushes, to the rotating side. This method is used in an actual circuit implementation to be covered in more detail in Chapter 7. Another method would be to use a rotating transformer for transmission of the encoded control signal from the stationary side to the rotor. This would involve a stationary primary winding and a rotating secondary winding. A third method would be to use short-range wireless transmission (e.g. with Blue Tooth, 802.11, or some other communications standard to communicate control information to the rotating side). The rotating transformer topology is studied and developed in Chapter 6.
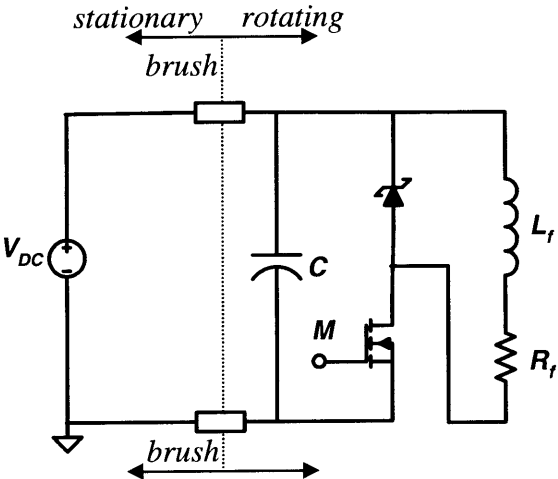
Figure 5.1: Circuit with DC/DC conversion on rotor that both regulates the field current and provides the conversion to reduce brush current. Replacing the diode with a synchronous rectifier can improve the efficiency of this circuit. The circuit is not used for fast field de-excitation.

5.2.2 DC/DC Converter on Rotor with De-excitation by Voltage Reversal

A simple modification of the circuit in Figure 5.1 allows for field de-excitation by the application of a negative voltage across the field winding. This new circuit is shown in Figure 5.2. Following a load dump overvoltage, the switch S and the MOSFET M on

the rotating side are both turned off. The current will then flow through D_{ovp}. The bus voltage is applied in reverse across the field winding. The voltage reversal ratio is the ratio of the magnitude of the negative applied voltage across the field winding after the load dump to the voltage across it during steady state prior to the load dump. The obtainable voltage reversal ratio is approximately equal to $1/D$ where D is the steady state duty ratio. Since the foil field winding will have fewer turns compared with the round wire field winding, its resistance will be lower than that of the conventional round wire field winding and therefore the duty ratio will be low in steady state. This implies that a high reversal ratio is achievable for a foil wound field winding. The PSpice simulation of the circuit in Figure 5.2 is shown in Figure 5.3. The field circuit model including the effects of the eddy currents are included in the simulation (c.f., chapter 3). The results of the simulation are shown in Figure 5.4. The voltage reversal obtained in this circuit is a factor k equal to 10. The results show the field current decaying to zero after less than 4 ms. Since, as shown in Equation 3.12, the output voltage envelope is proportional to the current through the field magnetizing inductance, it is the current I_{Lmf} which will have approximately the same form as the envelope of the overvoltage. The output voltage reaches about 1/5 of its peak value after 80 ms.

Adding a zener diode in series with the diode D_{ovp} as shown in Figure 5.5 will create a larger reverse voltage across the field winding. The new voltage reversal ratio therefore will be larger than $1/D$. Several zener diodes can be put in series to further increase the voltage reversal. The larger the voltage reversal, the faster the removal of field current and the closer we get to the performance achieved through instantly eliminating field current.
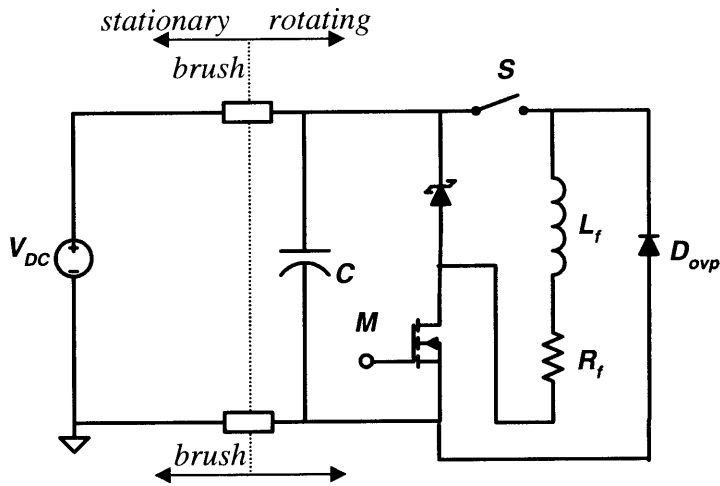
Figure 5.2: Circuit with DC/DC conversion on the rotor that regulates a larger field current, provides a voltage transformation to reduce brush currents, and allows for de-excitation by voltage reversal across the field winding.
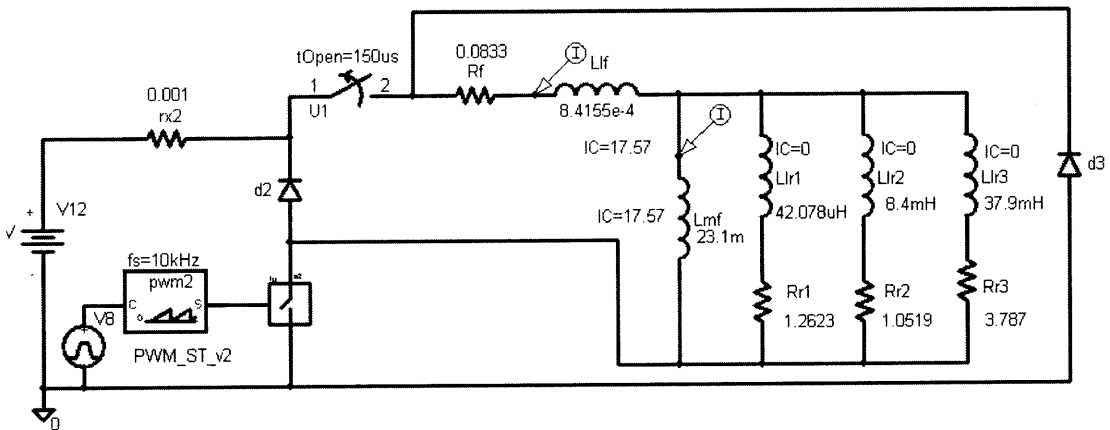
Figure 5.3: PSpice simulation of field de-excitation by voltage reversal.
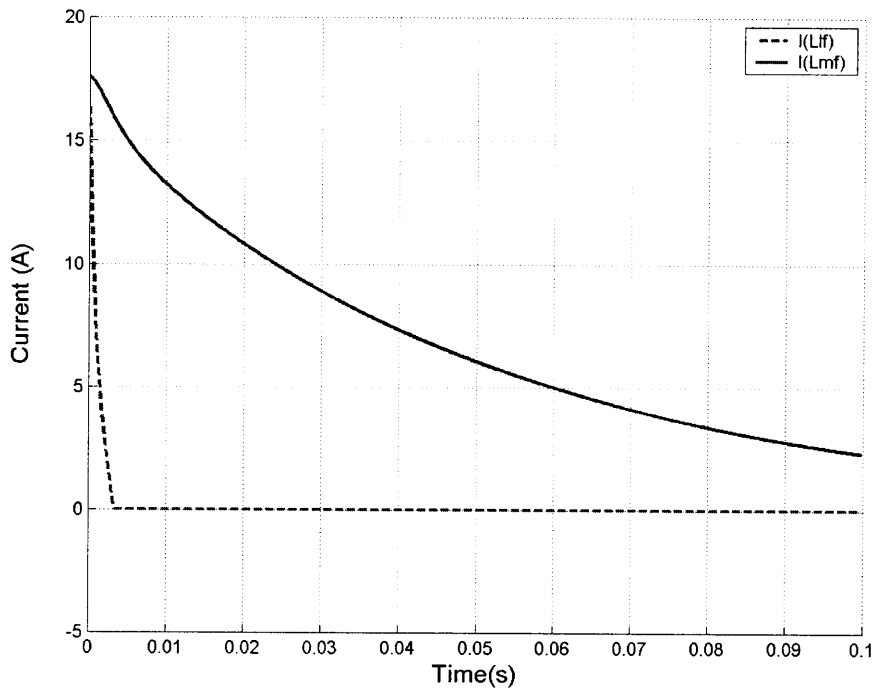
Figure 5.4: Simulation of the circuit in Figure 5.3, showing the field current (lower curve) and a scaled version of open circuit output voltage envelope (the solid curve is I_{Lmf} which is proportional to the envelope of the overvoltage) where $k=10$.
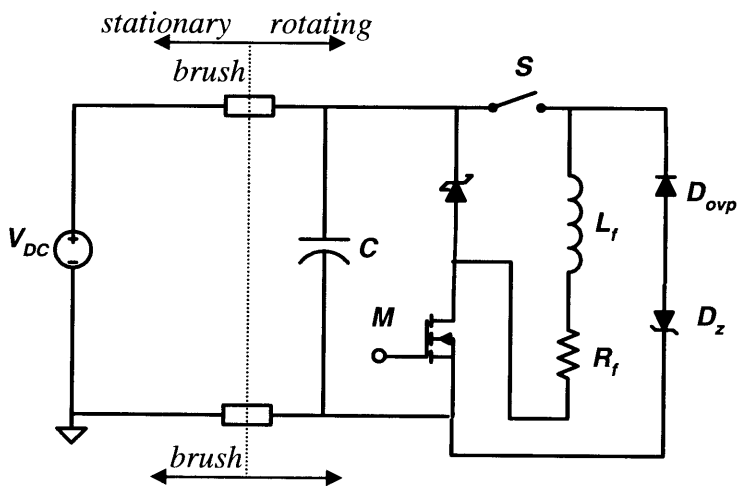
Figure 5.5: De-excitation circuit with the addition of a zener diode to increase voltage reversal.

5.2.3 DC/DC Converter on Rotor with De-excitation by Voltage Reversal while Allowing for Reverse Current

As explained in Chapter 3, the larger the voltage reversal, the faster the de-excitation. Increasing the voltage reversal, however, will create higher stresses on the components. It will also be more costly. A procedure that would facilitate faster de-excitation and reduced stress is to allow the field current to flow in the opposite direction. This would allow for a lower voltage reversal while maintaining the same de-excitation rate. The flux created by the reverse current will oppose the flux created by eddy currents, thus speeding up the de-excitation process. This, however, involves additional switches. The circuit in Figure 5.2 can be further modified to allow for a reverse current through the field winding as shown in Figure 5.6. A PSpice implementation of the circuit is shown in Figure 5.7.
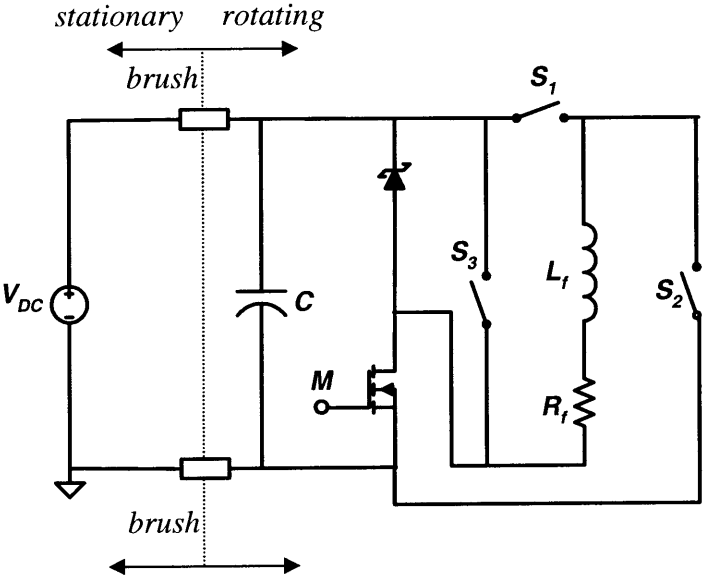
Figure 5.6: Circuit with DC/DC conversion on rotor enables for de-excitation by voltage and current reversal of the field winding.
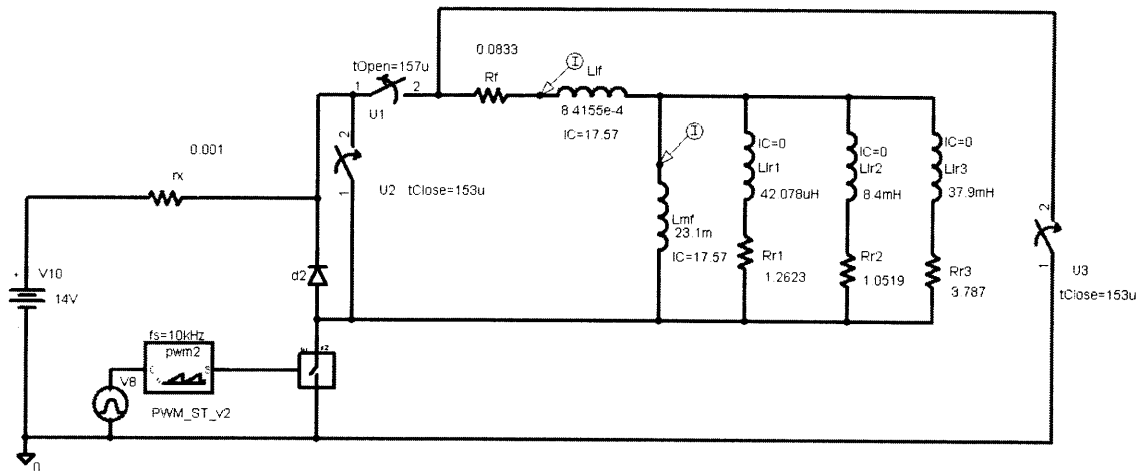
Figure 5.7: PSpice simulation of circuit used for de-excitation by voltage and current reversal.

To de-excite the field winding following the load dump, switches S_2 and S_3 are closed while S_1 and the MOSFET M are turned off. As a result, the reverse bus voltage is applied across the field winding. The field current will decrease. As a consequence, the output voltage will decrease. The field current is allowed to flow in the reverse direction after it reaches zero. The simulation results with k equal to 10 are shown in Figure 5.8. The results show that the output voltage reaches 1/5 of its peak value after only 28 ms. The simulation again shows that a reverse in field current can make a significant contribution to the de-excitation rate.
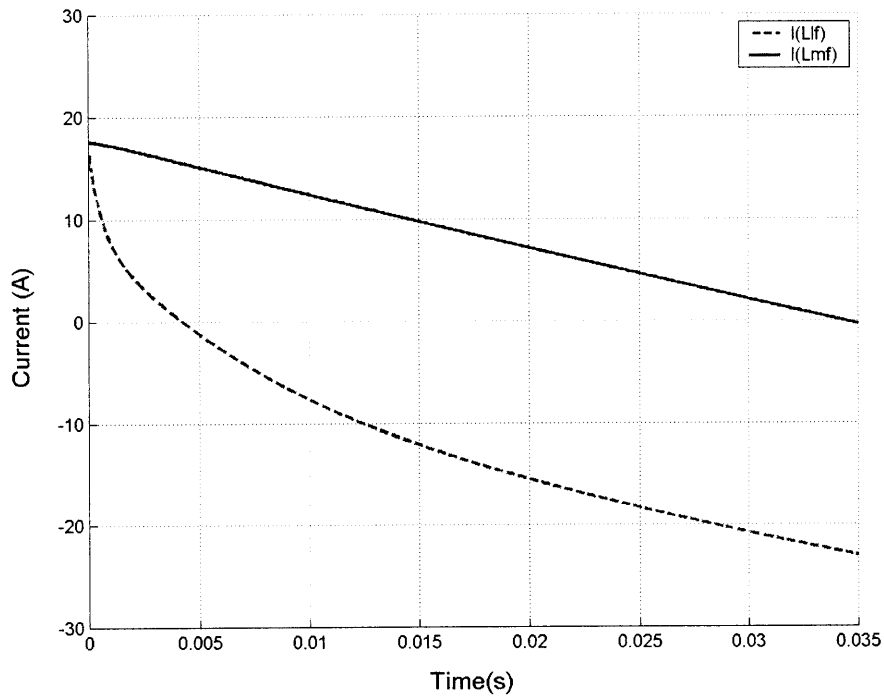
Figure 5.8: Simulation of circuit in Figure 5.7 showing field current (lower curve) and scaled version of open circuit voltage envelope (upper curve) where k=10. The field control circuit of Figure 5.6 is used as illustrated in Figure 5.7.

The above results show that fast de-excitation is achievable using these circuit topologies. Following de-excitation, after the overvoltage transient has reached an acceptable value, these circuits must be controlled such that the rectifier output voltage can be maintained at its steady state voltage and not further decrease. This would involve resuming the application of a positive voltage across the field winding.

5.2.4 Rotating Transformer Topology

Another circuit topology that will allow for the larger currents associated with a higher packing factor foil field winding uses a transformer with a stationary primary and a rotating secondary, thereby eliminating the brushes. Removal of the brushes will result in some additional benefits. Brush wear can limit the life of the alternator. Power losses associated with the brushes are averted by their removal.

One way to eliminate brushes is shown in Figure 5.9. This circuit used is a forward (isolated buck-derived) converter. Connected to the input 14 V bus voltage is an inverter, the output of which is connected to the stationary primary winding of the rotating transformer. The secondary winding of the rotating transformer rotates with the shaft. The secondary winding is connected to a rectifier such that DC currents can flow through the field winding. Such a topology has been used by others for contactless power transfer [18,19]. This circuit can function as the voltage regulator. The dc voltage output of the armature circuit may be monitored and feedback may be used to adjust the duty ratio (or phase shift, or frequency) of the switches in the inverter of the field circuit to regulate the voltage.
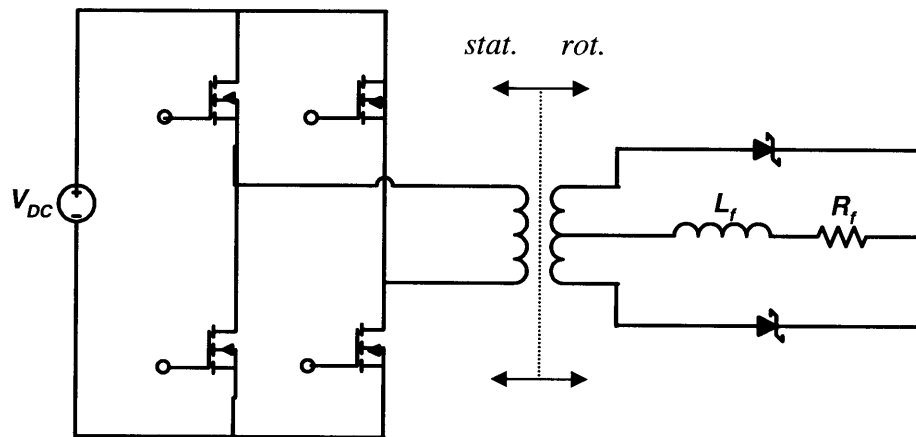
Figure 5.9: Voltage regulator with rotating transformer which eliminates the need for brushes. More efficient operation can be achieved using synchronous rectification in place of diodes.

5.2.5 Rotating Transformer Topology with De-excitation by Voltage Reversal

The circuit in Figure 5.9 can be modified to allow for fast field de-excitation. De-excitation can be achieved by applying a negative voltage across the field winding. One possible circuit is shown in Figure 5.10. The corresponding PSpice circuit is shown in Figure 5.11. The additional circuitry in the simulation is used for control of the switches. The additional switches in Figure 5.10 allow for the application of a negative voltage

across the field winding or 2 quadrant operation. The circuit includes two additional switches together with their control circuitry. During steady state operation, the circuit is connected as the typical forward isolated buck converter with the two additional switches held on. When a load dump occurs, the two additional switches are modulated on and off alternately, to impose a negative DC voltage across the field winding. The switching sequence used causes the rotating-side circuit to act as a current-source inverter and the stationary-side circuit to act as a rectifier, such that the energy is removed from the field and delivered back to the DC bus, minus any losses in transfer.
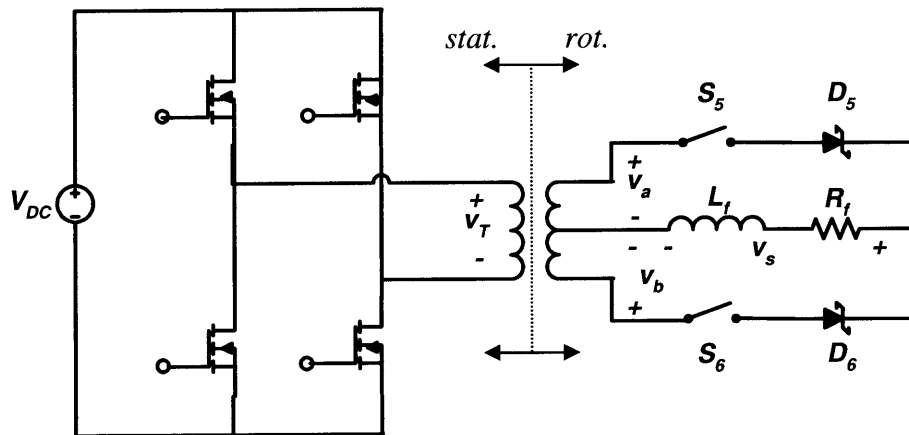
Figure 5.10: Voltage regulator with rotating transformer which allows for removal of the brushes and fast de-excitation of the field winding through two quadrant operation.
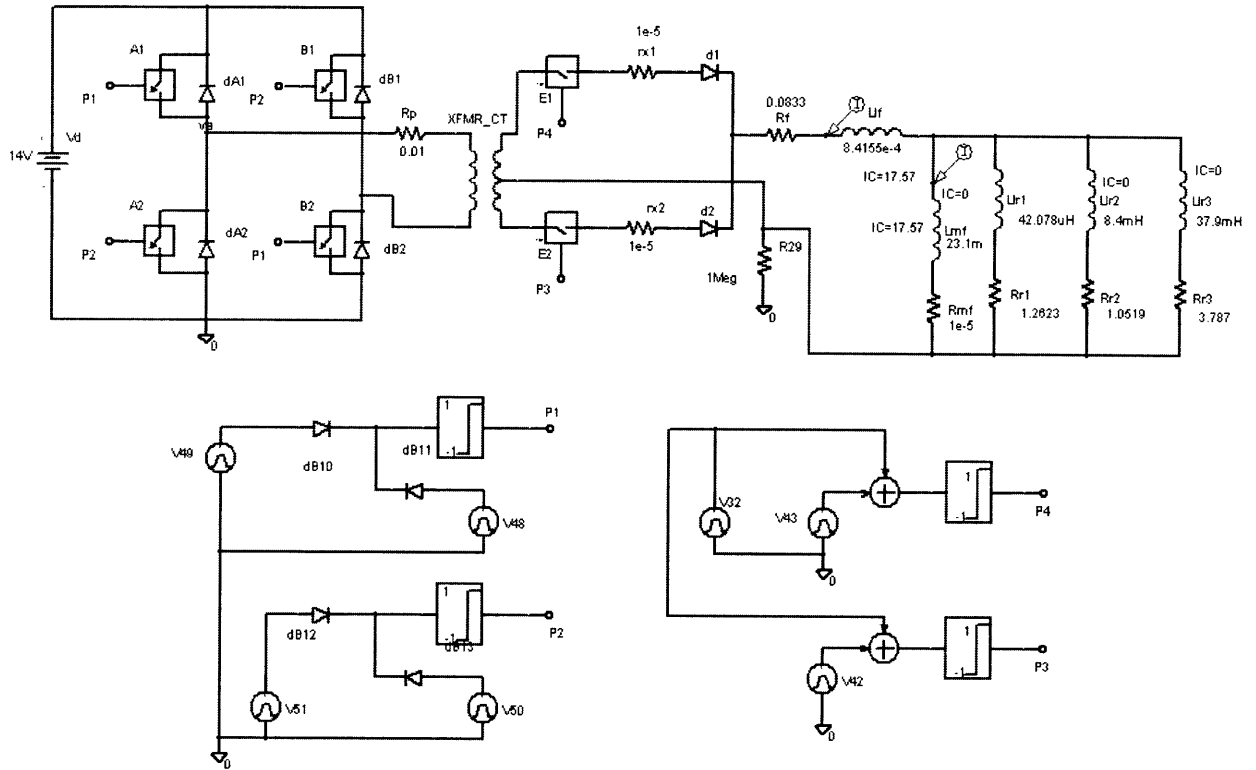
Figure 5.11: Pspice simulation of circuit used for de-excitation by voltage reversal.

The switching procedure for de-excitation is now explained in more detail. The waveforms in Figures 5.12-5.15 are the steady state waveforms of the converter when both S_5 and S_6 are closed [20]. The primary voltage is a stepped waveform as shown in Figure 5.12. The voltage across the field winding v_s is shown in Figure 5.13. Figures 5.14 and 5.15 show the currents through diodes D_5 and D_6 respectively, during steady state operation. The voltage v_a has the same waveform as v_T but is scaled by n, the transformer turns ratio. The voltage v_b is the negative of v_a. When v_a is positive, diode D_5 is forward biased and the load current flows through it. When v_T is zero, each diode carries half the load current. When v_b is positive, the load current flows through D_6.

During a load dump, the field winding is de-excited by applying a negative average voltage across it. The addition of two switches allows for the application of a negative voltage as shown in Figure 5.10. To de-excite the field winding, v_a is caused to be negative while D_5 is conducting and v_b is caused to be negative while D_6 is conducting. Assume that the load dump occurs at time 0^+ in Figure 5.16 with the current

flowing through D_5. At time t_y, S_6 is opened. Therefore, previously, when v_T becomes zero the current would split between both diodes. However, since S_6 is open, the current will continue to flow through D_5. During this time while v_T is zero, it does not matter where the current flows. The objective, though, is that when v_a goes negative, the current will still continue to flow through D_5 since S_6 is open. At some point, the current must be transferred to the lower branch anticipating v_b going negative. This can be done before T_s+DT_s (v_a still negative or v_b still positive) at $t_{x2} = T_s + t_x$ by closing S_6 so that the current will transfer naturally to D_6 since v_b is still positive. Shortly after this, while v_b is still positive, S_5 is opened at $t_{y2} = T_s + t_y$ so that the current does not split between both branches at T_s+DT_s. Current will now flow through D_6 and will continue during the time period when v_b goes negative. The switch timing procedure then repeats until the necessary de-excitation is achieved. The current through diode D_6 is shown in Figure 5.17. The voltage reversal magnitude can be increased by increasing the duty ratio of the inverter switches on the stationary side following a load dump. The time during which V_T is zero will then be reduced and the time during which the voltage is negative will increase. The voltage reversal ratio will be maximum when the duty ratio equals 1.0, in which case V_T never goes to zero. The voltage reversal ratio also increases when the current transfer from one branch to the other is delayed as much as possible while maintaining an unforced or natural current transfer. Referring back to the situation where the current is still flowing through D_5, the reversal ratio can be increased by making the transfer of current to the other branch as close as possible to T_s+DT_s while allocating some time to turn off S_5 before T_s+DT_s.

The figures show the current to be constant over a few periods. In reality, however, the current is decreasing slowly due to the average negative voltage across the field winding. Also, notice that the switches are turned off while no current is flowing through them (zero current switching). The current transfers to the other branch naturally.
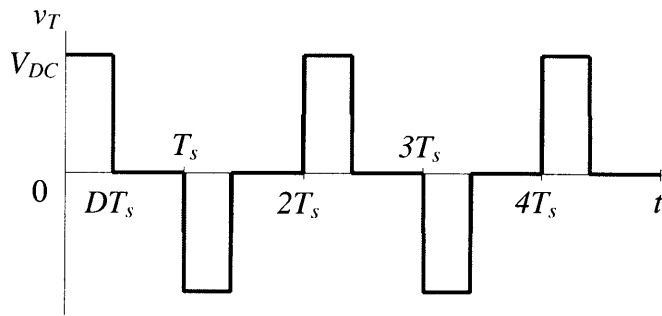
Figure 5.12: Transformer primary voltage, v_t (stationary side) during normal operation for the circuit of Figure 5.10.
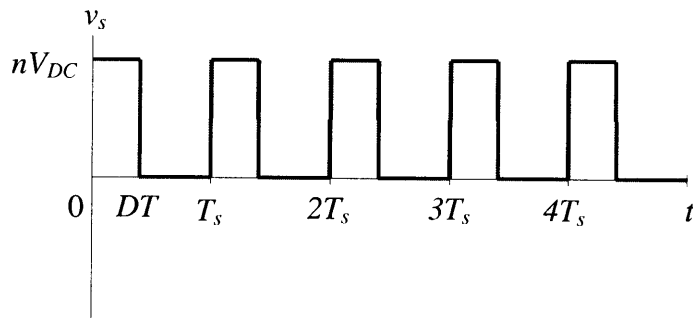
Figure 5.13: Rectified voltage applied across the field winding during normal operation for the circuit of Figure 5.10.
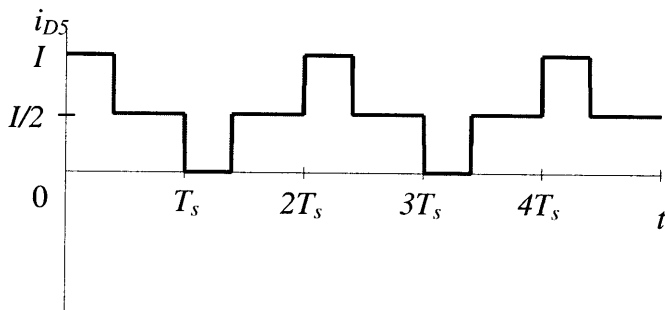
Figure 5.14: Current through D_5 during normal operation in steady state for the circuit of Figure 5.10, where I is the field current.
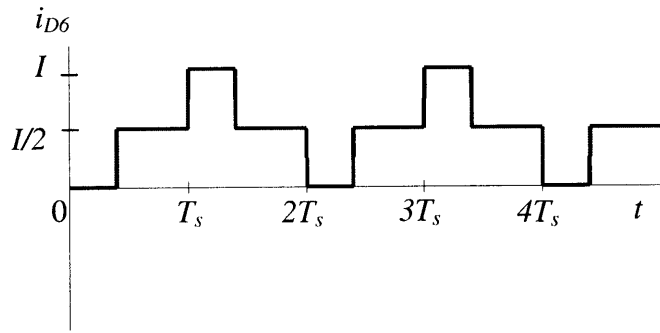
Figure 5.15: Current through D_6 during normal operation in steady state for the circuit in Figure 5.10, where I is the field current.
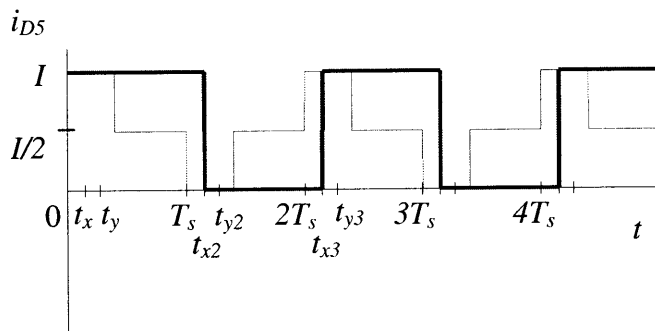
Figure 5.16: Current through D_5 during de-excitation for the circuit in Figure 5.10.
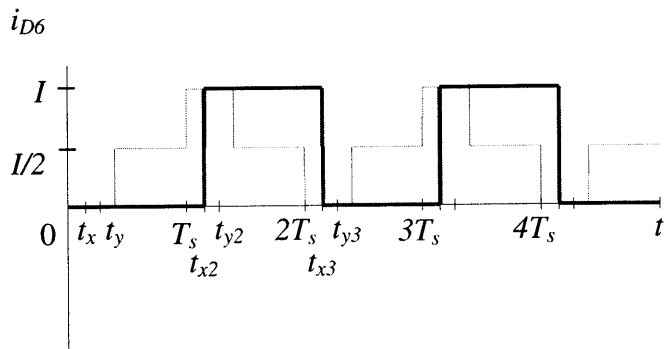
Figure 5.17: Current through D_6 during de-excitation for the circuit in Figure 5.10.

The higher the average reverse voltage applied across the field winding, the less time it takes for the current to decrease to zero. Having fewer turns with more current is actually desirable when considering de-excitation assuming the use of the DC/DC

100

converter. A simplified example would be to decrease the number of turns by a factor of 10 and increase the current by a factor of 10. The field resistance will decrease by a factor of 100 assuming the packing factor stays the same. The steady state duty ratio will then be a tenth of the original duty ratio. This allows for a significant voltage reversal by increasing the duty ratio following a load dump.

The circuit in Figure 5.10 allows for a uni-directional field current and thus when the field current reaches zero, it stays at zero. A simulation of the de-excitation of the circuit in Figure 5.11 can be found in Figure 5.18 using the field magnetic circuit parameters shown in Table 4.1. This simulation was done for a voltage reversal ratio of 4/3. The duty ratio following the load dump was 4/3 the pre-load dump duty ratio. The output voltage reaches 1/5 of its original voltage after 96 ms. It is desired that the overvoltage duration is as short as possible. A higher voltage reversal (and faster decay) can be achieved by increasing the duty ratio of the inverter switches following the load dump.
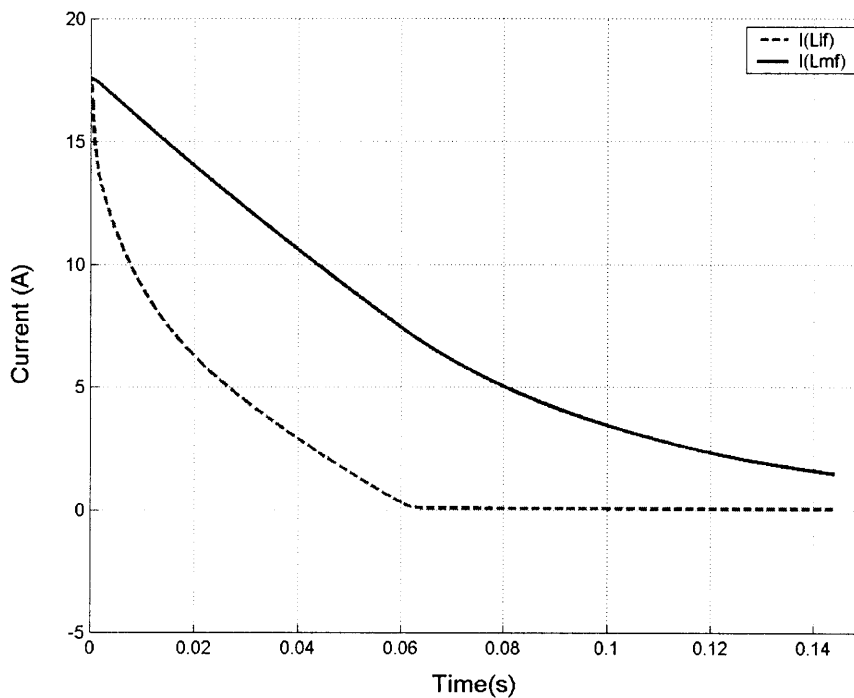
Figure 5.18: Simulation of the field control circuit in Figure 5.11, including field current (lower curve) and scaled version of output voltage envelope (upper curve) where the voltage reversal ratio $k=4/3$.

5.2.6 Rotating Transformer Topology with De-excitation by Voltage Reversal while Allowing for Reverse Current

Adding still more switches will allow for the current through the field winding to flow in the opposite direction. Such a circuit is shown in Figure 5.19. The corresponding PSpice circuit is shown in Figure 5.20. The additional circuitry is used to control the switching for full four quadrant (bi-directional voltage and current) operation. The stationary side is a voltage source inverter/rectifier, while the rotating side is a current-source inverter/rectifier. The results of the simulation are shown in Figure 5.21. During de-excitation, S_5 and S_6 are switched with the same timing as the simpler de-excitation circuit in Figure 5.10. However, when the field current reaches zero, it can be made to flow in the opposite direction if S_7 and S_8 are both turned on while S_5 and S_6 are turned off. The switches S_7 and S_8 are then kept on continuously to further de-excite the field winding.

The simulation was done for a voltage reversal of 4/3 while allowing for negative currents. The output voltage reaches 1/5 its maximum value after 92 ms, only several milliseconds better than voltage reversal alone. This is partly due to that period of time after the field current has reached zero and before it can go negative. This occurs because of the effects of eddy currents. The field current can only start flowing in the opposite direction when the magnitude of the voltage across the eddy current circuits has decreased sufficiently that the reverse direction diodes get forward biased. A larger reversal voltage will shorten the overvoltage duration.
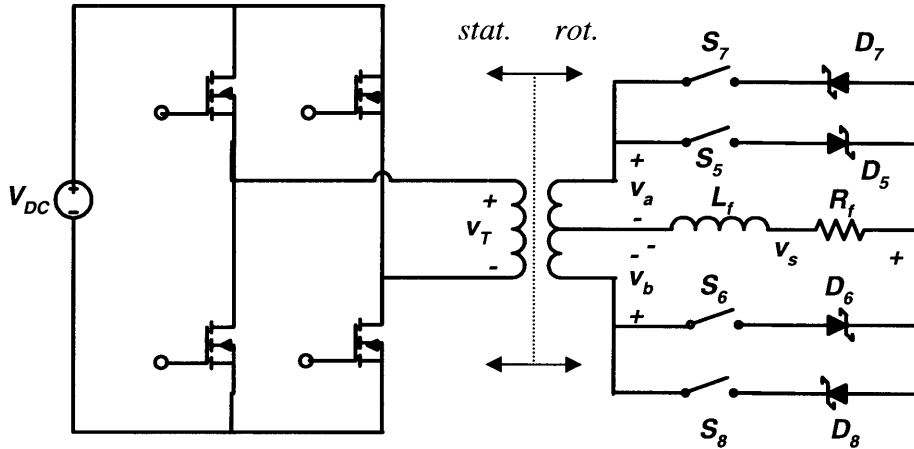
Figure 5.19: Modified full-bridge transformer isolated buck converter (bi-directional voltage, bi-directional current) for four quadrant operation.
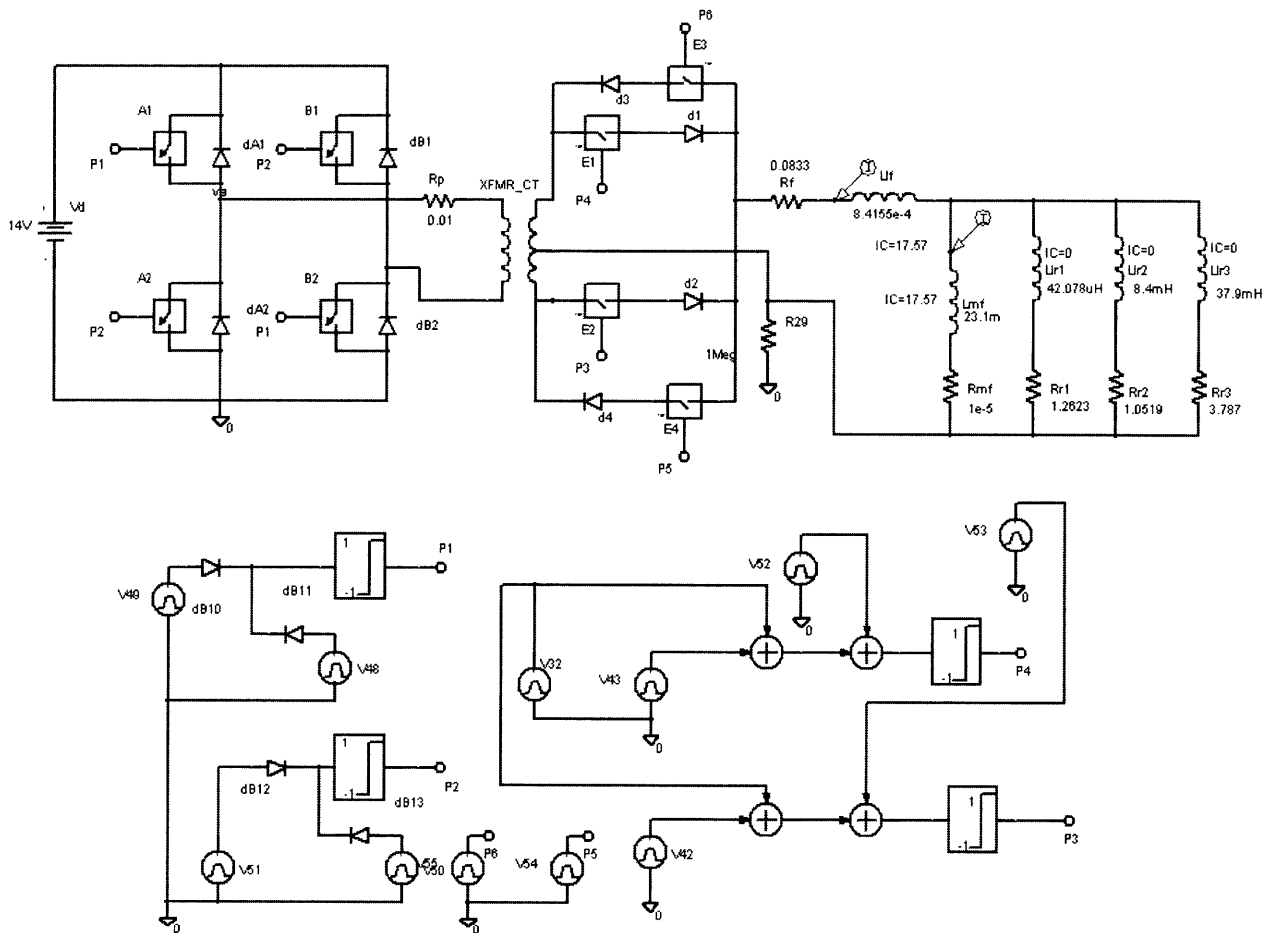
Figure 5.20: PSpice simulation of the circuit used in Figure 5.19 for de-excitation by voltage and current reversal.

As with the brushed bi-directional conversion topologies, additional control must be implemented to return the alternator back to steady state once the overvoltage transient reaches an acceptable value. In the case of four quadrant operation where the field current can reverse its direction, the field current must be increased when the output voltage has reached an acceptable value. It must go positive again afterwards.
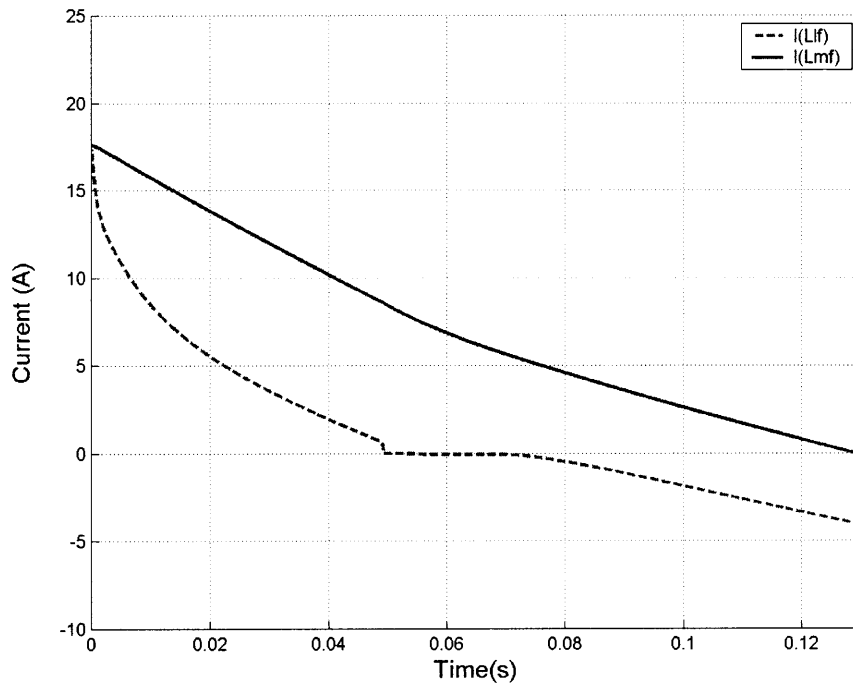
Figure 5.21: Simulation of circuit in Figure 5.20 which includes field current (lower curve) and scaled version of output voltage envelope (upper curve) where *k*=4/3.

5.3 Summary

This chapter illustrates the design of circuits that allow for higher-current excitation of the field winding, which is necessary if the foil winding is to be used. The first circuit involves the use of a DC/DC converter on the rotating side to increase the current delivered to the foil winding as compared to the current drawn from the bus. It has to be on the rotating side since there is a limit to the allowable current through the brushes. The second circuit involves the use of a rotating transformer that enables the

104

transfer of power from the stationary primary winding to the rotating secondary winding without the use of brushes. A rectifier is necessary on the rotating side. Further modifications of each of the circuits allow for voltage reversal across the field winding (two-quadrant operation) or voltage and current reversal through the field winding (four-quadrant operation). Simulations in PSpice demonstrate the feasibility of these circuit topologies, and show their use for fast-field de-excitation. In actual circuits, the goal is to have the shortest overvoltage duration possible. Shutting off the field current results in a 75 ms overvoltage due to the eddy currents. When implementing these de-excitation circuits by voltage reversal, this duration can be achieved and shorter durations can be obtained by increasing the voltage reversal or allowing for both voltage and current reversal (reversal ratio of at least 4).

Chapter 6

A Contactless Field Exciter Using a Printed Circuit Board Transformer

6.1 Motivation

Chapter 5 identified topologies that will enable the use of a foil winding and its larger field currents, and that allow for fast field de-excitation. Different means for transferring power to the rotating field circuit were also proposed, including the use of a rotating transformer-based contactless power transfer system. This chapter explores the design, implementation and experimental evaluation of the rotating transformer topology. For simplicity, fast field de-excitation is not implemented.

The transformer is implemented as a coreless structure with Printed Circuit Board (PCB) windings. This PCB transformer consists of two PCBs with spiral windings on each of the boards facing each other. Both boards are circular to provide rotational symmetry. One board is stationary and has the primary spiral winding and the other board is rotating with the field winding and has the secondary spiral winding. The gap between the windings is 0.635 mm. Both windings will be simply made out of copper traces. Such a transformer is small, easily repeatable and has the potential to be cost effective. This transformer has no magnetic core and is also known as an air-core printed circuit board transformer. As covered earlier in Chapter 5, an inverter is used to convert the DC bus voltage to AC, which is required for power transfer through the transformer. The voltage at the secondary winding is then rectified to provide a DC voltage across the field winding. A filter is used at the output of the rectifier (either inductive or capacitive) to achieve the desired power transfer characteristics. Since the field winding is highly inductive, the current ripple through the load is small.

A simplified schematic of the prototype system is shown in Figure 6.1 (details may be found in Appendix D). Alternative implementations of the inverter and rectifier are clearly possible, and more sophisticated versions (e.g. implementing synchronous rectification [38,39,40,41,42] and or current doubling [43,44]) could be used to realize improved efficiency. Nevertheless, the implementation in Figure 6.1 is sufficient to demonstrate the feasibility of the approach.
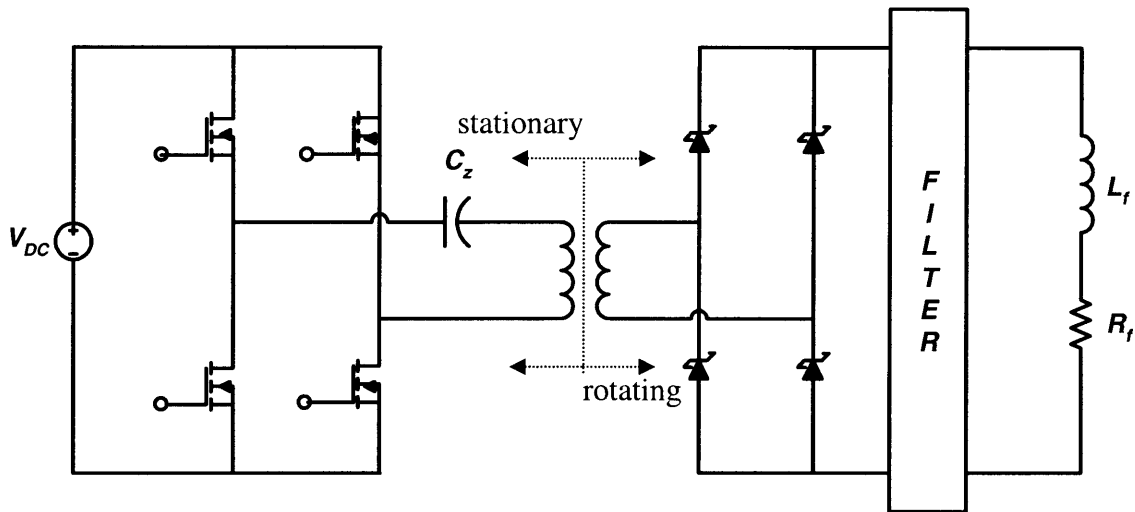
Figure 6.1: Circuit using rotating transformer to transfer power from stationary to rotating side. The copper traces are implemented in 4 ounce/ft^3 copper, and the conductor faces are spaced with approximately a 0.635 mm between the stationary and rotating winding.

6.2 PCB Transformer Design

A circuit with a PCB transformer was built to determine the feasibility of the proposed power transfer system. The PCB transformer designed and used is shown in Figure 6.2. Its dimensions are specified in Table 6.1. The windings are made of copper traces. The primary winding has four turns while the secondary winding has two turns. The design of the PCB transformer will be covered in the succeeding sections. Clearly, the transformer occupies a minimal amount of space and is very easy to produce. The design of the transformer is the more involved part. Fortunately, fairly accurate models of PCB transformers (for stationary applications) have already been formulated [21].

108

0 ⊢┼┼┼┼┤ 1 cm
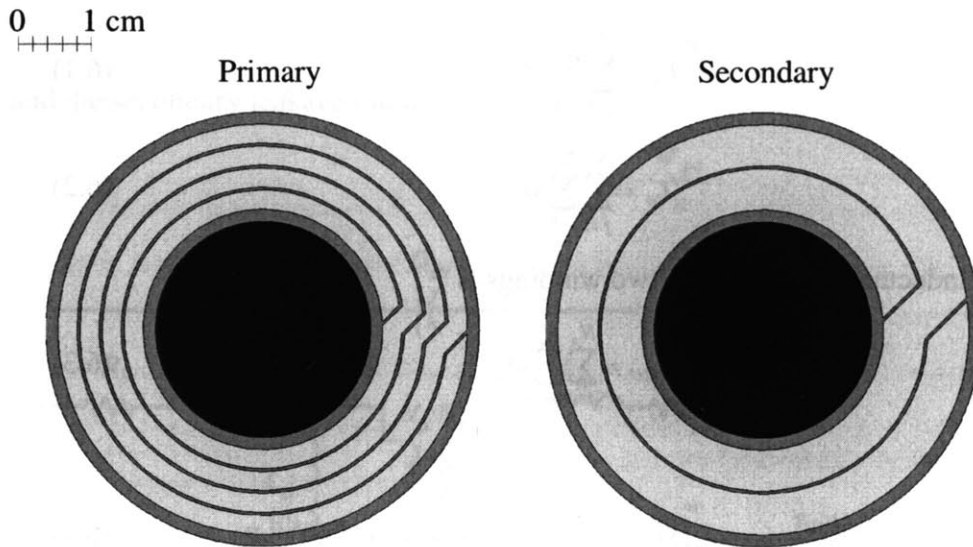
Primary   Secondary

Figure 6.2: PCB transformer (stationary primary and rotating secondary).

Table 6.1: PCB transformer dimensions.

Parameter	Primary winding	Secondary winding
Inner radius	16mm	16mm
Outer radius	27.3mm	27.3mm
Copper track width	2.5mm	5.5mm
Separation between tracks	0.381mm	0.381mm
Track height	0.137mm	0.137mm
Gap	0.635mm	

6.2.1 PCB Transformer Modeling

The analysis of PCB transformers (for stationary applications) has been done in previous research [21]. The following derivations are taken from [21]. For a PCB transformer with N_p primary turns and N_s secondary turns, the primary and secondary self inductances are

109

$$L_p = \sum_{j=1}^{N_p} \sum_{i=1}^{N_p} M_{ij} \tag{6.1}$$

$$L_s = \sum_{j=1}^{N_s} \sum_{i=1}^{N_s} M_{ij} \tag{6.2}$$

and the mutual inductance between the two windings is

$$M_{ps} = \sum_{j=1}^{N_p} \sum_{i=1}^{N_s} M_{ij} \tag{6.3}$$

with

$$M_{ij} = \frac{\mu_0 \pi}{h_1 \ln\left(\frac{r_2}{r_1}\right) h_2 \ln\left(\frac{a_2}{a_1}\right)} \int_0^\infty S(kr_2, kr_1) S(ka_2, ka_1) Q(kh_1, kh_2) e^{-k|z|} dk \tag{6.4}$$

where

$$S(kx, ky) = \frac{J_0(kx) - J_0(ky)}{k} \tag{6.5}$$

and

$$Q(kx, ky) = \frac{2}{k^2}\left(\cosh\left(k\frac{x+y}{2}\right) - \cosh\left(k\frac{x-y}{2}\right)\right) \tag{6.6}$$

and where the following notation holds:

J_o = order zero Bessel function of the first kind

a_1 = inner radius of the ith circular track

a_2 = outer radius of the ith circular track

r_1 = inn0er radius of the jth circular track

r_2 = outer radius of the jth circular track

h_1 = height or thickness of the ith circular track

h_2 = height or thickness of the jth circular track

z = axial separation between the two tracks

k = wave number.

The magnetizing inductance referred to the primary is

$$L_M = nM_{ps} \tag{6.7}$$

where n is the number of primary turns divided by the number of secondary turns. The primary leakage inductance is

$$L_{lp} = L_p - L_M \qquad (6.8)$$

and the secondary leakage inductance is

$$L_{ls} = L_s - \frac{M_{ps}}{n} \qquad (6.9)$$
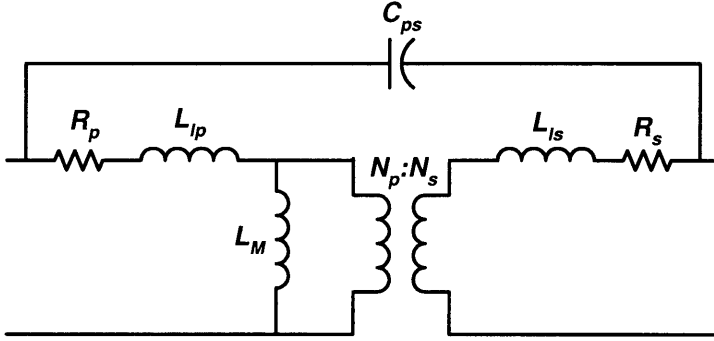
Figure 6.3: PCB transformer equivalent circuit.

Following [23], the equivalent circuit of Figure 6.3 can be transformed into the circuit shown in Figure 6.4 where

$$n = \frac{N_p}{N_s} \qquad (6.10)$$

$$L'_{ls} = n^2 L_{ls} \qquad (6.11)$$

$$R'_s = n^2 R_s \qquad (6.12)$$

$$C'_{ps} = \frac{C_{ps}}{n} \qquad (6.13)$$

$$C'_p = \frac{(n-1)}{n} C_{ps} \qquad (6.14)$$

$$C'_s = \frac{(1-n)}{n^2} C_{ps} \qquad (6.15)$$

The circuit in Figure 6.4 can be analyzed more easily if the components between any two nodes are combined into a single impedance. To do so, the circuit model can be converted into that shown in Figure 6.5.
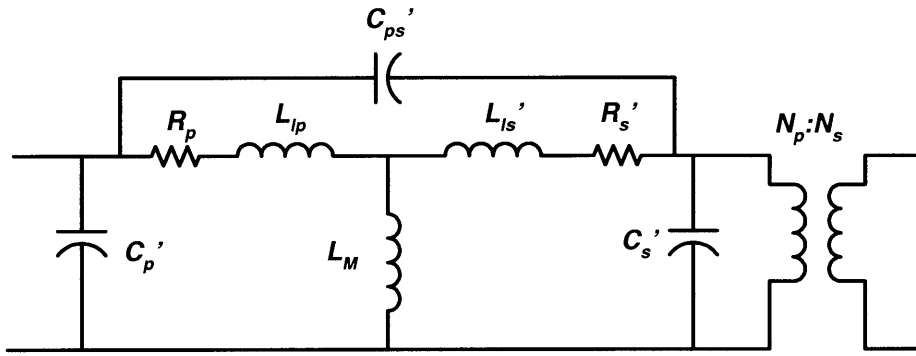
Figure 6.4: Equivalent transformer circuit.
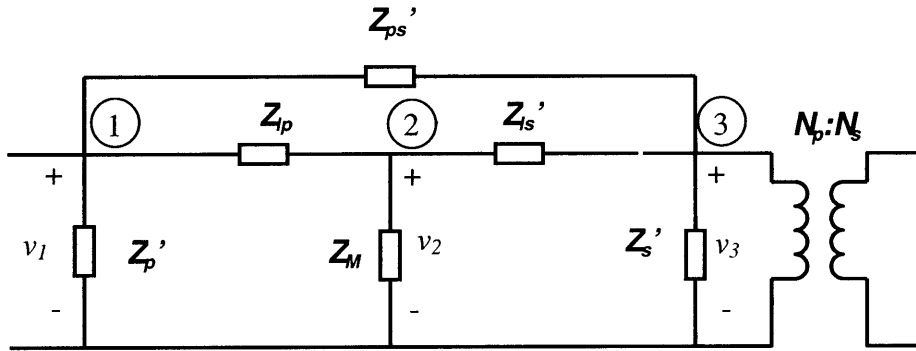
Figure 6.5: Transformer circuit using impedances.

The transformer is connected to a rectifier to provide a direct current to the field winding. The goal is to obtain an overall equivalent circuit model as shown in Figure 6.6, where the DC input voltage source, inverter, and transformer are transformed into an AC source in series with an inductance and a resistance. The Thevenin equivalent of the PCB transformer circuit can thus be obtained. The output impedance of the PCB transformer is obtained by shorting out v_1 and calculating the impedance looking into the output terminals. This impedance is derived to be

$$Z_{out} = \frac{\left(\left(Z_{lp} \mathbin{//} Z_M + Z_{ls}'\right) \mathbin{//} Z_s' \mathbin{//} Z_{ps}'\right)}{n^2} \tag{6.16}$$

This impedance is equal to the sum of a real and imaginary part. The output inductance at a particular frequency and output resistance can be found:

$$L_s = \frac{\mathrm{Im}(Z_{out})}{\omega}$$

(6.17)

$$R_s = \mathrm{Re}(Z_{out})$$

(6.18)

where L_s is the inductance and R_s is the resistance.

To calculate the equivalent source voltage, let the Y's be the admittances which are the reciprocals of each of the Z's or impedances. Using KCL at nodes 2 and 3 of the circuit in Figure 6.5, the following matrix equation can be obtained, for the case where there is no current in the transformer,

$$\begin{bmatrix} Y_{lp} + Y_{ls}' + Y_M & -Y_{ls}' \\ -Y_{ls}' & Y_{ps}' + Y_{ls}' + Y_s' \end{bmatrix} \begin{bmatrix} v_2 \\ v_3 \end{bmatrix} = \begin{bmatrix} Y_{lp} v_1 \\ Y_{ps}' v_1 \end{bmatrix}$$

(6.19)

where the voltage v_1 is the fundamental component of the output square wave of the inverter. Having solved for v_3, the equivalent Thevenin voltage can be found to be

$$v_S = \frac{v_3}{n}$$

(6.20)

The resulting equivalent circuit is then obtained as shown in Figure 6.6.
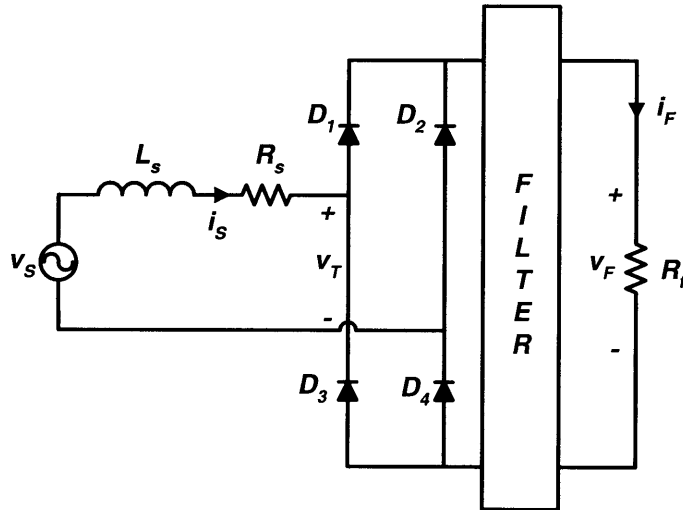
Figure 6.6: Equivalent circuit.

113

6.2.2 Equivalent Circuit Including Rectifier and Filter Modeling

Using the preceding model, the overall performance of the circuit when using an inductor or capacitor filter can be derived. Here we use the model to evaluate expected performance with inductive and capacitive filtering on the dc-side of the rectifier. Several models are presented with increasing accuracy.

6.2.2.1: Inductor Filter with No Diode Drop and No Series Resistor

The circuit with an inductor filter is first investigated and is shown in Figure 6.7. The simplest analysis when using the inductor filter ignores the diode drop and disregards the resistance in series with the commutating inductance L_s. Referring to Figure 6.7, the diode drops of D_1 to D_4 are ignored as well as the series resistance R_s.
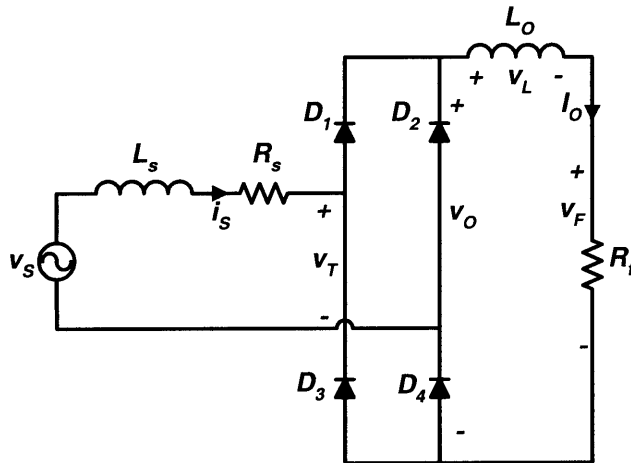
Figure 6.7: Equivalent circuit using inductor for a constant current load.

The output voltage v_O and source current i_S are shown in Figures 6.8 and 6.9, respectively. The filter inductor L_0 is assumed to be large enough such that the output current can be assumed to be constant and denoted by I_O. While v_S is positive, diodes D_1 and D_2 conduct and I_O flows through them. When v_S reaches zero at time π/ω, commutation begins, in which diodes D_2 and D_3 start to conduct current while D_1 and D_4 continue to conduct. The current through D_1 and D_4 decreases, while that through D_2 and

D_3 increases. Commutation ends when all of the current I_0 is transferred to D_2 and D_3. At this point, D_1 and D_4 stop conducting. The time it takes for current transfer called the commutation interval and is denoted by u in Figure 6.8. The commutating interval is determined as in [24] using
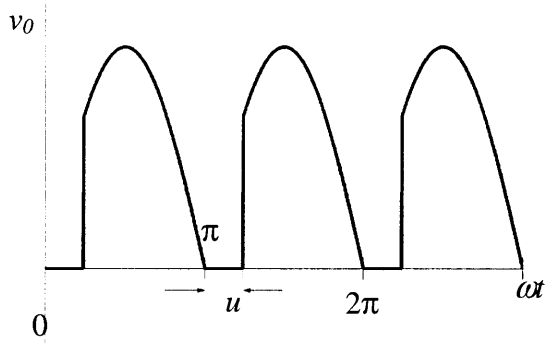
Figure 6.8: Output voltage of constant current load circuit.
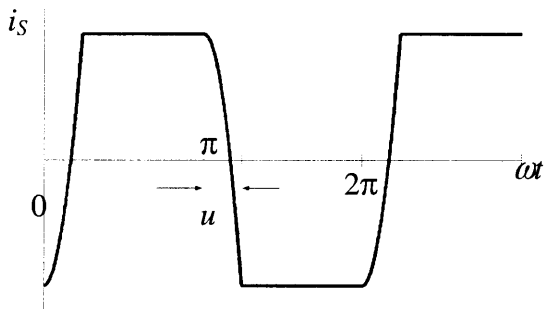
Figure 6.9: Current through inductor L_s.

$$-I_0 = I_0 + \frac{1}{\omega L_s} \int_\pi^{\pi+u} V_s \sin\theta d\theta \qquad (6.21)$$

where the change in current across an inductor is proportional to the time integral of the voltage across it. The relation for the commutation interval can then be found to be

$$\cos u = 1 - \frac{2I_0\omega L_s}{V_s} \qquad (6.22)$$

The average output voltage is

115

$$\langle v_0 \rangle = \frac{V_s}{\pi}(\cos u + 1) \tag{6.23}$$

and using Equation 6.22 can be expressed as

$$\langle v_0 \rangle = \frac{2V_s}{\pi}\left(1 - \frac{I_0 \omega L_s}{V_S}\right) \tag{6.24}$$

Since the average voltage across the inductor filter is zero, the average rectifier voltage is equal to the average voltage across the field winding

$$\langle v_0 \rangle = \langle v_F \rangle = I_0 R_f \tag{6.25}$$

Using Equations 6.24 and 6.25, the average output current is

$$I_0 = \frac{2V_s/\pi}{R_f + 2\omega L_s/\pi} \tag{6.26}$$

6.2.2.2: Inductor Filter with Diode Drop and No Series Resistor

For improved accuracy, the diode drops may be included in the calculation. The output voltage and current waveforms are shown in Figures 6.10 and 6.11, respectively, where the diode drops are exaggerated to show the effect on the wave shape. The input voltage to the rectifier v_T follows v_S while it is greater than twice the diode drop, or $2V_d$. Diodes D_1 and D_2 conduct and I_O will flow through them. Note that the drop across the inductor L_s is zero since the current through it is constant. When v_T decreases to $2V_d$, commutation begins. Diodes D_2 and D_3 will start to conduct current while D_1 and D_4 will continue to conduct. The voltage v_T jumps to zero while v_0 jumps to $-2V_d$. The current through D_1 and D_4 will decrease to zero, while that through D_2 and D_3 will increase. Commutation ends when all of the current I_0 is transferred to D_2 and D_3. At this point, D_1 and D_4 will stop conducting. A similar transition occurs when current is transferred back to diodes D_1 and D_4.

116
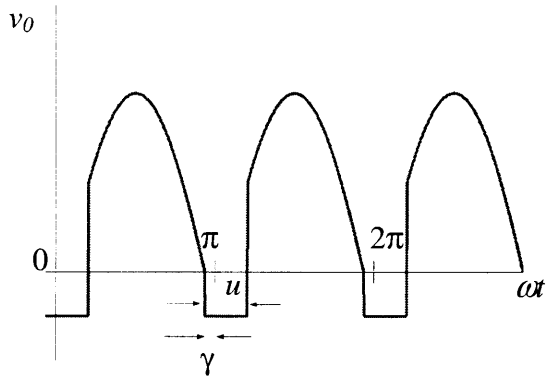
Fig. 6.10: Output voltage for constant current load circuit while including diode drop.
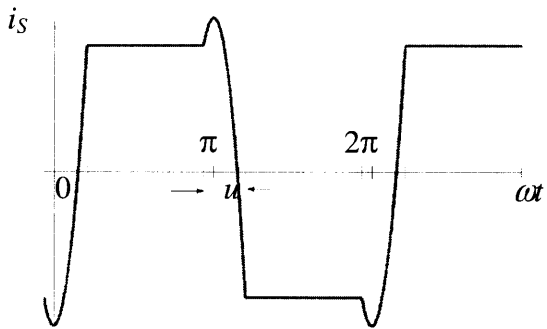
Fig. 6.11: Current through inductor L_s while including diode drop.

During commutation all 4 diodes are on and the output voltage is $-2V_d$. To solve for γ,

$$2V_d = V_s \sin \gamma$$

$$\gamma = \sin^{-1}\left(\frac{V_s}{2V_d}\right) \tag{6.27}$$

The currents before and after commutation are

$$i_S\left(\frac{\pi - \gamma}{\omega}\right) = I_0 \tag{6.28}$$

$$i_S\left(\frac{\pi - \gamma + u}{\omega}\right) = -I_0 \tag{6.29}$$

Since the change in current over time through the inductor is proportional to the integral of the voltage across it, the following relation holds

$$-I_0 = I_0 + \frac{1}{\omega L_s} \int_{\pi-\gamma}^{\pi-\gamma+u} V_s \sin\theta d\theta \qquad (6.30)$$

and therefore

$$I_0 = \frac{1}{2\omega L_s} V_s (\cos\gamma - \cos(u-\gamma)) \qquad (6.31)$$

The average output voltage is

$$\langle v_0 \rangle = \frac{1}{\pi} \int_{u-\gamma}^{\pi-\gamma} V_s \sin\theta d\theta - 2V_d \qquad (6.32)$$

$$\langle v_0 \rangle = \frac{V_s}{\pi} (\cos(u-\gamma) + \cos\gamma) - 2V_d \qquad (6.33)$$

Using Equations 6.25, 6.31, and 6.33, the following equation can be obtained which could be solved for the commutation interval u

$$\left(\frac{R_f}{2\omega L_s} - \frac{1}{\pi}\right) V_s \cos\gamma - \left(\frac{R_f}{2\omega L_s} + \frac{1}{\pi}\right) V_s \cos(u-\gamma) + 2V_d = 0$$

$$u = \cos^{-1}\left(\frac{\left(\frac{R_f}{2\omega L_s} - \frac{1}{\pi}\right) V_s \cos\gamma + 2V_d}{\left(\frac{R_f}{2\omega L_s} + \frac{1}{\pi}\right) V_s}\right) + \gamma \qquad (6.34)$$

Given u, the output current can be obtained using Equations 6.25 and 6.33.

$$I_O = \frac{\frac{V_s}{\pi}(\cos(u-\gamma) + \cos\gamma) - 2V_d}{R_f} \qquad (6.35)$$

6.2.2.3. Inductor Filter with Diode Drop and Series Resistor

For improved accuracy, the diode drops and series resistor are included in the analysis. The output voltage and source current waveforms are shown in Figures 6.12 and 6.13, respectively. The diode and resistive drops are also exaggerated to show their effect on the shape of the waveform.
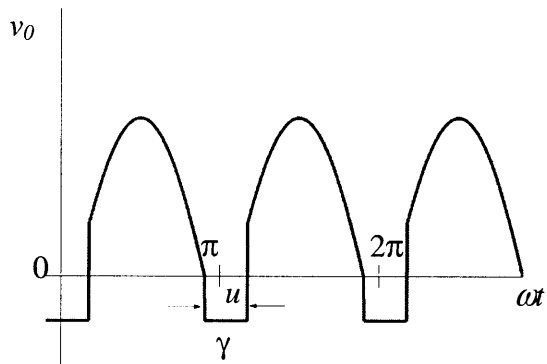
Fig. 6.12: Output voltage for constant current load circuit while including diode drop and resistance R_s.
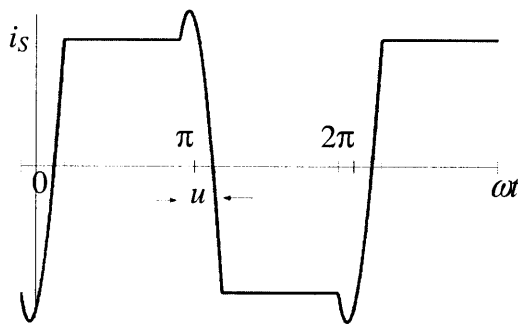
Fig. 6.13: Current through inductor L_s while including diode drop and resistance R_s.

The input voltage to the rectifier v_T equals v_S-I_OR_s or the source voltage minus the resistive drop when it is greater than twice the diode drop. Diodes D_1 and D_2 will be conducting and I_0 will be flowing through them. Note that the drop across the inductor L_s is zero since the current through it is constant. When v_T decreases to $2V_d$, commutation begins. Diodes D_2 and D_3 will start to conduct current while D_1 and D_4 will continue to conduct. The voltage v_T jumps to zero while v_O jumps to $-2V_d$. The current through D_1 and D_4 will decrease to zero, while that through D_2 and D_3 will increase. Commutation ends when all of the current I_O is transferred to D_2 and D_3. At this point, D_1 and D_4 will stop conducting.

During commutation all 4 diodes are on and the output voltage is $-2V_d$. To solve for γ,

$$V_s \sin \gamma = 2V_d + I_0 R_s$$

$$\gamma = \sin^{-1}\left(\frac{2V_d + I_0 R_s}{V_s}\right) \tag{6.36}$$

The currents before and after commutation are

$$i_S\left(\frac{\pi - \gamma}{\omega}\right) = I_0 \tag{6.37}$$

$$i_S\left(\frac{\pi - \gamma + u}{\omega}\right) = -I_0 \tag{6.38}$$

Durring commutation,

$$L_s \frac{di_S}{dt} = V_s \sin(\omega t) - i_S R_s \tag{6.39}$$

Define

$$\tau = t - \left(\frac{\pi - \gamma}{\omega}\right) \tag{6.40}$$

such that

$$i_S(\tau = 0) = I_0 \tag{6.41}$$

$$i_S\left(\tau = \frac{u}{\omega}\right) = -I_0 \tag{6.42}$$

Then using Kirchoff's Voltage Law (KVL),

$$L_s \frac{di_S}{d\tau} = V_s \sin(\omega\tau + \pi - \gamma) - i_S R_s \tag{6.43}$$

and therefore

$$\frac{di_S}{d\tau} + \frac{R_s}{L} i_S = \frac{V_s \sin(\omega\tau + \pi - \gamma)}{L} \tag{6.44}$$

The current will be composed of a homogeneous and particular solution.

$$i_S = i_{Sh} + i_{Sp} \tag{6.45}$$

The homogeneous solution can be found by setting the voltage source to zero such that

$$i_{Sh} = Ae^{-\left(R_s/L\right)\tau} \tag{6.46}$$

The particular solution will have the form

$$i_{Sp} = B \sin \omega \tau + C \cos \omega \tau \qquad (6.47)$$

Substituting Equation 6.47 into Equation 6.44 and solving for B and C will yield

$$B = \frac{\dfrac{V_s \omega \sin \gamma}{R_s} - \dfrac{V_s}{L_s} \cos \gamma}{\dfrac{\omega^2 L_s}{R_s} + \dfrac{R_s}{L_s}} \qquad (6.48)$$

$$C = \frac{V_s \sin \gamma - B \omega L_s}{R_s} \qquad (6.49)$$

and

$$i_S = Ae^{-\left(R_s/L_s\right)\tau} + B \sin \omega \tau + C \cos \omega \tau \qquad (6.50)$$

Substituting in the temporal boundary conditions

$$I_0 = A + C \qquad (6.51)$$

and

$$-I_0 = Ae^{-\left(R_s/L_s\right)\frac{u}{\omega}} + B \sin u + C \cos u \qquad (6.52)$$

and therefore

$$-I_0 = -(C + I_0)e^{-\left(R_s/L_s\right)\frac{u}{\omega}} + B \sin u + C \cos u \qquad (6.53)$$

The average output voltage is

$$\langle v_0 \rangle = \frac{1}{\pi} \int_{u-\gamma}^{\pi-\gamma} (V_s \sin \theta - I_0 R_s) d\theta - 2V_d \qquad (6.54)$$

$$\langle v_0 \rangle = \frac{V_s}{\pi} (\cos(u - \gamma) + \cos \gamma) - 2V_d - \frac{I_0 R_s (\pi - u)}{\pi} \qquad (6.55)$$

and using Equations 6.25 and 6.55, the average output current is

$$I_0 = \frac{\dfrac{V_s}{\pi} (\cos(u - \gamma) + \cos \gamma) - 2V_d}{R_f + \dfrac{R_s (\pi - u)}{\pi}} \qquad (6.56)$$

121

Then using Equations 6.48, 6.49, 6.53 and 6.56, an equation in terms of u and γ can be obtained. Then combining Equation 6.36 with Equation 6.56, another equation relating u and γ can be obtained. The two equations in two unknowns can then be solved numerically. Equation 6.56 will then yield the average output current I_O.

6.2.2.4. Capacitor Filter with No Diode Drop and No Series Resistor
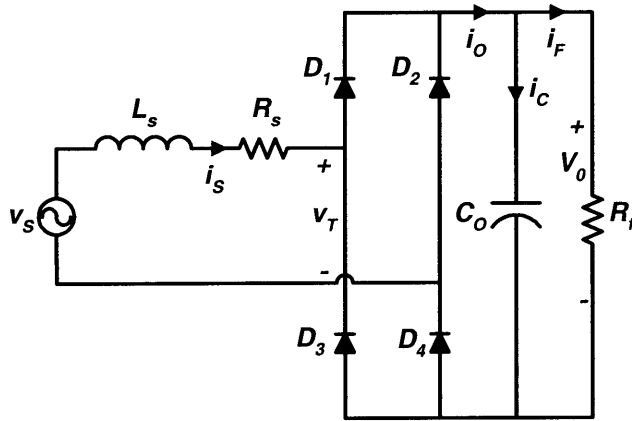
Figure 6.14: Equivalent circuit using capacitor for a constant voltage load.

When a capacitor filter is used, the capacitance is assumed to be large enough such that the voltage at the output is approximately constant at value V_0 [13]. The source current i_S with amplitude I_s lags the source voltage v_S by some angle and has frequency ω as shown in Figure 6.15 where the source voltage is a sine with zero phase. The voltage v_T is then a square wave with amplitude V_0 that is in phase with i_S as shown in Figure 6.16. The output current is the rectified version of i_S shown in Figure 6.17, the average of which is

$$i_0 = \frac{2}{\pi} I_s \qquad (6.57)$$

Since there is no average current through the capacitor, the average current at the output of the rectifier is equal to the average current through the field winding. Therefore,

$$\langle i_0 \rangle = \langle i_F \rangle = \frac{V_0}{R_f} \qquad (6.58)$$

Therefore, combining Equations 6.55 and 6.56, the amplitude of the phase current is

$$I_s = \frac{\pi V_0}{2R_f} \tag{6.59}$$

The voltage v_T is approximated by its fundamental with amplitude

$$V_t = \frac{4}{\pi} V_0 \tag{6.60}$$
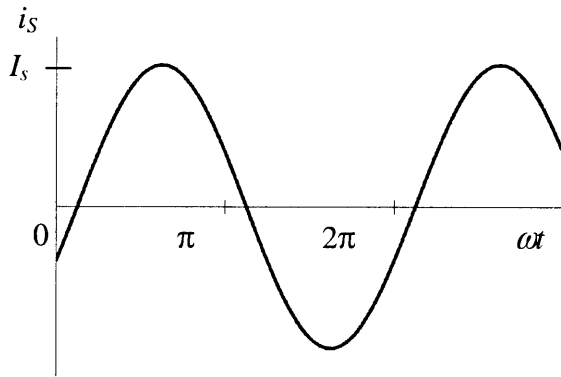
Figure 6.15: Current through inductance L_s for constant voltage load circuit.
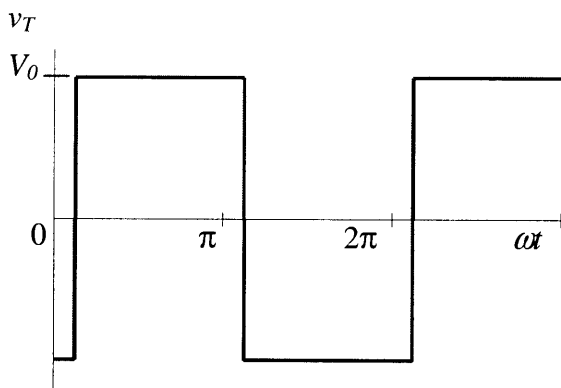
Figure 6.16: Terminal voltage for constant voltage load circuit.
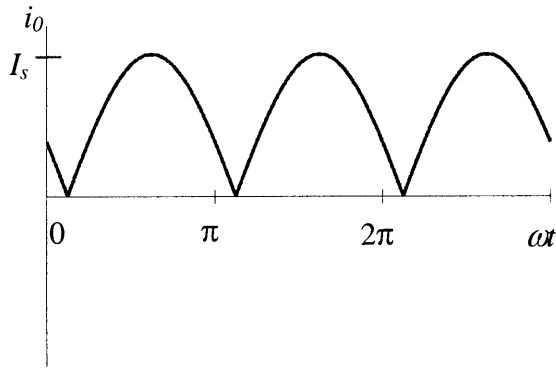
Figure 6.17: Output current for constant voltage load circuit.

A phasor diagram showing the relative phases of the various voltage drops can be drawn as shown in Figure 6.18.
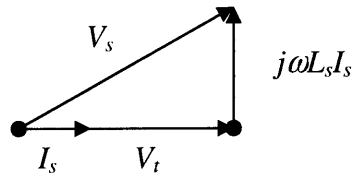
Fig. 6.18: Phasor diagram for constant voltage load circuit.

Based on the Pythagorean theorem,

$$V_s^2 = \left(\frac{4}{\pi}V_0\right)^2 + (\omega L_s I_s)^2 \qquad (6.61)$$

Using Equations 6.58, 6.59 and 6.61, the average output current can be obtained as

$$\langle i_0 \rangle = \frac{V_s \pi}{4\sqrt{R_f^2 + \left(\dfrac{\pi^2 \omega L_s}{8}\right)^2}} \qquad (6.62)$$

6.2.2.5: Capacitor Filter with Diode Drop and No Series Resistor

More accurate results are obtained when the diode drop is included in the calculation for output current. When the diode drop is included, the fundamental component of v_T is

$$V_t = \frac{4}{\pi}(V_0 + 2V_d)$$

(6.63)

Based on the Pythagorean theorem

$$V_s^2 = \left(\frac{4}{\pi}(V_0 + 2V_d)\right)^2 + (\omega L_s I_s)^2$$

(6.64)

Using Equations 6.59 and 6.64, a quadratic equation for V_O can be obtained from which the output current can be determined using Equation 6.58.

6.2.2.6: Capacitor Filter with Diode Drop and Series Resistor

The most accurate analysis uses the phasor diagram when both the diode drops and source resistor are included is shown in Figure 6.19.
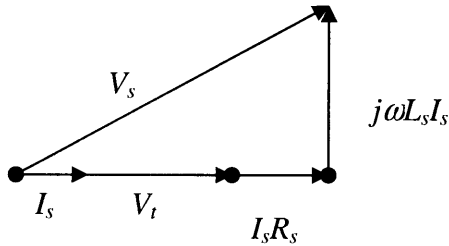
Fig. 6.19: Phasor diagram where resistance is included.

Using the Pythagorean theorem, the following relation holds

$$V_s^2 = \left(\frac{4}{\pi}(V_0 + 2V_d) + I_s R_s\right)^2 + (\omega L_s I_s)^2$$

(6.65)

Using equations 6.59 and 6.65, a quadratic equation can be solved for V_O from which the output current can be using 6.58.

6.3 Transformer Design and Implementation

Models for the entire circuit involving the DC voltage source, inverter, PCB transformer, rectifier, and load have been derived. The DC source and inverter can be combined with the model of the transformer, all of which can be represented as a series

125

combination of an AC voltage source, an inductance, and a resistance. The series combination is then connected to the rectifier with either of two filters, a capacitive filter or an inductive filter, and the calculations for output current are determined. This output current is the average field current since the load of the circuit is the field winding. This modeling of the entire system allows one to determine all the currents and voltages at all nodes given an arbitrary PCB transformer. We now address the design of a PCB transformer that enables sufficient power transfer and current excitation of the field winding on the rotating side.

For a PCB transformer mounted to a conventional Lundell alternator, the minimum inner radius is the radius of the shaft and the maximum outer radius has to be less than the inner radius of the fan blades. As expected, there is a limited area allowed for the PCB transformer. The primary and secondary windings will then have those inner and outer dimensions. Because of the fixed area, the winding can be selected as one turn of wide copper, two turns of copper tracks with approximately half the width, and so on. The narrower the width of the copper track, the less current allowed through it. Because of the set volume for the field winding in the bobbin, one can use more turns of thinner foil or fewer turns of thicker foil. As shown in Chapter 4, it is desirable to use fewer turns of thicker foil for improved packing factor. Note, however, because of the maximum current density limit of the copper tracks, there is a minimum number of turns of field winding that should be used since the PCB transformer will not allow an arbitrarily large amount of current through it given the limited area for the tracks or spiral windings. Note also that the secondary of the PCB transformer could be located near the metallic and magnetizable rotor claw, thus affecting the accuracy of the parameters obtained for an air core transformer. This must be a further consideration.

The number of turns selected is four for the primary winding and two for the secondary winding. A large number of turns is selected for the primary side to reduce the primary side current and associated losses. The larger the number of turns, the larger the magnetizing inductance, and therefore the smaller the peak to peak swing of the magnetizing current. The current through the primary winding will be smaller due to the step up in current to the secondary as well as having more turns on the stationary side that would result in relatively lower magnetizing current and therefore lower conduction

losses on the stationary side. Two turns is selected for the secondary side, in order to have wider traces to accommodate large current (close to 30 A) and at the same time have a step down in voltage. A step down in voltage by two creates a step up in the current available to the field winding while maintaining a sufficient voltage input to the rectifier and allows us to achieve the desired current. Schottky diodes are used due to their low voltage drops.

The PCB transformer was modeled [21,22,23], and the various inductances were calculated and compared with measurements as shown in Table 6.2. The resistance values used in the subsequent modeling were measured experimentally rather than computed theoretically since they increase with frequency in a complicated way due to skin and proximity effects (the gap between the primary and secondary winding is 0.635 mm). The capacitance C_{ps} is approximated using the generic capacitance formula where the area is that which covers the windings and the gap is the gap between the two windings (0.635 mm). The equivalent circuit of the PCB transformer was obtained and was shown previously in Figure 6.2 with parameter values measured at 160 kHz, shown in Table 6.2.

Table 6.2. Rotating transformer parameter values for the transformer of Figure 6.2 with a gap between the printed windings of 0.635 mm.

Parameter	Calculated Value	Measured Value
L_M	0.895 μH	0.767μH
L_p	0.9722μH	0.969μH
L_s	0.241 μH	0.307 μH
L_{lp}	0.0771μH	0.202 μH
L_{ls}	0.0176μH	0.115μH
N_p, N_s	4,2	4,2
C_{ps}	32.63pF	

The model for the rotating transformer was used together with the most accurate models (including series resistance and diode drop) for rectifiers with inductor [24] or capacitor filters [13] to determine how many ampere turns will be provided to the field winding versus frequency for each design. The resulting plot is shown in Figure 6.20

where the number of field turns used was 65 with a resistance of 0.9 Ω. Clearly, switching frequency control (frequency modulation) can be used to adjust field current. Alternatively, control of the dc voltage applied to the inverter can be used to regulate field current. From the analysis, the capacitor filter can be utilized at low frequencies where more field ampere turns are produced compared to the inductor filter. As the number of turns was varied, the same trend occurred where the capacitor output current was higher at lower frequencies, and so only the results for a turns count of 65 are shown, which corresponds to the actual number of turns used in the experiment.
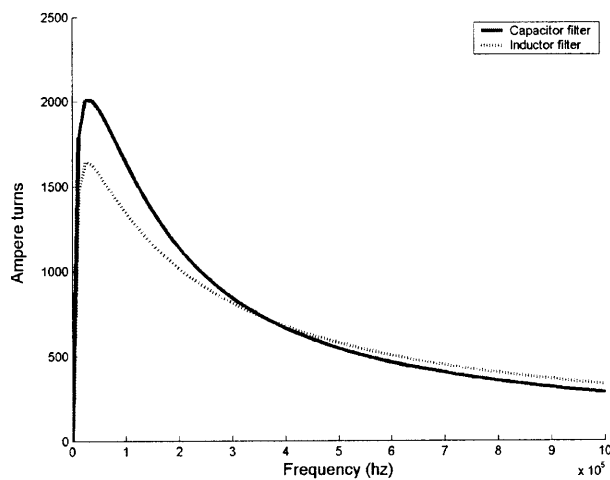
Figure 6.20: Rectifier output current with inductor (dashed) or capacitor (solid) filter.

The objective is to maximize the ampere turns and efficiency. There are several factors such as the field winding thickness and number of turns, and the frequency of operation that will affect the attainable ampere turns and efficiency. There is only a finite amount of space for the winding. The insulation thickness of the copper foil is constant. More turns of thinner copper or less turns of thicker copper can be used. Thinner copper can take less amperes. The number of turns affects the resistance of the field winding. The higher the number of turns, the higher the resistance. The output current and ampere turns were then plotted against frequency and resistance value as shown in Figures 6.21 and 6.22 while using a capacitor filter at the output. More ampere turns are achievable for fewer field turns and higher current. There are, however, thermal limits to increasing the current density of the field winding. The efficiency of the converter decreases with a decrease in resistance as shown in Figure 6.23. There is a trade-off then between the

number of field ampere turns and the efficiency obtained. For calculating the efficiency, the losses considered are the conduction losses in the MOSFETS, transformer windings, and diodes, and the switching losses in the MOSFETS. More details on the efficiency calculations can be found in Appendix D. The input power was also determined and is shown in Figure 6.24. At lower frequencies, the power required increases, partly because of the magnetizing current, which increases as drive frequency increases.
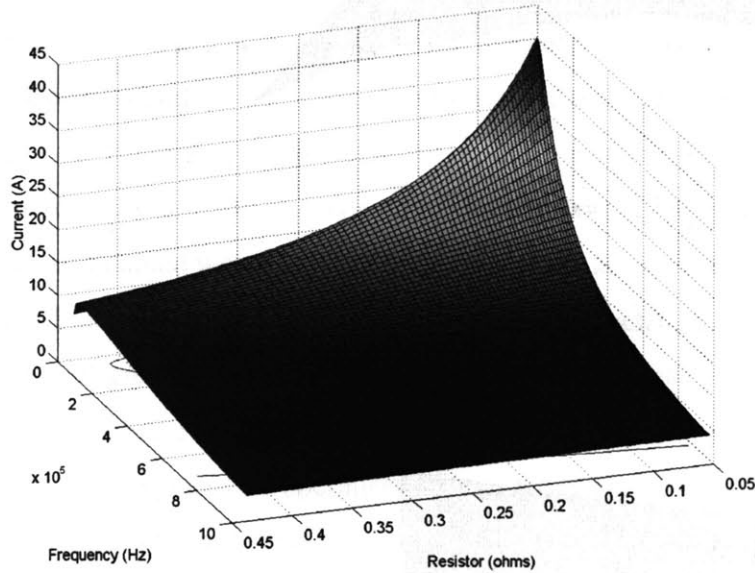
Figure 6.21: Field current vs. resistance and frequency.
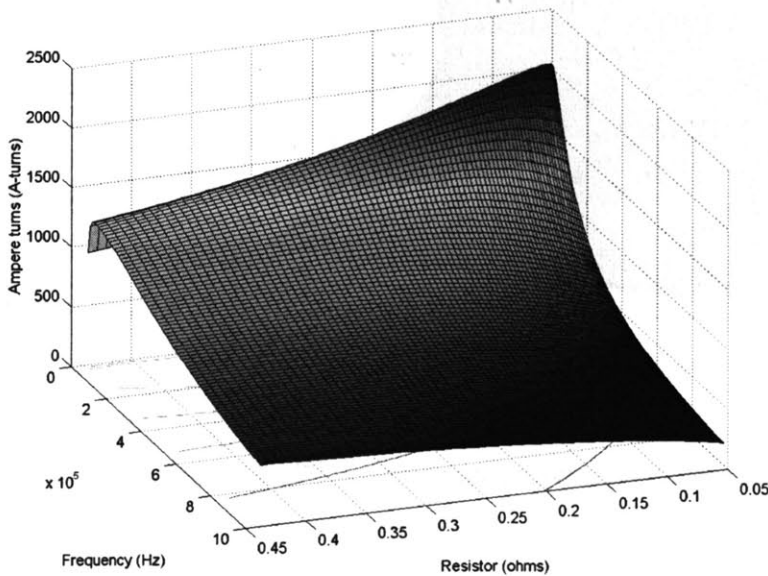
Figure 6.22: Field ampere turns vs. resistance and frequency.
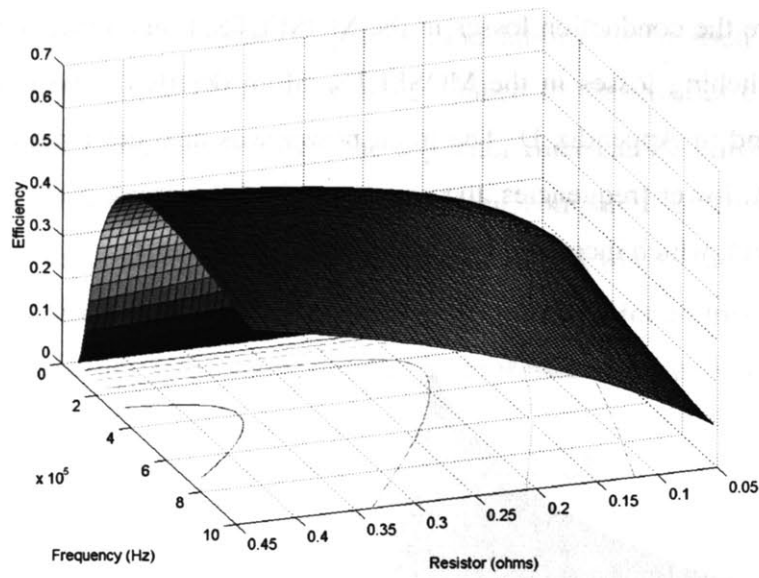
Figure 6.23: Efficiency vs. resistance and frequency.
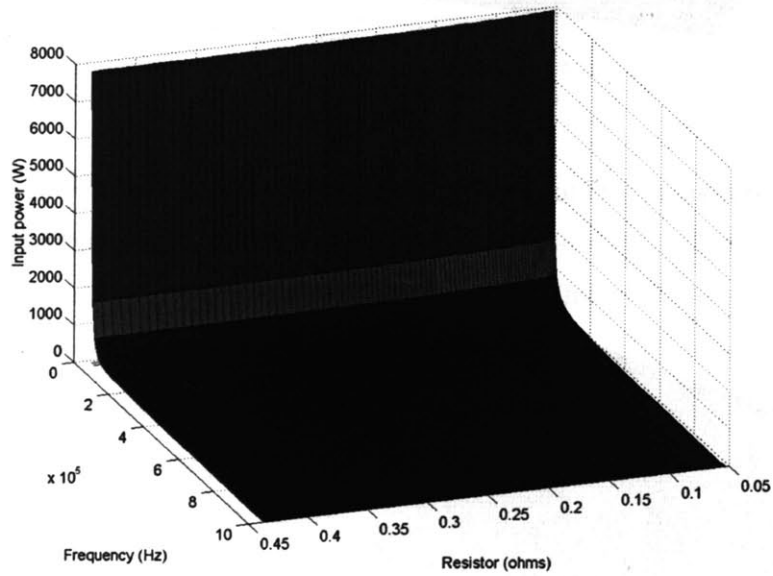
Figure 6.24: Input power vs. resistance and frequency.

130

6.4. Experimental Results

The converter was built and tested in a laboratory test fixture with both windings stationary (not in an alternator). This circuit was built separate from the alternator. Both windings were stationary for this experiment. The load was a foil field winding with 65 turns of 6.2 mil copper with 1.5 mil insulation yielding a resitance of 0.9 Ω. A simplified diagram of the circuit is shown in Figure 6.25. The actual circuit schematic is shown in Figures D.1 and D.2 of Appendix D. The output field ampere turns obtained at six different frequencies are compared with the theoretical curve in Figure 6.26. The flat line in the plot corresponds to the 1195 ampere turns that is achieved in the existing Lundell alternator. At frequencies below 200 kHz, the measured and experimental number of field ampere turns actually exceeds 1195 ampere turns. The maximum number of field ampere turns obtained was 1807 at 90 kHz. This was an increase of 51% over the 1195 in an existing Lundell.

The efficiencies and required input power at those same operating points are shown in Figures 6.27 and 6.28, respectively. The required power for the field circuit increases as the frequency of operation is lowered. Note, however, that more field ampere turns will result in higher output power, while having to consider other factors, such as saturation. At the load matched condition, the output power of the alternator rises as the number of field ampere turns squared, as shown in equation 2.20. The resulting output power could therefore more than compensate for the additional power required by the field circuit. Moreover, substantial efficiency improvements could be achieved using improved rectifier designs (e. g. incorporating synchronous rectification to reduce rectifier loss).

The corresponding measured current waveform at maximum output (90 kHz) has an average of 27.8 A as shown in Figure 6.29. The measured efficiency is 30% with an input power of 232 W and output power of 70 W. The corresponding output voltage at the operating point of 90 kHz is shown in Figure 6.30. The corresponding voltage across the primary winding of the PCB transformer is shown in Figure 6.31. The current through the primary winding of the PCB transformer is shown in Figure 6.32. It is equal to the sum of the magnetizing current and the reflected current from the secondary side.

131

The results show that the required field ampere turns can be improved significantly. However, challenges such as cooling and improvements in efficiency (lower than in existing voltage regulator) have to be dealt with especially when the circuit is integrated into an actual alternator. Means for achieving this include the use of lower-loss rectifier topologies (e.g. current doubler rectifiers [43,44] and/or the use of synchronous rectification [38,39,40,41,42]).
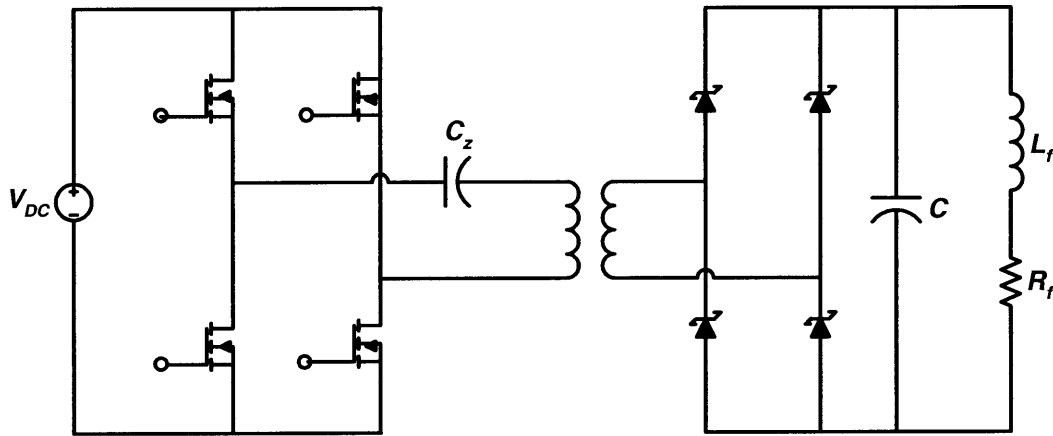
Figure 6.25: Diagram of PCB transformer circuit.
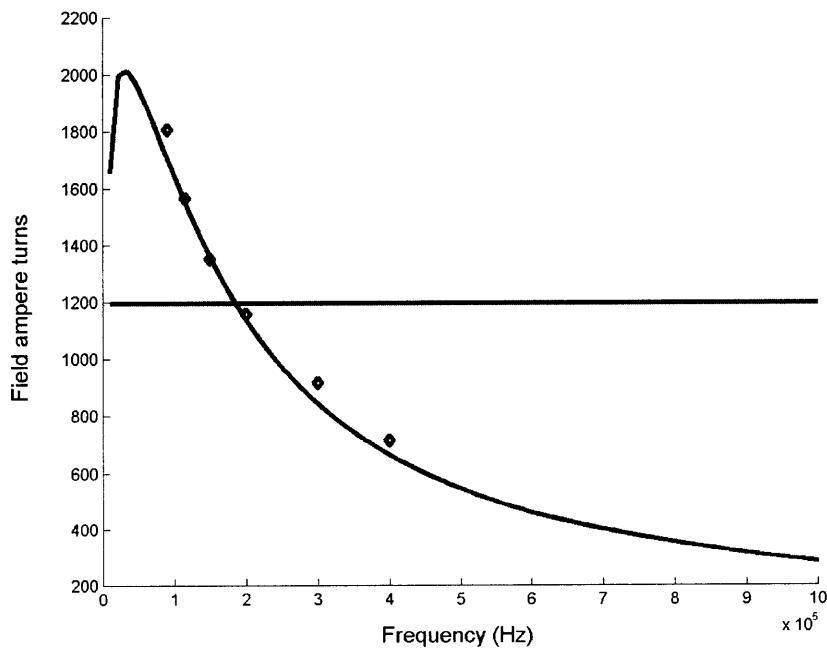
Figure 6.26: Comparison of experimental field ampere turns obtained with theoretical curve.

132
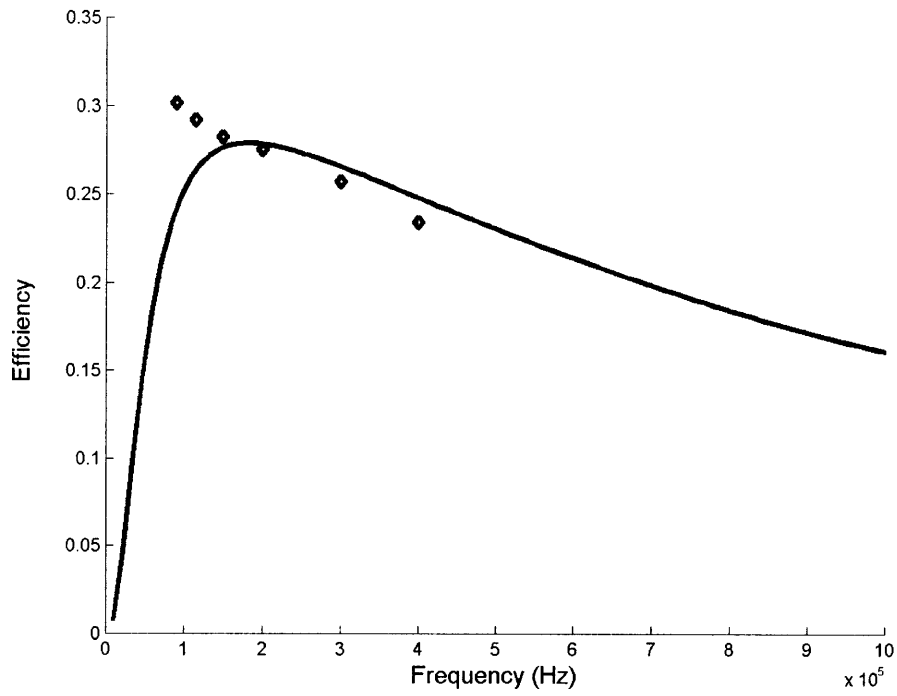
Figure 6.27: Comparison of measured efficiency with calculated efficiency.
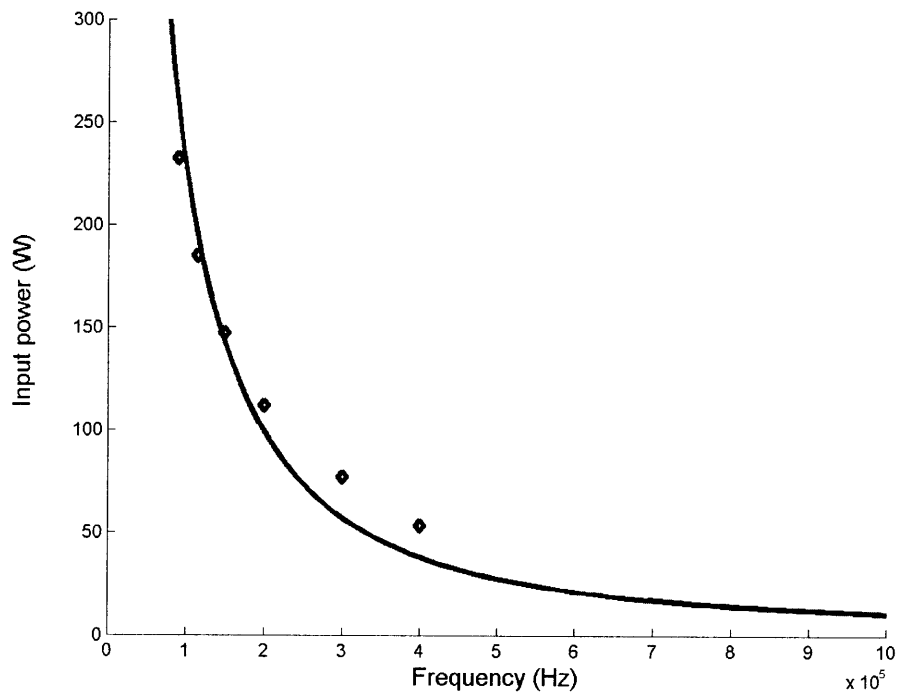
Figure 6.28: Comparison of measured input power to field circuit with theoretical curve.
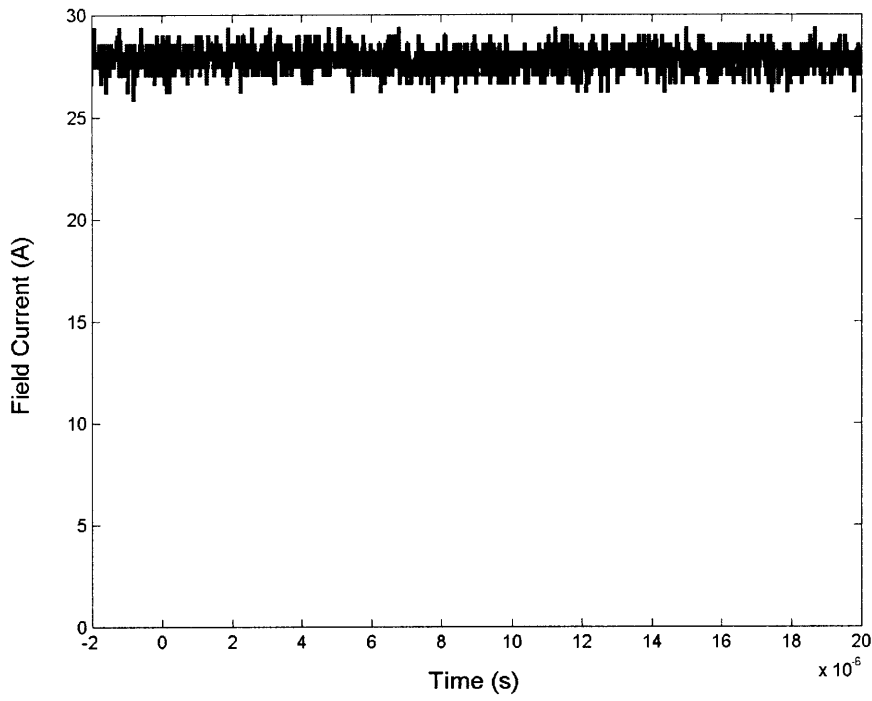
Figure 6.29: Field winding current at inverter switching frequency of 90 kHz.
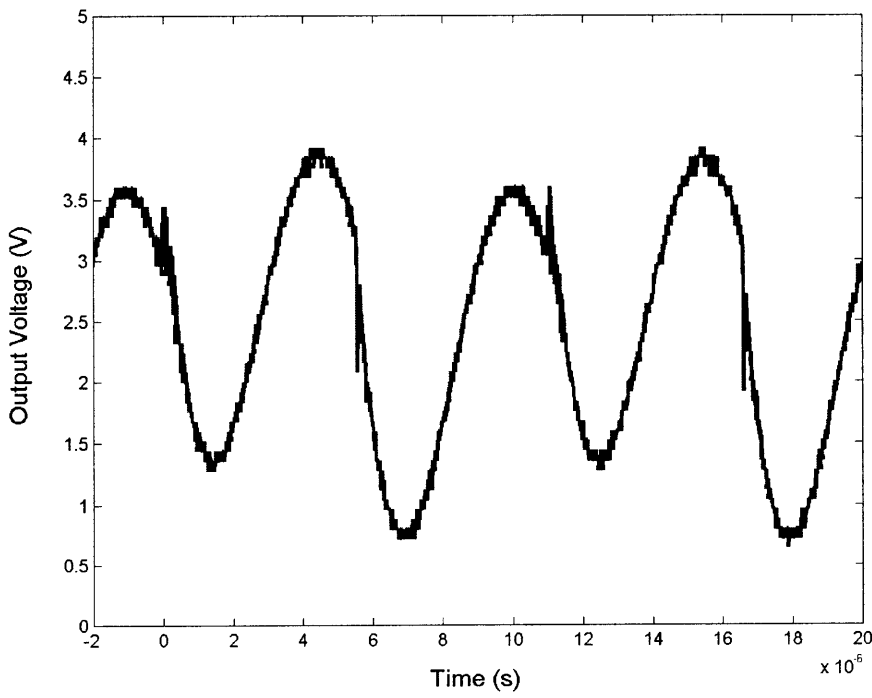
Figure 6.30: Field winding voltage at inverter switching frequency of 90 kHz.
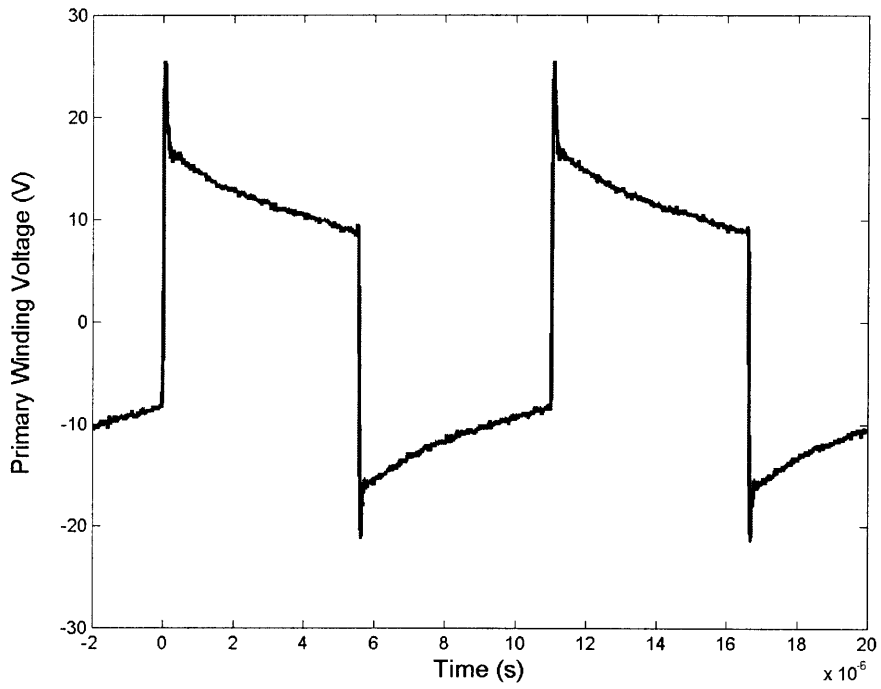
Figure 6.31: Inverter output voltage at inverter switching frequency of 90 kHz.
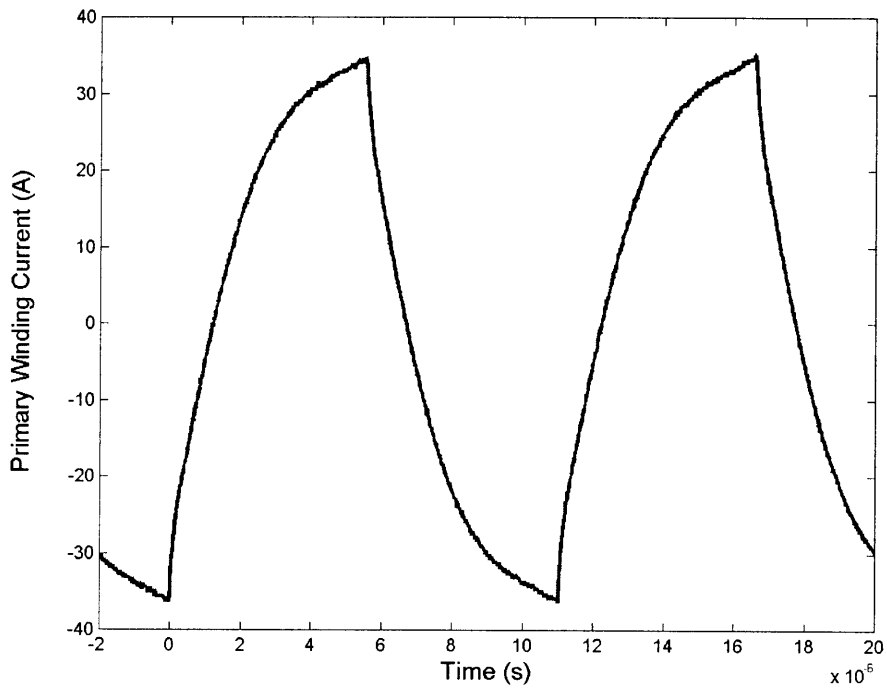
Figure 6.32: Primary winding current at inverter switching frequency of 90 kHz.

135

6.5 Summary

This chapter covered the modeling, design, construction and testing of a contactless field excitation circuit based on a printed circuit board transformer. This design would allow for an increase in field ampere turns with a foil field winding. With the use of a stationary primary and a rotating secondary PCB transformer, the field winding can be powered without the need for brushes and slip rings. Having modeled the PCB transformer and the associated circuitry, the entire circuit was designed and built together with a foil wound field winding. Significant increases in ampere turns of 51% were achieved at a switching frequency of 90 kHz.

Chapter 7

A Field Controller Based on a Rotating DC/DC Converter

7.1 Introduction

As shown in Chapter 5, the use of a foil field winding in a Lundell alternator can provide more field ampere turns than a conventional wire-wound design, enabling substantial performance benefits. This increase in ampere turns is achieved with fewer turns operating at higher currents, and thus requires some means of delivering the necessary power to the rotor that will not exceed the limited current carrying capability of the brushes. One approach that allows for large field currents while maintaining low brush currents is to use a DC/DC converter on the rotor. The DC/DC converter creates a step down in voltage and a step up in field current, enabling high field current while sourcing low current through the brushes.

Multiple design strategies are possible. The rotating converter can be operated at a fixed conversion ratio, with control of field current provided by an additional stationary DC/DC converter. Alternatively, control can be provided directly by the rotating converter if control information is communicated to the rotating frame. It is the latter strategy that is implemented in the experimental prototype.

7.2 Foil Field Winding

In order to achieve an improvement in power output by increasing the field excitation, an existing alternator (OE Plus 7776-10-8-N 130 ampere) is modified by replacing the alternator's round wire field winding (440 turns of approximately 40 mil diameter copper wire with a packing factor of 0.64) with copper foil (Alphacore 5 mil foil with 1 mil insulation). The room temperature resistance of the field winding was measured to be 2.73 Ω. The field winding was then unwound and 440 turns were counted. When obtaining more ampere turns with a modified field, a fair comparison must be made to the original design. While maintaining equal copper loss is a reasonable metric for comparison, comparison of designs at equivalent winding temperature rise is the most preferable metric.

Based on equation 4.4, which gives the resistance of the field winding, the ratio of the resistances of the foil and round wire windings can be found to be

$$\frac{R_{ffoil}}{R_{fround}} = \left(\frac{N_{ffoil}}{N_{fround}}\right)^2 \frac{k_{pfround}}{k_{pffoil}} \tag{7.1}$$

where R_{ffoil} and R_{fround} are the foil and round wire resistances, respectively, N_{ffoil} and N_{fround} are the foil and round wire turns count, respectively, and k_{pffoil} and $k_{pfround}$ are the foil and round wire packing factors, respectively. The ratio of the winding packing factors is

$$\frac{k_{pffoil}}{k_{pfround}} = \left(\frac{N_{ffoil}}{N_{fround}}\right)^2 \frac{R_{fround}}{R_{ffoil}} \tag{7.2}$$

The bobbin was then wound with 5 mil copper foil with 1 mil insulation (Alphacore, [Bridgeport, Connecticut]) and 90 turns of copper foil were obtained. The resistance of the foil winding was measured and found to be 0.10 Ω. To obtain good measured resistance ratios, the two windings were connected in series and driven from a dc supply and the voltages across each winding were measured. Repeated measurements showed that the ratio of winding resistances is

$$\frac{R_{fround}}{R_{ffoil}} = 27.43 \tag{7.3}$$

Therefore, the ratio of packing factors is

$$\frac{k_{pffoil}}{k_{pfround}} = 1.15 \tag{7.4}$$

demonstrating a 15% improvement in packing factor by using copper foil.

To achieve the same copper losses in both windings, we would want

$$I_{ffoil}^2 R_{ffoil} = I_{fround}^2 R_{fround} \tag{7.5}$$

where I_{ffoil} and I_{fround} are the foil and round wire field currents, respectively. Using Equation 4.4 for field winding resistance and substituting in Equation 7.5,

$$I_{ffoil}^2 \frac{N_{ffoil}^2}{k_{pffoil}} C = I_{fround}^2 \frac{N_{fround}^2}{k_{pfround}} C \tag{7.6}$$

where

$$C = \frac{\pi(R_i + R_o)}{\sigma A_s} \qquad (7.7)$$

cancels out from both sides. Therefore, the achievable number of field ampere turns for the foil winding with equal copper loss is

$$N_{ffoil} I_{ffoil} = \sqrt{\frac{k_{pffoil}}{k_{pfround}}} N_{found} I_{fround} \qquad (7.8)$$

when the same bobbin is used and copper is used for both windings. Therefore, given the same copper losses, the allowable number of ampere turns increases as the square root of the ratio of packing factors. Given the increase in packing factor by 15%, the number of ampere turns are allowed to increase by 7% if field copper losses are to be kept constant. Based on the formula for output power at the load matched condition shown in equation 4.1, the achievable output power increases as the ratio of ampere turns, squared. Therefore, based on Equations 4.1 and 7.8, the output power increases by the ratio of packing factors or 15% when going from round wire to copper foil.

Further measurements need to be made to determine the field excitations at which the winding temperatures are the same at steady state. Since copper foil has somewhat better thermal properties than round wire (because of easy heat transfer across a winding layer) the effective thermal resistance to ambient may be lower, and therefore allowing higher field excitation for a given maximum temperature.

This planned modification is expected to result in an increase in armature currents and alternator output, not to increase the cooling of the armature. As a result, our modified generator will not be able to sustain its increase in output under all conditions. However, demonstrating such an improvement is sufficient to show the efficiency of the approach. Other modifications to the stator design can be realized to lower armature heating to sustain (and even enhance) increased output. Moreover, as shown in [45,46], idle speed is not the worst case operating point of the alternator from a temperature standpoint, so improvement at idle should be sustainable even without further design changes.

The maximum number of ampere turns for the original round wire field winding (at full field under steady-state thermal operation) is approximately

$$N_f I_f = 440 \times 3.6A = 1584A \qquad (7.9)$$

This assumes 3.6 A of field current at thermal steady state, which was measured under laboratory conditions. The new field winding has 90 turns, so in order to increase the number of ampere turns in the new field winding by 7%, the thermal steady state current in the foil field winding must be at least

$$I_f = \frac{1.07 \times 1584A}{90\,turns} = 18.83A \tag{7.10}$$

(At ambient temperature, the maximum "full-field" current through the wire wound field winding is 4.7 A). In this case, 24.6 A of foil winding field current are required in ambient temperature in order for the foil winding to achieve a 7% increase in ampere turns). The DC/DC converter circuit should then be able to provide 24.6 A of current to the field winding at ambient temperature.

7.3 Rotating DC/DC Converter

The rotating converter system is illustrated in Figure 7.1. The rotating converter is functionally similar to the buck chopper circuit used in conventional field regulators, but employs a schottky diode to reduce conduction loss at low output voltage. Still lower losses could readily be achieved with synchronous rectification, at the expense of an additional active switch and floating gate driver (synchronous rectification was not implemented in the prototype for simplicity).

The main challenge in the design and implementation of the DC/DC converter is communicating field control information to the rotor. The method selected for the prototype is line carrier communication. This involves communicating the control signal through the power bus (across the brushes). The control signal is encoded by modulating the frequency of a high-frequency sinusoid, which is injected onto the voltage bus on the stationary side (from v_{tx}). The signal is then transmitted through the brushes and on to the rotating side where a receiver picks up the signal (v_{rcv}), and demodulates it. The field winding in the circuit of Figure 7.1 is represented by the inductance L_f and resistance R_f. The inductance L_1 and capacitance C_1 are used as a lowpass filter to isolate the modulated signal from the switching current, and inductance L_2 is used to isolate the control signal from the power input bus.
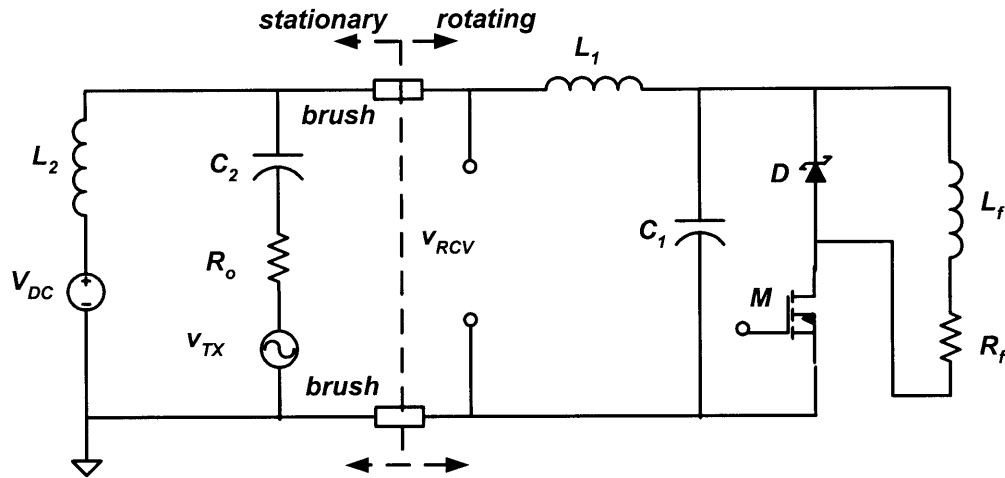
Figure 7.1: Circuit topology with DC/DC converter on rotor.

Two schemes were considered and tested for transmitting the required signals to control the MOSFET on the rotating side. Both involve using a control signal to modulate the frequency of a sinusoidal carrier on the stationary side, injecting the modulated signal into the voltage bus and receiving the signal on the rotating side.

In the first approach, the duty ratio signal is communicated to the rotating side through carrier frequency modulation. The demodulated signal is then fed to a pulse-width modulation circuit to generate MOSFET gating pulses. In a second approach, described in Appendix E, pulse-width modulation signals are generated on the stationary side and transmitted by frequency shift keying (FSK). This strategy eliminates the need of pulse width modulation on the rotating side (saving space) but requires very fast tracking of the FSK system. The first approach was found to be much more effective, and was adopted for the final system.

7.4 DC/DC Converter with FM Communications

The communications selected involves frequency Modulation (FM) of the error signal on the stationary side, transmission through the brushes to the secondary side and frequency demodulation on the secondary side. The circuit used for the FM modem is shown in Figure 7.2 (more details on the circuit design can be found in Appendix E). Amplifier A_1 produces a PID compensated error signal. The signal is converted directly to a frequency-modulated (FM) AC signal. This AC signal is buffered by A_2 and fed through the brushes to the rotating converter. On the rotor, an FM demodulator recreates the compensated error signal. The received signal is then used to create a pulse-width modulated gate signal used to drive the MOSFET.

The frequency of the transmitted signal is set to be a linear function of the desired duty ratio. A frequency range of 152 kHz to 167 kHz is transmitted to represent duty ratios from 0 to 1. Since duty ratio varies only slowly, the PLL demodulator can easily track the desired signal.

A simplified communications circuit is shown in Figure 7.3. The transmitted signal is a sinusoid that can be expressed as

$$v_{tx}(t) = v_{txm} \cos(\omega_{tx} t) \tag{7.11}$$

with amplitude v_{txm} and frequency ω_{tx}. Its Fourier transform is composed of two impulses at plus or minus the sinusoid frequency and can be expressed as

$$V_{tx}(j\omega) = v_{txm}\pi(\delta(\omega - \omega_{tx}) + \delta(\omega + \omega_{tx})) \tag{7.12}$$

It is shown in Figure 7.4. Because the transmitted signal is real and modeled as even (cosine), the Fourier transform is also real and even, and therefore only positive frequencies need be considered. The received FM signal is the output when the signal is passed through the system function $H_s(j\omega)$. The transfer function from the signal voltage source to the receiver input is:

$$H_s(j\omega) = \frac{Z_{L1} // (Z_{L1} + Z_{C1})}{Z_{L1} // (Z_{L1} + Z_{C1}) + Z_{C2} + R_0} \tag{7.13}$$

where the various impedances are defined as

$$Z_{L1} = j\omega L_1 \tag{7.14}$$

$$Z_{L2} = j\omega L_2 \tag{7.15}$$

142

$$Z_{C1} = 1/(j\omega C_1) \qquad\qquad (7.16)$$

$$Z_{C2} = 1/(j\omega C_2) \qquad\qquad (7.17)$$

The transfer function when using the actual components is shown in Figure 7.5. It increases with frequency. The higher the frequency, the smaller the attenuation. Therefore, it is preferable to operate the FM modem at high frequencies from the standpoint of maximizing the desired output or received signal to be demodulated. In the frequency domain, the Fourier transform of the output or received signal is the Fourier transform of the input multiplied by the transfer function. The received voltage due to the FM signal in the frequency domain is

$$V_{rs}(j\omega) = V_{tx}(j\omega) H_s(j\omega) \qquad\qquad (7.18)$$

$$V_{rs}(j\omega) = v_{txm} \pi \left(H_s(j\omega_{tx}) \delta(\omega - \omega_{tx}) + H_s(-j\omega_{tx}) \delta(\omega + \omega_{tx}) \right) \qquad\qquad (7.19)$$

which for positive frequencies is

$$V_{rs}(j\omega) = v_{txm} \pi H_s(j\omega_{tx}) \delta(\omega - \omega_{tx}) \qquad\qquad (7.20)$$

Note that $H_s(j\omega)$ is approximately an even function when R_0 is small. Since the input or transmitted signal is an impulse, the output is simply a scaled version of that impulse with the scale factor being the transfer function evaluated at the frequency of the sinusoid. The signal received is slightly attenuated by the transfer function $H_s(j\omega)$.
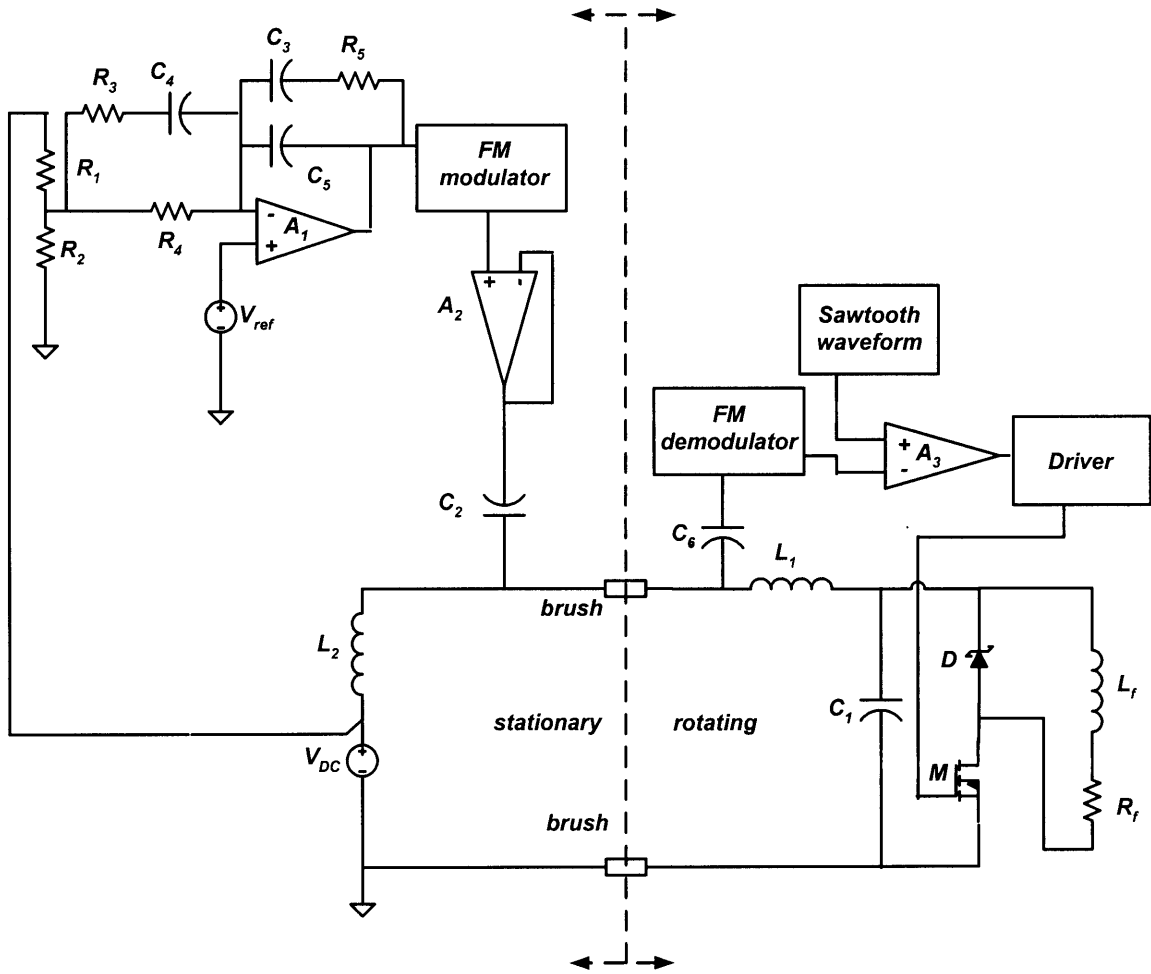
Figure 7.2: Detailed FM modulation circuit.
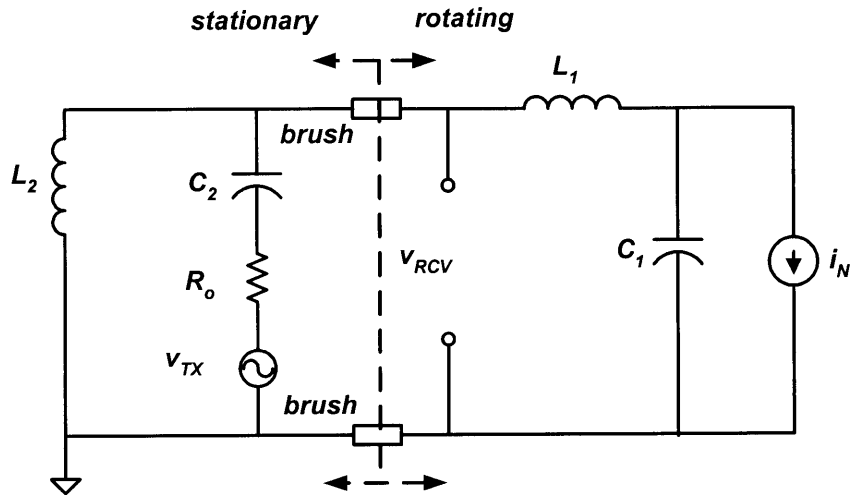
Figure 7.3: Simplified communications circuit.
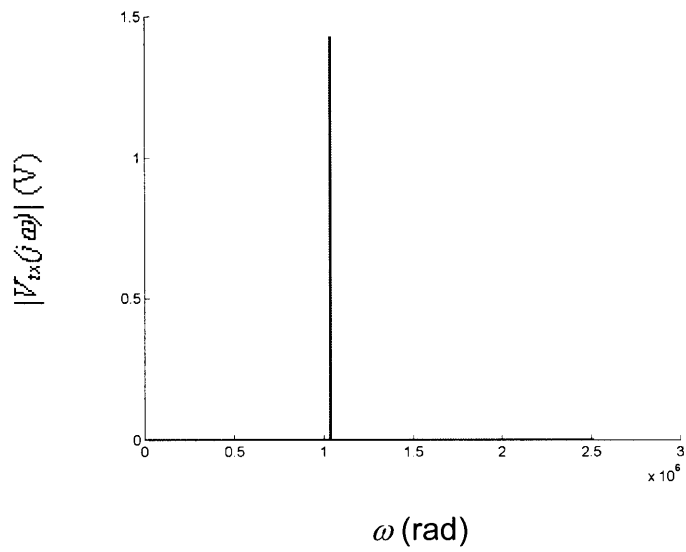
Figure 7.4: Spectrum of FM modulated signal.
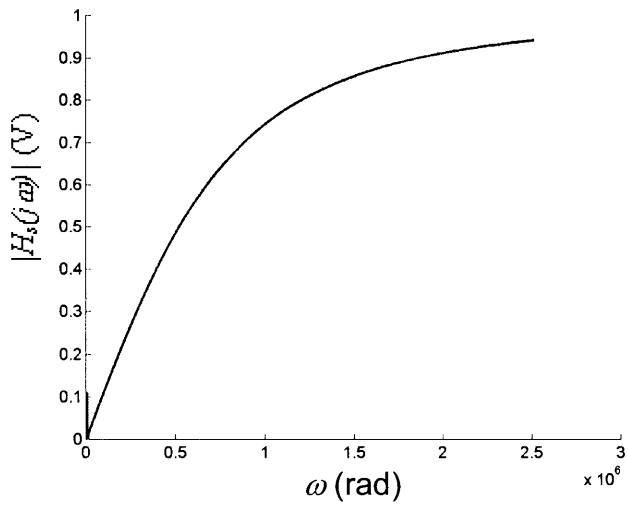
Figure 7.5: Spectrum of FM signal to receiver transfer function.
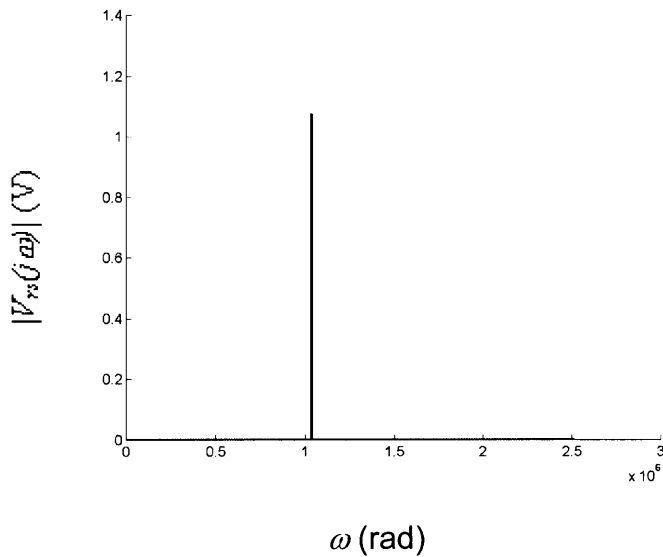
Figure 7.6: Spectrum of FM signal at receiver.

Just like almost every communication system, there is noise that can interfere with the transmitted signal. In this case, the main source of noise is the switching current from the MOSFET (and brush noise to a lesser extent). This can be modeled as a current sink i_N (shown in Figure 7.3), which equals the field current when the MOSFET is on and zero when the MOSFET is off. Being a periodic rectangular wave, the noise signal can be expressed using a Fourier series representation as

$$i_N(t) = I_f \sum_{m=-\infty}^{\infty} a_m e^{jm\omega_0 t} = I_f \left(a_0 + \sum_{m=-\infty}^{\infty} 2a_m \cos(m\omega_0 t) \right) \tag{7.21}$$

where

$$a_0 = D \tag{7.22}$$

$$a_m = \frac{1}{m\pi} \sin(m\pi D) \tag{7.23}$$

and therefore its Fourier transform can be expressed as

$$I_N(j\omega) = I_f \sum_{m=-\infty}^{\infty} 2\pi a_m \delta(\omega - m\omega_0) \tag{7.24}$$

which consists of impulses or delta functions spaced apart by ω_o and whose areas decay as a sinc function. Since $i_N(t)$ is real and modeled as even, its Fourier transform $I_N(j\omega)$ is real and even. Thus, only the Fourier transform for positive frequencies need to be

146

plotted. The areas of the impulses in the Fourier transform decrease as frequency is increased. The Fourier transform of the noise current for positive frequencies is shown in Figure 7.7.

The transfer function from the noise current source to the receiver input voltage is

$$H_n(j\omega) = \frac{Z_{C1}(Z_{L2} \,//\,(Z_{C2} + R_0))}{Z_{C1} + Z_{L1} + Z_{L2} \,//\,(Z_{C2} + R_0)} \tag{7.25}$$

The transfer function is shown in Figure 7.8. It decreases dramatically with frequency. It is therefore preferable to operate at higher frequencies from the standpoint of minimizing noise, although as can be seen, the noise transfer function is insignificant at the frequencies we are concerned with for signal transmission. The received voltage (Fourier transform) due to the noise current is

$$V_{rn}(j\omega) = I_N(j\omega)H_n(j\omega) \tag{7.26}$$

It is shown (frequency domain) in Figure 7.9. Since the system composed of passive elements is linear and time invariant, the output due to the noise current is

$$v_{rn}(t) = I_f\left(a_0 H_n(j0) + \sum_{m=1}^{\infty} 2a_m |H_n(jm\omega_0)|\cos(m\omega_0 t + \angle H_n(jm\omega_0)) \right) \tag{7.27}$$

where the output signal is the input signal sinusoids at different frequencies scaled by the magnitude of the transfer functions and phase shifted by the phase of the transfer functions at those frequencies.
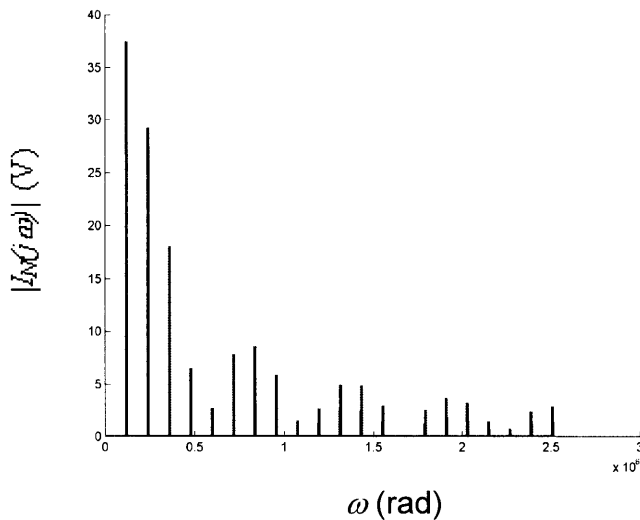
Figure 7.7: Spectrum of switching current at switching frequency of 19 kHz.

147
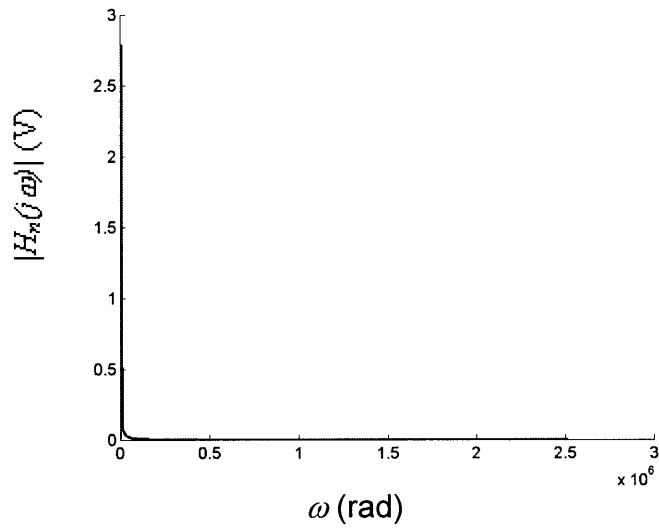
Figure 7.8: Spectrum of transfer function from switching current to receiver.
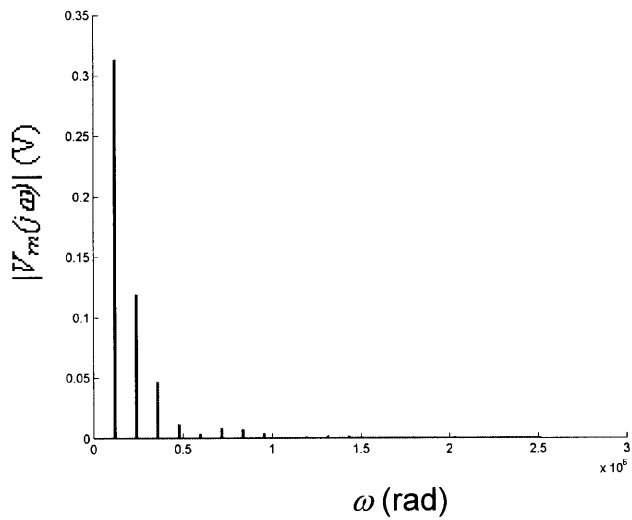
Figure 7.9: Spectrum of voltage at receiver due to switching current (switching frequency=19 kHz).
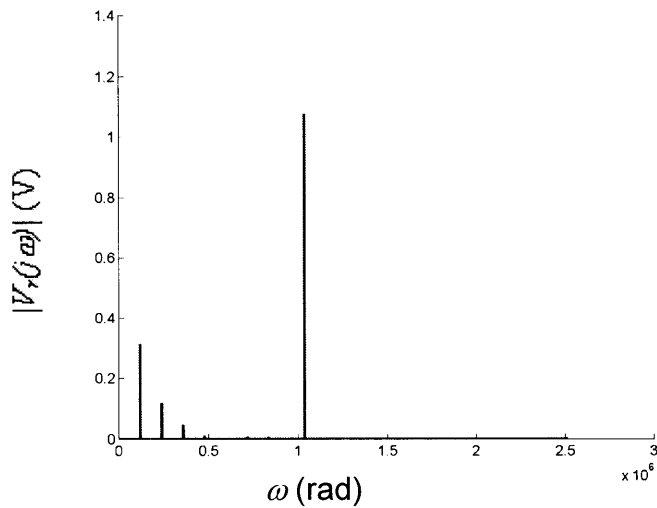
Figure 7.10: Spectrum of voltage at receiver due to FM signal and switching current.

The plots in the frequency domain due to the transmitted FM signal and the noise signal are shown in Figure 7.6 and 7.9, respectively. The combined signals are shown in Figure 7.10. The objective is to maximize V_{rs} and minimize V_{rn} in the frequency range used by the FM receiver. This can be seen as maximizing the signal to noise ratio. Note that due to the attenuation by the filter and the fact that the noise decays as a sinc function, the PWM switching noise content is negligible around the frequency of transmission (the noise decays as a sinc function).

For the selection of the switching frequency (19 kHz) and filter components, several factors had to be considered. It is desirable for the switching frequency to be high enough to minimize the size of the passive components such as L_1 and C_1 but not too large that the switching losses become considerable. As can be seen in Figure 7.7, the switching noise consists of samples of a sinc function that decay at higher frequencies. This decay is desirable since the modulated signal frequency can be made sufficiently large that the noise spectra are insignificant at those frequencies. The switching frequency of 19 kHz was selected and the frequency range of the modulated signals was from 152 kHz and 167 kHz so that this range would fall between two harmonics (8th and 9th) of the noise from the switching currents, which would isolate the frequency range of the modulated signal from the noise harmonics. Since the noise harmonics decrease with

149

frequency (noise spectrum decays as a sinc) and in addition, the filter attenuates these harmonics, the noise is not a concern in the vicinity of the frequency range used. The filter composed of L_1 and C_1 serves to further attenuate the noise spectra. Since $H_s(j\omega)$ is high pass, the frequency range of the modulated signal has to be high enough to be transmitted with minimal degradation. The attenuation of the noise by the filter is also reflected in the rapid decline of the frequency response $H_N(j\omega)$ as the frequency increases. Since the modulated signal frequency has to be significantly higher than the switching frequency, a limit on the switching frequency also has to be set. In designing the input filter, L_1 is used to block AC ripple from the noise source, and C_1 is used to absorb it. The bigger these two are, the more effective the filter becomes in isolating the received modulated signal from the switching current. The larger L_1 is, the smaller the noise transfer function $H_n(j\omega)$ and the larger the signal transfer function $H_s(j\omega)$. Therefore, L_1 is preferred to be large. A larger C_2 is desirable since the signal transfer function will be larger. There is a trade-off involving L_2 since, the larger it is, the larger the signal transfer function, but the larger the noise transfer function as well. A balance then has to be struck when selecting values of L_2. The larger C_1, the smaller the noise transfer function, but the smaller the signal transfer function as well which involves a trade-off. This trade-off regarding the selection of C_1, however, is not critical when L_1 is large (which is the case) since the two impedances are in series.

7.4.1. Experimental Results: Converter External to Alternator

Preliminary experiments involved testing the DC/DC converter circuit in series with the brushes of another alternator to include the effects of brush voltage drops and brush noise. The way the effects of brushes were included was by shorting out the field winding of another alternator and connecting the external terminals of the brushes in series with the stationary and rotating parts of the DC/DC converter circuit as shown in Figure 7.11. The duty ratio of the rotating active switch was varied, and the output current was measured as well as the input current, and brush terminal voltages. It was observed that there was a significant drop ($v_{prebrush}$-$v_{postbrush}$) across the brushes, as shown by the plot of brush terminal voltages versus output current in Figure 7.12. The

maximum brush drop measured was 4.72 V at the maximum output current measurement. The circuit was also tested without the brushes and it was evident that the brush drops were limiting the achievable output current and increasing the power losses. Due to the large brush drops, the voltage across the rotating circuit ($v_{postbrush}$) is much lower than that at the stationary side (by 4.72 V at maximum field current). This increased brush drop is due to loss in the DC/DC converter, especially due to diode conduction loss.
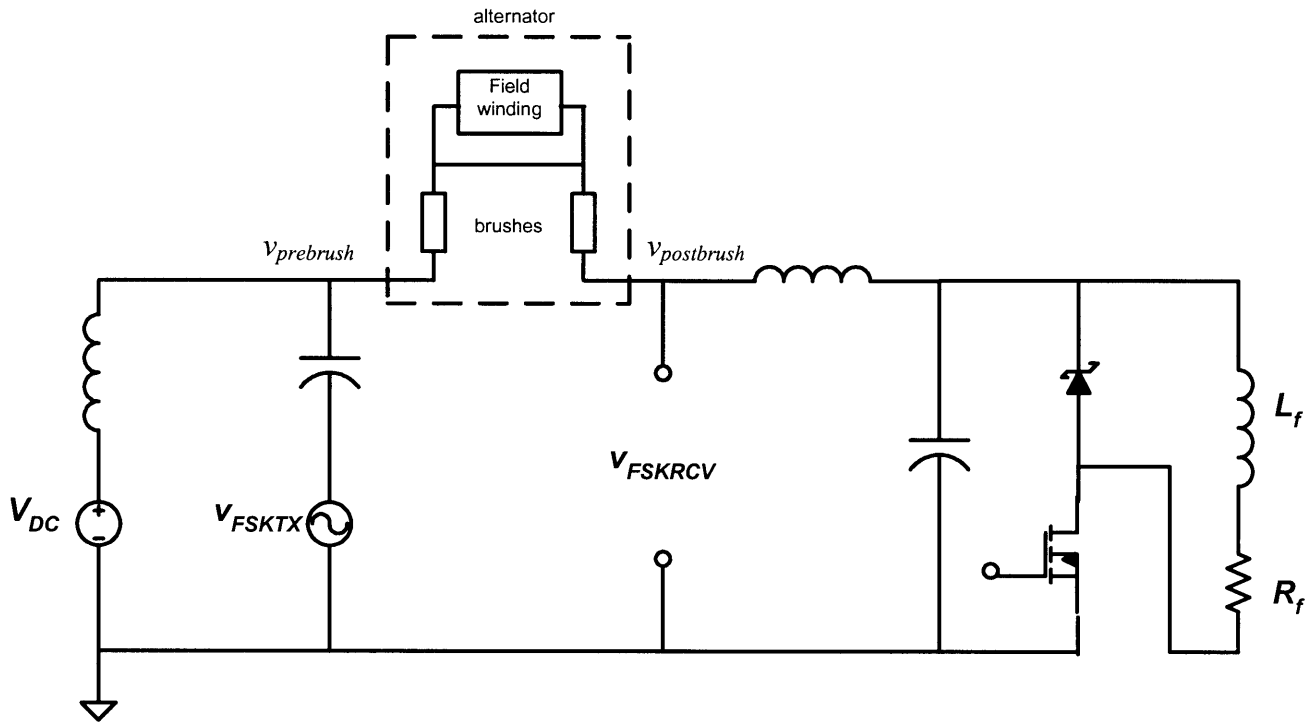
Figure 7.11: Converter tested in series with shorted brushes of existing Lundell alternator.
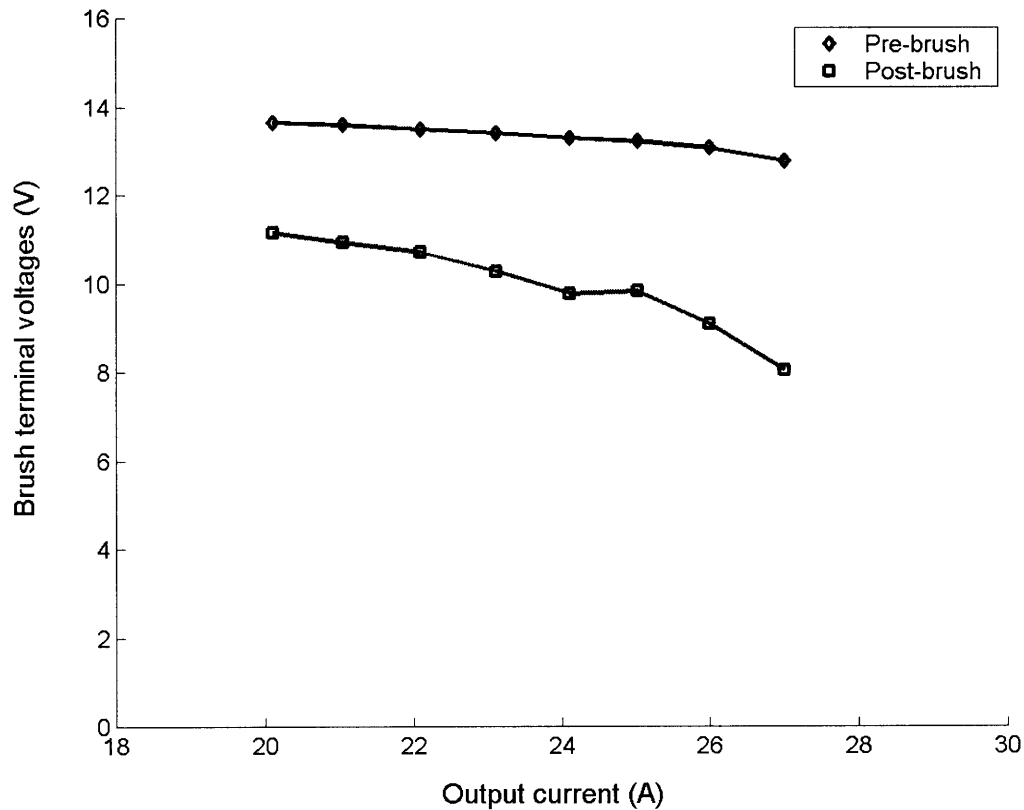
Figure 7.12: Brush terminal voltages versus output current (existing brushes)

In order to solve the problem of excessive brush drops at high output current and consequently, brush current, the brushes of the existing alternator were replaced by modified brushes as shown in Figure 7.13. The modified brushes involved fitting two pairs of brushes in parallel within the same amount of space allowed for the voltage regulator. Having the modified brushes results in each pair of brushes carrying approximately half the current that regular brushes have to carry. The voltage drops across the brushes are expected to decrease with the use of these combined brushes (can be seen looking at Figure 7.12 assuming half the current is used). A series of experiments were performed, where again, the duty ratio was varied, and the input current, output current, and brush terminal voltages were measured. The brush terminal voltages versus output current are shown below in Figure 7.14. The brush drops were reduced significantly. In addition, higher field currents were achieved. At the highest output current of 33.1 A, the brush drop is 1.77 V. This is less than half the original brush drop.

A plot showing the relation between duty ratio and output current is shown in Figure 7.15. The various input and corresponding output currents are shown in Figure 7.16. It should be noted that the need for increased brush area can be mitigated through improved DC/DC converter efficiency, and especially through the use of synchronous rectification.
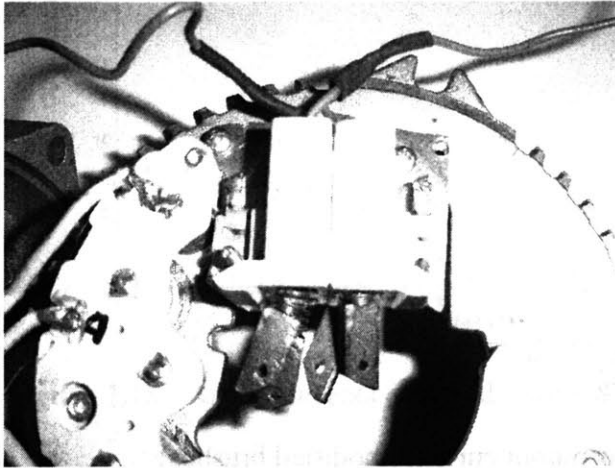
Figure 7.13: Modified brushes composed of two pairs of brushes in parallel.

The maximum field current achieved with the modified brushes was 33.1 A. The relevant waveforms associated with this particular peak output measurement are shown in Figures 7.17 to 7.21. Figure 7.17 shows the gate voltage of the active switch of the DC/DC converter. Figure 7.18 shows the output field current. Figure 7.19 shows the transmitted voltage prior to the brushes. The "pre-brush" voltage has the sinusoid on top of the power bus voltage. The frequency of the sinusoid is linearly related to the desired duty ratio. The received "post-brush" signal is shown in Figure 7.20. The voltage is lower than the pre-brush voltage by an amount equal to the drop across the two pairs of brushes in series. Note that the brushes being used are the modified brushes. Each brush drop is approximately half the drop across both brushes, or 0.89 V. The input current has an average value of approximately 13.7 A and is shown in Figure 7.21.
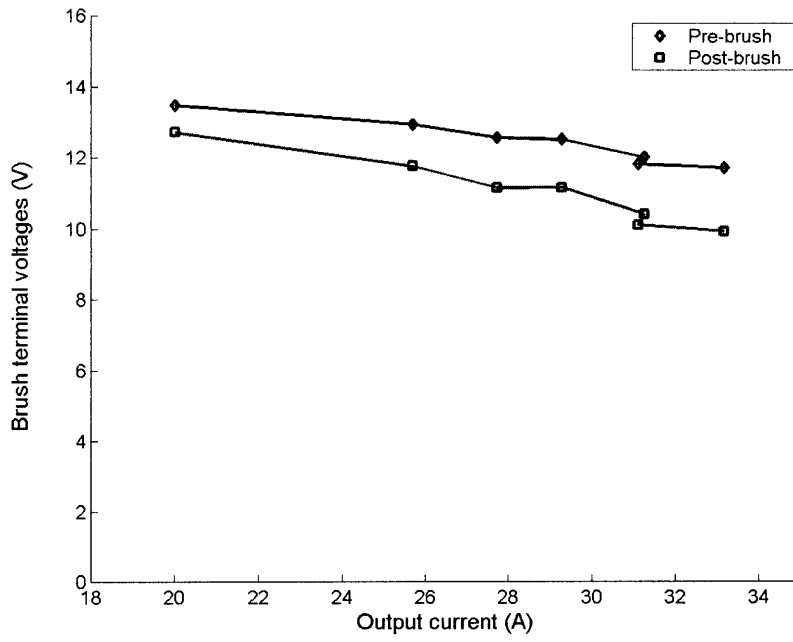
Figure 7.14: Brush terminal voltages versus output current (modified brushes)
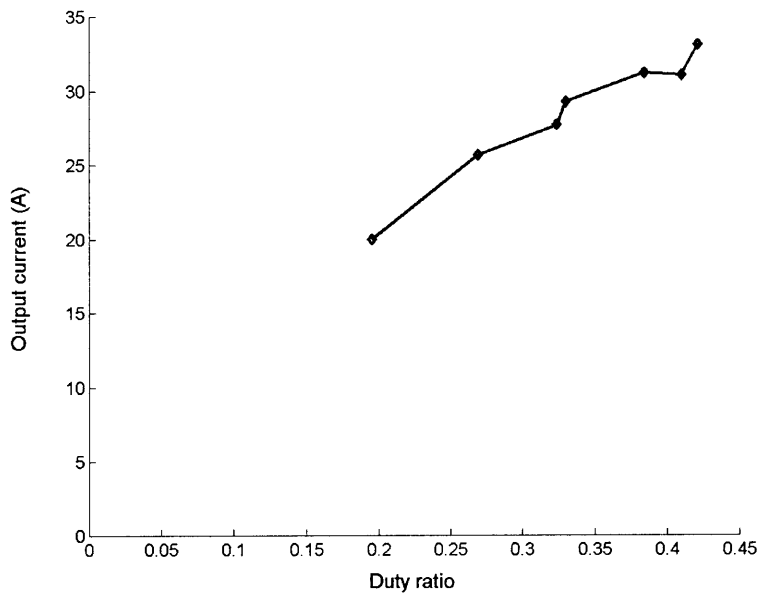
Figure 7.15: Output currents obtained at various duty ratios.

154
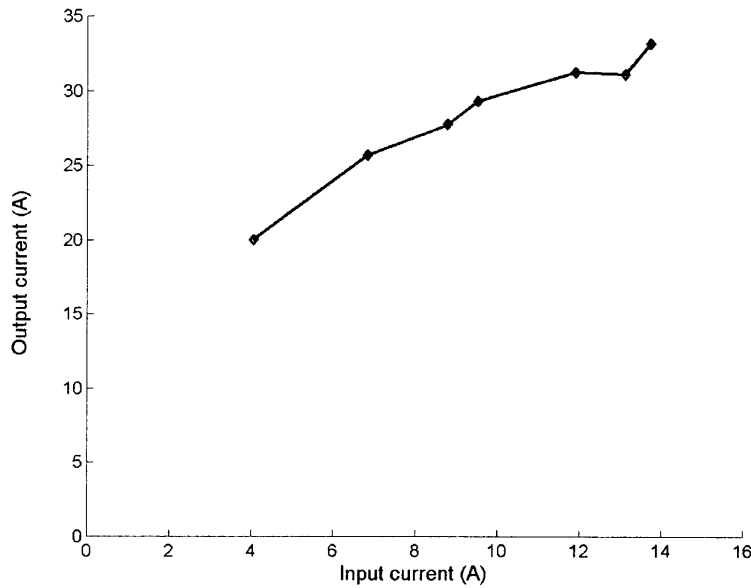
Figure 7.16: Output currents obtained versus input currents to converter.

The measured output current of 33.1 A shows the achievable level of field excitation. Given that the full field current at 13 V output voltage in the existing alternator is 4.7 A (measured at ambient temperature), the output current achieved results in an increase of 44% in ampere turns. For similar copper losses to the wire-wound field. The foil wound field current has to be around 24.6 A. This is clearly achievable by the circuit.

Recall that an increase in ampere turns of 7% is allowed if the copper losses are to be kept the same. If the foil field windings is operated to the same temperature as the wire-wound field, one might expect an increase in ampere turns of somewhat more than 7% due to the better heat transfer from the foil winding. It is highly unlikely, however, that a 44% increase in ampere turns can be used if temperature were to be kept constant. The increase in ampere turns should result in a corresponding increase in output power from the alternator so long as the stator saturation and thermal limits are not exceeded.

155
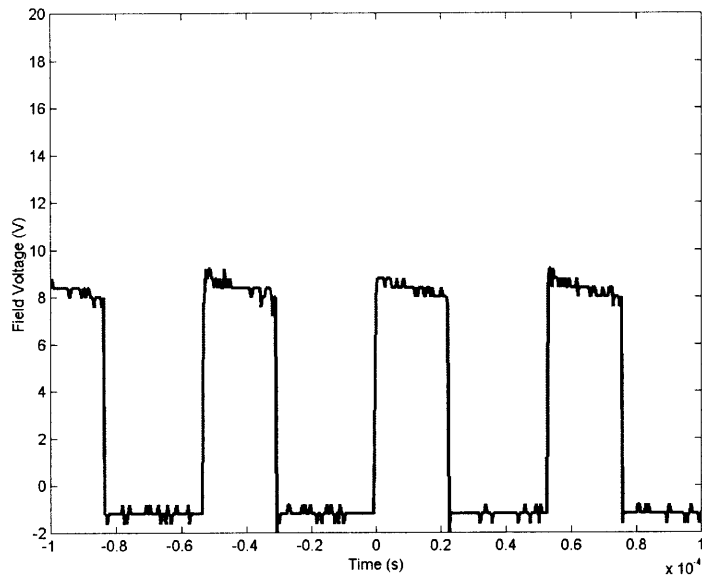
Figure 7.17: Field voltage (measured)
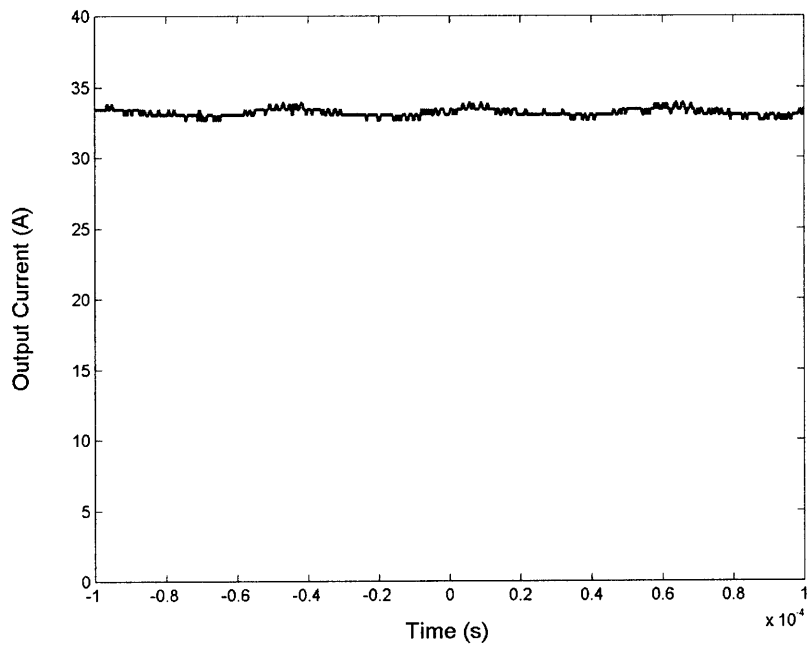
Figure 7.18: Measured field current (average of 33.1 A).
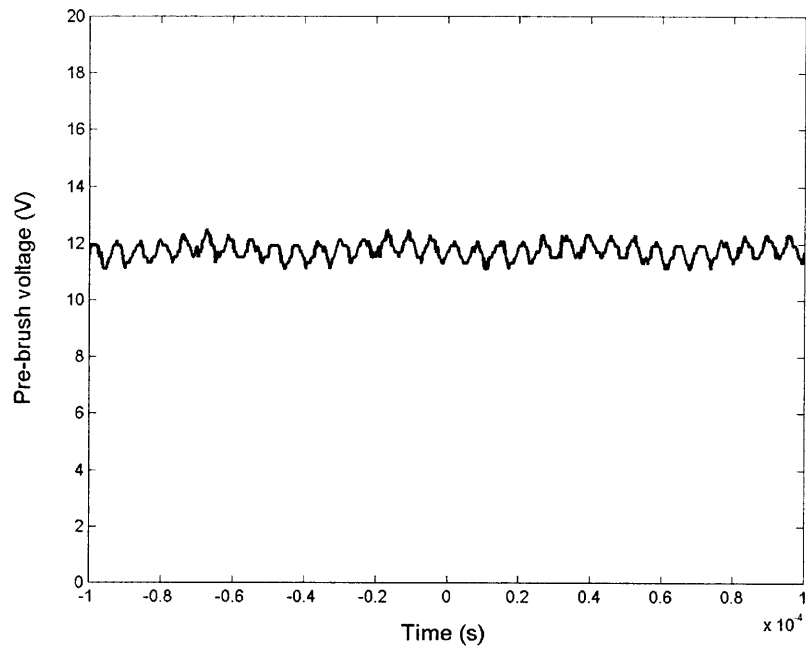
Figure 7.19: Pre-brush voltage (measured).
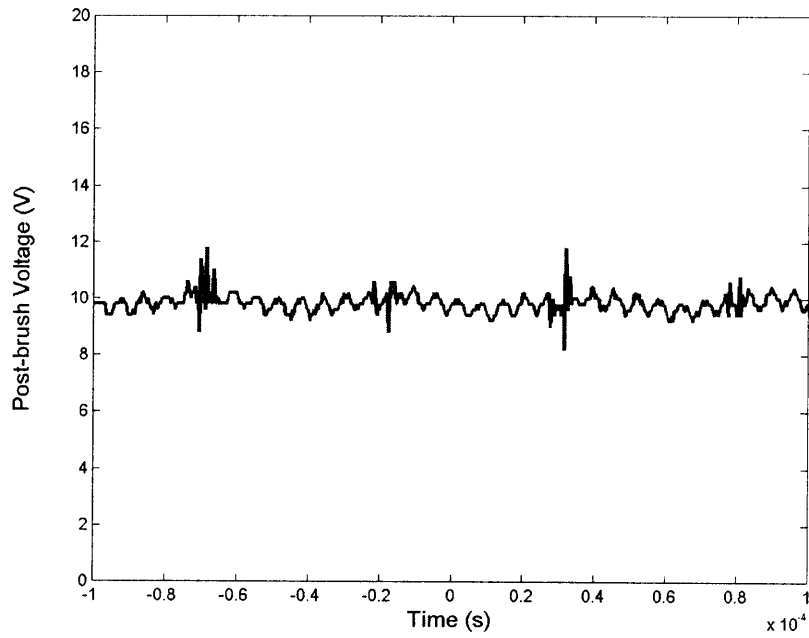
Figure 7.20: Post-brush voltage (measured).
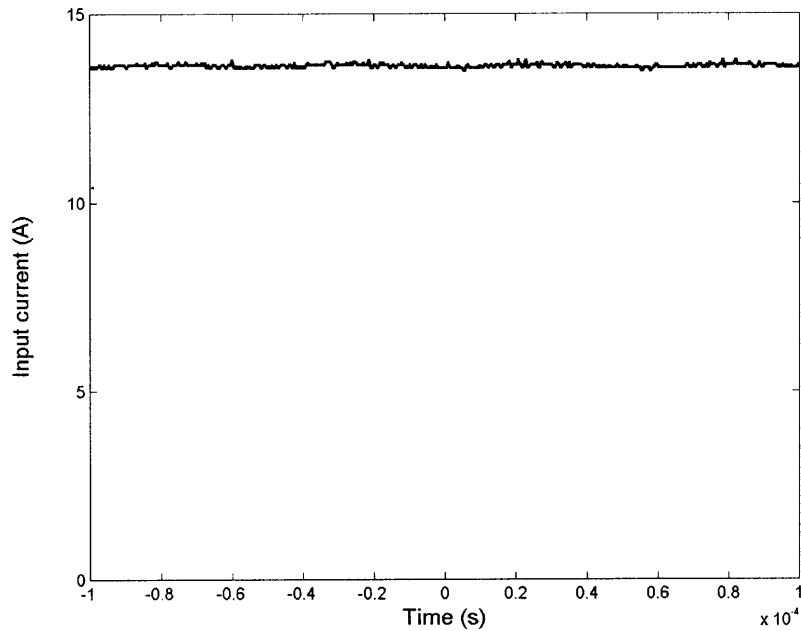
Figure 7.21: Measured input current (average of 13.7 A).

7.4.2. Experimental Results: Converter Embedded in Alternator

The power electronics were integrated into a 7776-10-8-N 130 A OE Plus alternator having the modified field winding described earlier.. The shaft was first pressed into the claws , which were then tightened on both sides of the field winding. The circuit board was then attached to the outer side of the claw, after which the slip rings were pressed just onto the top of the board. The circuit board was held in place by screws and electrically isolated from the claw by electrical tape. A picture of the completed rotor is shown in Figure 7.22.
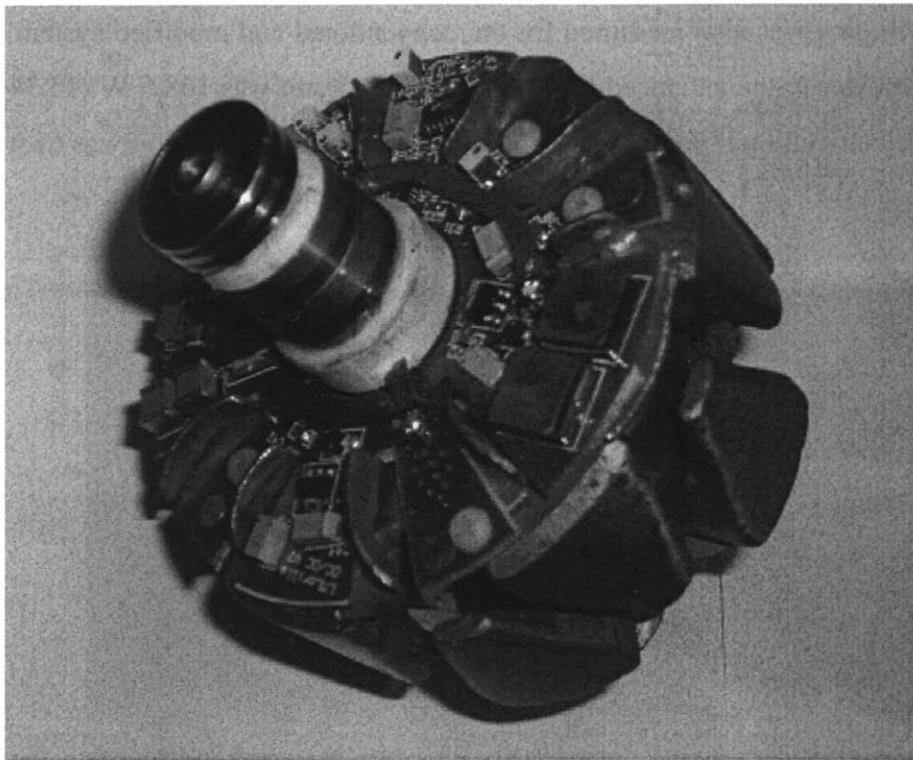
Figure 7.22: Pressed rotor claws with foil field winding and rotating converter.

The rotor with the converter was then placed inside the stator and the rest of the alternator case was assembled. The external circuit containing the FM modulator was connected to wires leading to the modified brushes. The alternator was then bolted onto the stand and connected to a drive motor that is used as the prime mover via a toothed belt. A picture of the setup is shown below in Figure 7.23.

To determine the maximum achievable output power under "manufacturer nominal" conditions, the tests were made at idle speed (alternator speed of 1500 rpm). The maximum output current was approximately 78.6 A at approximately 32 A of field current as shown in Figure 7.24. The average output power obtained is 1048 W (output voltage of 13.34 V shown in Figure 7.35). The quoted nominal output power of the alternator is 70 A at idle speed and 13 V output (such that the regulator generates full field current). The quoted output power is then 910 W. From experiments on a stock alternator, the maximum output power at idle speed obtained was 964 W at ambient temperature (73 A at 13.2 V). Therefore, the maximum output power increased by 8.7% under nominal conditions when the enhanced foil wound alternator was used. The input

power to the field winding was also measured for the conventional and modified system. The electrical input power to the enhanced foil field winding circuit was 168.6 W (13.34 V at 12.64 A). The electrical input power to the round wire field winding circuit was 61.4 W (4.7 A at 13 V).
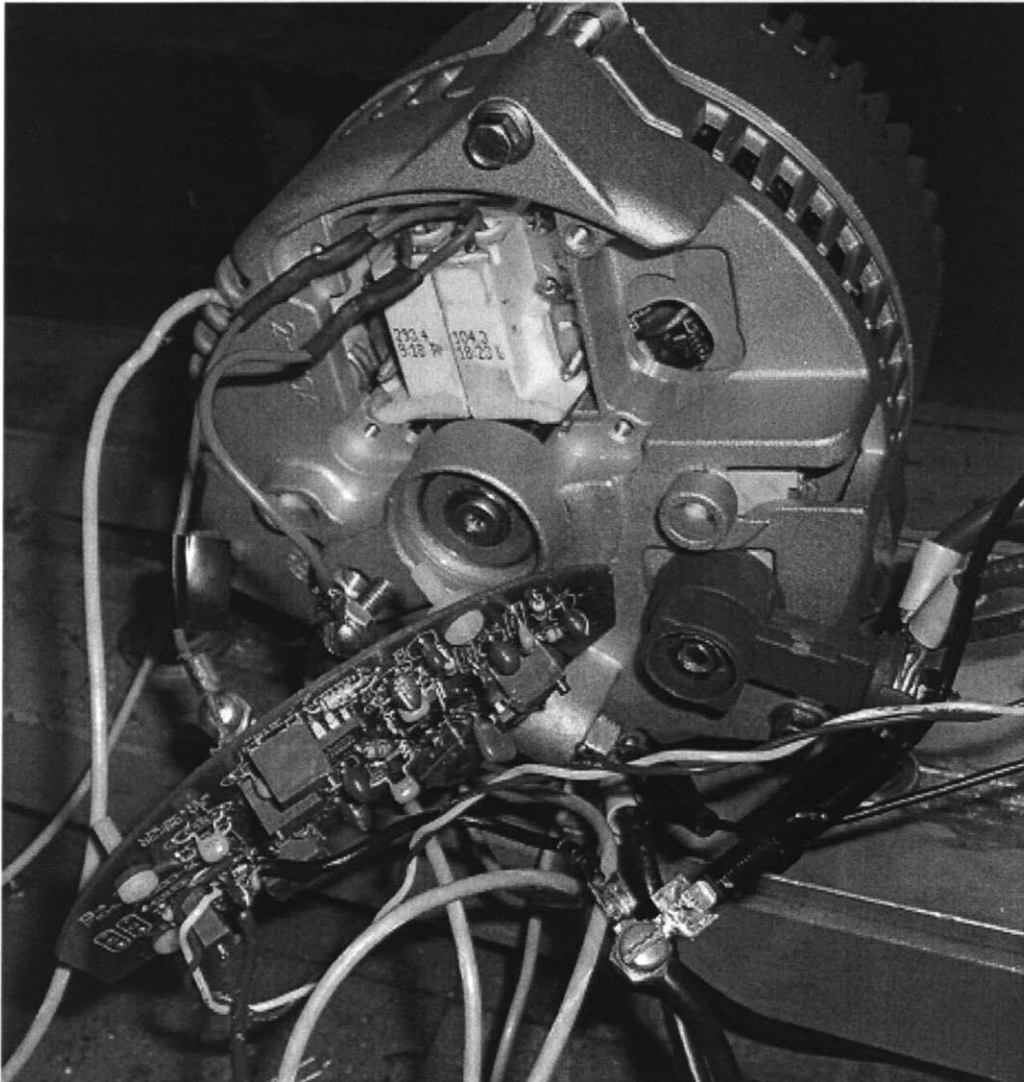
Figure 7.23: Experimental alternator with external communication circuit connected to modified brushes.
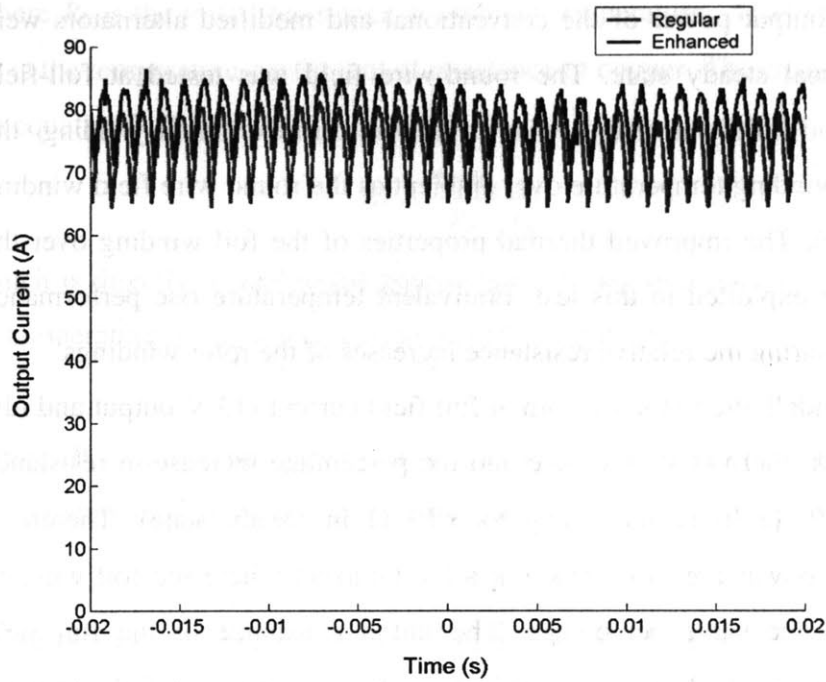
Figure 7.24: Comparison of maximum average output current obtained (average of 78.6 A for enhanced, 73 A for regular) at approximately 32 A of field current
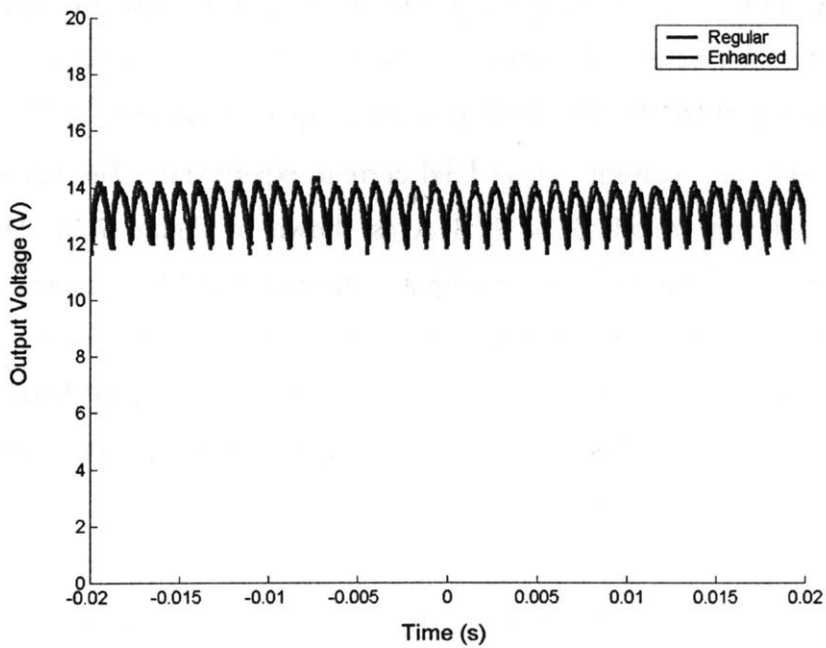
Figure 7.25: Output voltage at maximum output current (average of 13.34 V for enhanced, 13.2 V for regular)

The achievable output power of the conventional and modified alternators were also compared at thermal steady state. The round-wire field was tested at full-field conditions, while the foil field was tested with an ampere turn excitation yielding the same increase in rotor winding temperature over ambient as the round wire field winding (in thermal steady state). The improved thermal properties of the foil winding over the round wire winding are exploited in this test. Equivalent temperature rise performance was established by measuring the relative resistance increases of the rotor windings.

The existing Lundell alternator was run at full field current (13 V output and idle speed of 1500 rpm) until thermal steady state and the percentage increase in resistance was found to be 26.2% (2.36 Ω increasing to 3.19 Ω in steady state). Therefore, comparisons for output power are to be made at a field current where the foil winding resistance increases by the same percentage. The initial resistance of the foil field winding was measured to be 0.13 Ω under ambient conditions. The modified alternator was run at the same operating conditions (approximately 13 V output voltage and idle speed) and the field current was increased (by increasing the duty ratio) until the percentage increase in field resistance measured during brief operational stops (measured through a hole in the alternator case) was approximately 27%. The foil resistance was measured to be approximately 0.165 Ω. The field current was approximately 30 A based on previous duty ratio and input current versus field current experiments. The output current was measured and was found to be 71.3 A as shown in Figure 7.26. The corresponding output power was 940 W, with an output voltage of 13.17 V as shown in Figure 7.27. In thermal steady state, the output power of the conventional alternator was measured to be 819 W (63 A at 13 V). Therefore, the percentage increase in thermal steady state output power while maintaining the same winding temperature in both round wire and foil wound windings is 15 %.

The field current at which the steady state winding temperature would be the same can also be approximated. The dependence of copper wire resistance on temperature is

$$R = R_o \left(1 + k_{tc} \Delta T\right) \tag{7.28}$$

where R_0 is the initial resistance at ambient temperature, ΔT is the temperature rise, and k_{tc} is the temperature coefficient of resistance of copper. The change in temperature based on equation 7.28 is

$$\Delta T = \frac{R - R_o}{R_o} \frac{1}{k_{tc}} \qquad (7.29)$$

which is directly related to the percentage increase in resistance. The increase or change in temperature is linearly related to power dissipation:

$$\Delta T = k_p P \qquad (7.30)$$

where P is the power dissipation and k_p is the thermal resistance in $^oC/W$. The temperature change of the field winding is

$$\Delta T = k_p I_f^2 R \qquad (7.31)$$

To determine the thermal resistance k_p of the foil winding, it is excited with an arbitrary amount of current (e.g. 20 A) and the resistance is measured at thermal steady state. Using Equations. 7.29 and 7.31, the thermal resistance coefficient can be calculated as

$$k_p = \frac{\dfrac{R - R_o}{R_o}}{k_{tc} I_f^2 R} \qquad (7.32)$$

Given k_p, the current at which a 26.2% increase in the foil field winding resistance occurs can be determined by again using equations 7.29 and 7.31:

$$I_f = \sqrt{\frac{R - R_o}{R_o} \frac{1}{k_{tc} k_p R}} \qquad (7.33)$$

where R now is the desired resistance of the foil winding at steady state.

The initial resistance of the foil field winding was measured to be 0.13 Ω under ambient conditions. At a field current of 20 A, the resistance in thermal steady state was measured to be 0.145 Ω, representing an increase of 11.5%. The thermal resistance was calculated to be 0.46 $^oC/W$. Therefore, based on equation 7.33, the alternator can be excited at approximately 30 A of field current and the expected percent increase in resistance should be the same (26.2%), implying the same temperature rise, and therefore, the same steady state winding temperature. As approximated earlier, the field current of 30 A is the amount of current through the foil winding at which the percentage increase

163

in resistance of the foil winding measured earlier was around 27%. At this current of 30 A, approximately 30% more ampere turns is used when compared to the stock alternator while maintaining identical field winding temperatures.

Given this increase in ampere turns, more output power should be expected since output power scales approximately as the square of the number of ampere turns at the load matched condition. Therefore, the output power should increase by 70% given an increase of 30% in ampere turns. The measured increase is roughly 15%. The reason for the smaller increase is saturation of the stator steel brought about by the increase in field ampere turns with a corresponding increase in flux density. In order to decrease saturation, and therefore, increase output power, the back iron thicknesses can be increased. In addition, the air gap thickness can be increased such that the flux density increases by a smaller amount or can be maintained despite an increase in ampere turns, and the power output would still increase given the larger air gap, due to a lower armature inductance. The stator can also be redesigned to improve on the thermal conditions and decrease the heat flux from the armature windings. The slots depths could be increased and the armature wire size could also be increased.
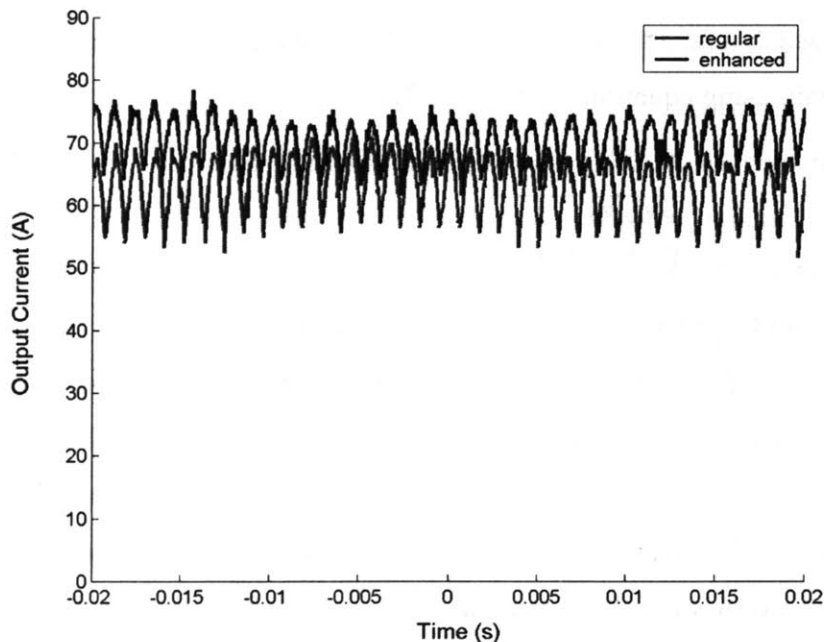
Figure 7.26: Comparison of output current at thermal steady state, same winding temperature (average of 71.3 A for modified alternator; 63.0 A for stock alternator)
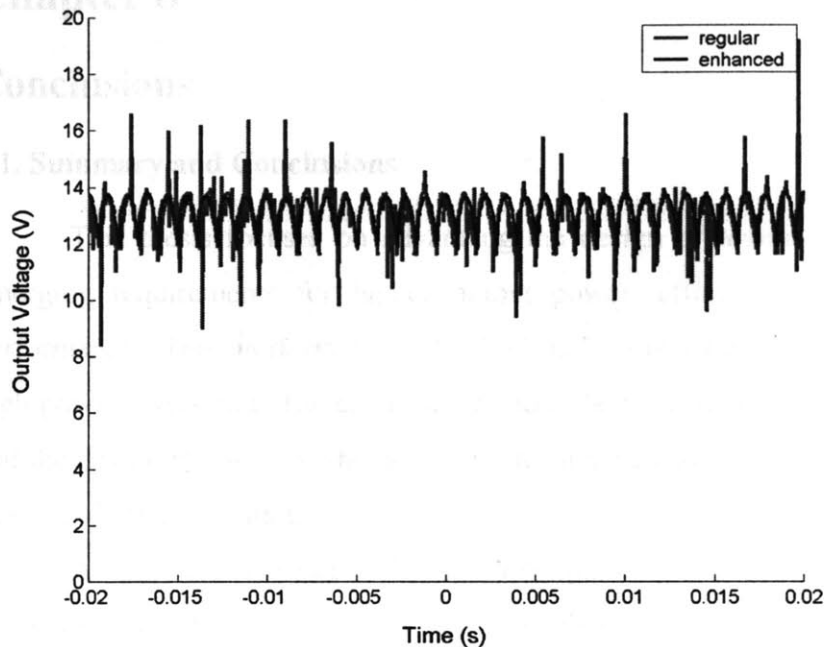
Figure 7.27: Comparison of output voltages (Average of 13.17 V for modified alternator; 12.97 V for stock alternator)

7.5 Summary

In this chapter, a foil found alternator is implemented using the rotating DC/DC converter and its associated electronics on the stationary side. The field winding is wound with 5 mil copper foil (plus 1 mil insulation), obtaining a 15% increase in packing factor. FM modulation is deemed the method of choice for implementing line-carrier transmission due to the ease with which the desired control signal can be tracked. The circuit is designed, built, and tested. A maximum increase of 44% in ampere turns is achievable neglecting thermal limits. At the same field winding temperature rise, a 15% increase in output power is obtained from the modified alternator as compared to the stock alternator under thermal steady state conditions and idle speed. The estimated increase of 30% in field ampere turns (for a similar temperature rise) could be exploited for further performance gains were the stator to be appropriately redesigned.

Chapter 8

Conclusions

8.1. Summary and Conclusions

This thesis focuses on advancing the design of automotive alternators to meet emerging requirements for higher output power, efficiency, and improved transient performance. This work encompasses both radical redesign of alternators to achieve the high power levels and efficiencies expected to be necessary for future electrical systems, and the development of methods to significantly extend the capabilities of contemporary Lundell alternator designs.

As outlined in Chapter 2, it is anticipated that future automobiles will require alternators operating at very high power levels (e.g., 4 – 6 kW across the speed range) and high efficiencies (e.g., > 75% for some operating points), and may utilize 42 V electrical systems. One focus of this thesis is the exploration of alternator designs capable of meeting these greatly increased requirements. As described in Chapter 2, four types of alternator machines were investigated and evaluated: the non-salient and salient-pole wound field alternators, the Lundell or claw-pole alternator, and the homopolar inductor alternator. The use of conventional diode rectifiers and switched-mode rectifiers were both considered as part of this study. Simplified lumped parameter models for each of the alternators were derived, and the approximate output power and efficiency at the load-matched condition were obtained. The analysis showed that the Lundell alternator was the most promising in terms of power generation and efficiency. The principal advantage of the Lundell was found to be the fact that its field winding excites all the poles simultaneously (the inductor alternator also does so, but less effectively).

Numerically optimized designs for each of the four alternators types were developed using a grid-search algorithm across design variables such as air gap radius, slot depths, active length, switched-mode rectifier duty ratio, etc. Designs were optimized numerically for minimum material cost (iron plus copper) while meeting constraints such as output power across speed (4kW at 600 engine rpm increasing linearly to 6 kW at 6000 engine rpm), efficiency (75% at 3250 W and 1500 engine rpm), heat flux, saturation, size, and mechanical stress limits. The comparison of the optimized designs

reveal that the Lundell alternator is the most effective on the basis of material cost, with the salient wound field alternator a close second. Moreover, the results confirm that the Lundell alternator is capable of meeting the greatly increased requirements anticipated for the future; this conclusion opposes the conventional wisdom that Lundell designs will be unsuitable at high power levels. A further conclusion of this work is that optimization of the design for use with a switched-mode rectifier provides significant advantages in machine size and cost. When optimized for a switched-mode rectifier instead of a diode rectifier, the material costs of the optimal machines were each reduced by at least 10%, and the optimal Lundell alternator material cost was reduced by 15%.

A well known limitation of Lundell alternators is the long "load dump" transient that occurs when the machine is quickly unloaded. This limitation is of particular concern for high-power 42 V alternators, due to the large energy levels that must be clamped to suppress the transient. A further contribution of this thesis, described in Chapter 3, is an investigation of the use and limitations of fast field de-excitation (rapid removal of current from the field winding) to reduce the duration and energy associated with the load dump transient. An experimental study of a Motorcraft 130 A, 14 V Lundell alternator revealed that eddy currents in the rotor poles limited the rate of decay of the transient overvoltage even with instantaneous removal of field current. Experimental measurements and subsequent modeling revealed approximate eddy current decay time constants of 15 ms and 100 ms, leading to transient durations of approximately 75 milliseconds for the alternator investigated. The effects of eddy currents appear not to be widely appreciated at present, and recognition of this effect may be useful for achieving the improved transient performance demanded in future designs.

As seen in the study of alternator machine design in Chapter 2, achievable alternator output power is related to the square of field ampere turns (at the load matched condition). Improvements in the design and excitation of the field can thus have a large impact on achievable alternator power. A further contribution of this thesis is the investigation of new field winding designs and excitation methods that enable significant improvements in the power density of Lundell alternators. Chapter 4 explores the replacement of the conventional wire-wound alternator field (having a copper packing factor of approximately 0.6) with a foil-wound field winding (which can achieve a

packing factor of 0.7 or higher). The higher packing factor of a foil field winding allows higher ampere turns at constant copper loss, and the improved thermal transfer characteristics of a foil winding allow higher copper losses for a constant field temperature rise.

As revealed in Chapter 5, use of a foil field winding with conventional insulation leads to higher field currents with fewer turns, and creates the need for circuitry to enable a higher field current excitation without exceeding the current limitations of the brushes. Chapter 5 explores multiple circuit approaches that would enable the use of a foil wound field winding with a higher ampere turn excitation. The first approach involves the use of a DC/DC converter on the rotor to provide the necessary step up in current to the field winding while limiting the currents through the brushes. Converter topologies that allow for fast de-excitation of the field winding are also explored.

A second approach explored in Chapter 5 for realizing higher current excitation of the foil-wound field winding involves the use of contactless power transfer to the rotating side by utilizing a rotating transformer with a stationary primary and a rotating secondary. An inverter is used to create the alternating voltage across the primary and a rectifier is used on the secondary side to provide the direct current to the field winding. Further modifications of the topology enable fast field de-excitation of the field winding by voltage or both voltage and current reversal.

Chapter 6 explores the implementation of the rotating transformer topology in Chapter 5. The transformer of choice is a printed circuit board (PCB) transformer because of its low cost, small size, and easy construction. The PCB transformer is modeled, designed and built together with the associated circuitry (inverter and rectifier) to excite a foil wound field winding with a higher current. An increase in ampere turns of 51% is demonstrated experimentally, which could lead to large increases in output power as long as the thermal and saturation conditions are within their limits. As explained in Chapter 4, the use of a foil winding allows for a higher field ampere turn excitation by virtue of its improved packing factor (lower resistance and therefore lower copper losses) and lower thermal resistance to ambient (lower temperature rise given same power dissipation). Further redesign of the stator could be done to fully exploit the increase in ampere turns. Such redesign would involve increasing the depth of the stator slots and armature wire

size to lessen the heating of the stator, and increasing the air gap width to decrease the amount of saturation.

Chapter 7 explores the implementation and experimental evaluation of the rotating DC/DC converter approach proposed in Chapter 5. The converter allows for a step up in current to the field winding while maintaining the current through the brushes. The main challenge in realizing this approach is communicating the needed control signal (e.g., duty ratio) from the stationary side to the rotating side. Line carrier communication is employed in the prototype design, wherein the required active switch duty ratio is encoded in the frequency of a sinusoid injected into the power bus on the stationary side and received on the rotating side. A filter is required on the rotating side to accurately demodulate the received signal despite noise from the switching currents.

To demonstrate this approach, a foil-field rotor is developed for an OE Plus 14 V, 130 A alternator (7776-10-8-N). A 5 mil copper with 1 mil insulation (kapton) foil winding (90 turns) is wound around the original bobbin and a 15% improvement in packing factor over the regular field winding is obtained. The DC/DC converter is designed, together with the filter and the communications receiver circuit, to be mounted directly on the rotor. An associated controller, transmitter, and filter unit is developed for the stationary side, in place of the conventional regulator.

The alternator is assembled together with the embedded electronics, tested, and compared to the performance of a stock alternator. Testing is conducted for idle speed operation (1500 rpm) and 13 V output to enable a comparison with the published specifications for the stock alternator. At non-thermal steady state conditions a maximum field current for the modified alternator of 33.1 amperes is obtained, yielding a 44% increase in ampere turns over that of the stock alternator. In order to make a fair comparison, the output power of the modified and stock alternator are compared at field excitations such that the field winding temperature rise at thermal steady state (over ambient) in both alternators is identical. The stock alternator is excited with full field current to thermal steady state and its percentage increase in field winding resistance (26.2%) is measured, which is proportional to its temperature increase. The output current measured is 63 A. The modified alternator is then excited with field current until its percentage increase in resistance is identical to that of the stock alternator

(approximately 30 A), implying an identical temperature rise. The output current at this operating point is 71.3 A. The result is an increase of 14.9 % in output power of the modified alternator over the stock alternator at thermal steady state and identical field winding temperatures.

At a field current of 30 A, an approximately 30 % increase in field ampere turns is used in the modified alternator over the stock alternator. In order to fully utilize the increase in ampere turns, the alternator stator can be redesigned to accommodate the more stressful thermal and saturation conditions. The armature winding heat flux can be decreased by increasing the stator slot depths and armature wire size. Saturation in the stator can be lessened by increasing the air gap and the back iron thickness. If more field ampere turns are to be used, the air gap can be increased proportionately while maintaining the air gap flux density and decreasing the armature reactance, and therefore still achieving an increase in output power while not saturating the alternator any further. It is anticipated that redesigning the alternator to accommodate the improved field capability would yield substantially more than the demonstrated 15% improvement in power.

8.2 Recommendations for Future Work

There are several extensions to the work described here that could be made in the future. The optimizations of the four alternators were all done using numerical and analytical models. Construction and testing of the optimized Lundell alternator and associated switched mode rectifier is a logical next step towards meeting the increased power and efficiency requirements of future automobiles.

The packing factor of the foil winding could be improved even further by using a thinner insulation. The initial prototype uses a commercial foil with 1 mil kapton insulation. Thinner insulation could certainly be achieved through use of a conformal coat (e.g., parylene or a spray-coated insulation), co-winding bare foil with a thinner insulator (as done in foil-wound capacitors), or by depositing a thin layer of Aluminum over the copper foil and developing an oxide insulation layer. Thinner insulation would

allow even higher packing factors and output power levels to be achieved, and could be used to reduce the voltage/current transformation needed for foil-wound field windings.

The rotating dc/dc converter approach could be simplified through multiple means. One approach to reduce the rotor circuit size and cost is to use wireless communications (e.g., Blue Tooth) to transmit control information to the rotating side. Another approach would be to eliminate the required communications by having a constant, synchronous rectified converter on the rotor and adding an additional controllable DC/DC converter on the stationary side. There would then be no need to transmit a signal to the rotating side, eliminating the need for communications circuitry.

References

[1] J. G. Kassakian, J. M. Miller, N. Traub, "Automotive Electronics Power Up," *IEEE Spectrum*, pp.34-39, May 2000.

[2] G. Kobe, "Jumping to 42 Volts," *AI (Automotive Industries)*, pp.29-34, August 1998.

[3] J. D. Dimech, "Standardized Automotive Load Dump Testing," *IEEE 1991 International Symposium on Electromagnetic Compatibility*, pp. 355-359, 1991.

[4] J. G. Kassakian, H. C. Wolf, J. M. Miller and C. J. Hurton, "Automotive Electrical Systems circa 2005," *IEEE Spectrum*, pp. 22-27, August 1996.

[5] P. Le Bars, "42 V Load Dump Transient and Centralised Active Suppression," *Passenger Car Electrical Architecture IEE Seminar,* London, UK, pp.4/1-4/3, 2000.

[6] D. Morrison, "A Power Shortage is Driving Automotive Applications to 42V," *Automotive Electronics*, August 2000.

[7] F. Liang, J. Miller, S. Zarei, "A Control Scheme to Maximize Output Power of a Synchronous Alternator in a Vehicle Electrical Power Generation System," *Industry Applications Conference, Thirty-First IAS Annual Meeting,* pp. 830-835, October 1996.

[8] F. Liang, J. Miller, X. Xu, "A Vehicle Electrical Power Generation System with Improved Output Power and Efficiency," *Industry Applications Conference, Thirty-Third IAS Annual Meeting*, Vol.1, pp. 50-56, October 1998.

[9] D. J. Perreault, V. Caliskan, "A New Design for Automotive Alternators," *International Conference on Transportation Electronics*, Detroit, MI, October 2000 (Convergence 2000), SAE Paper 2000-01-C084.

[10] J. N. Ellis, F. A. Collins, "Brushless Rotating Electrical Generators for Space Auxiliary Power Systems," *National Aeronautics and Space Administration, Contract No. NAS 3-2783*, Vol. 1, April 1965.

[11] G. A. Osborn, T. W. Salmon, "Application of the Electromagnetic Generator to Space Power Systems," *IEEE Transactions on Aerospace*, Vol. 2, No. 2, pp. 857-866, April 1964.

[12] L. G. Opel, "Design Features of Alternating Current Nadyne Generator," *IEEE Transactions on Aerospace*, Vol. 2, No. 2, pp. 888-895, April 1964.

[13] V. Caliskan, D. J. Perreault, T. M. Jahns, J. G. Kassakian, "Analysis of Three-Phase Rectifiers with Constant-Voltage Loads", *IEEE Transactions on Circuits and Systems-I: Fundamental Theory and Applications*, Vol. 50, No. 9, pp. 1220-1225, September 2003.

173

[14] A. Brown, "The Analysis and Design of a High-Power, High-Efficiency Generator," M.Eng. Thesis, Massachusetts Institute of Technology, Department of Electrical Engineering and Computer Science, May, 1999.

[15] L. Lorilla, "Investigation of the Homopolar Inductor Alternator for Automotive Applications", M. Eng. Thesis, Massachusetts Institute of Technology, Department of Electrical Engineering and Computer Science, May, 2000.

[16] C.-M. Ong, "Dynamic Simulation of Electric Machinery," New Jersey: Prentice Hall, 1992.

[17] L. M. Lorilla, T. A. Keim, J. H. Lang, D. J. Perreault, "Topologies for Future Automotive Generators," submitted to *2005 Vehicle Power and Propulsion (VPP) Conference*, Illinois Institute of Technology, Chicago, September 2005.

[18] A. L. Julian, G. Oriti, "New Brushless Alternator for Automotive Applications," *Industry Applications Conference, Thirty-Sixth IAS Annual Meeting*, Vol. 1, pp. 443-448, September 2001.

[19] H. C. Scott, G. W. Johnson, "Electric Machine with a Transformer Having a Rotating Component," U.S. Patent 5,519,275, May 21,1996.

[20] R. Erickson, D. Maksimovic, *Fundamentals of Power Electronics*, Massachusetts: Kluwer Academic Publishers, 2001.

[21] S.C. Tang, S.Y.R. Hui, H. Chung, "Characterization of Coreless Printed Circuit Board (PCB) Transformers," *IEEE Transactions on Power Electronics*, pp. 746-752, Nov. 2000.

[22] W. G. Hurley, "Calculation of Self and Mutual Impedances in Planar Magnetic Structures", *IEEE Transactions on Magnetics*, Vol. 31, No. 4, pp. 2416-2422, July 1995.

[23] S. C. Tang, S. Y. Hui, H. Chung, "Coreless Planar Printed-Circuit-Board (PCB) Transformers- A Fundamental Concept for Signal and Energy Transfer", *IEEE Transactions on Power Electronics*, Vol. 15, No. 5, pp. 931-941, Sep. 2000.

[24] J. G. Kassakian, M. F. Schlecht, G. C. Verghese, *Principles of Power Electronics*, Massachusetts:Addison-Wesley Publishing Company, 1991.

[25] C. S. Namuduri, B. V. Murty, M. G. Reynolds, "Load Dump Transient Control of a 42V Automotive Generator", *2004 35th Annual IEEE Power Electronics Specialists Conference*, pp. 389-394, Aachen, Germany, 2004.

[26] *Automotive Electrics and Electronics*, Robert Bosch GmbH, Stuttgart, 1999.

[27] Z. J. Shen, S. P. Robb, F. Y. Robb, M. Fuchs, D. Berels, and K. Hampton, "Load Dump Protection in 42 V Automotive Electrical Distribution Systems," *Sixteenth Annual IEEE Applied Power Electronics Conference and Exposition*, Volume 1, pp. 289-295, March 2001.

[28] D. J. Perreault, "Design and Evaluation of Cellular Power Converter Architectures," Ph.D. Thesis, Massachusetts Institute of Technology, Department of Electrical Engineering and Computer Science, June 1997.

[29] T. C. Neugebauer, "Computer-aided design and optimization of dc/dc power converters," S. M. Thesis, Massachusetts Institute of Technology, Department of Electrical Engineering and Computer Science, May 1999.

[30] D. J. Perreault, V. Caliskan, "Automotive power generation and control," *IEEE Transactions on Power Electronics*, Vol. 19, pp. 618-630, May 2004.

[31] E. Richter, "New Developments in Very High Speed Electrical Alternators," *Intersociety Energy Conversion Engineering Conference,* 1971.

[32] K.G. Burger, H. P. Groter, H. J. Lutz, F. Meyer, W. Scheluter, "Alternators in Automotive Applications-State of the Art and Development Trends, "symposium *"Nebenaggregate im Fahrzeug*, Haus der Technik Essen, Oct. 5 and 6, 1994.

[33] J. A. N. Msekela, P. N. Materu, A. H. Nzali, "Development of a Homopolar Electrical Machine for High Power Density High Speed Applications", *African Electrical Technology Conference*, 1996.

[34] G. C. Jain, " Design Aspects of a Homopolar Inductor Alternator", *IEEE Transactions on Power Apparatus and Systems*, Vol. 83, pp. 1009-1015, October 1964.

[35] J. H. Walker, "The Theory of the Inductor Alternator", *Journal of IEE*, Vol. 89, pp. 227-241, 1942.

[36] F. B. Reiter, Jr., K. Rajashekara, R. J. Krefta, "Salient Pole Generators for Belt-Driven Automotive Alternator Applications", *Industry Applications Conference*, 2001. Thirty-Sixth IAS Annual Meeting, Vol. 1, pp. 437-442, Sep.-Oct. 2001.

[37] V. Ostovic., J. M. Miller, V. K. Garg, R. D. Schultz, S. H. Swales, "A Magnetic Equivalent Circuit Based Performance Computation of a Lundell Alternator", *IEEE Transactions on Industry Applications*, Vol. 35, No. 4, July/August 1999.

[38] Stojcic, G., Nguyen, C., "MOSFET Synchronous Rectifiers for Isolated, Board-Mounted DC-DC Converters", *Telecommunications Energy Conference*, Twenty-second International, pp. 258-266, September 2000.

[39] Jitaru, I D., Cocina, G., "High Efficiency DC-DC Converter", *Applied Power Electronics Conference and Exposition*, Conference Proceedings, vol. 2, pp. 638-644, February, 1994,

[40] K. O'Meara, "A new output rectifier configuration optimized for high frequency operation," in *Proc. High Frequency Power Conv. Conf. (HFPC)*, , pp. 219-225, June 2001.

[41] C. Peng, M. Hannigan, and O. Seiersen, "New Efficient High Frequency Rectifier Circuit", in *Proc. High Frequency Power Conv. Conf. (HFPC)*, pp.236-243, June 1991.

[42] T. Gray, *Applied Electronics*, 2nd ed. New York: Wiley, 1954, p. 361.

[43] Huber, L., Jovanovic, M. M., "Forward Converter with Current-Doubler Rectifier: Analysis, Design, and Evaluation Results", *Applied Power Electronics Conference and Exposition*, Conference Proceedings, Vol. 2, pp. 605-611, February 1997.

[44] Sun, J., Mehrotra, V., "Unified Analysis of Half-Bridge Converters with Current-Doubler Rectifier", *Applied Power Electronics Conference and Exposition*, Sixteenth Annual IEEE, Vol. 1, pp. 514-520, March 2001.

[45] Rivas, J. M., Perreault, D. J., Keim, T., "Performance Improvement in Alternators with Switched-Mode Rectifiers", *Power Electronics Specialists Conference*, Vol. 5, pp. 4074-4084, June 2004.

[46] Tang, S. C., "Thermal Modelling of Lundell Alternators", *Power Electronics Specialists Conference*, Vol. 4, pp. 1919-1925, June 2001.

Appendix A. Lumped Parameter Derivations

The appendix provides the detailed derivations of the lumped parameters cited in Section 2.4 and forms the basis for the evaluation in Section 2.5. Table A.1 shows the nomenclature used:

Table A.1: Nomenclature

a	number of parallel windings
b_p	pole width
b_{pN}	pole width of north pole at a particular axial location
b_{pS}	pole width of south pole at a particular axial location
B	flux density
B_r	air gap flux density due to the field winding
B_s	air gap flux density due to the armature currents
F_r	MMF due to the field winding
F_s	MMF due to the three phase armature currents
g	air gap width
$g1$	shorter air gap width
$g2$	longer air gap width
i_a, i_b, i_c	armature phase currents
i_f	field current
I_s	magnitude of armature phase current
k_{wf}	field distribution winding factor
k_{wn}	armature distribution winding factor of nth harmonic
L	air gap length
L_{af}	field armature mutual inductance
L_s	synchronous inductance
$N_f I_f$	field ampere turns
N_s	series armature turns
p	pole pairs
P	output power
q	heat flux
R	equivalent resistance due to effects of diode rectifer
R_s	armature series resistance
R_{statin}	stator inner radius
$R_{statslotbot}$	stator slot bottom radius
r_a	physical armature resistance
V_d	diode drop
V_o	effective voltage at output of rectifier
V_{sa}, V_{sb}, V_{sc}	back-emf voltages
$W_{endturn}$	end turn width
X_d, X_q	direct and quadrature reactances
z	axial location
β	pole width over pole pair pitch

177

β'	pole width over pole pitch (pole fraction)
δ	electrical angle when t=0
Λ	permeance per unit area
λ	flux linked
λ_{af}	flux linked by armature winding due to field current
λ_{as}	flux linked by armature winding due to three phase armature currents
ω	electrical frequency in rad/s
θ_r	rotor angle in mechanical degrees
τ_p	pole pitch

A.1 General Fourier Series Representation of a Rectangular Waveform

The Fourier expansion for the flux densities in the air gap can be derived from the generalized rectangular waveform shown in Figure A.1.
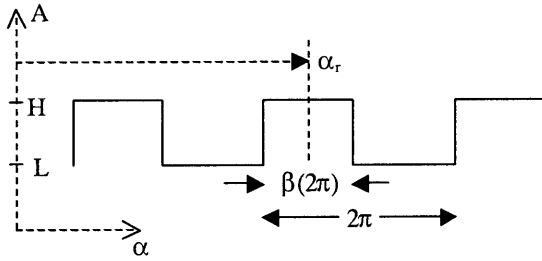
Figure A.1: Arbitrary rectangular waveform.

The waveform could be expressed mathematically as

$$A = \sum_{m=0}^{\infty} A_m \cos(m(\alpha - \alpha_r)) \tag{A.1}$$

$$A_0 = H\beta + L(1 - \beta) \tag{A.2}$$

$$A_m = \frac{2}{m\pi}(H - L)\sin(m\beta\pi) \tag{A.3}$$

For a square wave, centered about 0, $H=-L$ and $\beta=1/2$. The fourier series coefficients are

$$A_m = \frac{4}{m\pi} H \sin(m\pi/2) \tag{A.4}$$

$$A_0 = 0 \tag{A.5}$$

A.2 Field Flux Densities

A.2.1 Non-salient Wound-field Alternator Field Flux Density

For the wound-field non-salient pole machine, the step-like MMF is approximated by a square wave whose amplitude is affected by the distribution winding factor. The permeance per unit area is constant at μ_o/g or the permeability of free space divided by the air gap width. The MMF distribution can be written as

$$F_r = \sum_{\substack{n=1 \\ n\,\text{odd}}}^{\infty} \frac{4}{n\pi} \frac{N_f I_f}{2p} k_{wf} \sin\left(\frac{n\pi}{2}\right) \cos(np(\theta - \theta_r)) \tag{A.6}$$

The gap permeance can be defined as

$$\Lambda = \frac{\mu_0}{g} \tag{A.7}$$

Finally, the air gap flux density due to the field winding can be written as

$$B_r = F_r \Lambda = \left(\sum_{\substack{n=1 \\ n\,\text{odd}}}^{\infty} \frac{4}{n\pi} \frac{N_f I_f}{2p} k_{wf} \sin\left(\frac{n\pi}{2}\right) \cos(np(\theta - \theta_r)) \right) \frac{\mu_o}{g} \tag{A.8}$$

where n represents the nth harmonic, p for pole pairs, $N_f I_f$ for field ampere turns, and k_{wf} for the field winding factor. This flux density is shown in Figure A.2.
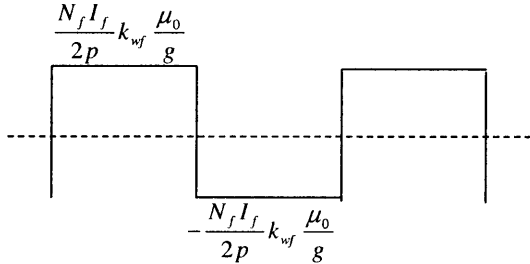
Figure A.2: Non-salient wound-field alternator flux density waveform.

A.2.2 Salient-pole Wound-field Alternator Field Flux Density

The air gap flux density in the salient-pole wound field alternator due to the field winding when expressed as the product of the MMF drop and the permeance per unit area can be expressed as the sum of two waveforms, one due to the north poles and the other

179

due to the south poles. The two waveforms are added together to get the actual flux density shown in Figure A.3.
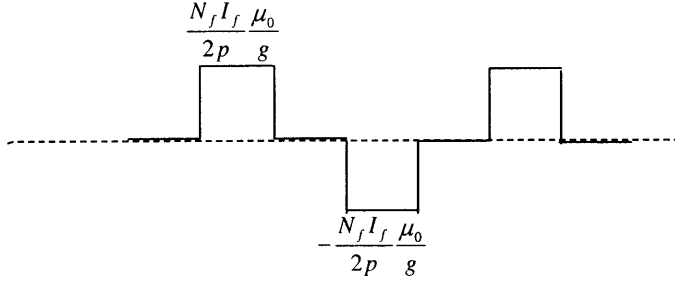
Figure A.3: Salient wound-field alternator field flux density waveform.

The flux density waveform due to the north poles can be expressed as

$$B_{rN} = \sum_{m=0}^{\infty} B_{rNm} \cos(mp(\theta - \theta_r)) \tag{A.9}$$

$$B_{rN0} = \beta\left(\frac{N_f I_f}{2p} \frac{\mu_0}{g}\right) = \left(\frac{N_f I_f}{2p}\right)\left(\beta\frac{\mu_0}{g}\right) = F_{rN}\Lambda_{N0} \tag{A.10}$$

$$B_{rNm} = \frac{2}{m\pi}\left(\frac{N_f I_f}{2p} \frac{\mu_0}{g}\right)\sin(m\beta\pi)$$

$$= \left(\frac{N_f I_f}{2p}\right)\left(\frac{2}{m\pi} \frac{\mu_0}{g}\sin(m\beta\pi)\right) = F_{rN}\Lambda_{Nm} \tag{A.11}$$

where m represents the mth harmonic, and β for the pole width divided by the width of a pole pair. The flux density waveform due to the south poles can be expressed as

$$B_{rS} = \sum_{m=0}^{\infty} B_{rSm} \cos(mp((\theta - \pi/p) - \theta_r)) \tag{A.12}$$

$$B_{rS0} = \beta\left(-\frac{N_f I_f}{2p} \frac{\mu_0}{g}\right) = \left(-\frac{N_f I_f}{2p}\right)\left(\beta\frac{\mu_0}{g}\right) = F_{rS}\Lambda_{S0} \tag{A.13}$$

$$B_{rSm} = \frac{2}{m\pi}\left(\frac{N_f I_f}{2p} \frac{\mu_0}{g}\right)\sin(m\beta\pi)$$

$$= \left(-\frac{N_f I_f}{2p}\right)\left(\frac{2}{m\pi} \frac{\mu_0}{g}\sin(m\beta\pi)\right) = F_{rS}\Lambda_{Sm} \tag{A.14}$$

The sum of the two waveforms give the total flux density waveform in the air gap due to the field winding which can be shown to be

$$B_r = B_{rN} + B_{rS} = \sum_{\substack{m=1 \\ m\,\text{odd}}}^{\infty} (B_{rNm} - B_{rSm})\cos(mp(\theta - \theta_r))$$

$$B_r = \sum_{\substack{m=1 \\ m\,\text{odd}}}^{\infty} (\frac{4}{m\pi}\frac{N_f I_f}{2p}\frac{\mu_0}{g}\sin(m\beta\pi))\cos(mp(\theta - \theta_r))$$

(A.15)

A.2.3 Lundell Alternator Field Flux Density

Looking at the Lundell alternator, along a slice at some circumferential position, the flux density waveform will look like the waveform shown in Figure A.4.
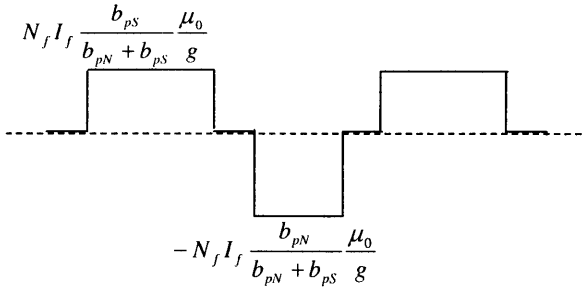
Figure A.4: Lundell alternator field flux density waveform.

The flux densities due to the north and south poles can be determined separately and added. The flux density contribution by the north poles can be expressed as

$$B_{rN} = \sum_{m=0}^{\infty} B_{rNm}\cos(mp(\theta - \theta_r))$$

(A.16)

$$B_{rN0} = \beta_N\left(\frac{N_f I_f}{2}\frac{\mu_0}{g}\right) = \left(\frac{N_f I_f}{2}\right)\left(\beta_N\frac{\mu_0}{g}\right) = F_{rN}\Lambda_{N0}$$

(A.17)

$$B_{rNm} = \frac{2}{m\pi}\left(\frac{N_f I_f}{2}\frac{\mu_0}{g}\right)\sin(m\beta_N\pi)$$

$$B_{rNm} = \left(\frac{N_f I_f}{2}\right)\left(\frac{2}{m\pi}\frac{\mu_0}{g}\sin(m\beta_N\pi)\right) = F_{rN}\Lambda_{Nm}$$

(A.18)

$$\beta_N = \frac{\frac{z}{L}b_{p2} + \left(1 - \frac{z}{L}\right)b_{p1}}{2\tau_p}$$

(A.19)

181

where b_{p2} and b_{p1} are the widths of the wider end and narrower end of a pole, respectively, and τ_p is a pole pitch. Similarly, the flux density waveforms due to the south poles are

$$B_{rS} = \sum_{m=0}^{\infty} B_{rSm} \cos(mp((\theta - \pi/p) - \theta_r)) \tag{A.20}$$

$$B_{rS0} = \beta_S \left(-\frac{N_f I_f}{2} \frac{\mu_0}{g} \right) = \left(-\frac{N_f I_f}{2} \right) \left(\beta_S \frac{\mu_0}{g} \right) = F_{rS} \Lambda_{S0} \tag{A.21}$$

$$B_{rSm} = \frac{2}{m\pi} \left(-\frac{N_f I_f}{2} \frac{\mu_0}{g} \right) \sin(m\beta\pi)$$

$$B_{rSm} = \left(-\frac{N_f I_f}{2} \right) \left(\frac{2}{m\pi} \frac{\mu_0}{g} \sin(m\beta\pi) \right) = F_{rS} \Lambda_{Sm} \tag{A.22}$$

$$\beta_S = \frac{\frac{z}{L} b_{p1} + \left(1 - \frac{z}{L}\right) b_{p2}}{2\tau_p} \tag{A.23}$$

The sum of both waveforms gives the total flux density due to the field winding which are

$$B_r = B_{rN} + B_{rS}$$

$$B_r = \sum_{\substack{m=0 \\ m\,\text{even}}}^{\infty} (B_{rNm} + B_{rSm}) \cos(mp(\theta - \theta_r)) + \sum_{\substack{m=1 \\ m\,\text{odd}}}^{\infty} (B_{rNm} - B_{rSm}) \cos(mp(\theta - \theta_r)) \tag{A.24}$$

where the different harmonic components are

$$B_{r0} = \left(\frac{N_f I_f}{2} \right) \left((\beta_N - \beta_S) \frac{\mu_0}{g} \right) \tag{A.25}$$

$$B_{rm} = \left(\frac{N_f I_f}{2} \right) \left(\frac{2}{m\pi} \frac{\mu_0}{g} \left(\sin(m\beta_N \pi) - \sin(m\beta_S \pi) \right) \right) \cdot \cos(mp(\theta - \theta_r)) \qquad m\,\text{even} \tag{A.26}$$

$$B_{rm} = \left(\frac{N_f I_f}{2} \right) \left(\frac{2}{m\pi} \frac{\mu_0}{g} \left(\sin(m\beta_N \pi) + \sin(m\beta_S \pi) \right) \right) \cdot \cos(mp(\theta - \theta_r)) \qquad m\,\text{odd} \tag{A.27}$$

A.2.4 Homopolar Inductor Alternator Field Flux Density

For the inductor alternator, the flux density on one stack can be found to be as shown in Figure A.5.
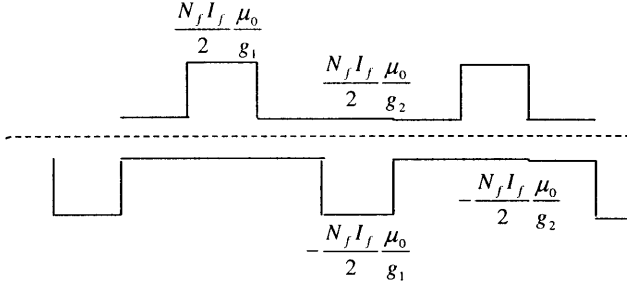
Figure A.5: Homopolar inductor alternator field flux density waveform

The expression for the waveform in the air gap where the north poles are located are

$$B_{rN0} = F_{rN}\Lambda_{N0} = \left(\frac{N_f I_f}{2}\right)\left(\beta\left(\frac{\mu_0}{g_1}\right) + (1-\beta)\left(\frac{\mu_0}{g_2}\right)\right) \qquad (A.28)$$

$$B_{rN0} = F_{rN}\Lambda_{N0} = \left(\frac{N_f I_f}{2}\right)\left(\beta\left(\frac{\mu_0}{g_1}\right) + (1-\beta)\left(\frac{\mu_0}{g_2}\right)\right) \qquad (A.29)$$

$$B_{rNm} = F_{rN}\Lambda_{Nm} = \left(\frac{N_f I_f}{2}\right)\left(\frac{2}{m\pi}\left(\frac{\mu_0}{g_1} - \frac{\mu_0}{g_2}\right)\sin(m\beta\pi)\right) \qquad (A.30)$$

where g_1 and g_2 are the shorter and longer air gap widths, respectively. Likewise, for the air gap where the south poles are, the flux density waveform due to the field winding can be shown to be

$$B_{rS} = \sum_{m=0}^{\infty} B_{rSm} \cos(mp((\theta - \pi/p) - \theta_r)) \qquad (A.31)$$

$$B_{rS0} = F_{rS}\Lambda_{S0} = \left(-\frac{N_f I_f}{2}\right)\left(\beta\left(\frac{\mu_0}{g_1}\right) + (1-\beta)\left(\frac{\mu_0}{g_2}\right)\right) \qquad (A.32)$$

$$B_{rSm} = F_{rS}\Lambda_{Sm} = \left(-\frac{N_f I_f}{2}\right)\left(\frac{2}{m\pi}\left(\frac{\mu_0}{g_1} - \frac{\mu_0}{g_2}\right)\sin(m\beta\pi)\right) \qquad (A.33)$$

A.3 Armature Flux Densities

For the armature windings as sources of MMF, the MMF due to each winding is approximated as a square wave with a winding factor k_{wn}

$$F_a = \sum_{\substack{n=1 \\ n\,\text{odd}}}^{\infty} \frac{4}{n\pi} \frac{N_s i_a}{2p} \frac{k_{wn}}{a} \cos(np\theta) \tag{A.34}$$

$$F_b = \sum_{\substack{n=1 \\ n\,\text{odd}}}^{\infty} \frac{4}{n\pi} \frac{N_s i_b}{2p} \frac{k_{wn}}{a} \cos(n(p\theta - 2\pi/3)) \tag{A.35}$$

$$F_c = \sum_{\substack{n=1 \\ n\,\text{odd}}}^{\infty} \frac{4}{n\pi} \frac{N_s i_c}{2p} \frac{k_{wn}}{a} \cos(n(p\theta - 4\pi/3)) \tag{A.36}$$

where N_s is the number of armature turns per phase. The combined MMF is

$$F_s = F_a + F_b + F_c$$

$$F_s = \sum_{n=1,7,\ldots,6k+1}^{\infty} \frac{3}{2} \frac{4}{n\pi} \frac{N_s I_s}{2p} \frac{k_{wn}}{a} \sin(p\theta_r - \phi - np\theta) + \sum_{n=5,11,\ldots,6k-1}^{\infty} \frac{3}{2} \frac{4}{n\pi} \frac{N_s I_s}{2p} \frac{k_{wn}}{a} \sin(p\theta_r - \phi + np\theta)$$

$$\tag{A.37}$$

of which only the fundamental is considered. In order to determine the fundamental flux density in the air gap due to the three-phase armature currents, the fundamental MMF is multiplied by the 0th component and 2nd harmonic of the air gap permeance function. There are slight modifications though to the air gap as seen from the armature winding compared to that seen by the field winding. The non-salient wound-field alternator still has the same permeance. The salient-pole has a slight change. The interpolar gaps are no longer seen to be of infinite gap width. Also, the north and south poles need not be considered separate. The new permeance function assumes the following form

$$\Lambda' = \sum_{m=0}^{\infty} \Lambda'_m \cos(m(2p)(\theta - \theta_r)) \tag{A.38}$$

$$\Lambda'_o = \beta'\left(\frac{\mu_0}{g_1}\right) + (1 - \beta')\left(\frac{\mu_0}{g_2}\right) \tag{A.39}$$

$$\Lambda'_m = \frac{2}{m\pi}\left(\frac{\mu_0}{g_1} - \frac{\mu_0}{g_2}\right) \sin(m\beta'\pi) \tag{A.40}$$

$$\beta' = b_p / \tau_p \tag{A.41}$$

$$\Lambda' \cong \Lambda'_0 + \Lambda'_1 \cos(2p(\theta - \theta_r)) \tag{A.42}$$

For the Lundell alternator, the two permeance functions determined separately can be combined as one permeance function. For the north poles, the permeance function is

$$\Lambda_N = \sum_{m=0}^{\infty} \Lambda_{Nm} \cos(mp(\theta - \theta_r)) \qquad \text{(A.43)}$$

$$\Lambda_{N0} = \beta_N \frac{\mu_0}{g} \qquad \text{(A.44)}$$

$$\Lambda_{Nm} = \left(\frac{2}{m\pi} \frac{\mu_0}{g} \sin(m\beta_N\pi) \right) \qquad \text{(A.45)}$$

For the south poles, the permeance function is

$$\Lambda_S = \sum_{m=0}^{\infty} \Lambda_{Sm} \cos(mp(\theta - \theta_r)) \qquad \text{(A.46)}$$

$$\Lambda_{S0} = \beta_S \frac{\mu_0}{g} \qquad \text{(A.47)}$$

$$\Lambda_{Sm} = \left(\frac{2}{m\pi} \frac{\mu_0}{g} \sin(m\beta_S\pi) \right) \qquad \text{(A.48)}$$

The combined permeance function can be shown to be

$$\Lambda = \Lambda_N + \Lambda_S = \sum_{m=0}^{\infty} (\Lambda_{Nm} + \Lambda_{Sm}) \cos(mp(\theta - \theta_r)) \qquad \text{(A.49)}$$

$$\Lambda \cong (\Lambda_{N0} + \Lambda_{S0}) + (\Lambda_{N2} + \Lambda_{S2}) \cos(2p(\theta - \theta_r)) \qquad \text{(A.50)}$$

Likewise, for the homopolar inductor alternator, the permeance function is approximated as

$$\Lambda_N \cong \Lambda_{N0} + \Lambda_{N2} \cos(2p(\theta - \theta_r)) \qquad \text{(A.51)}$$

for the north poles and

$$\Lambda_S \cong \Lambda_{S0} + \Lambda_{S2} \cos(2p(\theta - \theta_r)) \qquad \text{(A.52)}$$

for the south poles. The flux density is then the fundamental component of the MMF multiplied by the approximate permeance function from which the fundamental component is obtained

$$B_{s1} = \{(F_{s1} \sin(p(\theta - \theta_r) - \phi))(\Lambda_0 + \Lambda_2 \cos(2p(\theta - \theta_r)))\}_1$$

$$B_{s1} = F_{s1}(\Lambda_0 \sin(p(\theta - \theta_r) - \phi) - \frac{\Lambda_2}{2} \sin(p(\theta - \theta_r) + \phi)$$

$$\text{(A.53)}$$

where the subscript 1 is used to represent the fundamental component.

A.4. Flux Linkages

For the first three machines, the flux linked by the armature winding is

$$\lambda = \frac{N_s k_w}{a} \int_0^L \int_{-\pi/2p}^{\pi/2p} B_1 R \, d\theta \, dz \tag{A.54}$$

For the inductor alternator, the flux linked is

$$\lambda = \frac{N_s k_w}{a} \int_0^{L/2} \int_{-\pi/2p}^{\pi/2p} B_{N1} R \, d\theta \, dz + \frac{N_s k_w}{a} \int_{L'}^{L'+L/2} \int_{-\pi/2p}^{\pi/2p} B_{S1} R \, d\theta \, dz \tag{A.55}$$

which is the sum of the flux linked for the north and south poles separately. It can be shown that (A.54) and (A.55) are the same.

A.5 Lumped Parameters

The field armature mutual inductance is

$$L_{af} = \lambda_{af} / I_f \tag{A.56}$$

In order to determine the equivalent inductance and resistance due to armature reaction, the flux linked will end up having the following form

$$\lambda_a = (L_x) I_s \sin(p\theta - \phi) - (L_y) I_s \sin((p\theta - \phi) + 2\phi) \tag{A.57}$$

seen earlier. From these L_s and R_s can both be determined since

$$L_s = L_x - L_y \cos(2\phi) \tag{A.58}$$

$$R_s = r_a + \omega L_y \sin(2\phi) \tag{A.59}$$

The lumped parameters for each alternator can then be derived. The non-salient wound-field synchronous alternator has the following lumped parameters:

$$\lambda_a = \frac{N_s k_w}{a} RLF_{s1}\left(\frac{2}{p}\right)\left(\Lambda \sin(p\theta_r - \phi)\right) \tag{A.60}$$

$$L_{af} = \frac{N_s k_w}{a} RL\left(\frac{4}{\pi}\frac{N_f}{2p}k_{wf}\right)\left(\frac{\mu_0}{g}\right)\frac{2}{p}\cos(p\theta_r) \tag{A.61}$$

$$L_s = \frac{N_s k_w}{a} RL\left(\frac{3}{2}\frac{4}{\pi}\frac{N_s}{2p}\frac{k_w}{a}\right)\left(\frac{\mu_0}{g}\right)\frac{2}{p} \tag{A.62}$$

$$R_s = r_a \tag{A.63}$$

The salient wound-field synchronous alternator has the following lumped parameters:

$$\lambda_{af} = \frac{N_s k_w}{a} RL(F_{rN} - F_{rS})\Lambda_1 \left(\frac{2}{p}\cos(p\theta_r)\right) \tag{A.64}$$

$$\lambda_a = \frac{N_s k_w}{a} RLF_{s1}\left(\frac{2}{p}\right)\left(\Lambda_0' \sin(p\theta_r - \phi) - \frac{\Lambda_1'}{2}\sin(p\theta_r + \phi)\right) \tag{A.65}$$

$$L_{af} = \frac{N_s k_w}{a} RL\left(2\frac{N_f}{2p}\right)\left(\frac{2}{\pi}\frac{\mu_0}{g}\sin\left(\frac{b_p\pi}{2\tau_p}\right)\right)\frac{2}{p}\cos(p\theta_r) \tag{A.66}$$

$$L_s = \frac{N_s k_w}{a} RL\left(\frac{3}{2}\frac{4}{\pi}\frac{N_s}{2p}\frac{k_w}{a}\right)\left(\frac{2}{p}\right)\left(\Lambda_0' - \frac{\Lambda_1'}{2}\cos(2\phi)\right)$$

$$L_s = \frac{N_s k_w}{a} RL\left(\frac{3}{2}\frac{4}{\pi}\frac{N_s}{2p}\frac{k_w}{a}\right)\left(\frac{2}{p}\right)\cdot\left(\begin{array}{c}\left(\frac{b_p}{\tau_p}\left(\frac{\mu_0}{g_1}\right)+\left(1-\frac{b_p}{\tau_p}\right)\left(\frac{\mu_0}{g_2}\right)\right)\\-\frac{1}{2}\left(\frac{2}{\pi}\left(\frac{\mu_0}{g_1}-\frac{\mu_0}{g_2}\right)\sin\left(\frac{b_p\pi}{\tau_p}\right)\right)\cos(2\phi)\end{array}\right) \tag{A.67}$$

$$R_s = r_a + \omega\frac{N_s k_w}{a} RL\left(\frac{3}{2}\frac{4}{\pi}\frac{N_s}{2p}\frac{k_w}{a}\right)\left(\frac{2}{p}\right)\left(\frac{\Lambda_1'}{2}\sin(2\phi)\right)$$

$$R_s = r_a + \omega\frac{N_s k_w}{a} RL\left(\frac{3}{2}\frac{4}{\pi}\frac{N_s}{2p}\frac{k_w}{a}\right)\left(\frac{2}{p}\right)\cdot\left(\frac{1}{2}\left(\frac{2}{\pi}\left(\frac{\mu_0}{g_1}-\frac{\mu_0}{g_2}\right)\sin\left(\frac{b_p\pi}{\tau_p}\right)\right)\sin(2\phi)\right) \tag{A.68}$$

The Lundell alternator has the following lumped parameters:

$$L_{af} = \frac{8}{\pi}\frac{\mu_0 k_w N_f N_s RL}{pa\ (b_{p1}+b_{p2})\ g}\cdot\left(\begin{array}{c}\frac{b_{p1}+b_{p2}}{(b_{p2}-b_{p1})}\left(\cos\left(\frac{b_{p1}\pi}{2\tau_p}\right)-\cos\left(\frac{b_{p2}\pi}{2\tau_p}\right)\right)\\-\frac{4\tau_p}{(b_{p2}-b_{p1})\pi}\left(\sin\left(\frac{b_{p2}\pi}{2\tau_p}\right)-\sin\left(\frac{b_{p1}\pi}{2\tau_p}\right)\right)\\+\left(\cos\left(\frac{b_{p2}\pi}{2\tau_p}\right)+\cos\left(\frac{b_{p1}\pi}{2\tau_p}\right)\right)\end{array}\right)\left(\frac{2}{p}\cos(p\theta_r)\right) \tag{A.69}$$

$$\lambda_a = \frac{N_s k_w}{a} RLF_{s1}\left(\frac{2}{p}\right)$$

$$\cdot\left(\begin{array}{c}\left(\Lambda_{N0}+\Lambda_{S0}\right)\sin(p\theta_r-\phi)\\-\frac{1}{2}\left(\frac{2\mu_0}{2\pi g}\frac{2\tau_p}{(b_{p2}-b_{p1})\pi}\left(\cos\left(\frac{b_{p1}\pi}{\tau_p}\right)-\cos\left(\frac{b_{p2}\pi}{\tau_p}\right)\right)\right)\\\cdot\sin(p\theta_r+\phi)\end{array}\right) \tag{A.70}$$

$$\lambda_{af} = \frac{8}{\pi} \frac{\mu_0 k_w N_f I_f N_s RL}{pa(b_{p1}+b_{p2})g} \cdot \begin{pmatrix} \dfrac{b_{p1}+b_{p2}}{(b_{p2}-b_{p1})}\left(\cos\left(\dfrac{b_{p1}\pi}{2\tau_p}\right)-\cos\left(\dfrac{b_{p2}\pi}{2\tau_p}\right)\right) \\[2em] -\dfrac{4\tau_p}{(b_{p2}-b_{p1})\pi}\left(\sin\left(\dfrac{b_{p2}\pi}{2\tau_p}\right)-\sin\left(\dfrac{b_{p1}\pi}{2\tau_p}\right)\right) \\[2em] +\left(\cos\left(\dfrac{b_{p2}\pi}{2\tau_p}\right)+\cos\left(\dfrac{b_{p1}\pi}{2\tau_p}\right)\right) \end{pmatrix}\left(\frac{2}{p}\cos(p\theta_r)\right) \tag{A.71}$$

$$L_s = \frac{N_s k_w}{a} RL\left(\frac{3}{2}\frac{4}{\pi}\frac{N_s}{2p}\frac{k_w}{a}\right)\left(\frac{2}{p}\right)\cdot \begin{pmatrix} \left(\dfrac{b_{p1}+b_{p2}}{2\tau_p}\dfrac{\mu_0}{g}\right) \\[2em] -\dfrac{1}{2}\begin{pmatrix}\dfrac{2\mu_0}{2\pi g}\dfrac{2\tau_p}{(b_{p2}-b_{p1})\pi} \\[1.2em] \left(\cos\left(\dfrac{b_{p1}\pi}{\tau_p}\right)-\cos\left(\dfrac{b_{p2}\pi}{\tau_p}\right)\right)\end{pmatrix}\cos(2\phi) \end{pmatrix} \tag{A.72}$$

$$R_s = r_a + \omega\frac{N_s k_w}{a} RL\left(\frac{3}{2}\frac{4}{\pi}\frac{N_s}{2p}\frac{k_w}{a}\right)\left(\frac{2}{p}\right)\cdot \begin{pmatrix} \dfrac{1}{2}\begin{pmatrix}\dfrac{2\mu_0}{2\pi g}\dfrac{2\tau_p}{(b_{p2}-b_{p1})\pi} \\[1.2em] \left(\cos\left(\dfrac{b_{p1}\pi}{\tau_p}\right)-\cos\left(\dfrac{b_{p2}\pi}{\tau_p}\right)\right)\end{pmatrix}\sin(2\phi) \end{pmatrix} \tag{A.73}$$

And finally, the homopolar inductor alternator has the following lumped parameters:

$$\lambda_{af} = \frac{N_s k_w}{a} RL\frac{(F_{rN}-F_{rS})}{2}\Lambda_{N1}\left(\frac{2}{p}\cos(p\theta_r)\right) \tag{A.74}$$

$$\lambda_a = \frac{N_s k_w}{a} RLF_{s1}\left(\frac{2}{p}\right)\left(\Lambda_{N0}\sin(p\theta_r-\phi)-\frac{\Lambda_{N2}}{2}\sin(p\theta_r+\phi)\right) \tag{A.75}$$

$$L_{af} = \frac{N_s k_w}{a} RL\frac{\left(2\dfrac{N_f}{2}\right)\left(\dfrac{2}{\pi}\left(\dfrac{\mu_0}{g_1}-\dfrac{\mu_0}{g_2}\right)\sin\left(\dfrac{b_p\pi}{2\tau_p}\right)\right)}{2}\cdot\frac{2}{p}\cos(p\theta_r) \tag{A.76}$$

$$L_s = \frac{N_s k_w}{a} RL\left(\frac{3}{2}\frac{4}{\pi}\frac{N_s}{2p}\frac{k_w}{a}\right)\left(\frac{2}{p}\right)\left(\Lambda_{N0}-\frac{\Lambda_{N2}}{2}\cos(2\phi)\right)$$

$$L_s = \frac{N_s k_w}{a} RL\left(\frac{3}{2}\frac{4}{\pi}\frac{N_s}{2p}\frac{k_w}{a}\right)\left(\frac{2}{p}\right)\cdot \begin{pmatrix} \left(\dfrac{b_p}{2\tau_p}\left(\dfrac{\mu_0}{g_1}\right)+\left(1-\dfrac{b_p}{2\tau_p}\right)\left(\dfrac{\mu_0}{g_2}\right)\right) \\[2em] -\dfrac{1}{2}\left(\dfrac{2}{2\pi}\left(\dfrac{\mu_0}{g_1}-\dfrac{\mu_0}{g_2}\right)\sin\left(\dfrac{b_p\pi}{\tau_p}\right)\right)\cos(2\phi) \end{pmatrix} \tag{A.77}$$

$$R_s = r_a + \omega \frac{N_s k_w}{a} RL \left(\frac{3}{2} \frac{4}{\pi} \frac{N_s}{2p} \frac{k_w}{a} \right) \left(\frac{2}{p} \right) \left(\frac{\Lambda_{N2}}{2} \sin(2\phi) \right)$$

$$R_s = r_a + \omega \frac{N_s k_w}{a} RL \left(\frac{3}{2} \frac{4}{\pi} \frac{N_s}{2p} \frac{k_w}{a} \right) \left(\frac{2}{p} \right) \cdot \left[\frac{1}{2} \left(\frac{2}{2\pi} \left(\frac{\mu_0}{g_1} - \frac{\mu_0}{g_2} \right) \sin \left(\frac{b_p \pi}{\tau_p} \right) \right) \sin(2\phi) \right]$$

(A.78)

Note that the general forms of L_s and R_s from which L_{s0} and L_{s2} can be obtained are

$$L_s = \frac{N_s k_w}{a} RL \frac{F_{s1}}{I_s} \left(\frac{2}{p} \right) \left(\Lambda_0 - \frac{\Lambda_2}{2} \cos(2\phi) \right)$$

(A.79)

$$R_s = r_a + \omega \frac{N_s k_w}{a} RL \frac{F_{s1}}{I_s} \left(\frac{2}{p} \right) \left(\frac{\Lambda_2}{2} \cos(2\phi) \right)$$

(A.80)

A.6 Simplified Lumped Parameters

In order to obtain the simplified power comparisons in Section 2.5, some simplifying assumptions were made. As can be found in Section 2.5, Equation 2.20, the power delivered to an impedance-matched load is based on the mutual inductance L_{af} and the synchronous inductance L_s. This section obtains these simplified inductances. For the non-salient wound field alternator, no simplifying assumptions are made and therefore (A.61) and (A.62) are used. For the salient wound field alternator, the pole width is assumed to be half a pole pitch ($b_p = \tau_p / 2$), the larger air gap is ignored ($g_2 \rightarrow \infty$), and saliency is ignored ($\cos(2\phi)$ term). The simplified inductances are

$$L_{af} = \frac{N_s k_w}{a} RL \left(2 \frac{N_f}{2p} \right) \left(\frac{2}{\pi} \frac{\mu_0}{g} \frac{1}{\sqrt{2}} \right) \frac{2}{p} \cos(p\theta_r)$$

(A.81)

$$L_s = \frac{N_s k_w}{a} RL \left(\frac{3}{2} \frac{4}{\pi} \frac{N_s}{2p} \frac{k_w}{a} \right) \left(\frac{2}{p} \right) \left(\frac{1}{2} \left(\frac{\mu_0}{g_1} \right) \right)$$

(A.82)

For the Lundell alternator, the poles are assumed to be rectangular and with widths equal to a pole pitch ($b_{p1} = b_{p2} = \tau_p$). In addition, saliency is ignored. The simplified inductances are

$$L_{af} = \frac{8}{\pi} \frac{\mu_0 k_w N_f N_s RL}{pa(2\tau_p)g} (2\tau_p \pi) \left(\frac{2}{p} \cos(p\theta_r) \right)$$

(A.83)

189

$$L_s = \frac{N_s k_w}{a} RL\left(\frac{3}{2}\frac{4}{\pi}\frac{N_s}{2p}\frac{k_w}{a}\right)\left(\frac{2}{p}\right)\left(\frac{\mu_0}{g}\right) \tag{A.84}$$

For the homopolar inductor alternator, the width of a pole is made to span a pole pitch ($b_p = \tau_p$), and the larger air gap is ignored ($g_2 \to \infty$)

$$L_{af} = \frac{N_s k_w}{a} RL\frac{\left(2\frac{N_f}{2}\right)\left(\frac{2}{\pi}\left(\frac{\mu_0}{g_1}\right)\right)}{2}\frac{2}{p}\cos(p\theta_r) \tag{A.85}$$

$$L_s = \frac{N_s k_w}{a} RL\left(\frac{3}{2}\frac{4}{\pi}\frac{N_s}{2p}\frac{k_w}{a}\right)\left(\frac{2}{p}\right)\left(\frac{1}{2}\left(\frac{\mu_0}{g_1}\right)\right) \tag{A.86}$$

Appendix A.7 Air Gap Flux Densities

A.7.1 Fundamental Flux Densities

The fundamental flux density can be found by adding the contributions due to the field excitation and the three phase armature excitations. The contributions are traveling waves with the same spatial and temporal frequencies which when added yield a sinusoidal waveform with the same frequencies.The fundamental flux densities for each of the four alternators are derived next.

A.7.1.1 Non-salient Wound-field Synchronous Alternator Fundamental Flux Density

$$\{B\}_1 = \left(F_{r1}\cos(p(\theta - \theta_r)) + F_{s1}\sin(p(\theta_r - \theta) - \phi)\right)\Lambda$$
$$\{B\}_1 = \left(F_{r1}\Lambda - F_{s1}\Lambda\sin(\phi)\right)\cos(p\theta_r - p\theta) + F_{s1}\Lambda\cos(\phi)\sin(p\theta_r - p\theta) \tag{A.87}$$

A.7.1.2 Salient Wound-field Synchronous Alternator Fundamental Flux Density

$$\{B\}_1 = 2F_{rN}\Lambda_{N1}\cos(p(\theta - \theta_r)) + F_{s1}(\Lambda_0'\sin(p(\theta - \theta_r) - \phi) - \frac{\Lambda_1'}{2}\sin(p(\theta - \theta_r) + \phi))$$

$$\{B\}_1 = \left(2F_{rN}\Lambda_{N1} - F_{s1}\left(\Lambda_0' + \frac{\Lambda_1'}{2}\right)\sin(\phi)\right)\cos(p\theta_r - p\theta) + \left(F_{s1}\left(\Lambda_0' - \frac{\Lambda_1'}{2}\right)\cos(\phi)\right)\sin(p\theta_r - p\theta)$$

$$\tag{A.88}$$

A.7.1.3 Lundell Alternator Fundamental Flux Density

$$
\begin{aligned}
\{B\}_1 &= F_{rN}\left(\Lambda_{N1}+\Lambda_{S1}\right)\cos(p(\theta-\theta_r)) \\
&\quad + F_{s1}\left((\Lambda_{N0}+\Lambda_{S0})\sin(p(\theta-\theta_r)-\phi)\right. \\
&\quad \left. -\frac{(\Lambda_{N2}+\Lambda_{S2})}{2}\sin(p(\theta-\theta_r)+\phi)\right)
\end{aligned}
$$

$$
\begin{aligned}
\{B\}_1 &= \left(\begin{array}{c} F_{rN}\left(\Lambda_{N1}+\Lambda_{S1}\right) \\ -F_{s1}\left((\Lambda_{N0}+\Lambda_{S0})+\dfrac{(\Lambda_{N2}+\Lambda_{S2})}{2}\right)\sin(\phi) \end{array}\right)\cdot\cos(p\theta_r-p\theta) \\
&\quad +\left(F_{s1}\left((\Lambda_{N0}+\Lambda_{S0})-\frac{(\Lambda_{N2}+\Lambda_{S2})}{2}\right)\cos(\phi)\right)\cdot\sin(p\theta_r-p\theta)
\end{aligned}
$$

(A.89)

A.7.1.4 Homopolar Inductor Alternator Fundamental Flux Density

$$
\begin{aligned}
\{B\}_1 &= F_{rN}\Lambda_{N1}\cos(p(\theta-\theta_r)) \\
&\quad + F_{s1}\left(\Lambda_{N0}\sin(p(\theta-\theta_r)-\phi)-\frac{\Lambda_{N2}}{2}\sin(p(\theta-\theta_r)+\phi)\right) \\
\{B\}_1 &= \left(F_{rN}\Lambda_{N1}-F_{s1}\left(\Lambda_{N0}+\frac{\Lambda_{N2}}{2}\right)\sin(\phi)\right)\cos(p\theta_r-p\theta) \\
&\quad +\left(F_{s1}\left(\Lambda_{N0}-\frac{\Lambda_{N2}}{2}\right)\cos(\phi)\right)\sin(p\theta_r-p\theta)
\end{aligned}
$$

(A.90)

The relation

$$
A\cos(x)+B\sin(x)=\sqrt{A^2+B^2}\,\cos\left(x-\tan^{-1}\left(\frac{B}{A}\right)\right)
$$

(A.91)

is then applied from which the amplitude of the fundamental can be determined for each alternator.

A.8 Average Flux Densities

The average component of flux density exists only for the homopolar inductor alternator. The average component due to the field winding can be determined from the product of the fundamental MMF and permeance function.

For the inductor alternator,

$$\{B\}_0 = F_{rN}\Lambda_{N0} - F_{s1}\Lambda_{N1}\frac{\sin(\phi)}{2}$$ (A.92)

The flux density in the air gap is thus

$$B \cong \{B\}_0 + \{B\}_1$$ (A.93)

Appendix B. Optimization Flow Chart
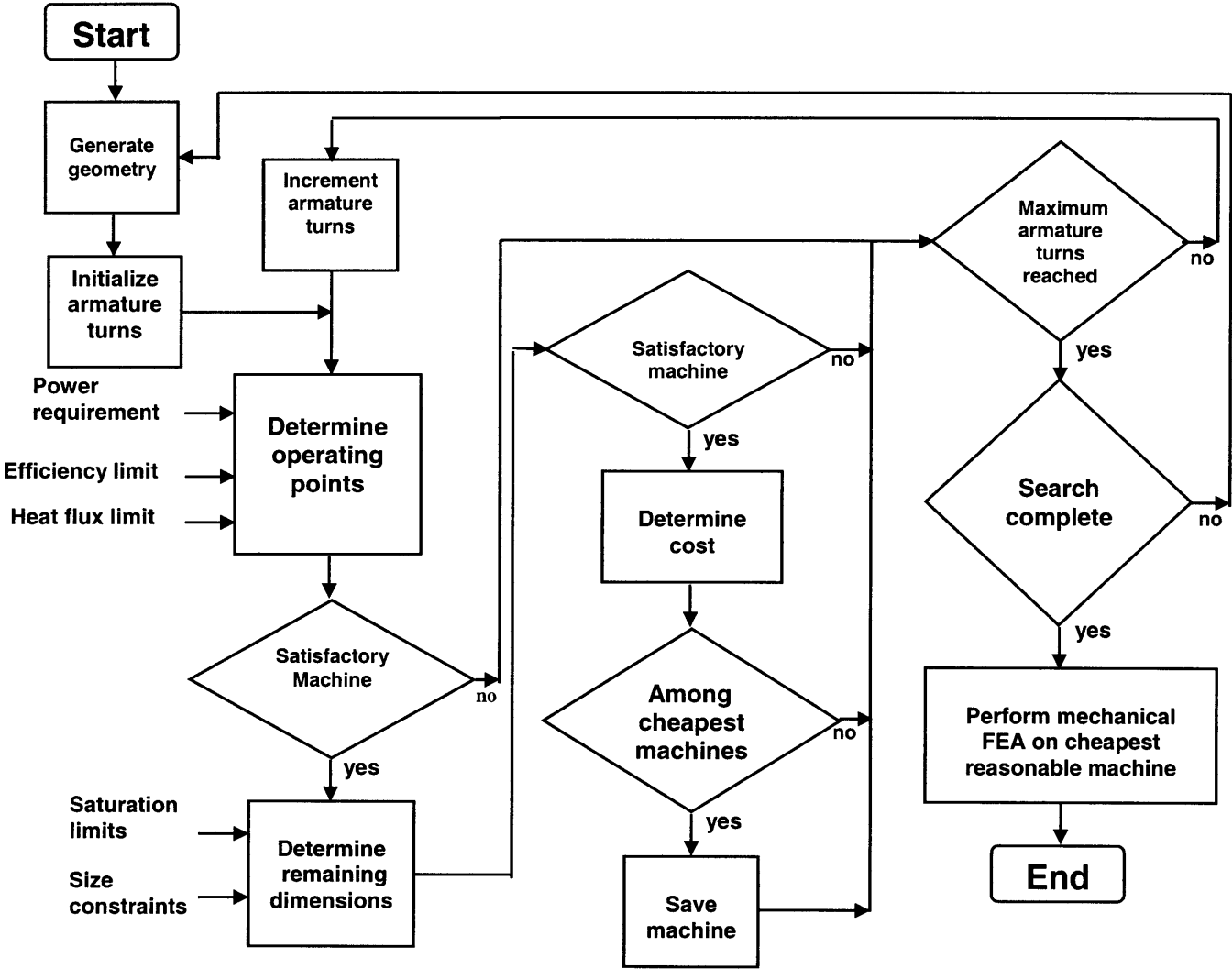
Figure B.1: Cost optimization flow chart

Appendix C. Fast Field De-excitation

C.1 Fast Field De-excitation Using Capacitor

Figure 3.1 from Chapter 3 is shown again below in Figure C.1. During steady state, the input command signal is high and the switch (MOSFET) is on. To simulate de-excitation via the capacitor, the input signal is quickly changed from high to low, which turns off the MOSFET. The current then flows through the diode and capacitor until it reaches zero, at which point it stays at zero because of the diode.
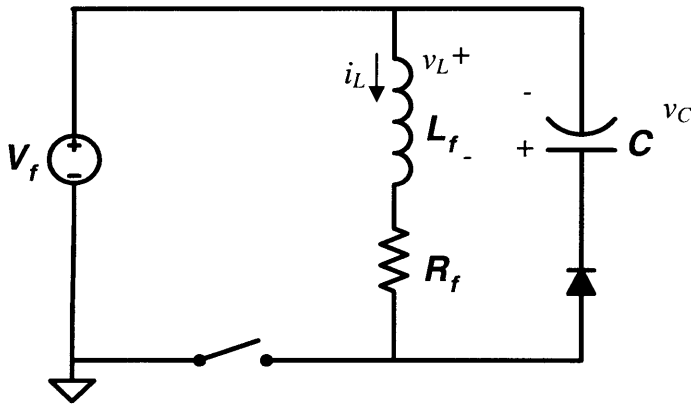
Figure C.1: Circuit for fast de-excitation of field winding using capacitor.

Ignoring the resistance R_f and the voltage drop across the diode, a circuit analysis is conducted to determine the field current. The initial conditions are

$$i_L(t = 0) = I_o \qquad \text{(C.1)}$$

$$v_L(t = 0) = 0 \qquad \text{(C.2)}$$

The following constitutive relations hold for the capacitor and inductor

$$v_L = L\frac{di_L}{dt} = -v_C \qquad \text{(C.3)}$$

$$i_C = C\frac{dv_C}{dt} = i_L \qquad \text{(C.4)}$$

A differential equation for the field current can be obtained

$$i_C = -CL\frac{d^2 i_L}{dt} = i_L \tag{C.5}$$

$$\frac{d^2 i_L}{dt} + \omega_o^2 i_L = 0 \tag{C.6}$$

where we let

$$\omega_o = \frac{1}{\sqrt{LC}} \tag{C.7}$$

The solution of the differential equation is of the form

$$i_L(t) = A\cos(\omega_o t) + B\sin(\omega_o t) \tag{C.8}$$

The initial conditions yield the values for A and B

$$i_L(t = 0) = A = I_o \tag{C.9}$$

$$v_L(t = 0) = LB\omega_o = 0 \tag{C.10}$$

$$B = 0 \tag{C.11}$$

Therefore

$$i_L(t) = I_o \cos\left(\frac{1}{\sqrt{LC}}t\right) \quad \text{for } 0 < t < \frac{\pi}{2}\sqrt{LC} \tag{C.12}$$

$$i_L(t) = 0 \quad \text{for } t > \frac{\pi}{2}\sqrt{LC} \tag{C.13}$$

The field current goes to zero after a quarter of a cycle. As the capacitor value is decreased, the time to zero will decrease. Therefore, the capacitor can be made very small to make the time to zero very short. In the actual experiment, L is the inductance of the field winding, and C was selected to be 1 μF. The voltage across the field winding was adjusted such that the steady state current prior to de-excitation, I_o was equal to 1 A. Figure C.2 below is a more detailed version of the circuit used for de-excitation via a capacitor.

196
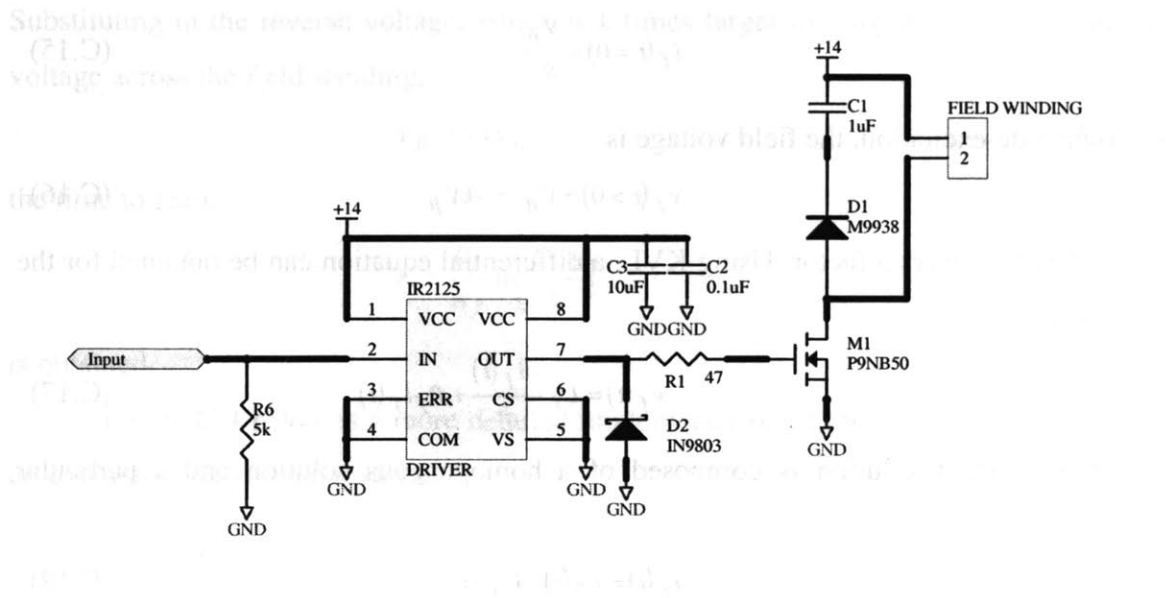
Figure C.2: Implementation of field de-excitation circuit using capacitor.

C.2 Fast Field De-excitation by Voltage Reversal

Following a voltage reversal across the field winding, the duration it takes for the field current to reach zero was given in Equation 3.1. Below is a detailed derivation of the time to zero.
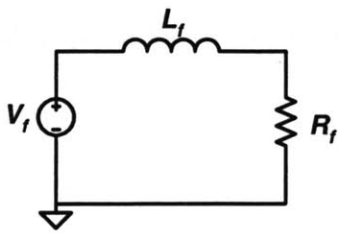
Figure C.3: Simple field winding model with applied voltage used which is reversed.

Initially, the field voltage is equal to

$$v_f(t=0) = V_{fi} \tag{C.14}$$

and the field current is

$$i_f(t = 0) = \frac{V_{fi}}{R_f} \qquad (C.15)$$

Following de-excitation, the field voltage is

$$v_f(t > 0) = V_{ff} = -kV_{fi} \qquad (C.16)$$

where k is the reversal factor. Using KVL, a differential equation can be obtained for the field current

$$v_f(t) = L_f \frac{di_f(t)}{dt} + R_f i_f(t) \qquad (C.17)$$

The field current solution is composed of a homogeneous solution and a particular solution

$$i_f(t) = i_{fh}(t) + i_{fp}(t) \qquad (C.18)$$

To determine the homogeneous solution, let

$$i_{fh}(t) = Ae^{st} \qquad (C.19)$$

And substituting into the differential equation with the input voltage equal to zero,

$$0 = L_f \frac{di_f}{dt} + R_f i_f \qquad (C.20)$$

we obtain a homogeneous solution of the form

$$i_{fh}(t) = Ae^{\frac{-R_f}{L_f}t} \qquad (C.21)$$

The particular solution is obtained by setting the derivative of the field current equal to zero

$$i_{fp}(t) = \frac{V_{ff}}{R_f} \qquad (C.22)$$

Using the initial condition,

$$i_f(t) = \frac{V_{fi} - V_{ff}}{R_f} e^{\frac{-R_f}{L_f}t} + \frac{V_{ff}}{R_f} \qquad (C.23)$$

Solving for the time at which the field current is zero

$$t_z = \frac{L_f}{R_f} \ln\left(\frac{V_{ff} - Vi}{V_{ff}}\right) \qquad (C.24)$$

Substituting in the reverse voltage, which is k times larger in magnitude than the initial voltage across the field winding,

$$V_{ff} = -kV_{fi}$$

(C.25)

the time to zero,

$$t_z = \frac{L_f}{R_f} \ln\left(\frac{k+1}{k}\right)$$

(C.26)

is obtained.

Figure C.4 below is a more detailed implementation of the bridge circuit used for de-excitation via voltage reversal.
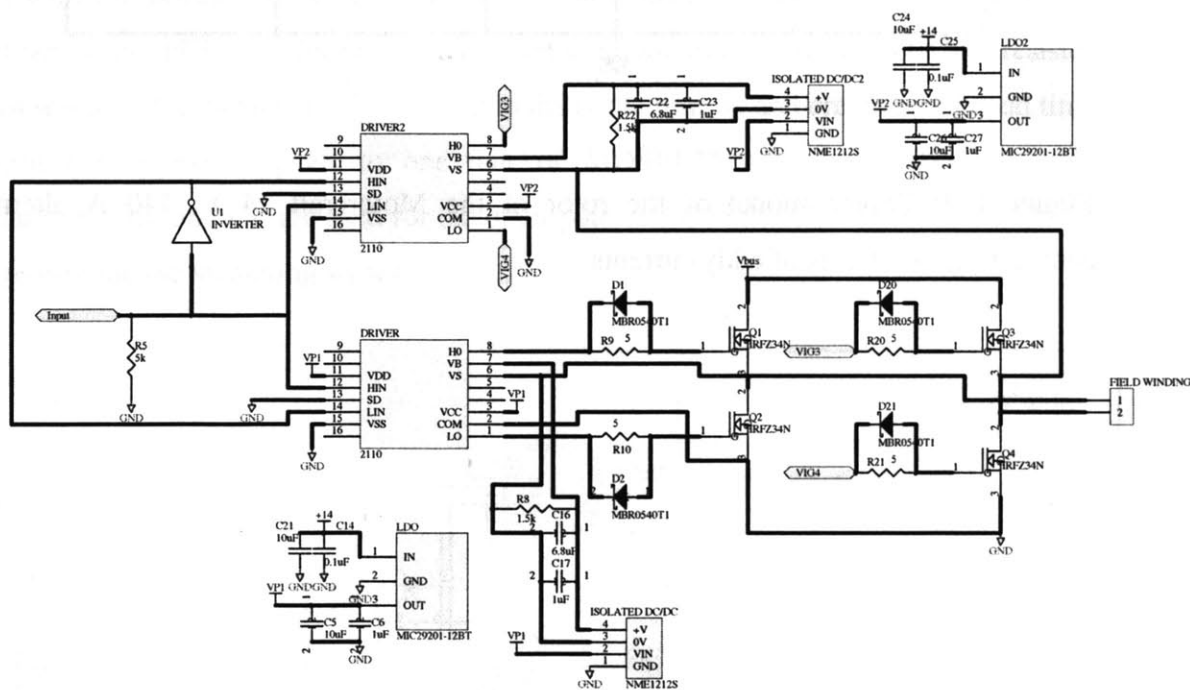
Figure C.4: Detailed model of circuit used for reversal of field voltage using a bridge.

C.3 PSpice Rotor Model

Below is the PSpice model of the rotor. The three branches on the right are used to model the effects of the eddy currents which extend the duration of the overvoltage.

199
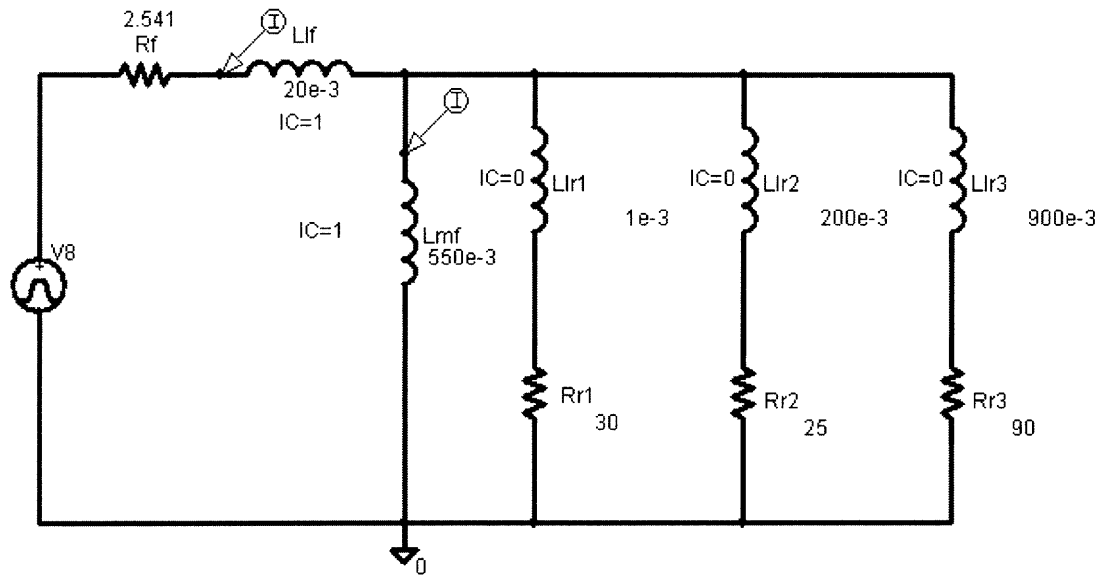
Figure C.5: PSpice model of the rotor of the Motorcraft 14 V, 140 A alternator considering the effects of eddy currents

Appendix D. Rotating Transformer Topology

D.1 PCB Transformer Circuit

This appendix covers in more detail the contactless field excitation circuit described in Chapter 6. This design utilizes an air core printed circuit board transformer with a stationary primary and rotating secondary. The stationary side of the PCB transformer circuit is shown below in Figure D.1. The circuit is essentially a full-bridge inverter with four IRFZ44N MOSFETS driven by two IR2110 drivers . A bus capacitor of 294 µF (C_{34}, C_{35}, C_{38}, C_{39} in parallel) is used to stabilize the bus voltage. A parallel combination of capacitors equivalent to 62 µF (C_{30}, C_{33}, C_{36}, C_{37} in parallel) is placed in series with the primary winding of the PCB transformer in order to prevent any DC offset across the PCB transformer. The parallel combination of a diode (D_3) and resistor (R_6) in series with a capacitor (C_{12}) is used to delay the turn on and create some dead time between the opposite signals to one pair of MOSFETS to prevent shoot-through. Similarly, D_4, R_7, and C_{13} are used for the other pair. A UC3824 pulse width modulator is used to provide the switching signal.
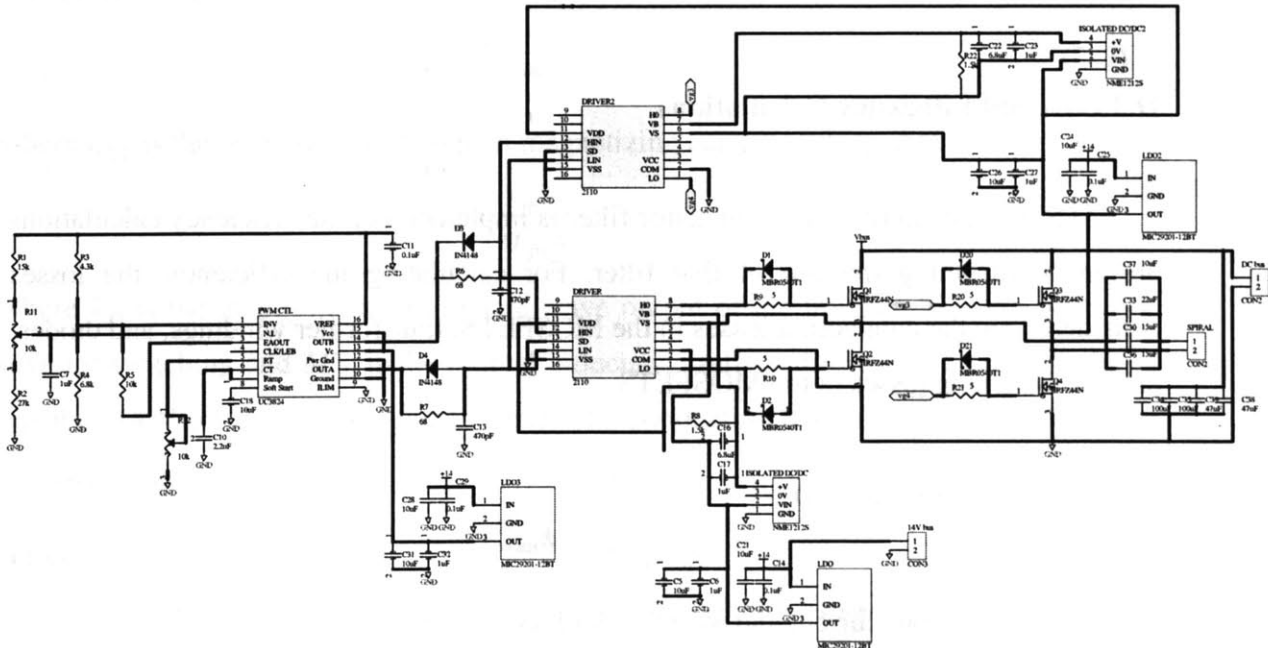
Figure D.1: PCB transformer circuit, stationary side.

The rotating side of the PCB transformer circuit is shown below in Figure D.2. Four 40L15CT Schottky diodes are placed on the rotating side and form the rectifier that provides a DC current to the field winding. A 10uF ITW CS4 CAPSTICK film capacitor is used as the filter to hold the voltage at the rectifier output approximately constant over a switching cycle.
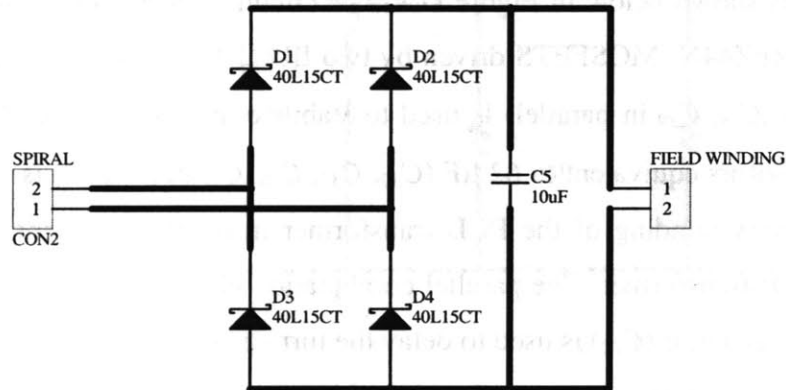
Figure D.2. PCB transformer circuit, rotating side.

D.2 Loss and Efficiency Calculations

Since the circuit with a capacitor filter is implemented, the efficiency calculations are made assuming the use of that filter. For calculating the efficiency, the losses considered are the conduction losses in the MOSFETS, transformer windings, and diodes, and the switching losses in the MOSFETS.

The output power is equal to

$$P_o = I_o^2 R_f \tag{D.1}$$

where I_o is the output current and R_f is the field winding resistance.

The diode losses are equal to

$$P_d = 2V_d I_o \tag{D.2}$$

where V_d is the diode drop. This is obtained assuming the field current is always flowing through a pair of diodes. The transformer secondary winding losses are equal to

$$P_{\text{sec}} = \frac{I_s^2 R_s}{2} \tag{D.3}$$

where I_s is the magnitude of the fundamental component of the current through the secondary winding. The transformer primary winding losses are equal to

$$P_{prim} = I_{prms}^2 R_p \tag{D.4}$$

where I_{prms} is the rms of the primary winding current which is composed of the reflected secondary current and the fundamental component of the magnetizing current.

$$I_{prms} = \frac{\sqrt{I_p^2 + I_m^2}}{\sqrt{2}} \tag{D.5}$$

The reflected or ideal primary winding current is

$$I_p = \frac{N_p}{N_s} I_s \tag{D.6}$$

and the magnitude of the fundamental of the magnetizing current (assumed to be triangular wave) is

$$I_m = \frac{8}{\pi^2} I_{mpp} \tag{D.7}$$

where I_{mpp} is the peak to peak change in magnetizing current and equal to

$$I_{mpp} = \frac{V_m T}{M'_{ps} 4} \tag{D.8}$$

where V_m is the amplitude of the square wave output of the inverter, T is the period of inverter switching and M'_{ps} is the mutual inductance reflected to the primary side. V_m is equal to 14 V for the full-bridge converter. The conduction loss of each MOSFET in the inverter is equal to

$$P_{tcon} = I_{prms}^2 k_t R_{DSon} \tag{D.9}$$

where k_t is a coefficient that increases with temperature and R_{DSon} is the drain to source on resistance of the MOSFET.

The switching loss calculations were taken from [28,29]. The turn off losses can be calculated by multiplying the energy lost per turn off by the switching frequency.

There are two dominant switching losses during turn-off. The first occurs when the parasitic capacitance, C_{gd}, between the gate and the drain begins to charge. Based on [28,29], that loss is equal to

$$E_{bc} = \frac{2I_{pk}K_{gd}(V_{bus})^{3/2}}{3I_{drive}}$$ (D.10)

where I_{drive} is the drive current, I_{pk} is the peak drain current, and V_{bus} is the bus voltage of 14 V. K_{gd} can be calculated as C_{rss} multiplied by the square root of the voltage at which it was measured, which can be obtained from the datasheet. The other significant turn-off loss occurs during that time for the current to overcome the inductance in the leads and discharge the gate to source capacitance C_{gs} [28,29]. The duration of this interval is the time it takes for the gate-source voltage to decrease from the saturation voltage V_{SAT} to the threshold voltage V_T. The loss in this period is equal to

$$E_{dc} = \frac{t_{dc}V_{bus}I_{pk}}{2}$$ (D.11)

where the duration of the time interval is

$$t_{dc} = T_2 + \frac{C_{gs}\left(V_{sat}\cos\left(\frac{T_2}{\sqrt{L_s C_{gs}}}\right) - V_T\right)}{I_{drive}}$$ (D.12)

$$T_2 = \sqrt{L_s C_{gs}}\,\sin^{-1}\left(\frac{I_{drive}}{V_{sat}}\sqrt{\frac{L_s}{C_{gs}}}\right)$$ (D.13)

where L_s is the lead inductance, and C_{gs} is the gate source capacitance:

$$C_{gs} = \frac{Q_g}{V_g}$$ (D.14)

where Q_g is the charge on the gate when a voltage V_g is put across it. The total turn-off losses are equal to

$$P_{off} = (E_{cb} + E_{dc})f_{sw}$$ (D.15)

where f_{sw} is the switching frequency.

Since only rough approximations for the switching losses are being made, the turn-on losses are assumed to be equal to the turn-off losses and therefore the total switching losses can be assumed to be twice the turn-off losses

$$P_{tsw} \approx 2P_{off} \qquad\qquad (D.16)$$

The total power loss is the sum of all the conduction and switching losses:

$$P_L = P_d + P_{sec} + P_{prim} + P_{tcon} + P_{tsw} \qquad\qquad (D.17)$$

The efficiency is equal to the output power divided by the input power

$$\eta = \frac{P_o}{P_i} \qquad\qquad (D.18)$$

where the input power is equal to the sum of the output power and the losses.

$$P_i = P_o + P_L \qquad\qquad (D.19)$$

Appendix E. Rotating DC/DC Converter Topology

E.1 Frequency Modulation (FM) Circuit

The circuit used for the DC/DC converter employing FM modulation to transmit the error signal or duty ratio is shown in Figure E.1. The TL5001 is a PWM controller which produces the error signal that dictates the required duty ratio. Its internal op amp is used to produce an output range from 0.7 V to 1.3 V. For open loop control, the components R_1 (100 kΩ), R_2 (5.1 kΩ), R_{25} (5 kΩ potentiometer), and R_5 (15 kΩ) are selected to produce this output range. The OPA2244 contains two op amps and sets an adjustable maximum and minimum limit on the error voltage and therefore, on the duty ratio, using the associated resistors. The error level corresponding to the required duty ratio of the MOSFET is used to frequency modulate the sinusoid that is transmitted to the rotating side through the brushes and power bus. The sinusoid frequency ranges from 152 kHz to 167 kHz, which corresponds to the entire range of duty ratios from 1 down to 0. A linear relation holds between the frequency of the transmitted sinusoid and the error level or duty ratio:

$$f_t = f_{ot} + K_{ot}(V_c - V_{kt})$$ (E.1)

where f_t is the frequency of the transmitted sinusoid

$$f_{ot} = \frac{1}{R_{10}C_{12}}$$ (E.2)

is the center frequency

$$K_{ot} = \frac{-1}{3R_9C_{12}}$$ (E.3)

is the gain of the voltage controlled oscillator in the transmitter and

$$V_{kt} = 3 \text{ V}$$ (E.4)

is a constant voltage offset. The error level or duty ratio is represented by V_c. The resistances R_{10} (R in datasheet) and R_9 (R_c in datasheet) have values of 9.1 kΩ and 13.3 kΩ, respectively, and the capacitance C_{12} (C in datasheet) has value 1 nF. When V_c equals 1.3 V, the sinusoid assumes the minimum frequency 152 kHz corresponding to the duty ratio of 1. A voltage level V_c of 0.7 V corresponds to the maximum transmitted frequency of 167 kHz and a duty ratio of 0. The duty ratio of 0.5 corresponds to a voltage of 1 V

and frequency of 160 kHz. The BUF634 chip is used as a buffer and has a low output impedance of 10 Ω compared with the output impedance of the XR2206 chip of 600 Ω. On the stationary side, 12 V regulators are used to provide steady voltages to the various chips. Connected to the DC bus V_{BUSS} is a series combination of two inductors (L_3 and L_4 in the schematic) that serve to isolate the power supply from the transmitted control signal. The capacitor C_{21} is used for DC blocking purposes. On the rotating side, the inductors L_1 and L_2 and the capacitors C_{23} (a to e) form the filter that isolates the switching currents from the received control signal.
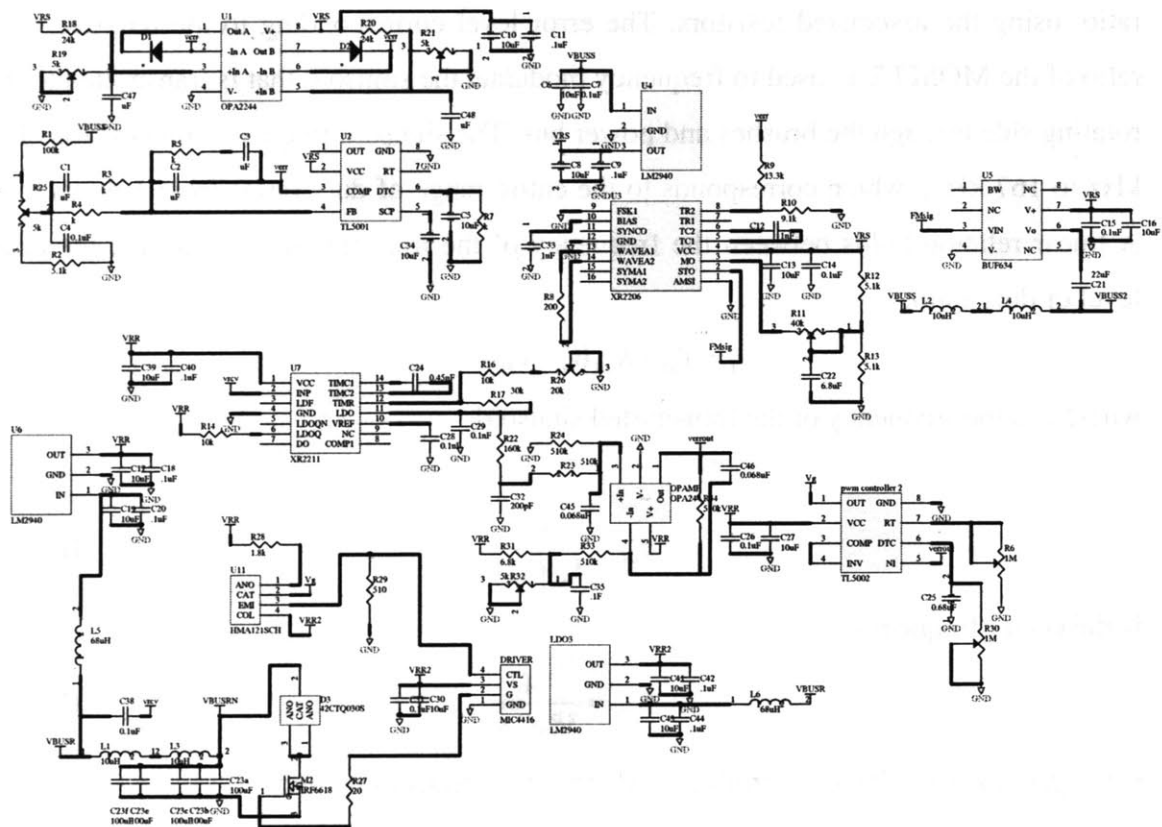
Figure E.1: Schematic of circuit used for FM modulation.

The receiver uses the transmitted sinusoid as the input to a phase locked loop. When in lock, the frequency of the output signal of the phase locked loop is equal to that of the input. The output of the VCO of the phase locked loop has a frequency of

$$f_r = f_{or} + K_{or}\left(V_p - V_{kr}\right) \tag{E.5}$$

where

$$f_{or} = \frac{1}{(R_{16} + R_{26})C_{24}} \qquad (E.6)$$

is the center frequency and

$$K_{or} = \frac{-1}{V_{kr}C_{24}R_{17}} \qquad (E.7)$$

is the gain of the VCO. In the circuit schematic, R_{16} plus R_{26} (R_0 in the datasheet) has value 13.9 kΩ, C_{24} (C_0 in the datasheet) has value 0.45 nF, and R_{17} (R_1 in the datasheet) has value 30 kΩ. These are used to have the center frequency at 160 kHz and gain such that as the incoming signal frequency varies from 152 kHz to 167 kHz, the DC value of the phase detector output varies over 0.6 volts. The voltage at the output of the phase detector is filtered through $F_2(s)$ to remove the output of the phase detector whose frequencies are composed of the sum of the input and VCO output frequencies (twice the input frequency when in lock). The output of the filter has a value of

$$V_p = \frac{f_r - f_{or}}{K_{or}} + V_{kr} \qquad (E.8)$$

When in lock, the frequency of the output of the VCO equals that of the input signal

$$f_r = f_t \qquad (E.9)$$

and therefore

$$V_p = \frac{f_{ot} - f_{or}}{K_{or}} + V_{kr} - \frac{K_{ot}}{K_{or}}V_{kt} + \frac{K_{ot}}{K_{or}}V_c \qquad (E.10)$$

If the receiver VCO gain K_{or} is selected to equal the VCO gain K_{ot} of the FM modulator, then

$$V_p = \frac{f_{ot} - f_{or}}{K_{or}} + V_{kr} - V_{kt} + V_c \qquad (E.11)$$

where the filtered output of the phase detector V_p is a linear function of the error voltage, V_c. If f_{or} or the center frequency of the receiver is selected as

$$f_{or} = f_{ot} + K_{ot}(V_{cmid} - V_{kt}) \qquad (E.12)$$

that is, f_{or} is equal to the midpoint of the transmit frequency range (160 kHz), then

$$V_p = V_{kr} - V_{cmid} + V_c \qquad (E.13)$$

$$V_{kd} = V_{kr} - V_{cmid} \qquad (E.14)$$

$$V_p = V_{kd} + V_c \qquad (E.15)$$

In the particular case of the circuit, V_{kr} = Vcc/2 –650 mV = 3.35 V and V_{cmid} = 1 V. This will facilitate locking of the PLL. In addition, a minimum capture range is required if the center or free-wheeling frequency of the PLL is equal to the midpoint of the frequency range that it receives. As indicated earlier, the output of the phase detector is low pass filtered using $F_2(s)$ to remove the component whose frequency twice the input frequency, when in lock. This filter is a simple first-order RC lowpass filter. V_p is simply the sum of V_c and a constant. A subtractor can be used to subtract the offset to get V_{cout} which should exactly follow the error voltage V_c and ranges from 0.7 to 1.3 volts. To implement the subtractor, an OPA244 op amp was utilized. The value of the error signal V_{cout} is compared with a sawtooth waveform and yields the rectangular wave input signal to the gate of the MOSFET. Note that an additional filter $F_2(s)$ was used and V_p was not obtained at the output of $F(s)$ for additional flexibility. This is due to trade-offs between the parameters of $F(s)$ and the dynamics of the phase locked loop.

The phase locked loop of the receiver block diagram is shown in figure E.2. Using Black's Formula, the closed loop transfer function from the input phase to the output phase is:

$$\frac{\theta_o(s)}{\theta_i(s)} = \frac{K_d F(s)\dfrac{K_o}{s}}{1 + K_d F(s)\dfrac{K_o}{s}} \qquad (E.16)$$

where

$$F(s) = \frac{1}{1 + sR_1C_1} \qquad (E.17)$$

is the transfer function of the low pass filter. The phase detector gain is

$$K_d = \frac{V_{kr}R_1}{5000}\left(\frac{V}{Hz}\right) \qquad (E.18)$$

and the voltage controlled oscillator (VCO) gain is

$$K_o = -\frac{1}{V_{kr}C_oR_1}\left(\frac{Hz}{V}\right) \qquad (E.19)$$

Substituting equations E.17, E.18, and E.19 into E.16, the closed loop system function is

210

$$\frac{\theta_o(s)}{\theta_i(s)} = \frac{\dfrac{K_d K_o}{R_1 C_1}}{s^2 + \dfrac{1}{R_1 C_1}s + \dfrac{K_d K_o}{R_1 C_1}} \tag{E.20}$$

which is a typical second-order system with the form

$$H(s) = \frac{\omega_n^2}{s^2 + 2\xi\omega_n s + \omega_n^2} \tag{E.21}$$

Matching parameters, the natural frequency of the system is

$$\omega_n = \sqrt{\frac{1}{5000 C_o R_1 C_1}} \tag{E.22}$$

and the damping ratio is

$$\xi = \sqrt{\frac{1250 C_o}{R_1 C_1}} \tag{E.23}$$

Therefore ω_n is selected to be 3.85×10^5 rad/s for a sufficiently fast enough response and ξ is selected to be 0.44 in order to not have excessive peaking or overshoot but at the same time have the cut-off frequency of the lowpass filter $F(s)$ be low enough to attenuate the higher frequency content of the output of the phase detector that is composed of the sum of the input frequency f_t and the output of the VCO f_r, which is twice f_t assuming the PLL is in lock.
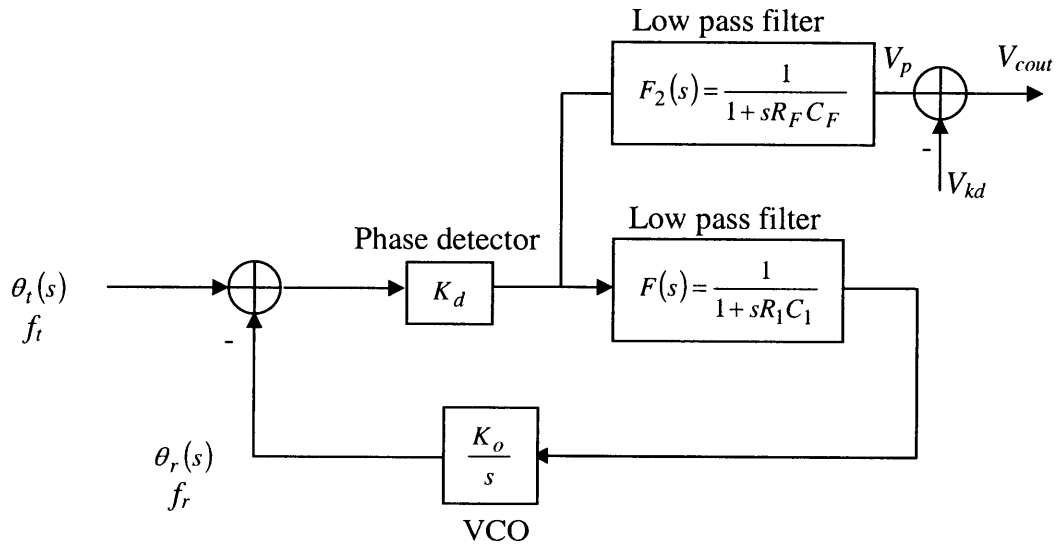
Figure E.2: Block diagram of phase locked loop used in FM demodulator.

Another component on the rotating side is the HMA121SCH optocoupler. This was used in order to isolate the ground plane in the area of the switching with the ground plane associated with the communications circuitry.

E.2 DC/DC Converter printed circuit board
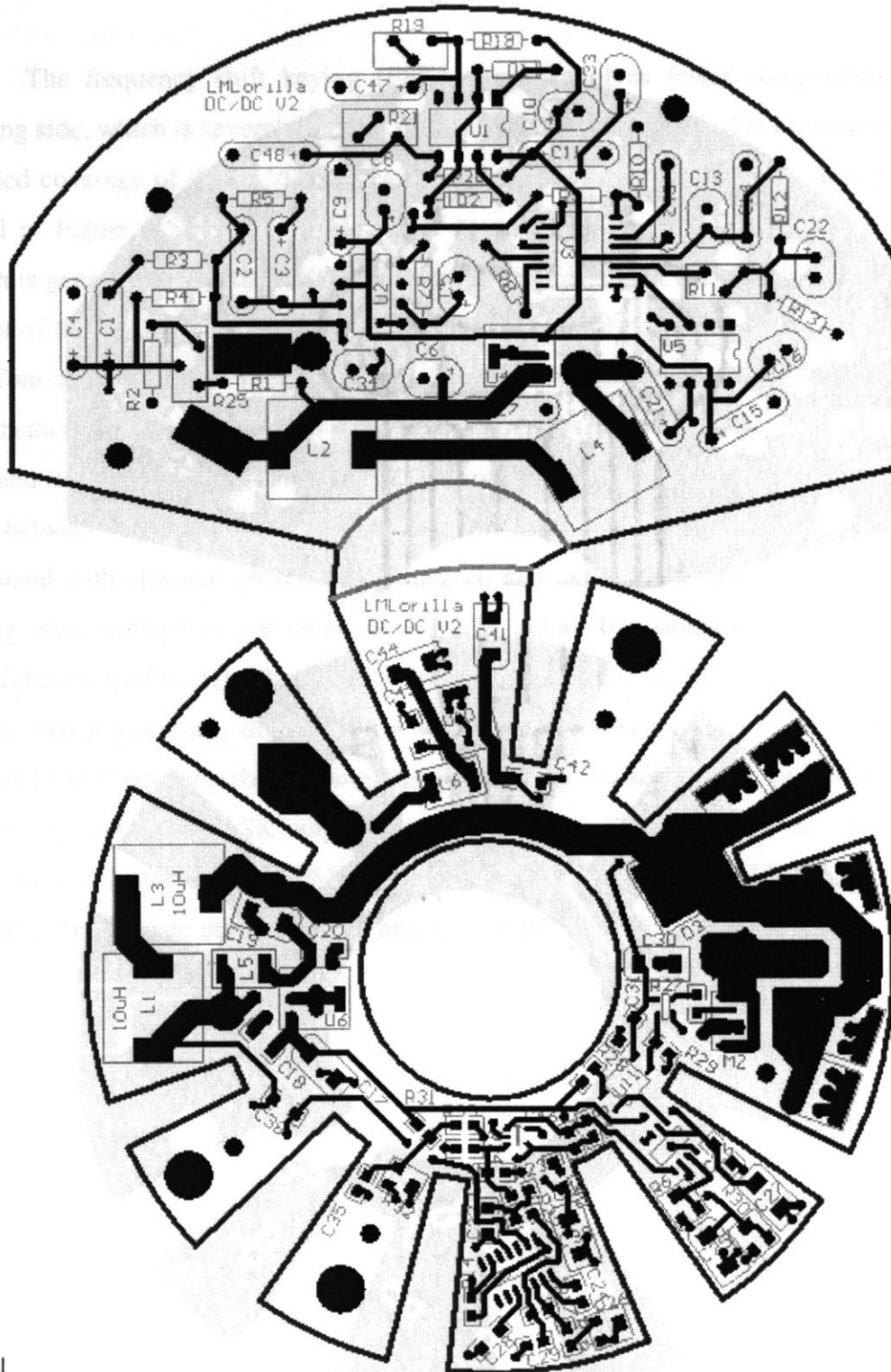
Figure E.3: DC/DC Converter with FM modem (top Layer)
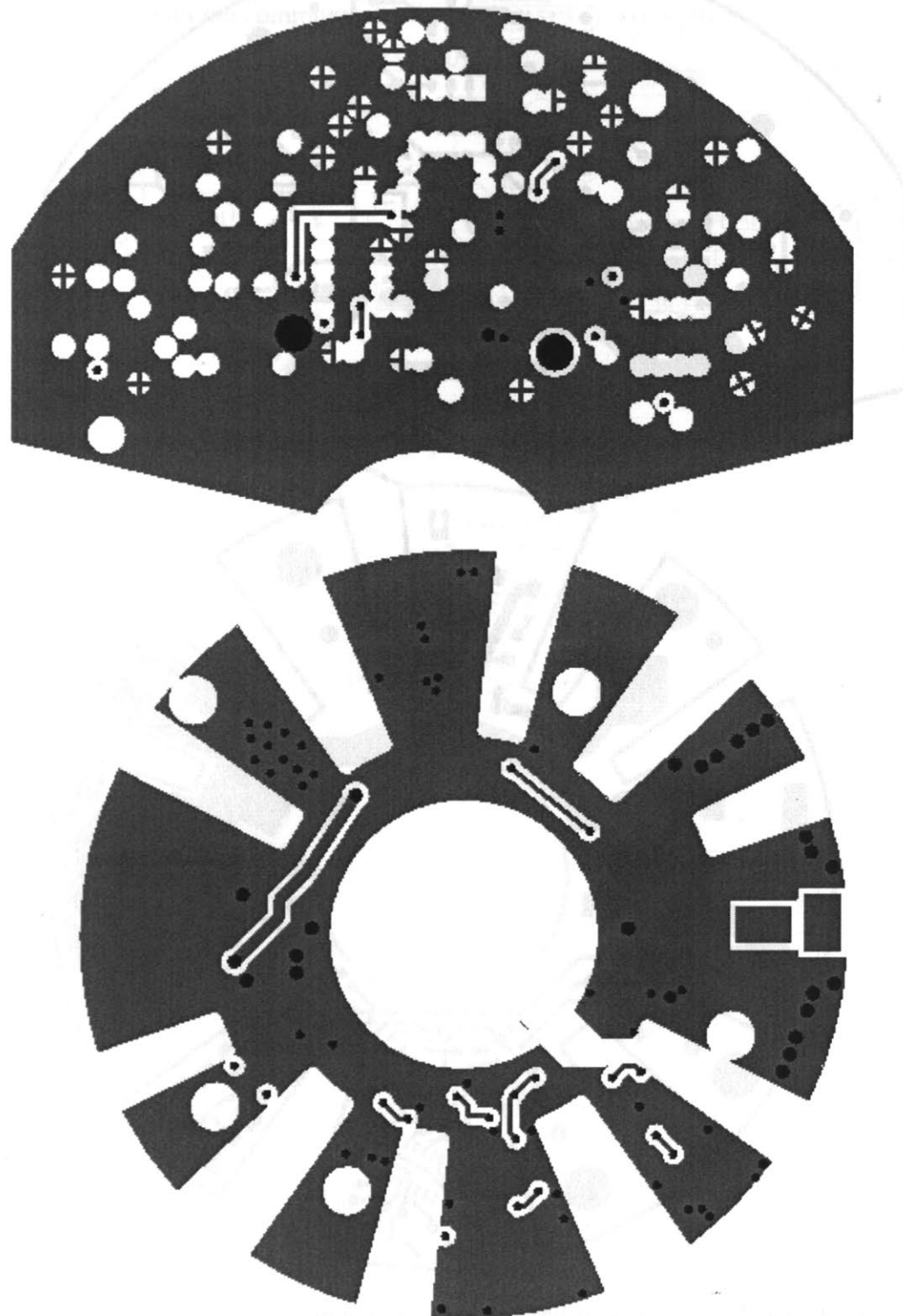
Figure E.4: DC/DC Converter with FM modem (bottom layer)

E.3 DC/DC Converter with FSK Communications

The frequency shift keying (FSK) circuit involves fewer components on the rotating side, which is severely limited in terms of allowable space. This section is a more detailed coverage of the DC/DC converter utilizing an FSK modem. The circuit can be found in Figure E.5. The frequency shift keying (FSK) method uses the gate signal, which is generated by pulse width modulating the error signal between the voltage at the output of the rectifier and a reference voltage. The gate signal will be a digital signal and therefore, the transmitted signal will be a sinusoid at either of two frequencies, depending on whether a high or low signal is being communicated. The amplifier A_1 in the upper left, and its associated input and feedback circuit, produces a signal proportional to the error between the voltage V_{DC}, produced by the generator stator, and a reference voltage, combined with classical proportional, integral, and derivative (PID) compensation. The analog error voltage is converted to a PWM signal by comparing it to a sawtooth waveform (amplifier A_2). The PWM waveform is a digital signal which is converted to one of two frequencies, depending on whether the PWM signal is high or low, by a special FSK (frequency-shift keying) modulator chip. A_3 serves as a buffer with a low output impedance. The FSK output is sent to the field circuit through the DC blocking capacitor C_2. On the rotor, an FSK demodulator recreates the digital PWM signal, which is used to drive a gate drive amplifier and operate the MOSFET.
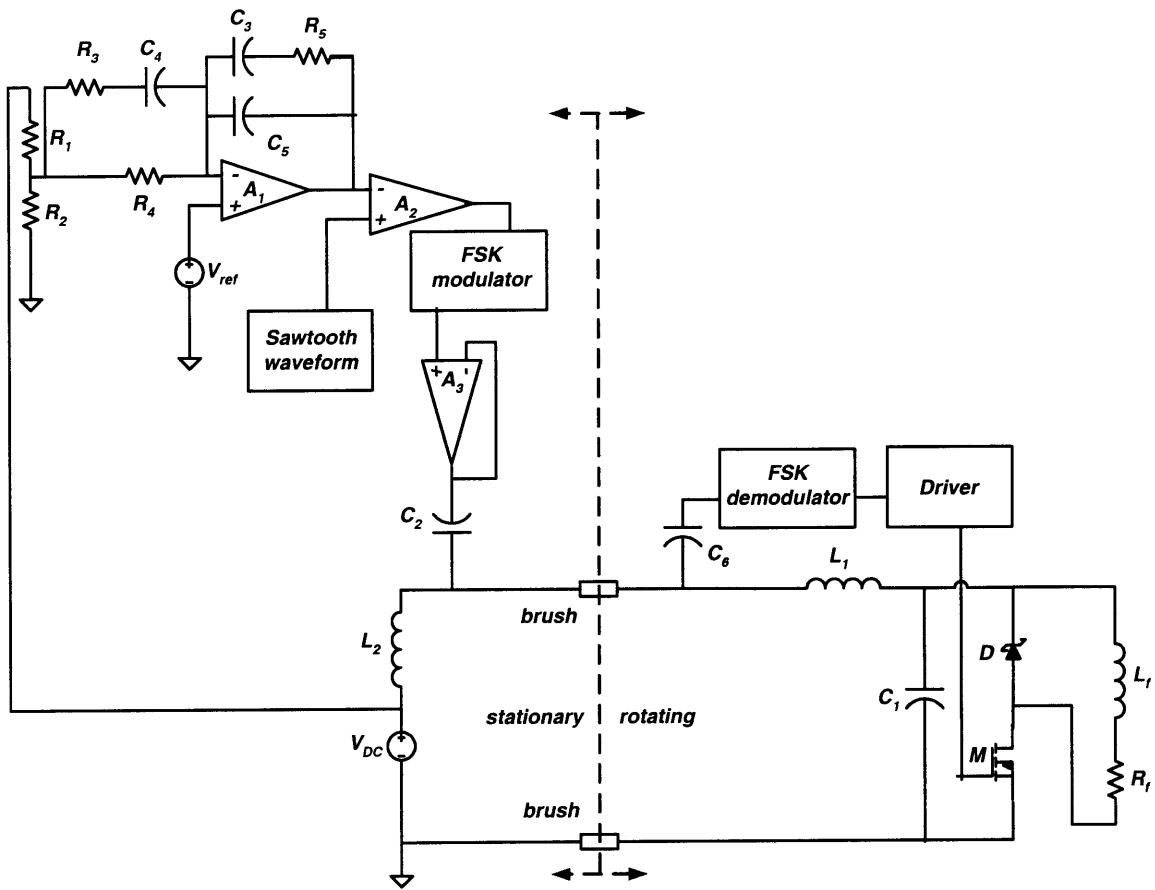
Figure E.5: Detailed FSK modulation circuit.

For illustration purposes, a possible signal command and the corresponding transmitted FSK signal are shown in Figures E.6 and E.7 respectively.
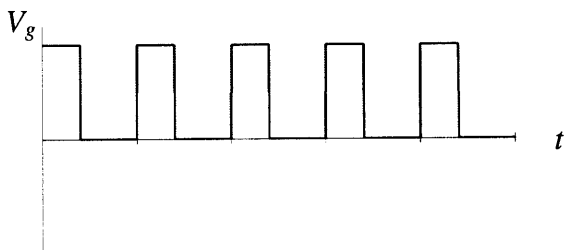
Figure E.6: Gate signal command.
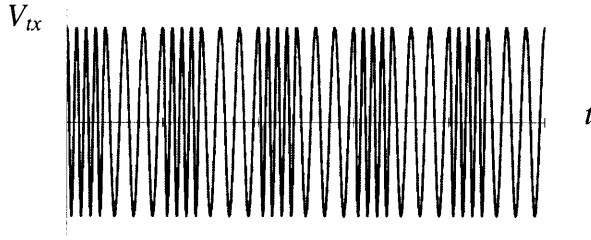
Figure E.7: Frequency shift signal transmitted.

The waveform is to be sent through the brushes and received on the rotating side by an FSK demodulator. An accurate decision has to be made on which logic level was sent despite the switching noise. Since only two frequencies are used, they can be spaced sufficiently far apart to be easily distinguishable.

To facilitate the design and determine the necessary operating conditions as well as the circuit components, a time-domain and frequency domain analysis of the FSK system was conducted. The transmitted time-domain signal was generated and is shown in Figure E.9 where the frequencies sent were 232 and 121 kHz. The transmitted waveform can be expressed mathematically as:

$$v_{tx}(t) = v_{txm}\left(r_H(t)\cos(\omega_H t) + r_L(t)\cos(\omega_L t)\right)$$ (E.24)

where

$$r_H(t) = r(t)$$ (E.25)

$$r_L(t) = 1 - r(t)$$ (E.26)

and v_{txm} is the amplitude of the carrier sinusoid, ω_H is the carrier frequency for a high level and ω_L is the carrier frequency for a low level. The waveform $r(t)$ is shown in Figure E.8. Since $r_H(t)$ is periodic, a Fourier series representation of it can be obtained.

$$r_H(t) = \sum_{m=-\infty}^{\infty} a_m e^{jm\omega_0 t}$$ (E.27)

The Fourier transform of $r_H(t)$ is

$$R_H(j\omega) = \sum_{m=-\infty}^{\infty} 2\pi a_m \delta(\omega - m\omega_0)$$ (E.28)

where the Fourier series coefficients a_m are

$$a_m = \frac{1}{m\pi}\sin(m\omega_0 T_1)$$ (E.29)

217

And since

$$\omega_0 = \frac{2\pi}{T} \qquad (E.30)$$

$$T_1 = \frac{DT}{2} \qquad (E.31)$$

the Fourier series coefficients can be expressed as

$$a_m = \frac{1}{m\pi}\sin(m\pi D) \qquad (E.32)$$

$$a_0 = D \qquad (E.33)$$

The Fourier transform $R_H(j\omega)$ is composed of samples of a sinc function where the impulses are located ω_0 apart, which is the switching frequency in radians per second and decay as the magnitude of the frequency increases. Referring to equation (E.26), the Fourier transform of $r_L(t)$ is

$$R_L(j\omega) = 2\pi\delta(\omega) - R_H(j\omega) \qquad (E.34)$$

The magnitude of the Fourier transform of $R_L(j\omega)$ is therefore identical to that of $R_H(j\omega)$ except at zero frequency where

$$R_L(j0) = 2\pi\delta(\omega) - R_H(j0) \qquad (E.35)$$

Since the Fourier transform of $\cos(\omega_H t)$ is composed of impulses at $+/-\omega_H$ (and similarly for $\cos(\omega_L t)$), the Fourier transform of the transmitted signal is

$$V_{tx}(j\omega) = \frac{v_{txm}}{2}\left(R_H\left(j(\omega-\omega_H)\right) + R_H\left(j(\omega+\omega_H)\right) + R_L\left(j(\omega-\omega_L)\right) + R_L\left(j(\omega+\omega_L)\right)\right) \qquad (E.36)$$

Therefore the Fourier transform of the transmitted/modulated signal is composed of shifted copies of the spectra of $R_H(j\omega)$ and $R_L(j\omega)$ to plus or minus their respective carrier frequencies, i.e. $+/-\omega_H$,$+/-\omega_L$ respectively . Both spectra decay away from their carrier frequencies as samples of sinc functions. The magnitude of the Fourier transform of the modulated signal is shown in Figure E.10. For FSK transmission with a constant duty ratio, the Fourier transform of the modulated signal consists of impulses at each of the two carrier frequencies and at multiples of the modulating (switching) frequency away from the carrier frequency that decay away as sinc functions.
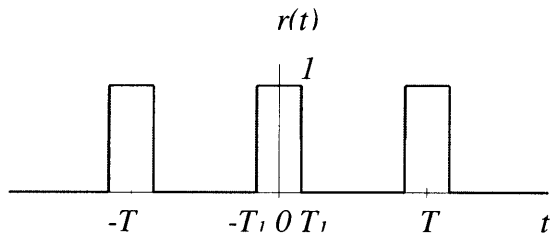
Figure E.8: FSK modulation of command signal.
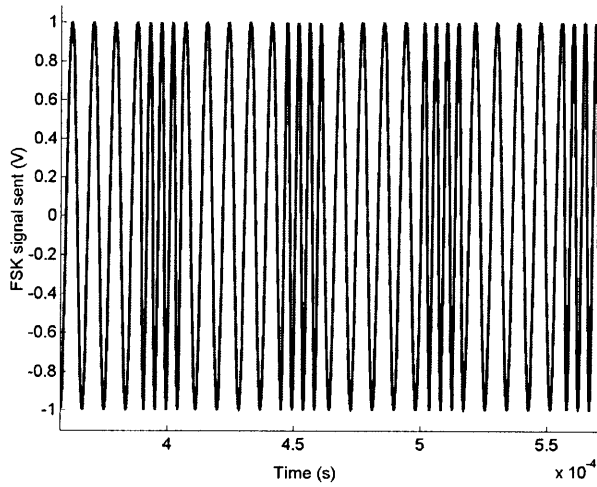
Figure E.9: FSK modulation of command signal.
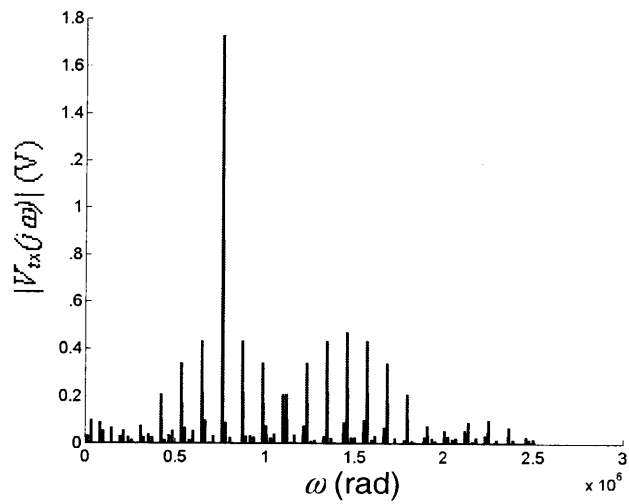
Figure E.10: Spectrum of FSK modulated signal.
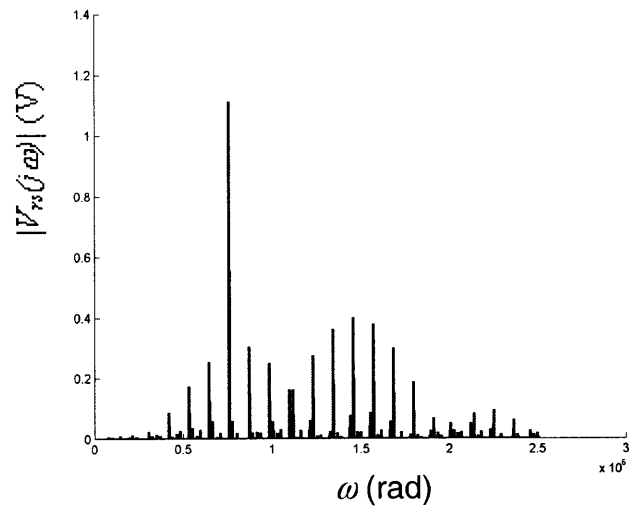
Figure E.11: Spectrum of FSK signal at receiver.
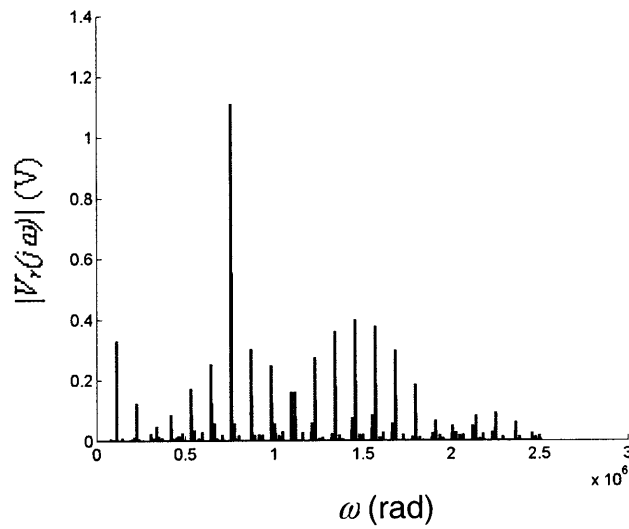
Figure E.12: Spectrum of voltage at receiver due to FSK signal and switching current.

An analysis of the spectra of the various signals is conducted. The switching frequency is 18 kHz. For experimental purposes, the gate command is set at a constant duty ratio of 0.3 (run open-loop). The frequencies corresponding to a high and low level of the MOSFET control (gate) signal are at 232 kHz and 121 kHz, respectively. The peaks occur at 232 kHz and 121 kHz and at multiples of the switching (modulating) frequency of 18 kHz away from them. The low level has a carrier sinusoid at a frequency of 121 kHz. Its part of the spectrum is composed of the peak at 121 kHz and the nearby peaks, analyzed earlier as the shifted version of $R_L(j\omega)$. Similarly, for a high level, its part of the spectrum is the peak of 232 kHz and the peaks close to it, analyzed earlier as the shifted version of $R_H(j\omega)$.

A similar analysis for the noise spectra is performed as in Chapter 7. The plots in the frequency domain due to combined spectra of the transmitted FSK signal and the noise signal is shown in Figure E.12. The objective is to maximize V_{rs} and minimize V_{rn} in the frequency range used by the FSK receiver. This can be seen as maximizing the signal to noise ratio. The phase locked loop demodulator must have a lock range wide enough to include both the mark and space frequencies and the larger sidebands. However, it must not be too large such that the PLL could lock onto noise which occurs at the switching frequency and its harmonics.

Experiments were first conducted without loading the circuit to see whether the gate signals could be modulated, transmitted and demodulated. As stated earlier, the desired switching frequency was 18 kHz. However, due to limitations in the phase-locked loop circuitry, it had to be reduced significantly. The main limitation was the speed at which the phase locked loop could track the step changes in frequency which correspond to transitions in the gate signal from high to low and vice versa. The settling time or the time it takes before the FSK system can track an input signal was a significant part of the switching signal period at 18 kHz. Therefore, the switching frequency had to be reduced. At switching frequencies beyond 5 kHz, the modem could not respond at a desirable rate due to limitations in terms of settling time. The switching frequency was therefore lowered to 3.4 kHz and the results are shown in Figures E.13 and E.14, which are the command signal and demodulated signal, respectively. The results had larger delays relative to the switching period when the switching frequency was increased. That is, the

delays covered a larger fraction of the source signal period. Due to this limitation in tracking high frequency step changes in frequency, the FM modulation technique is more suitable for the communications specifications of this particular converter.
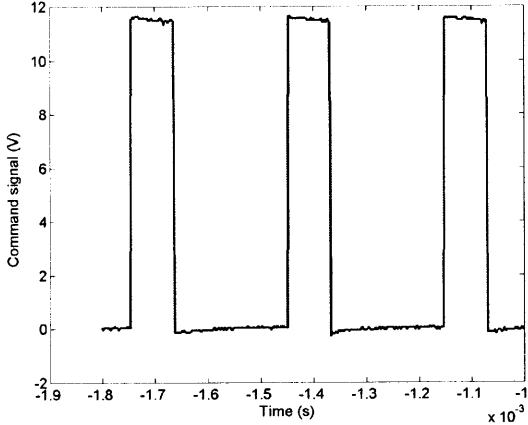
Figure E.13: Desired gate signal transmitted from stationary side.
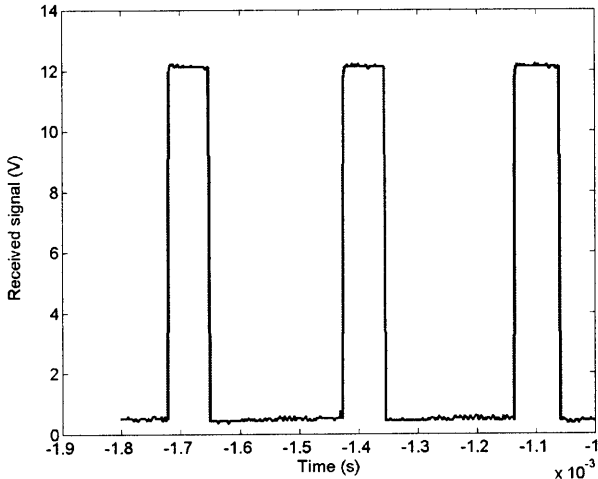
Figure E.14: Received demodulated signal at rotating side.

The actual FSK circuit implementation is shown in Figure E.15. The UC3824 PWM controller compares the output voltage of the alternator with a reference voltage and generates an error signal whose output is then compared with an internal sawtooth waveform. The output of the chip is the control signal for the MOSFET, which is a digital signal. The control signal is then input to the XR2206 monolithic function generator. The output of the XR2206 is a sinusoid at either of two frequencies depending on whether a high level or low level is being transmitted. The two frequencies called the mark and

222

space frequencies are set by R_9 (R_1 in datasheet), R_{10} (R_2 in datasheet), and C_{12} (C in datasheet). The mark frequency is determined by R_9 and is equal to

$$f_1 = \frac{1}{R_9 C_{12}}$$
(E.37)

And similarly, the space frequency can be determined using

$$f_2 = \frac{1}{R_{10} C_{12}}$$
(E.38)

where the values R_9 = 8.2 kΩ, R_{10} = 4.3 kΩ, and C_{12} = 1 nF are selected such that the mark and space frequencies are 121 kHz and 232 kHz, respectively. The resistor R_{11} (R_3 in datasheet) is a potentiometer that adjusts the amplitude of the sinusoid. The sinusoid is transmitted through the brushes and received on the rotating side through capacitor C_{38}. The capacitor C_7 is used for DC blocking. The inductor L_2 is used to isolate the transmitted sinusoid from the DC bus. The inductor L_1 and capacitor C_{23} (a to e) are used to isolate the switching current from the transmitted signal. As shown in figure E.12, the effects of the switching currents are negligible at the FSK receiver end due to the filter.

The demodulator circuit uses an XR2211 chip. It returns a high level if it receives the high frequency sinusoid (232 kHz) and returns a low level if it receives a low frequency sinusoid (121 kHz). The appropriate center frequency of its VCO is found using

$$f_0 = \sqrt{f_1 f_2}$$
(E.39)

and is equal to 168 kHz. This can be set using the capacitor C_{24} (C_0 in datasheet) with value 0.45 nF and the resistor $R_{16}+R_{26}$ (R_0 in datasheet) with value 13.95 kΩ. The resistance value can be varied continuously since R_{26} is a potentiometer. The resistance R_{17} (R_1 in datasheet) is selected using

$$R_{17} = \frac{2(R_{16} + R_{26})f_0}{|f_1 - f_2|}$$
(E.40)

which provides the appropriate tracking bandwidth. The value used is 39.2 kΩ. R_{18} (R_F in datasheet) is selected to be at least 5 times R_{17} and equal to 200 kΩ and R_{15} is selected to be at least 5 times R_{18} or 1 MΩ. These values are selected to prevent loading. C_{25} (C_1 in datasheet) is selected to have the value 0.47 nF to have a damping ratio, ξ, close to 0.5. C_{25} is determined using

$$C_{25} = \frac{1250 C_{24}}{R_{17} \xi^2} \tag{E.41}$$

C_{27} is selected to be 10 pF and is determined based on the baud rate (1.3×10^5 /sec) using

$$C_{27} = \frac{0.25}{R_{sum}(baudrate)} \tag{E.42}$$

This affects how fast the demodulator is able to track the rectangular wave or digital control signal. R_{sum} can be found using

$$R_{sum} = \frac{(R_{18} + R_{17})R_{15}}{(R_{18} + R_{17} + R_{15})} \tag{E.43}$$

These design procedures can be found in the XR2206 datasheet.
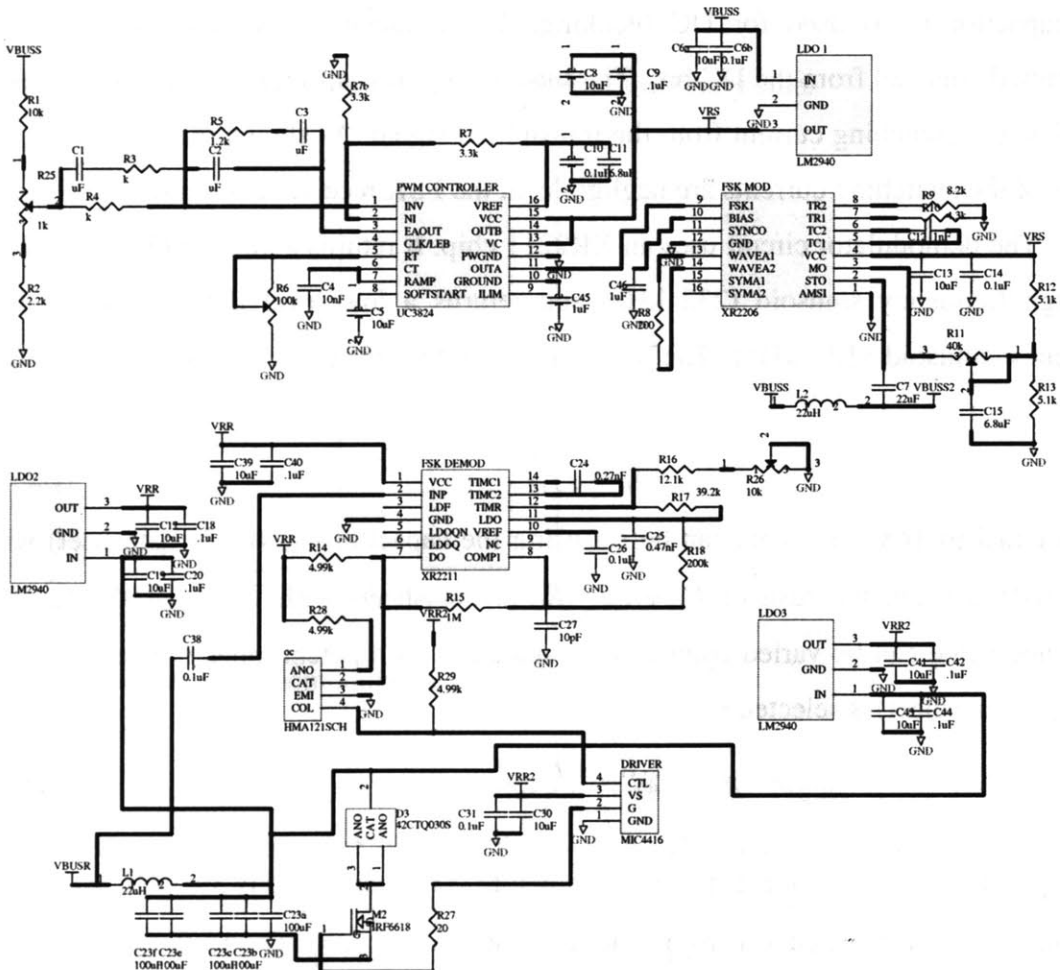
Figure E.15: Schematic of circuit used for FSK modulation.

Appendix F. Matlab Code

F.1. Alternator Optimization Code

F.1.1. Non-salient Wound Field Alternator Optimizer

```
%%%%%%%%%%%%
%opt_NSWF.m%
%%%%%%%%%%%%
%optimizes non-salient wound field alternator
filename='opt_NSWF_best.mat'
start=1; %1:new run, 0:continuing run
totcheapmachines=100; %number of saved machines
geomsize=10; %number of design variables
costloc=6;    %index of cost
voltmax=42; %maximum output voltage
outputvoltage=voltmax;
fieldheatlim=7.2873e4; %field heat flux density limit
if start
geom=ones(totcheapmachines,geomsize)*9e9;
counter=0;
else
load(eval('filename'));
end
machinetype=1;
idlepower=4000;
midpower=3250;
highpower=6000;
exact=1;
Routmax=.2; %maximum outer radius
rimin=.02; %minimum inner radius
p=6; %number of pole pairs
nspp=6; %number of slots per pole
nstatteeth=2*p*6; %number of stator teeth
minslotar=0.75;
maxslotar=5;
noconv=0;
gridsize=0.005;
di=2*1/1000*2.54/100;
%determine outer radius
Rmax=Routmax/(1+minslotar*pi/nstatteeth);
Rmin=rimin/(1-minslotar*pi/nstatteeth);
Rndiv=floor((Rmax-Rmin)/gridsize);
lastcheapfind=Rndiv;
for n1=1:Rndiv
R=Rmin+(Rndiv-n1+1)*gridsize;
%determine rotor slot bottom radius
rsbmax=R*(1-minslotar*pi/nstatteeth);
rsbmin=max(rimin,R*(1-maxslotar*pi/nstatteeth));
rsbndiv=floor((rsbmax-rsbmin)/gridsize);
for n2=1:rsbndiv
rsb=rsbmin+(rsbndiv-n2+1)*gridsize;
kslotrot=(R-rsb)/R;
%determine stator slot bottom radius
rstatslotbotmax=min(Routmax,R*(1+maxslotar*pi/nstatteeth));
rstatslotbotmin=R*(1+minslotar*pi/nstatteeth);
rstatslotbotndiv=floor((rstatslotbotmax-rstatslotbotmin)/gridsize);
for n3=1:rstatslotbotndiv
rstatslotbot=rstatslotbotmin+n3*gridsize;
kslotstat=(rstatslotbot-R)/R;
g=0.000635;
%determine length
Lmax=0.1;
Lmin=0.025;
Lndiv=floor((Lmax-Lmin)/(gridsize));
for n4=1:Lndiv
L=Lmin+n4*gridsize;
%vary output voltages
for ov1=42:-1:1
for ov2=42:-1:1
for ov3=42:-1:1
%determine number of armature turns
```

```
det_Na
outputvoltage=ov2;
voltmax=ov2;
speed=2*1500;
omega=2*pi*(p*speed/60);
Power=midpower;
%determine field ampere turns and back-emf
det_excite
effmidprev
checkpow(2)=noconv;
if ~noconv
NfIfa(2)=NfIfNS;
Isa(2)=IsNS;
%determine efficiency
efficiency
effmid=eff;
if effmid>0.75 %if meets efficiency requirements
outputvoltage=ov3;
voltmax=ov3;
speed=2*6000;
omega=2*pi*(p*speed/60);
Power=highpower;
%determine field ampere turns and back-emf
det_excite
checkpow(3)=noconv;
if ~noconv %if convergers
NfIfa(3)=NfIfNS;
Isa(3)=IsNS;
outputvoltage=ov1;
voltmax=ov1;
speed=2*600;
omega=2*pi*(p*speed/60);
Power=idlepower;
%determine field ampere turns and back-emf
det_excite
checkpow(1)=noconv;
if ~noconv
NfIfa(1)=NfIfNS;
Isa(1)=IsNS;
%determine heat flux density
heatflux
%check whether heat flux density is acceptable
if all(heatcoeff2NSa<7.2873e4) & all(heatcoeff4NSa<7.2873e4)
%check for saturation, determine saturation related dimensions
saturation1
addgeomNS
if Rout<Routmax & (rimin+T)<rsb & ~satsomewhere
%determine materials cost
cost
satmac=1;
drawfigure=0;
if drawfigure
draw_cs_NSWF
draw_side_NSWF
end
costNS
counter=counter+1
[maxcost,maxcostloc]=max(geom(:,costloc));
if costNS<maxcost
geom(maxcostloc,1)=n1;
geom(maxcostloc,2)=n2;
geom(maxcostloc,3)=n3;
geom(maxcostloc,4)=n4;
geom(maxcostloc,5)=Na;
geom(maxcostloc,6)=costNS;
geom(maxcostloc,7)=effmid;
geom(maxcostloc,8)=ov1;
geom(maxcostloc,9)=ov2;
geom(maxcostloc,10)=ov3;
lastcheapfind=n1;
```

```
save(eval('filename'),'geom','machinetype','counter','n1','lastcheapfind','Rndiv','R','n2
','n3','n4','ov1','ov2','ov3','gridsize');
end
end
end
end
end
end
end
end %for ov3
end %for ov2
end %for ov1
end
end
end
save(eval('filename'),'geom','machinetype','counter','n1','lastcheapfind','Rndiv','R','n2
','n3','gridsize');
if n1>(lastcheapfind+1) & counter>0
    break;
end
end
```

F.1.2. Salient Wound Field Alternator Optimizer

```
%%%%%%%%%%%
%opt_SWF.m%
%%%%%%%%%%%
%optimizes salient wound field alternator
filename='opt_SWF_best.mat'
totcheapmachines=100; %number of saved machines
start=1; %1:new run, 0:continuing run
geomsize=7; %number of design variables
costloc=6; %index of cost
voltmax=42; %maximum output voltage
outputvoltage=voltmax;
if start
geom=ones(totcheapmachines,geomsize)*9e9; %% using savecheap.m
else
load(eval('filename'));
end
exact=1;
machinetype=2;
idlepower=4000; %power requirements
midpower=3250;
highpower=6000;
Routmax=.2; %maximum outer radius
rimin=.02; %minimum inner radius
p=6; %number of pole pairs
di=2*1/1000*2.54/100;
nstatteeth=2*p*6; %number of stator teeth
minslotar=0.75;
maxslotar=5;
lastcheapfind=0;
if start
counter=0;
end
%load(eval('filename'));
noconv=0;
gridsize=0.001;
fieldheatlim=7.2873e4; %field heat flux density limit
%determine rotor radius
Rmax=Routmax/(1+minslotar*pi/nstatteeth);
Rmin=rimin/(1-minslotar*pi/nstatteeth);
Rndiv=floor((Rmax-Rmin)/gridsize);
lastcheapfind=Rndiv;
for n1=1:Rndiv
R=Rmin+(Rndiv-n1+1)*gridsize;
%determine rotor slot bottom radis
rsbmax=R*(1-minslotar*pi/nstatteeth);
```

227

```
rsbmin=max(rimin,R*(1-10*pi/nstatteeth));
rsbndiv=floor((rsbmax-rsbmin)/gridsize);
for n2=1:rsbndiv
rsb=rsbmin+(rsbndiv-n2+1)*gridsize; %new change
kslotrot=(R-rsb)/R;
%determine stator slot bottom radius
rstatslotbotmax=min(Routmax,R*(1+maxslotar*pi/nstatteeth));
rstatslotbotmin=R*(1+minslotar*pi/nstatteeth);
rstatslotbotndiv=floor((rstatslotbotmax-rstatslotbotmin)/gridsize);
for n3=1:rstatslotbotndiv
rstatslotbot=rstatslotbotmin+n3*gridsize;
kslotstat=(rstatslotbot-R)/R;
g=0.000635;
%determine length
Lmax=0.1;
Lmin=0.025;
Lndiv=floor((Lmax-Lmin)/(gridsize));
for n4=1:Lndiv
L=Lmin+n4*gridsize;
%vary output voltages
for ov1=42:-1:1
for ov2=42:-1:1
for ov3=42:-1:1
%determine number of armature turns
det_Na
outputvoltage=ov2;
voltmax=ov2;
speed=2*1500;
omega=2*pi*(p*speed/60);
Power=midpower;
%determine field ampere turns and back-emf
det_excite
effmidprev
checkpow(2)=noconv;
if ~noconv
NfIfa(2)=NfIfS;
Isa(2)=IsS;
%determine efficiency
efficiency
effmid=eff;
if effmid>0.75
outputvoltage=ov3;
voltmax=ov3;
speed=2*6000;
omega=2*pi*(p*speed/60);
Power=highpower;
%determine field ampere turns and back-emf
det_excite
checkpow(3)=noconv;
if ~noconv
NfIfa(3)=NfIfS;
Isa(3)=IsS;
outputvoltage=ov1;
voltmax=ov1;
speed=2*600;
omega=2*pi*(p*speed/60);
Power=idlepower;
%determine field ampere turns and back-emf
det_excite
checkpow(1)=noconv;
if ~noconv
NfIfa(1)=NfIfS;
Isa(1)=IsS;
%determine heat flux density
heatflux
%check whether heat flux density is within limits
if all(heatcoeff2Sa<7.2873e4) & all(heatcoeff4Sa<7.2873e4)
%check for saturation, determine saturation related dimensions
saturation1
addgeomS
if Rout<Routmax & (rimin+Trot)<rsb & ~satsomewhere
```

```
%determine materials cost
cost
satmac=1;
drawfigure=0;
if drawfigure
draw_cs_SWF
draw_side_SWF
end
costS
counter=counter+1
[maxcost,maxcostloc]=max(geom(:,costloc));
if costS<maxcost
geom(maxcostloc,1)=n1;
geom(maxcostloc,2)=n2;
geom(maxcostloc,3)=n3;
geom(maxcostloc,4)=n4;
geom(maxcostloc,5)=Na;
geom(maxcostloc,6)=costS;
geom(maxcostloc,7)=effmid;
geom(maxcostloc,8)=ov1;
geom(maxcostloc,9)=ov2;
geom(maxcostloc,10)=ov3;
lastcheapfind=n1;
save(eval('filename'),'geom','machinetype','counter','n1','lastcheapfind','Rndiv','rsbndi
v','rstatslotbotndiv','Lndiv','R','n2','n3','n4','gridsize');
end
end %ov
end %ov
end %ov
end
end
end
end
end
end
end
end
end
end
end
save(eval('filename'),'geom','machinetype','counter','n1','lastcheapfind','Rndiv','rsbndi
v','rstatslotbotndiv','Lndiv','R','n2','n3','n4','gridsize');
if n1>(lastcheapfind+1) & counter>0
     break;
end
end
```

F.1.3. Lundell Alternator Optimizer

```
%%%%%%%%%%%%%%%
%opt_Lundell.m%
%%%%%%%%%%%%%%%%
%optimizes Lundell alternator
filename='opt_Lundell_best.mat'
totcheapmachines=100; %number of saved machines
start=1; %1:new run, 0:continuing run
geomsize=13; %number of design variables
costloc=8; %index of cost
voltmax=42; %maximum output voltage
outputvoltage=voltmax;
parallelsidewalls=0;
adjustk1=0;
if start
geom=ones(totcheapmachines,geomsize)*9e9; %% using savecheap.m
else
load(eval('filename'));
end
optimize=1;
exact=1;
machinetype=3;
fieldlossinc=1;
```

229

```
%tp=2*pi/2/p*R; % pole pitch
idlepower=4000;
midpower=3250;
highpower=6000;
fixedpolefrac=1;
Routmax=.2;
rimin=.02;
p=6;
di=2*1/1000*2.54/100;
nstatteeth=2*p*6;
kpeb=0.9;
minslotar=0.75;
maxslotar=5;
numinc=7;
lastcheapfind=0;
if start
counter=0;
end
noconv=0;
fieldheatlim=6200; %field heat flux density limit
gridsize=0.001;
%determine rotor radius
Rmax=Routmax/(1+minslotar*pi/nstatteeth);
Rmin=rimin/(1-minslotar*pi/nstatteeth);
Rndiv=floor((Rmax-Rmin)/gridsize);
lastcheapfind=Rndiv;
for n1=1:Rndiv
R=Rmin+(Rndiv-n1+1)*gridsize;
rpeb=R*kpeb;
%determine outer radius of coil
rcoiltopmax=rpeb;
rcoiltopmin=0.025;
rcoiltopndiv=floor((rcoiltopmax-rcoiltopmin)/gridsize);
for n2=1:rcoiltopndiv
rcoiltop=rcoiltopmin+n2*gridsize;
k1=rcoiltop/R;
%determine stator slot bottom radius
rstatslotbotmax=min(Routmax,R*(1+maxslotar*pi/nstatteeth));
rstatslotbotmin=R*(1+minslotar*pi/nstatteeth);
rstatslotbotndiv=floor((rstatslotbotmax-rstatslotbotmin)/gridsize);
for n3=1:rstatslotbotndiv
rstatslotbot=rstatslotbotmin+n3*gridsize;
kslotstat=(rstatslotbot-R)/R;
%determine inner radius of coil
rcoilbotmax=0.95*rcoiltop;
rcoilbotmin=rimin;
rcoilbotndiv=floor((rcoilbotmax-rcoilbotmin)/gridsize);
for n4=1:rcoilbotndiv
rcoilbot=rcoilbotmin+n4*gridsize;
k2=rcoilbot/R;
kslotrot=(rcoiltop-rcoilbot)/R;
kLcoil=1;
g=0.000635;
%determine length
Lmax=0.08;
Lmin=0.025;
Lndiv=floor((Lmax-Lmin)/(gridsize));
for n5=1:Lndiv
L=Lmin+n5*gridsize;

%vary output voltage
for ov3=42:-1:1
    for ov2=42:-1:1
        for ov1=42:-1:1
%determine number of armature turns
det_Na
outputvoltage=ov2;
voltmax=ov2;
speed=2*1500;
omega=2*pi*(p*speed/60);
Power=midpower;
```

```
%determine ampere turns and back-emf
det_excite
effmidprev
checkpow(2)=noconv;
if ~noconv
NfIfa(2)=NfIfL;
Isa(2)=IsL;
%determine efficiency
efficiency
effmid=eff;
if effmid>0.75
outputvoltage=ov3;
voltmax=ov3;
speed=2*6000;
omega=2*pi*(p*speed/60);
Power=highpower;
%determine ampere turns and back-emf
det_excite
checkpow(3)=noconv;
if ~noconv
NfIfa(3)=NfIfL;
Isa(3)=IsL;
outputvoltage=ov1;
voltmax=ov1;
speed=2*600;
omega=2*pi*(p*speed/60);
Power=idlepower;
%determine ampere turns and back-emf
det_excite
checkpow(1)=noconv;
if ~noconv
NfIfa(1)=NfIfL;
Isa(1)=IsL;
%determine heat flux density
heatflux
%check whether heat flux density is within limits
if all(heatcoeff2La<fieldheatlim) & all(heatcoeff4La<7.2873e4)
%check for saturation and determine saturation related dimensions
saturation1
addgeomL
if Rout<Routmax & k1<k1lim & Rcpo<k2*R & ~satsomewhere & (L+2*Ls)<0.1
%determine materials cost
cost
satmac=1;
drawfigure=0;
if drawfigure
draw_cs_Lundell
draw_side_Lundell
end
costL
counter=counter+1
[maxcost,maxcostloc]=max(geom(:,costloc));
if costL<maxcost
geom(maxcostloc,1)=n1;
geom(maxcostloc,2)=n2;
geom(maxcostloc,3)=n3;
geom(maxcostloc,4)=n4;
geom(maxcostloc,5)=n5;
geom(maxcostloc,6)=0;
geom(maxcostloc,7)=Na;
geom(maxcostloc,8)=costL;
geom(maxcostloc,9)=effmid;
geom(maxcostloc,10)=Rout;
geom(maxcostloc,11)=ov1;
geom(maxcostloc,12)=ov2;
geom(maxcostloc,13)=ov3;
lastcheapfind=n1;
save(eval('filename'),'geom','machinetype','counter','gridsize','n1','lastcheapfind','Rnd
iv','rcoiltopndiv','rstatslotbotndiv','rcoilbotndiv','Lndiv','R','n2','n3','n4','n5','gri
dsize','ov1','ov2','ov3');
end
```

```
end
end
end
end
end
end
end %ov
end %ov
end %ov
end
end
end
end
save(eval('filename'),'geom','machinetype','counter','gridsize','n1','lastcheapfind','Rnd
iv','rcoiltopndiv','rstatslotbotndiv','rcoilbotndiv','Lndiv','R','n2','n3','n4','n5','gri
dsize','ov1');
if n1>(lastcheapfind+1) & counter>0
     break;
end
end
```

F.1.4. Homopolar Inductor Alternator Optimizer

```
%%%%%%%%%%%%%%%%
%opt_Lundell.m%
%%%%%%%%%%%%%%%%
%optimizes Lundell alternator
filename='opt_Lundell_best.mat'
totcheapmachines=100; %number of saved machines
start=1; %1:new run, 0:continuing run
geomsize=13; %number of design variables
costloc=8; %index of cost
voltmax=42; %maximum output voltage
outputvoltage=voltmax;
parallelsidewalls=0;
adjustk1=0;
if start
geom=ones(totcheapmachines,geomsize)*9e9; %% using savecheap.m
else
load(eval('filename'));
end
optimize=1;
exact=1;
machinetype=3;
fieldlossinc=1;
%tp=2*pi/2/p*R; % pole pitch
idlepower=4000;
midpower=3250;
highpower=6000;
fixedpolefrac=1;
Routmax=.2;
rimin=.02;
p=6;
di=2*1/1000*2.54/100;
nstatteeth=2*p*6;
kpeb=0.9;
minslotar=0.75;
maxslotar=5;
numinc=7;
lastcheapfind=0;
if start
counter=0;
end
noconv=0;
fieldheatlim=6200; %field heat flux density limit
gridsize=0.001;
%determine rotor radius
Rmax=Routmax/(1+minslotar*pi/nstatteeth);
Rmin=rimin/(1-minslotar*pi/nstatteeth);
Rndiv=floor((Rmax-Rmin)/gridsize);
lastcheapfind=Rndiv;
```

```
for n1=1:Rndiv
R=Rmin+(Rndiv-n1+1)*gridsize;
rpeb=R*kpeb;
%determine outer radius of coil
rcoiltopmax=rpeb;
rcoiltopmin=0.025;
rcoiltopndiv=floor((rcoiltopmax-rcoiltopmin)/gridsize);
for n2=1:rcoiltopndiv
rcoiltop=rcoiltopmin+n2*gridsize;
k1=rcoiltop/R;
%determine stator slot bottom radius
rstatslotbotmax=min(Routmax,R*(1+maxslotar*pi/nstatteeth));
rstatslotbotmin=R*(1+minslotar*pi/nstatteeth);
rstatslotbotndiv=floor((rstatslotbotmax-rstatslotbotmin)/gridsize);
for n3=1:rstatslotbotndiv
rstatslotbot=rstatslotbotmin+n3*gridsize;
kslotstat=(rstatslotbot-R)/R;
%determine inner radius of coil
rcoilbotmax=0.95*rcoiltop;
rcoilbotmin=rimin;
rcoilbotndiv=floor((rcoilbotmax-rcoilbotmin)/gridsize);
for n4=1:rcoilbotndiv
rcoilbot=rcoilbotmin+n4*gridsize;
k2=rcoilbot/R;
kslotrot=(rcoiltop-rcoilbot)/R;
kLcoil=1;
g=0.000635;
%determine length
Lmax=0.08;
Lmin=0.025;
Lndiv=floor((Lmax-Lmin)/(gridsize));
for n5=1:Lndiv
L=Lmin+n5*gridsize;

%vary output voltage
for ov3=42:-1:1
    for ov2=42:-1:1
        for ov1=42:-1:1
%determine number of armature turns
det_Na
outputvoltage=ov2;
voltmax=ov2;
speed=2*1500;
omega=2*pi*(p*speed/60);
Power=midpower;
%determine ampere turns and back-emf
det_excite
effmidprev
checkpow(2)=noconv;
if ~noconv
NfIfa(2)=NfIfL;
Isa(2)=IsL;
%determine efficiency
efficiency
effmid=eff;
if effmid>0.75
outputvoltage=ov3;
voltmax=ov3;
speed=2*6000;
omega=2*pi*(p*speed/60);
Power=highpower;
%determine ampere turns and back-emf
det_excite
checkpow(3)=noconv;
if ~noconv
NfIfa(3)=NfIfL;
Isa(3)=IsL;
outputvoltage=ov1;
voltmax=ov1;
speed=2*600;
omega=2*pi*(p*speed/60);
```

```
Power=idlepower;
%determine ampere turns and back-emf
det_excite
checkpow(1)=noconv;
if ~noconv
NfIfa(1)=NfIfL;
Isa(1)=IsL;
%determine heat flux density
heatflux
%check whether heat flux density is within limits
if all(heatcoeff2La<fieldheatlim) & all(heatcoeff4La<7.2873e4)
%check for saturation and determine saturation related dimensions
saturation1
addgeomL
if Rout<Routmax & k1<k1lim & Rcpo<k2*R & ~satsomewhere & (L+2*Ls)<0.1
%determine materials cost
cost
satmac=1;
drawfigure=0;
if drawfigure
draw_cs_Lundell
draw_side_Lundell
end
costL
counter=counter+1
[maxcost,maxcostloc]=max(geom(:,costloc));
if costL<maxcost
geom(maxcostloc,1)=n1;
geom(maxcostloc,2)=n2;
geom(maxcostloc,3)=n3;
geom(maxcostloc,4)=n4;
geom(maxcostloc,5)=n5;
geom(maxcostloc,6)=0;
geom(maxcostloc,7)=Na;
geom(maxcostloc,8)=costL;
geom(maxcostloc,9)=effmid;
geom(maxcostloc,10)=Rout;
geom(maxcostloc,11)=ov1;
geom(maxcostloc,12)=ov2;
geom(maxcostloc,13)=ov3;
lastcheapfind=n1;
save(eval('filename'),'geom','machinetype','counter','gridsize','n1','lastcheapfind','Rnd
iv','rcoiltopndiv','rstatslotbotndiv','rcoilbotndiv','Lndiv','R','n2','n3','n4','n5','gri
dsize','ov1','ov2','ov3');
end
end
end
end
end
end
end
end %ov
end %ov
end %ov
end
end
end
end
save(eval('filename'),'geom','machinetype','counter','gridsize','n1','lastcheapfind','Rnd
iv','rcoiltopndiv','rstatslotbotndiv','rcoilbotndiv','Lndiv','R','n2','n3','n4','n5','gri
dsize','ov1');
if n1>(lastcheapfind+1) & counter>0
     break;
end
end
```

F.1.5 Parameters Set

```
%%%%%%%%%%%
%initopt.m%
%%%%%%%%%%%
%initializes optimization

%slot depths and machine turns aren't initialized
voltdiv=1; %1,10,100 ; interval is 1/voltdiv
incendwindleak=0; %include end winding leakage
initillus=0; %for illustration purposes
sizingtype=1;%1 only based on saturation and magnetics
ver=0;
VERWFSANS=0;
drawmachines=0 ;
kpffoilref=0.35;
if exact==1
incslotleak=1;
else
incslotleak=0;
end
drawsize=0.2;
mu0=4*pi*1e-7;
a=2*p; %number of parallel windings
%decided on number of turns per slot.. increase If to increase NfIf for WFSANS
nspp=6; %slots per pole
mspp=nspp/3; %slots per pole per phase
kw=sin(mspp*pi/nspp/2)/mspp/sin(pi/nspp/2); %armature winding factor
Ns=Na*nspp*2*p/3; %total number of stator turns
nslots=nspp*(2*p); %total number of stator slots
nstatteeth=nslots;
tp=2*pi/2/p*R; % pole pitch
Lturnwoew= 2*L; %for thermal ; exclude end windings in dissipation
g1=g;
if exact==1
g2=kslotrot*R+g1;
else
g2=inf;
end
toothfrac=.5; %assume 0.5 for both stator and rotor where it applies
sigma=4.45e7; %conductivity
Bsat=1.8; %1.8 %saturation flux density
Vd=0; %default but overwritten when necessary
ro=R-g/2;
rstatin=R+g/2;
rstatslotbot=R*(1+kslotstat);
rsb=(1-kslotrot)*R;
stattoothwid=toothfrac*2*pi/nstatteeth*R;
stattoothht=rstatslotbot-rstatin;
statslotht=stattoothht;
statslotwid=1/2*( rstatin*(2*pi/nstatteeth-2*asin(stattoothwid/2/rstatin)) +
rstatslotbot*(2*pi/nstatteeth-2*asin(stattoothwid/2/rstatslotbot)));
theta=asin(statslotwid/(statslotwid+stattoothwid));
seglen=(3*stattoothwid+2.5*statslotwid)/cos(theta);
Lturn= 2*L + 4*seglen + 2*pi*(statslotwid/2); %for saturation
statendturnwid=(3*stattoothwid+2.5*statslotwid)*tan(theta)+statslotwid;
Aslot=(pi*(rstatslotbot^2-rstatin^2)-nstatteeth*stattoothwid*stattoothht)/nslots;
kpfold=0.35;
kpf=(2*Na*pi/Aslot)*(sqrt(kpfold*Aslot/(2*pi*Na))-di)^2; %taking insulation
kpf=0.35;
kpffoil=kpffoilref;
steeldensity=7462; %kg per m^3
copperdensity=8960; %kg per m^3
steelcostdensity=0.45*2.205; %2.205 lbs per kg
coppercostdensity=2.27*2.205; %2.205 lbs per kg
if machinetype==1
ntps=1; %turns per slot for the field winding of wound-field non-salient
Nf=ntps*nspp*p; %can be used only for winding factor kwf
kwf=sin(Nf/(ntps*p)*pi/nspp/2)/(Nf/(ntps*p)*sin(pi/nspp/2));
%independent of Nf
rottoothfrac=0.5; %default
```

```
nrotteeth=2*p*nspp;
rottoothwid=rottoothfrac*2*pi/nrotteeth*R;
rottoothht=ro-rsb;
rotslotwid=1/2*( rsb*(2*pi/nrotteeth-2*asin(rottoothwid/2/rsb)) + ro*(2*pi/nrotteeth-
2*asin(rottoothwid/2/ro)));
LeffNS=L+3/2*pi*(rottoothwid+rotslotwid);
Aslotrot=(pi*(ro^2-rsb^2)-nrotteeth*rottoothwid*rottoothht)/nslots;
CNS=4*LeffNS/sigma/kpf/Aslotrot/nslots;


elseif machinetype==2
kwindS=0.25; %fraction for winding width
kwindtS=0.2; %fraction of pole length for pole top
polefrac=0.5; %pole fraction
polefracS=polefrac;
LeffS=L+2*ro*sin(1/2*polefrac*2*pi/2/p);
CS=1/(2*p)*2*LeffS/sigma/kpf/(ro-rsb)/(kwindS*ro*polefrac*2*pi/(2*p));
bp=polefracS*tp;
elseif machinetype==3
if fixedpolefrac
betap2=1;betap1=0.5;%.4;
betap3=kLcoil*betap2-(kLcoil-1)*betap1;
else
betap2=betap3/kLcoil+(1-1/kLcoil)*betap1;
end
if initillus==1
betap3=0.8;%for initial illustration of Lundell
betap1=0.45;%for initial illustration of Lundell
betap2=betap3/kLcoil+(1-1/kLcoil)*betap1;
kLcoil=1.2; %for initial illustration
end
kc=(kLcoil+1)/2; %claw length divided by active length L
Lc=kc*L;
kfpout=k1;
rfpout=kfpout*R;
rpeb=kpeb*R;
if k1==k2
k2=k1-1e-3;
end
CL=pi*(k1+k2)/(k1-k2)/kLcoil/L/kpffoil/sigma;
bp1=betap1*tp;
bp2=betap2*tp;
bp3=betap3*tp;
else
polefrac=0.5;
polefracH=2*polefrac; %pole width as a fraction of pole pair!
if initillus==1
polefracH=0.8; %for initial illustration of HIA
end
kbiH=(statbotrad-rstatslotbot)/R;
if kbiH==0
kbiH=1e-6;
end
CH=pi*(2+2*kslotstat+kbiH)/kbiH/kHcoil/L/kpffoil/sigma;
bp=polefracH*tp;
end


%%%%%%%%%%%%%
%addgeomNS.m%
%%%%%%%%%%%%%%
%dimensions following saturation
rstatout=Rout;
rr=3;
statendturnwid=(3*stattoothwid+2.5*statslotwid)*tan(theta)+statslotwid
ri=.02;


%%%%%%%%%%%%%
%addgeomS.m%
%%%%%%%%%%%%%
%dimensions following saturation
rstatout=Rout;
```

```
x01=ro*cos(1/2*polefrac*2*pi/(2*p));
y01=ro*sin(1/2*polefrac*2*pi/(2*p));
x02=x01-(ro-rsb)*kwindtS;;%10
y02=y01;
x03=x02;
y03=y02-kwindS*ro*polefrac*2*pi/(2*p);%20
x04=rsb*cos(asin(y03/rsb));
y04=y03;
x01S=x01;
x02S=x02;
y02S=y02;
y03S=y03;
x03S=x03;
x04S=x04;
fieldcopperareaS=(y02-y03)*(x03-x04);
ri=.02;


%%%%%%%%%%%
%addgeomL.m%
%%%%%%%%%%%
%dimensions following saturation check
rfpout=kfpout*R;%80
rpeb=kpeb*R;%90
rr=3/1000;
drawcircles=0;
tp=2*pi*R/(2*p);
thetap=2*pi/(2*p);
rstatout=Rout
ri=0.02;


%%%%%%%%%%%%
%addgeomH.m%
%%%%%%%%%%%%
%set following saturation check
rr=3;
rstatout=Rout;
ri=.02;
```

F.1.6 Determine Number of Armature Turns

```
%%%%%%%%%
%detNa.m%
%%%%%%%%%
%determines number of armature turns
observe=0;
Na=5;
effmidprev=-Inf;
heatcoeff2aprev=Inf;
heatcoeff4aprev=Inf;
checkpowprev=[1 1 1];
while (1) & Na<50
initopt %initialization
noconv=0;
satsomewhere=0;
outputvoltage=ov2;
voltmax=ov2;
speed=2*1500;
omega=2*pi*(p*speed/60);
Power=midpower;
%determine ampere turns and back-emf
det_excite
checkpow(2)=noconv;
if checkpowprev(2)<checkpow(2)
    break;
else
    checkpowprev(2)=checkpow(2);
if ~noconv
%determine efficiency
efficiency
effmid=eff;
```

```
effa(Na)=effmid;
NfIfa(2)=NfIf;
Isa(2)=Is(mv);
outputvoltage=ov3;
voltmax=ov3;
speed=2*6000;
omega=2*pi*(p*speed/60);
Power=highpower;
%determine ampere turns and back emf
det_excite
checkpow(3)=noconv;
if checkpowprev(3)<checkpow(3)
    break;
else
    checkpowprev(3)=checkpow(3);
if ~noconv
NfIfa(3)=NfIf;
Isa(3)=Is(mv);
outputvoltage=ov1;
voltmax=ov1;
speed=2*600;
omega=2*pi*(p*speed/60);
Power=idlepower;
%determine ampere turns and back-emf
det_excite
checkpow(1)=noconv;
if checkpowprev(1)<checkpow(1)
    break;
else
    checkpowprev(1)=checkpow(1);
if ~noconv
NfIfa(1)=NfIf;
Isa(1)=Is(mv);
%determine heat flux density
heatflux
%check whether heat flux densities meet limits
if (effmid<0.75 & effmidprev>effmid) | (~all(heatcoeff4a<7.2873e4) &
all(heatcoeff4aprev<7.2873e4)) | (~all(heatcoeff2a<fieldheatlim) &
all(heatcoeff2aprev<fieldheatlim))
    break;
end
effmidprev=effmid;
heatcoeff2aprev=heatcoeff2a;
heatcoeff4aprev=heatcoeff4a;
var(Na,:)=heatcoeff4a;
effa(Na)=effmid;
end
end
end
end
end
end
Na=Na+1;
end
Na=Na-1;
```

F.1.7 Determine Ampere Turn Excitation

```
%%%%%%%%%%%%%%%
%det_Excite.m%
%%%%%%%%%%%%%%%
%determine field ampere turns
observedraw=1;
if machinetype==1
initopt %initialize
det_param %determine lumped parameters
validEaf=0;
Vd=1; %diode drop
%determine approximate backemf
[Vsapprox,validEaf]=backemfapprox(Lsdc,Lsac,outputvoltage,Vd,Power,CNS,omega,LafmoverNf);
%for salient machine
```

```
if validEaf==1
[Vs,validEaf,powang]=backemfexact(Lsdc,Lsac,outputvoltage,Vd,Power,CNS,Ra,omega,LafmoverN
f,Vsapprox);
end
if validEaf==0
    noconv=1;
else
NfIf=Vs/(omega*LafmoverNf);
NfIfNS=NfIf;
IsNS=(pi/3)*(Power+NfIfNS^2*CNS)/outputvoltage;
mv1=outputvoltage;
mv=mv1;
Is(mv1)=IsNS;
thetai_array(mv1)=powang; %power angle
end
elseif machinetype==2
initopt %initialize
det_param %determine lumped parameters
validEaf=0;
Vd=1; %diode drop
%determine approximate backemf
[Vsapprox,validEaf]=backemfapprox(Lsdc,Lsac,outputvoltage,Vd,Power,CS,omega,LafmoverNf);
%for salient machine
%determine exact backemf
if validEaf==1
[Vs,validEaf,powang]=backemfexact(Lsdc,Lsac,outputvoltage,Vd,Power,CS,Ra,omega,LafmoverNf
,Vsapprox);
end
if validEaf==0
    noconv=1;
else
NfIf=Vs/(omega*LafmoverNf);
NfIfS=NfIf;
IsS=(pi/3)*(Power+NfIfS^2*CS)/outputvoltage;
mv2=outputvoltage;
mv=mv2;
Is(mv2)=IsS;
thetai_array(mv2)=powang;
end


elseif machinetype==3
initopt %initialize
det_param %determine lumped parameters
validEaf=0;
Vd=1; %diode drop
%determine approximate back-emf
[Vsapprox,validEaf]=backemfapprox(Lsdc,Lsac,outputvoltage,Vd,Power,CL,omega,LafmoverNf);
%for salient machine
if validEaf==1
[Vs,validEaf,powang]=backemfexact(Lsdc,Lsac,outputvoltage,Vd,Power,CL,Ra,omega,LafmoverNf
,Vsapprox);
end
if validEaf==0
    noconv=1;
else
NfIf=Vs/(omega*LafmoverNf);
NfIfL=NfIf;
IsL=(pi/3)*(Power+NfIfL^2*CL)/outputvoltage;
mv3=outputvoltage;
mv=mv3;
Is(mv3)=IsL;
thetai_array(mv3)=powang;
end


elseif machinetype==4
initopt %initialize
det_param %determine lumped parameters
validEaf=0;
Vd=1; %diode drop
```

```
%determine approximate backemf
[Vsapprox,validEaf]=backemfapprox(Lsdc,Lsac,outputvoltage,Vd,Power,CH,omega,LafmoverNf);
%for salient machine
%determine exact backemf
if validEaf==1
[Vs,validEaf,powang]=backemfexact(Lsdc,Lsac,outputvoltage,Vd,Power,CH,Ra,omega,LafmoverNf
,Vsapprox);
end
if validEaf==0
    noconv=1;
else
NfIf=Vs/(omega*LafmoverNf);
NfIfH=NfIf;
IsH=(pi/3)*(Power+NfIfH^2*CH)/outputvoltage;
mv4=outputvoltage;
mv=mv4;
Is(mv4)=IsH;
thetai_array(mv4)=powang;
end
end
```

F.1.8 Determine Lumped Parameters

```
%%%%%%%%%%%%%%
%det_param.m%
%%%%%%%%%%%%%%
%determine lumped parameters

if machinetype==1
%WFSA:NS
%Lafm=4/pi*mu0*kwf*Nf*kw*Ns/(p^2)/a*R*L/g;
LafmoverNf=4/pi*mu0*kwf*kw*Ns/(p^2)/a*R*L/g; %one turn field armature mutual
Lsdc=3/2*4/pi*mu0*(Ns^2)/(p^2)*R*L*((kw/a)^2)/g; % armature inductance
LsNS=Lsdc;
Lsac=0;
Rsac=0;
elseif machinetype==2
%WFSA:S
%Lafm=4/pi*mu0*Nf*Ns*kw/(p^2)*R*L/a/g1*sin(bp*pi/2/tp);
LafmoverNf=4/pi*mu0*Ns*kw/(p^2)*R*L/a/g1*sin(bp*pi/2/tp); %one turn field armature mutual
Lsdc=3/2*4/pi*(Ns^2)/(p^2)*(kw^2)/(a^2)*L*R*mu0*(1/g2+bp/tp*(1/g1-1/g2)); %armature
inductance
LsS=Lsdc;
Lsac=-3/2*4/pi*(Ns^2)/(p^2)*(kw^2)/(a^2)*L*R*mu0/pi*(1/g1-1/g2)*sin(bp*pi/tp);
Rsac=-omega*Lsac; %equivalent resistance
elseif machinetype==3
%Lundell
if bp1==bp2
f1e=pi/2/tp*sin(bp1*pi/2/tp);
f2e=pi/tp*sin(bp1*pi/tp);
%Lafm=4/pi*mu0*Nf*Ns/p/g*kw/a*R*(2/pi*tp*L*f1e);
LafmoverNf=4/pi*mu0*Ns/p/g*kw/a*R*(2/pi*tp*L*f1e); %one turn field armature mutual
Lsdc=3/2*4/pi*(Ns^2)/p*(kw^2)/(a^2)*L*R*mu0/p/g*(bp1+bp2)/2/tp; %armature inductance
Lsac=-3/2*4/pi*(Ns^2)/p*(kw^2)/(a^2)*L*R*mu0*tp/pi/g/pi/p*f2e;
Rsac=-omega*Lsac; %equivalent armature resistance
else
f1=(cos(bp1*pi/2/tp)-cos(bp2*pi/2/tp))/(bp2-bp1);
f2=(cos(bp1*pi/tp)-cos(bp2*pi/tp))/(bp2-bp1);
%Lafm=4/pi*mu0*Nf*Ns/p/g*kw/a*R*(2/pi*tp*L*f1);
LafmoverNf=4/pi*mu0*Ns/p/g*kw/a*R*(2/pi*tp*L*f1); %one turn field armature mutual
inductance
Lsdc=3/2*4/pi*(Ns^2)/p*(kw^2)/(a^2)*L*R*mu0/p/g*(bp1+bp2)/2/tp; %armature inductance
Lsac=-3/2*4/pi*(Ns^2)/p*(kw^2)/(a^2)*L*R*mu0*tp/pi/g/pi/p*f2;
Rsac=-omega*Lsac; %equivalent armature resistance
end
LsL=Lsdc;
else
%HIA
%note L=2*(stack length)
%Lafm=Ns*Nf*R*L/p*kw/a*(2*mu0/pi*(1/g1-1/g2)*sin(bp*pi/2/tp));
```

```
LafmoverNf=Ns*R*L/p*kw/a*(2*mu0/pi*(1/g1-1/g2)*sin(bp*pi/2/tp)); %one turn field armature
mutual inductance
Lsdc=3/2*2/pi*(Ns^2)/(p^2)*(kw^2)/(a^2)*L*R*(2*mu0*(1/g2+bp/2/tp*(1/g1-1/g2))); %armature
inductance
Lsac=-3/2*2/pi*(Ns^2)/(p^2)*(kw^2)/(a^2)*L*R*(mu0/pi*(1/g1-1/g2)*sin(bp*pi/tp));
Rsac=-omega*Lsac; %equivalent armature resistance
LsH=Lsdc;


Ll=Na^2*8/3*mu0/(2*p)*L*statslotht/statslotwid; %leakage inductance
if incendwindleak==1
Le=((Ns/p)^2)*(2*p)*3*(13/36*(tp*100/2.54-4)+3)*1e-8;
Ll=Ll+Le;
end
if incslotleak==1
Lsdc=Lsdc+Ll;
end
if machinetype==4
Lturn=Lturn+2*(kHcoil*L);
Lturnwoew=Lturnwoew+2*(kHcoil*L);
end
if ver==1
Ra=Rarm*Na^2; %VER only using HIA or WFSA:NS
Lsdc=Lsdc+Ll; %VER only using HIA or WFSA:NS
else
Ra=(Ns^2)*Lturn/sigma/kpf/Aslot/(nspp/3)/p/(a^2); %armature resistance
Rawoew=(Ns^2)*Lturnwoew/sigma/kpf/Aslot/(nspp/3)/p/(a^2);
end
if machinetype==4
RaH=Ra;
end
```

F.1.9 Determine Efficiency

```
%%%%%%%%%%%%%%%
%efficiency.m%
%%%%%%%%%%%%%%%%
%efficiency calculations
if machinetype==1
diodelossNS=3/pi*IsNS* 2*Vd;
armcopperlossNS=3/2*IsNS^2*Ra; %included end winding
fieldcopperlossNS= CNS*NfIfNS^2;
effNS= (Power)/(Power+diodelossNS+armcopperlossNS+fieldcopperlossNS);
eff=effNS;

elseif machinetype==2
diodelossS=3/pi*IsS* 2*Vd;
armcopperlossS=3/2*IsS^2*Ra ;
fieldcopperlossS= CS*NfIfS^2 ;
effS= (Power)/(Power+diodelossS+armcopperlossS+fieldcopperlossS);
eff=effS;

elseif machinetype==3
diodelossL=3/pi*IsL* 2*Vd;
armcopperlossL=3/2*IsL^2*Ra ;
fieldcopperlossL= CL*NfIfL^2 ;
effL= (Power)/(Power+diodelossL+armcopperlossL+fieldcopperlossL);
eff=effL;

else
diodelossH=3/pi*IsH* 2*Vd;
armcopperlossH=3/2*IsH^2*Ra;
fieldcopperlossH= CH*NfIfH^2 ;
effH= (Power)/(Power+diodelossH+armcopperlossH+fieldcopperlossH);
eff=effH;
end
```

F.1.10 Determine Heat Flux

```
%%%%%%%%%%%%
%heatflux.m%
%%%%%%%%%%%%
%calculates heat flux
```

```
if machinetype==1

a2=2*(pi*(ro^2-rsb^2)+2*pi*(rsb+ro)*2.5*(rotslotwid+rottoothwid));
a4=2*(pi*(rstatslotbot^2-rstatin^2)+2*pi*(rstatslotbot+rstatin)*statendturnwid);
IsNSa=Isa;
NfIfNSa=NfIfa;
armcopperlossNS= Ra*3/2*(IsNSa).^2; %replace Rawoew with Ra
fieldcopperlossNS= CNS*NfIfNSa.^2;
heatcoeff2NSa=fieldcopperlossNS/a2;
heatcoeff4NSa=armcopperlossNS/a4;

heatcoeff2a=heatcoeff2NSa;
heatcoeff4a=heatcoeff4NSa;

elseif machinetype==2
a4=2*(pi*(rstatslotbot^2-rstatin^2)+2*pi*(rstatslotbot+rstatin)*statendturnwid);
a2=2*(ro*polefrac*pi/p*(2*kwindS+1)+L)*kslotrot*R*(2*p);
IsSa=Isa;
NfIfSa=NfIfa;
armcopperlossS=Ra*3/2*(IsSa).^2; %replace Rawoew with Ra
fieldcopperlossS=CS*NfIfSa.^2;
heatcoeff2Sa=fieldcopperlossS/a2;
heatcoeff4Sa=armcopperlossS/a4;

heatcoeff2a=heatcoeff2Sa;
heatcoeff4a=heatcoeff4Sa;

elseif machinetype==3
a4=2*(pi*(rstatslotbot^2-rstatin^2)+2*pi*(rstatslotbot+rstatin)*statendturnwid);
a2=2*pi*k1*R*kLcoil*L;
IsLa=Isa;
NfIfLa=NfIfa;
armcopperlossL=Ra*3/2*(IsLa).^2; %replace Rawoew with Ra
fieldcopperlossL= CL*NfIfLa.^2;
heatcoeff2La=fieldcopperlossL/a2;
heatcoeff4La=armcopperlossL/a4;

heatcoeff2a=heatcoeff2La;
heatcoeff4a=heatcoeff4La;

else
id);
a4=2*(pi*(rstatslotbot^2-rstatin^2)+2*pi*(rstatslotbot+rstatin)*statendturnwid);
a2=2*pi*(1+kslotstat)*R*kHcoil*L;
IsHa=Isa;
NfIfHa=NfIfa;
armcopperlossH=Ra*3/2*(IsHa).^2;
fieldcopperlossH= CH*NfIfHa.^2;
heatcoeff2Ha=fieldcopperlossH/a2;
heatcoeff4Ha=armcopperlossH/a4;

heatcoeff2a=heatcoeff2Ha;
heatcoeff4a=heatcoeff4Ha;

end
```

F.1.11 Test for Saturation

```
%%%%%%%%%%%%%%%
%saturation1.m%
%%%%%%%%%%%%%%%%%
%calculates flux densities and determines some dimensions based on saturation
%note: at the same power output, therefore express Ns*Is approprIs(mv1)tely
%based on hand calculations
if machinetype==1
%WFSA:NS
if ver==1
mv1=42*voltdiv;
end
Fr=4/pi*NfIf/2/p*kwf; %field MMF per pole
```

```
Fs=3/2*4/pi*Ns*Is(mv1)/2/p*kw/a; %armature MMF per pole
phi=thetai_array(mv1);
B1=sqrt( (Fr-Fs*sin(phi))^2 + (Fs*cos(phi))^2) * mu0/g; %fundamental component
Btstat=B1/toothfrac; %stator tooth flux density
Btrot=B1/rottoothfrac; %rotor tooth flux density
Bt=Btstat;
if Btstat>Bsat | Btrot>Bsat
satsomewhere=1; %flag for saturation
end
BtNS=max(Btstat,Btrot);
BtNSstat=Btstat;
BtNSrot=Btrot;
poleflux=2*B1/p*R*L;
polefluxstatNS=poleflux;
cA=2*L*R/p*Fr*mu0/g;
cB=-2*R*L/p*Fs*mu0/g;
cC=-cB;
polefluxcheck=sqrt((cA+cB*sin(phi))^2+(cC*cos(phi))^2);
T=B1/Bsat*R/p; %minimum
maxpoleflux=(NfIf/2/p+3/2*Ns*Is(mv1)/2/p/a)*mu0/g*tp*L;

kbi=T/R;
if sizingtype==1
Rout=R*(1+kslotstat+kbi);
ri=R*(1-kslotrot-kbi);
else
Rout=max(R*(1+kslotstat+kbi),(1+1.7*kslotstat)*R);
ri=min(R*(1-kslotrot-kbi),(1-1.7*kslotrot)*R);
end
RoutNS=Rout;
ri=0.02;
riNS=ri;

if drawmachines
drawwfsans1
sidewfsans1
end


elseif machinetype==2
%WFSA:S
Fr=NfIf/2/p; %field MMF per pole
Fs=3/2*4/pi*Ns*Is(mv2)/2/p*kw/a; %armature MMF per pole
phi=thetai_array(mv2);
polefluxrot=abs(NfIf/2/p*mu0/g*bp*L - 2*L*R*Fs/p*sin(phi)*sin(p*bp/2/R)*mu0/g);
polefluxrotS=polefluxrot;
Rslotbot=polefluxrot/Bsat*R/bp/L; %for radial side walls
%polewidth=polefluxrot/Bsat/L; %for square teeth
y03S=ro*sin(1/2*polefrac*2*pi/(2*p))-kwindS*ro*polefrac*2*pi/(2*p);
if 2*y03S<polefluxrot/Bsat/L
satsomewhere=1; %invalid machine
end
Trot=polefluxrot/2/Bsat/L;

%stator
lambda1=2*mu0/pi/g1*sin(bp/2/tp*pi);
lambda0prime=mu0*(1/g2+bp/tp*(1/g1-1/g2));
lambda1prime=2*mu0/pi*(1/g1-1/g2)*sin(bp/tp*pi);
B1=sqrt( (Fr*2*lambda1 -Fs*(lambda0prime+lambda1prime/2)*sin(phi))^2 + (Fs*(lambda0prime-
lambda1prime/2)*cos(phi))^2 );
Bt=B1/toothfrac; %tooth flux density
if Bt>Bsat
satsomewhere=1;
end
BtS=Bt;
polefluxstat=R*L*B1*2/p; %note Rstatin is approximated as R used as Rrotout
cA=4/pi*Fr*mu0/g*sin(bp*pi/2/tp)*2*R*L/p;
cB=-2/p*L*R*Fs*lambda0prime;
cC=1/p*L*R*Fs*lambda1prime;
polefluxstatcheck=sqrt((cA+(cB-cC)*sin(phi))^2+((cB+cC)*cos(phi))^2);
polefluxstatS=polefluxstat;
Tstat=polefluxstat/2/Bsat/L;
```

```
maxpoleflux=(NfIf/2/p+3/2*Ns*Is(mv2)/2/p/a)*mu0/g*tp*L;
kbirot=Trot/R;
kbistat=Tstat/R;
if sizingtype==1
Rout=R*(1+kslotstat+kbistat);
ri=R*(1-kslotrot-kbirot);
else
Rout=max(R*(1+kslotstat+kbistat),(1+1.7*kslotstat)*R);
ri=min(R*(1-kslotrot-kbirot),(1-1.7*kslotrot)*R);
end
RoutS=Rout;
ri=0.02;
riS=ri;

if drawmachines
drawwfsas1
sidewfsas1
end


elseif machinetype==3
%Lundell
Fr=NfIf/2; %field winding flux density
Fs=3/2*4/pi*Ns*Is(mv3)/2/p*kw/a; %armature flux density
phi=thetai_array(mv3);
%rotor


%rotor pole flux calculations
if bp1==bp2
polefluxrot=abs(NfIf/2*mu0/g*L*bp1  -
Fs*mu0/g*R/p*2*sin(phi)*2*L/p*R*pi/2/tp*sin(bp1*pi/2/tp));
polefluxrotL=polefluxrot;
else
polefluxrot=abs(NfIf*mu0/g*L/(bp1+bp2)*(1/6*(bp2-bp1)^2+bp2*bp1)  +
Fs*mu0/g*R/p*2*sin(phi)*2*L/p/(bp2-bp1)*R*(cos(p/2*bp2/R)-cos(p/2*bp1/R)));%got rid of p
in first term
polefluxrotL=polefluxrot;
end


if parallelsidewalls
hs=polefluxrot/bp3/Bsat;
else %if radial side walls
    hs=R-sqrt((R^2)-2*polefluxrot/Bsat*R/bp3);
end


%new addition
for zn=1:100
z=zn*L/100;
bpz=z/L*bp2+(1-z/L)*bp1;
if bp1==bp2
polefluxrotz=NfIf/2*mu0*z/g-Fs*mu0/g*4*(R^2)/(p^2)*z*sin(phi)*pi/2/tp*sin(bpz*pi/2/tp);
else
polefluxrotz=NfIf/(bp1+bpz)*mu0*z/g*(1/6*(bpz-bp1)^2+bpz*bp1)-
Fs*mu0/g*4*(R^2)/(p^2)*z*sin(phi)*(cos(p/2*bp1/R)-cos(p/2*bpz/R))/(bpz-bp1);
end
if parallelsidewalls
%if parallel sidewalls,required rbot is at most
rbotreqd=ro-polefluxrotz/Bsat/bpz;
else
%if radial sidewalls, required rbot is at most
rbotreqd=sqrt(ro^2-2*polefluxrotz*R/Bsat/bpz);
end
if adjustk1
    %kfpout=.8237; %for kpf=.35
     rfpout=.05; %for kpf=.8;
end

rbot=z/Lc*rfpout+(1-z/Lc)*rpeb;
rbotreqdarray(zn)=rbotreqd;
rbotarray(zn)=rbot;
if rbot>rbotreqd
satsomewhere=1;
```

```
break;
end
end


if sizingtype==1 & ~optimize
k1=(R-g/2-hs)/R;
elseif ~optimize
k1=(R-g/2-max(hs,0.7*kslotrot*R))/R;
else
k1lim=(R-g/2-hs)/R;
end
kfpout=k1; %arbitrary
if adjustk1
    %kfpout=.8237; %for kpf=.35
     kfpout=rfpout/R; %for kpf=.8;
end

if ~optimize
k2=k1-kslotrot; %arbitrary
else
Rcpo=sqrt(p*polefluxrot/pi/Bsat + 0.02^2); %want k2*R>Rcpo
end


if ~optimize
Ls=max(p*polefluxrot/Bsat/2/pi/(k2*R),0.2*kc*L);
else
Ls=p*polefluxrot/Bsat/2/pi/(k2*R);
end


hc=(k2*R)-sqrt((k2*R)^2-(p*polefluxrot/Bsat/pi));


%stator

if bp1==bp2
z=0.5*L; %doesn't matter if bp1=bp2
betaN=(z/L*(bp2-bp1)+bp1)/2/tp;
betaS=(z/L*(bp1-bp2)+bp2)/2/tp;
lambda1N=2*mu0/pi/g*sin(betaN*pi);
lambda1S=2*mu0/pi/g*sin(betaS*pi);
lambda2N=2*mu0/2/pi/g*sin(2*betaN*pi);
lambda2S=2*mu0/2/pi/g*sin(2*betaS*pi);
lambda1a=(2*mu0/pi/g1*(sin(betaN*pi)-sin(betaS*pi)));
B0=Fr*mu0/g*(betaN-betaS)-Fs*sin(phi)/2*lambda1a;
B1=sqrt( (Fr*(lambda1N+lambda1S)-
Fs*(mu0/g/2/tp*(bp1+bp2)+(lambda2N+lambda2S)/2)*sin(phi))^2 +
(Fs*((mu0/g/2/tp*(bp1+bp2))-(lambda2N+lambda2S)/2)*cos(phi))^2);
Bt=(B0+B1)/toothfrac; %tooth flux density
if Bt>Bsat
satsomewhere=1;
end
polefluxstat=R*L*B1*2/p; %made assumption that R=Rstatin=Rrotout
polefluxstatL=polefluxstat;
else
for zn=1:100
z=zn*L/100;
betaN=(z/L*(bp2-bp1)+bp1)/2/tp;
betaS=(z/L*(bp1-bp2)+bp2)/2/tp;
bpN=betaN*2*tp;
bpS=betaS*2*tp;
lambda1N=2*mu0/pi/g*sin(betaN*pi);
lambda1S=2*mu0/pi/g*sin(betaS*pi);
lambda2N=2*mu0/2/pi/g*sin(2*betaN*pi);
lambda2S=2*mu0/2/pi/g*sin(2*betaS*pi);
lambda1a=(2*mu0/pi/g1*(sin(betaN*pi)-sin(betaS*pi)));
B0array(zn)=NfIf/(bp1+bp2)*mu0/g*(bpS*betaN-bpN*betaS)-Fs*sin(phi)/2*lambda1a;
B1array(zn)=sqrt( (NfIf/(bp1+bp2)*(bpS*lambda1N+bpN*lambda1S)-
Fs*(mu0/g/2/tp*(bp1+bp2)+(lambda2N+lambda2S)/2)*sin(phi))^2 +
(Fs*((mu0/g/2/tp*(bp1+bp2))-(lambda2N+lambda2S)/2)*cos(phi))^2);
end
Barray=B0array+B1array;
```

```
[Bmax,Bmaxindex]=max(Barray);
Bt=Bmax/toothfrac;
if Bt>Bsat
satsomewhere=1;
end
%B0=B0array(Bmaxindex);
%B1=B1array(Bmaxindex);
B1=max(B1array); %not exact but approximate
polefluxstat=R*L*B1*2/p; %made assumption that R=Rstatin=Rrotout
polefluxstatL=polefluxstat;
cA=R*2/p*NfIf/(bp1+bp2)*(2*mu0/pi/g)*(L*2*tp/pi*(bp2+bp1)/(bp2-bp1)*(cos(bp1*pi/2/tp)-
cos(bp2*pi/2/tp)-8*(tp^2)*L/(bp2-bp1)/(pi^2)*(sin(bp2*pi/2/tp)-
sin(bp1*pi/2/tp))+2*L*tp/pi*(cos(bp2*pi/2/tp)+cos(bp1*pi/2/tp))));
cB=-Fs*(mu0/g)*(bp1+bp2)/tp/p*R*L;
cC=Fs*(1/p)*(mu0/pi/g)*2*tp*L/(bp2-bp1)/pi*(cos(bp1*pi/tp)-cos(bp2*pi/tp))*R;
cD=cA+(cB-cC)*sin(phi);
cE=(cB+cC)*cos(phi);
polefluxstat=sqrt(cD^2+cE^2);
polefluxstatL=polefluxstat;
end
BtL=Bt;
T=polefluxstat/2/Bsat/L;
maxpoleflux=(NfIf/2+3/2*Ns*Is(mv3)/2/p/a)*mu0/g*tp*L;

ks=Ls/L;
if sizingtype==1
Rout=R*(1+kslotstat)+T;
ri=R*k2-hc;
else
Rout=max(R*(1+kslotstat)+T,(1+1.7*kslotstat)*R);
ri=min(R*k2-hc,(1-2.4*kslotrot)*R);
end
RoutL=Rout;
ri=0.02;
riL=ri;
k3=ri/R;

if drawmachines
drawlundell2
sidelundell2
end

else
%HIA
if ver==1
mv4=42*voltdiv; %VER
end
Fr=NfIf/2;
Fs=3/2*4/pi*Ns*Is(mv4)/2/p*kw/a;
phi=thetai_array(mv4);
%rotor
polefluxrot=abs(NfIf/2*mu0/g*bp*(L/2) - (L/2)*Fs*mu0/g*R/p*2*sin(phi)*sin(p*bp/2/R)) ;
polefluxrotH=polefluxrot;
if rsb<polefluxrot/Bsat*R/bp/(L/2)
satsomewhere=1;
end
lambda0=mu0*(1/g2+bp/2/tp*(1/g1-1/g2));
lambda1=2*mu0/pi*(1/g1-1/g2)*sin(bp/2/tp*pi);
lambda2=2*mu0/2/pi*(1/g1-1/g2)*sin(2*bp/2/tp*pi);
lambda1a=2*mu0/pi*(1/g1-1/g2)*sin(bp/2/tp*pi);
B0=Fr*lambda0-Fs*lambda1a*sin(phi)/2;
B1=sqrt( (Fr*lambda1-Fs*(lambda0+lambda2/2)*sin(phi))^2 + (Fs*(lambda0-
lambda2/2)*cos(phi))^2 );
totalfluxrot=polefluxrot*p;
Rcpi=sqrt(rsb^2-totalfluxrot/Bsat/pi);
%stator

Bt=(B0+B1)/toothfrac;
BtH=Bt;
if Bt>Bsat
satsomewhere=1;
```

```
end
%note that for polefluxstat we are ignoring DC
polefluxstat=R*(L/2)*B1*2/p ;
polefluxstatH=polefluxstat;
polefluxstat2=R*(L/2)*B1*2/p+B0*tp*(L/2);
cA=2*R*(L/2)/p*Fr*lambda1;
cB=-2/p*(L/2)*R*Fs*lambda0;
cC=1/p*(L/2)*R*Fs*lambda2;
polefluxstatcheck=sqrt((cA+(cB-cC)*sin(phi))^2+((cB+cC)*cos(phi))^2);
B0statslotbot=B0/(1+kslotstat);
if B0statslotbot>Bsat
%T=inf;
satsomewhere=1;
end
T=polefluxstat/2/(L/2)/(sqrt(Bsat^2-B0statslotbot^2));
T2=polefluxstat2/2/Bsat/(L/2);
totalfluxstat=B0*2*pi*R*(L/2);

if statbotrad<R*(1+kslotstat)+T
satsomewhere=1;
end

maxpoleflux=(NfIf/2+3/2*Ns*Is(mv4)/2/p/a)*mu0/g*tp*(L/2);

if sizingtype==1
ri=Rcpi;
else
ri=min(Rcpi,(1-1.7*kslotrot)*R);
end
if sizingtype==1
Router=sqrt(totalfluxstat/Bsat/pi+(statbotrad)^2);
else
Router=max(sqrt(totalfluxstat/Bsat/pi+(statbotrad)^2),sqrt(rsb^2-ri^2+statbotrad^2));
end
Rout=Router;
RoutH=Rout;
ri=0.02;
riH=ri;

if sizingtype==1
kbiH=T/R;
else
kbiH=max(kbi*R,T)/R;
end

if drawmachines
drawhia1
sidehia1
end

end
```

F.1.12 Determine Materials Cost
```
%%%%%%%
%cost.m%
%%%%%%%
%determine materials cost
if machinetype==1
%non-salient pole wound field
mrotback=pi*(rsb^2 - rimin^2)*L*steeldensity; %mass of rotor back iron
mrotteeth=pi*(ro^2-rsb^2)*L*toothfrac*steeldensity; %mass of rotor teeth
Lpolewire=LeffNS*nspp; %length of wire spanning one pole
%mass of field winding
mrotwind=pi*(ro^2-rsb^2)*(1-toothfrac)/nslots*(2*p)*Lpolewire*kpf*copperdensity;
%rotor cost
costrotNS=(mrotback+mrotteeth)*steelcostdensity+mrotwind*coppercostdensity;
%mass of stator back iron
mstatbackiron=pi*(Rout^2-rstatslotbot^2)*L*steeldensity;
%mass of stator teeth
```

```
mstatteeth=stattoothwid*(rstatslotbot-rstatin)*L*nstatteeth*steeldensity;
%mass of armature winding
mstatwind=nslots*(Lturn/2)*Aslot*kpf*copperdensity;
%stator cost
coststatNS=(mstatbackiron+mstatteeth)*steelcostdensity+mstatwind*coppercostdensity;
%mass of machine
massNS=(mrotback+mrotteeth)+mrotwind+(mstatbackiron+mstatteeth)+mstatwind;
%cost of machine
costNS=costrotNS+coststatNS;


elseif machinetype==2
%salient pole wound field
mrotback=pi*(rsb^2 - (rimin)^2)*L*steeldensity;
Lhip=(rsb+ro)/2*pi/p*(1-polefrac)/4;
Lturni=2*L+(rsb+ro)*pi/2/p*(polefrac+1)+4*Lhip;
%mass of rotor poles
mrotpoles=2*p*((2*y03S)*(x03S-x04S)*L+(x01S-x02S)*(2*y02S)*L)*steeldensity;
%mass of rotor winding
mrotwind=2*p*((y02S-y03S)*(x03S-x04S)*L+2*(2*y02S)*(x03S-x04S)*(y02S-
y03S))*copperdensity;
%cost of rotor winding
costrotS=(mrotback+mrotpoles)*steelcostdensity+mrotwind*coppercostdensity;
%mass of stator back iron
mstatbackiron=pi*(Rout^2-rstatslotbot^2)*L*steeldensity;
%mass of stator teeth
mstatteeth=stattoothwid*(rstatslotbot-rstatin)*L*nstatteeth*steeldensity;
%mass of armature winding
mstatwind=nslots*(Lturn/2)*Aslot*kpf*copperdensity;
%cost of stator
coststatS=(mstatbackiron+mstatteeth)*steelcostdensity+mstatwind*coppercostdensity;
%mass of stator
massS=(mrotback+mrotpoles)+mrotwind+(mstatbackiron+mstatteeth)+mstatwind;
%cost of machine
costS=costrotS+coststatS;


elseif machinetype==3
%Lundell alternator
kc=(kLcoil+1)/2;
Lc=kc*L; %claw length
bp1=betap1*pi/p*R;
bp2=betap2*pi/p*R;
rpeb=kpeb*R;
if adjustk1
    kfpout=.8237; %for kpf=.35
    %kfpout=.05/R; %for kpf=.8;
end
rfpout=kfpout*R;
cb=rpeb-rfpout;
ca=bp1-bp2;
mcp=pi*(k2^2*(R^2)-rimin^2)*(kLcoil+2*ks)*L*steeldensity;
%mass of flux plate
mfluxplate=pi*(kpeb^2-k2^2)*(R^2)*ks*L*steeldensity;
%mass of pole top side
mpoletopside=pi*(ro^2-kpeb^2*(R^2))*ks*L*steeldensity*bp2/(2*tp);
%mass of field winding
mrotwind=pi*(k1^2-k2^2)*(R^2)*kLcoil*L*kpf*copperdensity;
%mass of pole top
mpoletop=(ro^2-kpeb^2*(R^2))/4*(betap1+betap2)*pi/p*kc*L*steeldensity;
kA=(bp1-bp2)/R/Lc;
B=(rpeb-rfpout)/Lc;
acon=(bp1-bp2)/Lc;
bcon=(rpeb-rfpout)/Lc;
acon1=bp1-bp2;
bcon1=rpeb-rfpout;
%mass of pole bottom
mpolebot=steeldensity*Lc/2/ro*((bp1+bp2)/2*rpeb^2-
acon1*(bcon1^2/4+2*rfpout*bcon1/3+rfpout^2/2)-bp2*(bcon1^2/3+2*rfpout*bcon1/2+rfpout^2));
%rotor cost
costrotL=(mcp+2*mfluxplate+2*mpoletopside+2*p*mpoletop+2*p*mpolebot)*steelcostdensity+mro
twind*coppercostdensity;
%mass of stator back iron
```

```
mstatbackiron=pi*(Rout^2-rstatslotbot^2)*L*steeldensity;
%mass of stator teeth
mstatteeth=stattoothwid*(rstatslotbot-rstatin)*L*nstatteeth*steeldensity;
%mass of armature winding
mstatwind=nslots*(Lturn/2)*Aslot*kpf*copperdensity;
%mass of stator
coststatL=(mstatbackiron+mstatteeth)*steelcostdensity+mstatwind*coppercostdensity;
%cost of machine
costL=costrotL+coststatL;
%mass of machine
massL=(mstatbackiron+mstatteeth)+mstatwind+(mcp+2*mfluxplate+2*mpoletopside+2*p*mpoletop+
2*p*mpolebot)+mrotwind;
else
%HIA
%mass of rotor back iron
mrotback=pi*(rsb^2 - (rimin)^2)*(1+kHcoil)*L*steeldensity;
%mass of rotor poles
mrotpoles=pi*(ro^2-rsb^2)*L*polefrac*steeldensity;
%cost of rotor
costrotH=(mrotback+mrotpoles)*steelcostdensity;
%mass of stator yoke
mstatyoke=pi*(Rout^2-statbotrad^2)*L*(1+kHcoil)*steeldensity;
%mass of stator back iron
mstatbackiron=pi*(statbotrad^2-rstatslotbot^2)*L*steeldensity;
%mass of stator teeth
mstatteeth=stattoothwid*(rstatslotbot-rstatin)*L*nstatteeth*steeldensity;
%mass of stator winding
mstatwind=nslots*(Lturn/2)*Aslot*kpf*copperdensity;
%mass of field winding
mstatfieldwind=pi*(statbotrad^2-rstatslotbot^2)*L*kHcoil*kpf*copperdensity;
%cost of stator
coststatH=(mstatyoke+mstatbackiron+mstatteeth)*steelcostdensity+(mstatfieldwind+mstatwind
)*coppercostdensity;
%mass of machine
massH=(mrotback+mrotpoles)+(mstatyoke+mstatbackiron+mstatteeth)+(mstatfieldwind+mstatwind
);
%cost of machine
costH=costrotH+coststatH;

end
```

F.1.13 Approximate Back-emf Calculation

```
%%%%%%%%%%%%%%%%%%
%backemfapprox.m%
%%%%%%%%%%%%%%%%%%%
%calculates approximate back-emf
function
[Eaf,validEaf]=backemfapprox(Lsdc,Lsac,loadvoltage,diodedrop,netoutputpower,Rfield,omegae
lec,Lafm)
%backemfapprox.m
%calculates backemf while ignoring armature resistance
%if Xd==Xq
%    Xq=Xq-1e-6;
%end

if Lsac==0
Lsac=1e-6;
end

y=((2*loadvoltage+4*diodedrop)/pi)^2;
m=omegaelec*Lsdc;
n=omegaelec*Lsac;
r=netoutputpower./loadvoltage;
s=Rfield/loadvoltage./(omegaelec*Lafm).^2;
f=3/pi;
a=s.^2.*(m-n).^2;
b=2*r.*s.*(m-n).^2-f.^2+4*n.*y.*s.^2.*(m-n);
c=f.^2*y+r.^2.*(m-n).^2+8.*n.*y.*r.*s.*(m-n)+4.*n.^2*y.^2.*s.^2;
d=4.*n.*y.*r.^2.*(m-n)+8*n.^2*y.^2.*r.*s;
e=4.*n.^2.*y.^2.*r.^2;
```

```
[Eafsquaredmat(:,1)]=roots([a(1),b(1),c(1),d(1),e(1)])
[Eafmat(:,1)]=sqrt(Eafsquaredmat(:,1));
Eaf=[];
validEaf=0;

if(all(imag(Eafmat(2,:))==0))
    validEaf=1;
    Eaf=Eafmat(2,:);
end

if validEaf
Xeq=m+n.*(2*y./(Eaf.^2)-1); %equivalent reactance
powerfactor=sqrt(y./Eaf.^2);
end
```

F.1.14 Exact Back-emf Calculation

```
%%%%%%%%%%%%%%%%%
%backemfexact.m%
%%%%%%%%%%%%%%%%%
%exact calculation of back-emf

function
[Eaf,validEaf,powang]=backEafexact(Lsdc,Lsac,loadvoltage,diodedrop,netoutputpower,Rfield,
Rarm,omegaelec,Lafm,Eafapprox)
r=netoutputpower./loadvoltage;
s=Rfield/loadvoltage./(omegaelec*Lafm).^2;
Vodp=loadvoltage/2+diodedrop;
k3=(4*Vodp/pi);
powerangle1=acos(4*Vodp/pi./Eafapprox);
%loadvoltage
%if Xd==Xq
%    Xq=Xq-1e-6;
%end
%if Lsac==0
%Lsac=1e-6;
%end
[Eaftemp powangtemp
validEaf]=findet(omegaelec,Lsdc,Lsac,Eafapprox,powerangle1,Rarm,r,s,k3);
Eaf=Eaftemp;
powang=powangtemp;

if validEaf==0
    return
end


%%%%%%%%%%
%findet.m%
%%%%%%%%%%

function [Emf,thetai,validEaf]=findet(omegaelec,Lsdc,Lsac,Emf,thetai,Rarm,r,s,k3)
%findet.m
%uses Newton's method to determine back-emf and internal power angle
deltaEmf=1;
deltathetai=1;
f1=1;
f2=1;
h=0.0001;
iter=0;
validEaf=1;
%implements Newton's method to solve nonlinear equation
while norm([deltaEmf deltathetai])>.01 | norm([f1 f2])>.01
%while norm([deltaEmf deltathetai])>.001 | norm([f1 f2])>.001
iter=iter+1;

if iter>500
    validEaf=0;
    return;
end
```

```
f1=getf1(omegaelec,Lsdc,Lsac,Emf,thetai,Rarm,r,s,k3);
f2=getf2(omegaelec,Lsdc,Lsac,Emf,thetai,Rarm,r,s,k3);

df1bydEmf=cendiff(1,1,omegaelec,Lsdc,Lsac,Emf,thetai,Rarm,r,s,k3,h);
df1bydthetai=cendiff(1,2,omegaelec,Lsdc,Lsac,Emf,thetai,Rarm,r,s,k3,h);
df2bydEmf=cendiff(2,1,omegaelec,Lsdc,Lsac,Emf,thetai,Rarm,r,s,k3,h);
df2bydthetai=cendiff(2,2,omegaelec,Lsdc,Lsac,Emf,thetai,Rarm,r,s,k3,h);
jac=[df1bydEmf df1bydthetai; df2bydEmf df2bydthetai];

xx=inv(jac)*[-f1;-f2];
deltaEmf=xx(1);
deltathetai=xx(2);
Emf=Emf+deltaEmf;
thetai=thetai+deltathetai;
if imag(Emf)~=0 | imag(thetai)~=0
    validEaf=0;
    return
end
end


%%%%%%%%%%%
%cendiff.m%
%%%%%%%%%%%
%approximates derivative by using central differenc
function dfdx=cendiff(f,x,omegaelec,Lsdc,Lsac,Emf,thetai,Rarm,r,s,k3,h)
%cendiff.m
if f==1
    if x==1
        fplus=getf1(omegaelec,Lsdc,Lsac,Emf+h,thetai,Rarm,r,s,k3);
        fminus=getf1(omegaelec,Lsdc,Lsac,Emf-h,thetai,Rarm,r,s,k3);
    else
        fplus=getf1(omegaelec,Lsdc,Lsac,Emf,thetai+h,Rarm,r,s,k3);
        fminus=getf1(omegaelec,Lsdc,Lsac,Emf,thetai-h,Rarm,r,s,k3);
    end
else
    if x==1
        fplus=getf2(omegaelec,Lsdc,Lsac,Emf+h,thetai,Rarm,r,s,k3);
        fminus=getf2(omegaelec,Lsdc,Lsac,Emf-h,thetai,Rarm,r,s,k3);
    else
        fplus=getf2(omegaelec,Lsdc,Lsac,Emf,thetai+h,Rarm,r,s,k3);
        fminus=getf2(omegaelec,Lsdc,Lsac,Emf,thetai-h,Rarm,r,s,k3);
    end
end
dfdx=(fplus-fminus)/(2*h);

%%%%%%%%%
%getf1.m%
%%%%%%%%%
function f1=getf1(omegaelec,Lsdc,Lsac,Emf,thetai,Rarm,r,s,k3)
%getf1.m
%determines first of two nonlinear equations used to determine
%backemf and internal power angle

%equivalent synchronous reactance
Xs=omegaelec*(Lsdc+Lsac.*cos(2.*thetai));
%Xs=omegaelec*Lsdc;
%equivalent armature resistance
Rs=-omegaelec*Lsac.*sin(2.*thetai)+Rarm;
R=(((Emf.^2)*Rs+k3*sqrt((Xs.^2).*(Emf.^2-k3^2)+Rs.^2.*Emf.^2))./(Emf.^2-k3^2));
f1=3/pi*Emf/sqrt( Xs^2 + (R)^2) - r - Emf^2* s;

%%%%%%%%%
%getf2.m%
%%%%%%%%%
function f2=getf2(omegaelec,Lsdc,Lsac,Emf,thetai,Rarm,r,s,k3)
%determines second of two nonlinear equations used to determine
%backemf and internal power angle
%equivalent synchronous reactance
Xs=omegaelec*(Lsdc+Lsac.*cos(2.*thetai));
%equivalent armature resistance
Rs=-omegaelec*Lsac.*sin(2.*thetai)+Rarm;
```

251

```
%power angle equation; searching for zero
R=(((Emf.^2)*Rs+k3*sqrt((Xs.^2).*(Emf.^2-k3^2)+Rs.^2.*Emf.^2))./(Emf.^2-k3^2));
f2=tan(thetai)- Xs/(R);
```

F.1.15 Draw Non-salient Wound Field Alternator

```
%%%%%%%%%%%%%%%%
%draw_cs_NSWF.m%
%%%%%%%%%%%%%%%%%%
%draws cross-section of NSWF
figure(1)
clf reset
drawcircles=0;
if drawcircles==0
subplot(121)
end
axis square
hs=drawsize;
axis([-drawsize drawsize -drawsize drawsize])
hold on
axis off
rstatout=Rout;
fill(rstatout*cos(linspace(0,2*pi)),rstatout*sin(linspace(0,2*pi)),'w');
line(ri*cos(linspace(0,2*pi)),ri*sin(linspace(0,2*pi)));
rotht=min(3/8*(2*pi/nrotteeth*ro-rottoothwid),rottoothwid/2);
roth0=min(rottoothht/10,rotht);
y04=rottoothwid/2;
x04=rsb*cos(asin(rottoothwid/2/rsb));
x03=ro-roth0-rotht;
y03=y04;
x02=x03+rotht;
y02=y03+rotht;
x01=ro*cos(asin(y02/ro));
y01=y02;
rang=0;
linx1=linspace(x02,x01);
liny1=linspace(y02,y01);
linx2=linspace(x03,x02);
liny2=linspace(y03,y02);
linx3=linspace(x04,x03);
liny3=linspace(y04,y03);
xc=[x03,rsb*cos(linspace(asin(y04/rsb),2*pi/nrotteeth-
asin(y04/rsb))),sqrt(x03^2+y03^2)*cos(linspace(2*pi/nrotteeth-
asin(y03/x03),asin(y03/x03)))];
yc=[y03,rsb*sin(linspace(asin(y04/rsb),2*pi/nrotteeth-
asin(y04/rsb))),sqrt(x03^2+y03^2)*sin(linspace(2*pi/nrotteeth-
asin(y03/x03),asin(y03/x03)))];
xcg=[x01,x02,sqrt(x03^2+y03^2)*cos(linspace(asin(y03/x03),1/2*2*pi/nrotteeth)),ro*cos(1/2
*2*pi/nrotteeth)];
ycg=[y01,y02,sqrt(x03^2+y03^2)*sin(linspace(asin(y03/x03),1/2*2*pi/nrotteeth)),ro*sin(1/2
*2*pi/nrotteeth)];
for copy=1:nrotteeth
fill(xc*cos(rang)-yc*sin(rang),yc*cos(rang)+xc*sin(rang),'y');
fill(xcg*cos(rang)-ycg*sin(rang),ycg*cos(rang)+xcg*sin(rang),'k');
fill(xcg*cos(rang)+ycg*sin(rang),-ycg*cos(rang)+xcg*sin(rang),'k');
line(ro*cos(linspace(-asin(y02/ro)+rang,asin(y02/ro)+rang)),ro*sin(linspace(-
asin(y02/ro)+rang,asin(y02/ro)+rang)));
line(rsb*cos(linspace(asin(y03/rsb)+rang,1/2*2*pi/nrotteeth+rang)),
rsb*sin(linspace(asin(y03/rsb)+rang,1/2*2*pi/nrotteeth+rang)));
line(rsb*cos(linspace(-asin(y03/rsb)+rang,-1/2*2*pi/nrotteeth+rang)), rsb*sin(linspace(-
asin(y03/rsb)+rang,-1/2*2*pi/nrotteeth+rang)));
line(linx1*cos(rang)-liny1*sin(rang),liny1*cos(rang)+linx1*sin(rang));
line(linx1*cos(rang)+liny1*sin(rang),-liny1*cos(rang)+linx1*sin(rang));
line(linx2*cos(rang)-liny2*sin(rang),liny2*cos(rang)+linx2*sin(rang));
line(linx2*cos(rang)+liny2*sin(rang),-liny2*cos(rang)+linx2*sin(rang));
line(linx3*cos(rang)-liny3*sin(rang),liny3*cos(rang)+linx3*sin(rang));
line(linx3*cos(rang)+liny3*sin(rang),-liny3*cos(rang)+linx3*sin(rang));
rang=rang+2*pi/nrotteeth;
end
```

```
if drawcircles==1
rr=rotht/2;
[xa,ya,xb,yb,x3,y3]=connect2lines(x01,y01,x02,y02,x03,y03,rr); %123
x07=xa(1);
y07=ya(1);
x08=xb(1);
y08=yb(1);
figure(1)
line(x3(1)+rr*cos(linspace(0,2*pi)),y3(1)+rr*sin(linspace(0,2*pi)))
line(x3(1)+rr*cos(linspace(0,2*pi)),-y3(1)+rr*sin(linspace(0,2*pi)))
[xa,ya,xb,yb,x3,y3]=connect2lines(x02,y02,x03,y03,x04,y04,rr); %234
x09=xa(1);
y09=ya(1);
x10=xb(1);
y10=yb(1);
figure(1);
line(x3(1)+rr*cos(linspace(0,2*pi)),y3(1)+rr*sin(linspace(0,2*pi)));
line(x3(1)+rr*cos(linspace(0,2*pi)),-y3(1)+rr*sin(linspace(0,2*pi)));
[xa,ya,xb,yb,x3,y3]=connecthorlinearc(x01,y01,x02,y02,ro,rr);
figure(1)
choice=7;
line(x3(choice)+rr*cos(linspace(0,2*pi)),y3(choice)+rr*sin(linspace(0,2*pi)));
line(x3(choice)+rr*cos(linspace(0,2*pi)),-y3(choice)+rr*sin(linspace(0,2*pi)));
x05=xa(choice);
y05=ya(choice);
x06=xb(choice);
y06=yb(choice);
[xa,ya,xb,yb,x3,y3]=connecthorlinearc(x04,y04,x03,y03,rsb,(rotslotwid/3));
figure(1)
choice=1;
line(x3(choice)+(rotslotwid/3)*cos(linspace(0,2*pi)),y3(choice)+(rotslotwid/3)*sin(linspa
ce(0,2*pi)));
line(x3(choice)+(rotslotwid/3)*cos(linspace(0,2*pi)),-
y3(choice)+(rotslotwid/3)*sin(linspace(0,2*pi)));
x11=xb(choice);
y11=yb(choice);
x12=xa(choice);
y12=ya(choice);
end
ht=min(3/8*(2*pi/nstatteeth*rstatin-stattoothwid),stattoothwid/2);
h0=min(stattoothht/10,ht);
y24=stattoothwid/2;
alpha=asin(stattoothwid/2/rstatslotbot);
x24=rstatslotbot*cos(asin(alpha));
x23=x24-stattoothht+h0+ht;
y23=y24;
x22=x23-ht;
y22=y23+ht;
y21=y22;
x21=rstatin*cos(asin(y22/rstatin));
x25=rstatslotbot*cos(1/2*2*pi/nstatteeth);
y25=rstatslotbot*sin(1/2*2*pi/nstatteeth);
x26=rstatin*cos(1/2*2*pi/nstatteeth);
y26=rstatin*sin(1/2*2*pi/nstatteeth);
rang=0;
linx21=linspace(x22,x21);
liny21=linspace(y22,y21);
linx22=linspace(x23,x22);
liny22=linspace(y23,y22);
linx23=linspace(x24,x23);
liny23=linspace(y24,y23);
xcoordsf=[x23,rstatslotbot*cos(linspace(asin(alpha),2*pi/nstatteeth-
asin(alpha))),sqrt(x23^2+y23^2)*cos(linspace(2*pi/nstatteeth-
asin(y23/x23),asin(y23/x23)))];
ycoordsf=[y23,rstatslotbot*sin(linspace(asin(alpha),2*pi/nstatteeth-
asin(alpha))),sqrt(x23^2+y23^2)*sin(linspace(2*pi/nstatteeth-
asin(y23/x23),asin(y23/x23)))];
xcoordsg=[x21,x22,sqrt(x23^2+y23^2)*cos(linspace(asin(y23/x23),1/2*2*pi/nstatteeth)),x26]
;
```

```
ycoordsg=[y21,y22,sqrt(x23^2+y23^2)*sin(linspace(asin(y23/x23),1/2*2*pi/nstatteeth)),y26]
;
for copy=1:nstatteeth
line(rstatin*cos(linspace(-
asin(y21/rstatin)+rang,asin(y21/rstatin)+rang)),rstatin*sin(linspace(-
asin(y21/rstatin)+rang,asin(y21/rstatin)+rang)));
line(rstatslotbot*cos(linspace(asin(alpha)+rang,2*pi/2/nstatteeth+rang)),
rstatslotbot*sin(linspace(asin(alpha)+rang,2*pi/2/nstatteeth+rang)));
line(rstatslotbot*cos(linspace(-asin(alpha)+rang,-2*pi/2/nstatteeth+rang)),
rstatslotbot*sin(linspace(-asin(alpha)+rang,-2*pi/2/nstatteeth+rang)));
line(linx21*cos(rang)-liny21*sin(rang),liny21*cos(rang)+linx21*sin(rang));
line(linx21*cos(rang)+liny21*sin(rang),-liny21*cos(rang)+linx21*sin(rang));
line(linx22*cos(rang)-liny22*sin(rang),liny22*cos(rang)+linx22*sin(rang));
line(linx22*cos(rang)+liny22*sin(rang),-liny22*cos(rang)+linx22*sin(rang));
line(linx23*cos(rang)-liny23*sin(rang),liny23*cos(rang)+linx23*sin(rang));
line(linx23*cos(rang)+liny23*sin(rang),-liny23*cos(rang)+linx23*sin(rang));
fill(xcoordsf*cos(rang)-ycoordsf*sin(rang),ycoordsf*cos(rang)+xcoordsf*sin(rang),'r');
fill(xcoordsg*cos(rang)-ycoordsg*sin(rang),ycoordsg*cos(rang)+xcoordsg*sin(rang),'k');
fill(xcoordsg*cos(rang)+ycoordsg*sin(rang),-ycoordsg*cos(rang)+xcoordsg*sin(rang),'k');
rang=rang+2*pi/nstatteeth;
end
line(rstatout*cos(linspace(0,2*pi)),rstatout*sin(linspace(0,2*pi)));
fill([rstatin*cos(linspace(0,2*pi))
ro*cos(linspace(0,2*pi))],[rstatin*sin(linspace(0,2*pi)) ro*sin(linspace(0,2*pi))],'k');
fill([ri*cos(linspace(0,2*pi)) ],[ri*sin(linspace(0,2*pi))],'w');




%%%%%%%%%%%%%%%%%%
%draw_side_NSWF.m%
%%%%%%%%%%%%%%%%%%
%draws a sectional cut of non-salient wound field alternator
figure(1);
if drawcircles==0
subplot(122)
end
imdim=drawsize;
axis([-1 1 -1 1]*imdim);
axis('square','off');
hold on;
sh=statendturnwid;
rh=2.5*(rotslotwid+rottoothwid);
rout=Rout;
rsin=rstatin;
rrout=ro;
rin=ri;
rbs=rstatslotbot;
rbr=rsb;
fill([-L/2 L/2 L/2 -L/2],[rout rout -rout -rout],'w')
fill([-L/2 L/2 L/2 -L/2],[rsin rsin -rsin -rsin],'k')
fill([-L/2 L/2 L/2 -L/2],[rrout rrout -rrout -rrout],'w')
fill([-L/2 L/2 L/2 -L/2],[rin rin -rin -rin],'w')
fill([-(L/2+sh) -L/2 -L/2 -1*(L/2+sh)],[rbs rbs (rsin+h0+ht) (rsin+h0+ht)],'r')
fill([(L/2+sh) L/2 L/2 (L/2+sh)],[rbs rbs (rsin+h0+ht) (rsin+h0+ht)],'r')
fill([-(L/2+rh) -L/2 -L/2 -1*(L/2+rh)],[(rrout-roth0-rotht) (rrout-roth0-rotht) rbr
rbr],'y')
fill([(L/2+rh) L/2 L/2 (L/2+rh)],[(rrout-roth0-rotht) (rrout-roth0-rotht) rbr rbr],'y')
fill([-(L/2+sh) -L/2 -L/2 -1*(L/2+sh)],[-rbs -rbs -(rsin+h0+ht) -(rsin+h0+ht)],'r')
fill([(L/2+sh) L/2 L/2 (L/2+sh)],[-rbs -rbs -(rsin+h0+ht) -(rsin+h0+ht)],'r')
fill([-(L/2+rh) -L/2 -L/2 -1*(L/2+rh)],[-(rrout-roth0-rotht) -(rrout-roth0-rotht) -rbr -
rbr],'y')
fill([(L/2+rh) L/2 L/2 (L/2+rh)],[-(rrout-roth0-rotht) -(rrout-roth0-rotht) -rbr -
rbr],'y')
```

F.1.16 Draw Salient Wound Field Alternator

```
%%%%%%%%%%%%%%%%%%
%draw_cs_SWF.m%
%%%%%%%%%%%%%%%%%%
%draws cross-section of SWF
figure(2)
```

```
drawcircles=0;
clf reset
if drawcircles==0
subplot(121)
end
axis square
axis([-drawsize drawsize -drawsize drawsize])
hold on
axis off
rstatout=Rout;
fill(rstatout*cos(linspace(0,2*pi)),rstatout*sin(linspace(0,2*pi)),'w');
line(ri*cos(linspace(0,2*pi)),ri*sin(linspace(0,2*pi)));
x01=ro*cos(1/2*polefrac*2*pi/(2*p));
y01=ro*sin(1/2*polefrac*2*pi/(2*p));
x02=x01-(ro-rsb)*kwindtS;;%10
y02=y01;
x03=x02;
y03=y02-kwindS*ro*polefrac*2*pi/(2*p);%20
x04=rsb*cos(asin(y03/rsb));
y04=y03;
x01S=x01;
x02S=x02;
y02S=y02;
y03S=y03;
x03S=x03;
x04S=x04;
fieldcopperareaS=(y02-y03)*(x03-x04);
rang=0;
linx1=linspace(x02,x01);
liny1=linspace(y02,y01);
linx2=linspace(x03,x02);
liny2=linspace(y03,y02);
linx3=linspace(x04,x03);
liny3=linspace(y04,y03);

xc=[x04,x03,x02,x01,ro*cos(linspace(1/2*polefrac*2*pi/(2*p),1/2*2*pi/(2*p))),rsb*cos(lins
pace(1/2*2*pi/(2*p),asin(y03/rsb)))];
yc=[y04, y03, y02, y01, ro*sin(linspace(1/2*polefrac*2*pi/(2*p),1/2*2*pi/(2*p))),
rsb*sin(linspace(1/2*2*pi/(2*p),asin(y03/rsb)))];
xcw=[x04,x03,x02,x04];
ycw=[y04,y03,y02,y02];

for copy=1:2*p
line(ro*cos(linspace(-
1/2*polefrac*2*pi/(2*p)+rang,1/2*polefrac*2*pi/(2*p)+rang)),ro*sin(linspace(-
1/2*polefrac*2*pi/(2*p)+rang,1/2*polefrac*2*pi/(2*p)+rang)));
line(rsb*cos(linspace(asin(y03/rsb)+rang,1/2*2*pi/(2*p)+rang)),
rsb*sin(linspace(asin(y03/rsb)+rang,1/2*2*pi/(2*p)+rang)));
line(rsb*cos(linspace(-asin(y03/rsb)+rang,-1/2*2*pi/(2*p)+rang)), rsb*sin(linspace(-
asin(y03/rsb)+rang,-1/2*2*pi/(2*p)+rang)));

fill(xc*cos(rang)-yc*sin(rang),yc*cos(rang)+xc*sin(rang),'k');
fill(xc*cos(rang)+yc*sin(rang),-yc*cos(rang)+xc*sin(rang),'k');
fill(xcw*cos(rang)-ycw*sin(rang),ycw*cos(rang)+xcw*sin(rang),'y');
fill(xcw*cos(rang)+ycw*sin(rang),-ycw*cos(rang)+xcw*sin(rang),'y');

line(linx1*cos(rang)-liny1*sin(rang),liny1*cos(rang)+linx1*sin(rang));
line(linx1*cos(rang)+liny1*sin(rang),-liny1*cos(rang)+linx1*sin(rang));
line(linx2*cos(rang)-liny2*sin(rang),liny2*cos(rang)+linx2*sin(rang));
line(linx2*cos(rang)+liny2*sin(rang),-liny2*cos(rang)+linx2*sin(rang));
line(linx3*cos(rang)-liny3*sin(rang),liny3*cos(rang)+linx3*sin(rang));
line(linx3*cos(rang)+liny3*sin(rang),-liny3*cos(rang)+linx3*sin(rang));
rang=rang+2*pi/(2*p);
end
if drawcircles==1
rr=(ro-rsb)*kwindtS/2;
[xa,ya,xb,yb,x3,y3]=connecthorlinearc(x01,y01,x02,y02,ro,rr);
figure(2)
choice=7;
line(x3(choice)+rr*cos(linspace(0,2*pi)),y3(choice)+rr*sin(linspace(0,2*pi)));
line(x3(choice)+rr*cos(linspace(0,2*pi)),-y3(choice)+rr*sin(linspace(0,2*pi)));
```

255

```
x05=xa(choice);
y05=ya(choice);
x06=xb(choice);
y06=yb(choice);

rrb=(kwindS*ro*polefrac*2*pi/(2*p))/2;
[xa,ya,xb,yb,x3,y3]=connecthorlinearc(x04,y04,x03,y03,rsb,rrb);
figure(2)
choice=1;
line(x3(choice)+rrb*cos(linspace(0,2*pi)),y3(choice)+rrb*sin(linspace(0,2*pi)));
line(x3(choice)+rrb*cos(linspace(0,2*pi)),-y3(choice)+rrb*sin(linspace(0,2*pi)));
x12=xa(choice);
y12=ya(choice);
x11=xb(choice);
y11=yb(choice);
x07=x02+rr;
y07=y02;
x08=x02;
y08=y02-rr;
line(x07+rr*cos(linspace(0,2*pi)),y08+rr*sin(linspace(0,2*pi)));
line(x07+rr*cos(linspace(0,2*pi)),-y08+rr*sin(linspace(0,2*pi)));
x09=x03;
y09=y03+rr;
x10=x03-rr;
y10=y03;
line(x10+rr*cos(linspace(0,2*pi)),y09+rr*sin(linspace(0,2*pi)));
line(x10+rr*cos(linspace(0,2*pi)),-y09+rr*sin(linspace(0,2*pi)));


%%%%%%%%%%%%%%%%%%
%draw_side_SWF.m%
%%%%%%%%%%%%%%%%%%
%draws sectional cut of SWF

figure(2)
subplot(122)
%clf reset;
imdim=drawsize;
axis([-1 1 -1 1]*imdim);
axis('square','off');
hold on;
sh=statendturnwid;
rh=y02-y03;
rout=rstatout;
rsin=rstatin;
rrout=ro;
rbs=rstatslotbot;
rbr=rsb;
rin=ri;
fill([-L/2 L/2 L/2 -L/2],[rout rout -rout -rout],'w')
fill([-L/2 L/2 L/2 -L/2],[rsin rsin -rsin -rsin],'k')
fill([-L/2 L/2 L/2 -L/2],[rrout rrout -rrout -rrout],'w')
fill([-L/2 L/2 L/2 -L/2],[rin rin -rin -rin],'w')
fill([-(L/2+sh) -L/2 -L/2 -1*(L/2+sh)],[rbs rbs (rsin+h0+ht) (rsin+h0+ht)],'r')
fill([(L/2+sh) L/2 L/2 (L/2+sh)],[rbs rbs (rsin+h0+ht) (rsin+h0+ht)],'r')
fill([-(L/2+rh) -L/2 -L/2 -1*(L/2+rh)],[(rrout-(ro-rsb)*kwindtS) (rrout-(ro-rsb)*kwindtS) rbr rbr],'y')
fill([(L/2+rh) L/2 L/2 (L/2+rh)],[(rrout-(ro-rsb)*kwindtS) (rrout-(ro-rsb)*kwindtS) rbr rbr],'y')
fill([-(L/2+sh) -L/2 -L/2 -1*(L/2+sh)],[-rbs -rbs -(rsin+h0+ht) -(rsin+h0+ht)],'r')
fill([(L/2+sh) L/2 L/2 (L/2+sh)],[-rbs -rbs -(rsin+h0+ht) -(rsin+h0+ht)],'r')
fill([-(L/2+rh) -L/2 -L/2 -1*(L/2+rh)],[-(rrout-(ro-rsb)*kwindtS) -(rrout-(ro-rsb)*kwindtS) -rbr -rbr],'y')
fill([(L/2+rh) L/2 L/2 (L/2+rh)],[-(rrout-(ro-rsb)*kwindtS) -(rrout-(ro-rsb)*kwindtS) -rbr -rbr],'y')
```

F.1.17 Draw Lundell Alternator

```
%%%%%%%%%%%%%%%%
%draw_cs_Lundell.m%
%%%%%%%%%%%%%%%%%%
%draws cross-section of Lundell

figure(3)
clf reset
%subplot(121)
axis square
axis([-drawsize drawsize -drawsize drawsize])
hold on
axis off
rfpout=kfpout*R;%80
rpeb=kpeb*R;%90
rr=3/1000;
drawcircles=0;
tp=2*pi*ro/(2*p); %only for drawing purposes
thetap=2*pi/(2*p);

rstatout=Rout;
fill(rstatout*cos(linspace(0,2*pi)),rstatout*sin(linspace(0,2*pi)),'w');
line(ri*cos(linspace(0,2*pi)),ri*sin(linspace(0,2*pi)));
x01=ro*cos(1/2*betap3*thetap);
y01=ro*sin(1/2*betap3*thetap);
x02=rfpout*cos(asin(y01/rfpout));
y02=y01;
x02=rfpout*cos(1/2*betap3*thetap);
y02=rfpout*sin(1/2*betap3*thetap);
x01e=ro*cos(1/2*betap1*thetap);
y01e=ro*sin(1/2*betap1*thetap);
x02e=rpeb*cos(asin(y01e/rpeb));
y02e=y01e;
x02e=rpeb*cos(1/2*betap1*thetap);
y02e=rpeb*sin(1/2*betap1*thetap);
rang=thetap;
linx1=linspace(x02,x01);
liny1=linspace(y02,y01);
linx1e=linspace(x02e,x01e);
liny1e=linspace(y02e,y01e);
linx2e=linspace(x02,x02e);
liny2e=linspace(y02,y02e);
xc=[x02,x01,ro*cos(linspace(1/2*betap1*thetap,1/2*2*pi/(2*p))),rfpout*cos(linspace(1/2*2*
pi/(2*p),asin(y02/rfpout)))];
yc=[y02,y01,ro*sin(linspace(1/2*betap1*thetap,1/2*2*pi/(2*p))),rfpout*sin(linspace(1/2*2*
pi/(2*p),asin(y02/rfpout)))];
for copy=1:2*p
fill(xc*cos(rang)-yc*sin(rang),yc*cos(rang)+xc*sin(rang),'k');
fill(xc*cos(rang)+yc*sin(rang),-yc*cos(rang)+xc*sin(rang),'k');
line(rfpout*cos(linspace(asin(y02/rfpout)+rang,1/2*thetap+rang)),rfpout*sin(linspace(asin
(y02/rfpout)+rang,1/2*thetap+rang)));
line(rfpout*cos(linspace(-asin(y02/rfpout)+rang,-1/2*thetap+rang)),rfpout*sin(linspace(-
asin(y02/rfpout)+rang,-1/2*thetap+rang)));
line(ro*cos(linspace(-1/2*betap3*thetap+rang,1/2*betap3*thetap+rang)),ro*sin(linspace(-
1/2*betap3*thetap+rang,1/2*betap3*thetap+rang)));
line(linx1*cos(rang)-liny1*sin(rang),liny1*cos(rang)+linx1*sin(rang));
line(linx1*cos(rang)+liny1*sin(rang),-liny1*cos(rang)+linx1*sin(rang));
rang=rang+thetap;
end
rang=thetap;
for copy=1:p
line(rfpout*cos(linspace(-
asin(y02/rfpout)+rang,asin(y02/rfpout)+rang)),rfpout*sin(linspace(-
asin(y02/rfpout)+rang,asin(y02/rfpout)+rang)));
line(rpeb*cos(linspace(-asin(y02e/rpeb)+rang,asin(y02e/rpeb)+rang)),rpeb*sin(linspace(-
asin(y02e/rpeb)+rang,asin(y02e/rpeb)+rang)));
line(linx1e*cos(rang)-liny1e*sin(rang),liny1e*cos(rang)+linx1e*sin(rang));
line(linx1e*cos(rang)+liny1e*sin(rang),-liny1e*cos(rang)+linx1e*sin(rang));
line(linx1e*cos(rang)-liny1e*sin(rang),liny1e*cos(rang)+linx1e*sin(rang));
line(linx1e*cos(rang)+liny1e*sin(rang),-liny1e*cos(rang)+linx1e*sin(rang));
```

```
line(linx2e*cos(rang)-liny2e*sin(rang),liny2e*cos(rang)+linx2e*sin(rang));
line(linx2e*cos(rang)+liny2e*sin(rang),-liny2e*cos(rang)+linx2e*sin(rang));
rang=rang+2*thetap;
end
if drawcircles==1
[xa,ya,xb,yb,x3,y3]=connectlinearc(x01,y01,x02,y02,ro,rr);
figure(3)
ind=5;
line(x3(ind)+rr*cos(linspace(0,2*pi)),y3(ind)+rr*sin(linspace(0,2*pi)));
line(x3(ind)+rr*cos(linspace(0,2*pi)),-y3(ind)+rr*sin(linspace(0,2*pi)));
x03=xa(ind);
y03=ya(ind);
x04=xb(ind);
y04=yb(ind);
[xa,ya,xb,yb,x3,y3]=connectlinearc(x02,y02,x01,y01,rfpout,rr);
figure(3)
ind=9;
line(x3(ind)+rr*cos(linspace(0,2*pi)),y3(ind)+rr*sin(linspace(0,2*pi)));
line(x3(ind)+rr*cos(linspace(0,2*pi)),-y3(ind)+rr*sin(linspace(0,2*pi)));
x06=xa(ind);
y06=ya(ind);
x05=xb(ind);
y05=yb(ind);
ind=7;
line(x3(ind)+rr*cos(linspace(0,2*pi)),y3(ind)+rr*sin(linspace(0,2*pi)));
line(x3(ind)+rr*cos(linspace(0,2*pi)),-y3(ind)+rr*sin(linspace(0,2*pi)));
x09=xb(ind);
y09=yb(ind);
x10=xa(ind);
y10=ya(ind);

[xa,ya,xb,yb,x3,y3]=connectlinearc(x01e,y01e,x02e,y02e,ro,rr);
figure(3)
ind=5;
line(x3(ind)+rr*cos(linspace(0,2*pi)),y3(ind)+rr*sin(linspace(0,2*pi)));
line(x3(ind)+rr*cos(linspace(0,2*pi)),-y3(ind)+rr*sin(linspace(0,2*pi)));
x03e=xa(ind);
y03e=ya(ind);
x04e=xb(ind);
y04e=yb(ind);
[xa,ya,xb,yb,x3,y3]=connectlinearc(x02e,y02e,x01e,y01e,rpeb,rr);
figure(3)
ind=7;
line(x3(ind)+rr*cos(linspace(0,2*pi)),y3(ind)+rr*sin(linspace(0,2*pi)));
line(x3(ind)+rr*cos(linspace(0,2*pi)),-y3(ind)+rr*sin(linspace(0,2*pi)));
x06e=xa(ind);
y06e=ya(ind);
x05e=xb(ind);
y05e=yb(ind);
end
rstatin=R+g/2;
nstatteeth=2*p*6;
realstattoothfrac=toothfrac;
toothwidth=2*pi/nstatteeth*(ro+rstatin)/2*realstattoothfrac;
rstatslotbot=R*(1+kslotstat);
rstatout=Rout;
stattoothwid=realstattoothfrac*2*pi/nstatteeth*(ro+rstatin)/2;
statslotwid=1/2*( rstatin*(2*pi/nstatteeth-2*asin(stattoothwid/2/rstatin)) +
rstatslotbot*(2*pi/nstatteeth-2*asin(stattoothwid/2/rstatslotbot)));
theta=asin(statslotwid/(statslotwid+stattoothwid));
statendturnwid=(3*stattoothwid+2.5*statslotwid)*tan(theta)+statslotwid;
stattoothht=rstatslotbot-rstatin;
ht=min(3/8*(2*pi/nstatteeth*rstatin-stattoothwid),stattoothwid/2);
h0=min(stattoothht/10,ht);
y24=stattoothwid/2;
alpha=asin(stattoothwid/2/rstatslotbot);
x24=rstatslotbot*cos(asin(alpha));
x23=x24-stattoothht+h0+ht;
y23=y24;
x22=x23-ht;
y22=y23+ht;
```

```
y21=y22;
x21=rstatin*cos(asin(y22/rstatin));
x25=rstatslotbot*cos(1/2*2*pi/nstatteeth);
y25=rstatslotbot*sin(1/2*2*pi/nstatteeth);
x26=rstatin*cos(1/2*2*pi/nstatteeth);
y26=rstatin*sin(1/2*2*pi/nstatteeth);
rang=0;
linx21=linspace(x22,x21);
liny21=linspace(y22,y21);
linx22=linspace(x23,x22);
liny22=linspace(y23,y22);
linx23=linspace(x24,x23);
liny23=linspace(y24,y23);
xcoordsf=[x23,rstatslotbot*cos(linspace(asin(alpha),2*pi/nstatteeth-
asin(alpha))),sqrt(x23^2+y23^2)*cos(linspace(2*pi/nstatteeth-
asin(y23/x23),asin(y23/x23)))];
ycoordsf=[y23,rstatslotbot*sin(linspace(asin(alpha),2*pi/nstatteeth-
asin(alpha))),sqrt(x23^2+y23^2)*sin(linspace(2*pi/nstatteeth-
asin(y23/x23),asin(y23/x23)))];
xcoordsg=[x21,x22,sqrt(x23^2+y23^2)*cos(linspace(asin(y23/x23),1/2*2*pi/nstatteeth)),x26]
;
ycoordsg=[y21,y22,sqrt(x23^2+y23^2)*sin(linspace(asin(y23/x23),1/2*2*pi/nstatteeth)),y26]
;
for copy=1:nstatteeth
line(rstatin*cos(linspace(-
asin(y21/rstatin)+rang,asin(y21/rstatin)+rang)),rstatin*sin(linspace(-
asin(y21/rstatin)+rang,asin(y21/rstatin)+rang)));
line(rstatslotbot*cos(linspace(asin(alpha)+rang,2*pi/2/nstatteeth+rang)),
rstatslotbot*sin(linspace(asin(alpha)+rang,2*pi/2/nstatteeth+rang)));
line(rstatslotbot*cos(linspace(-asin(alpha)+rang,-2*pi/2/nstatteeth+rang)),
rstatslotbot*sin(linspace(-asin(alpha)+rang,-2*pi/2/nstatteeth+rang)));
line(linx21*cos(rang)-liny21*sin(rang),liny21*cos(rang)+linx21*sin(rang));
line(linx21*cos(rang)+liny21*sin(rang),-liny21*cos(rang)+linx21*sin(rang));
line(linx22*cos(rang)-liny22*sin(rang),liny22*cos(rang)+linx22*sin(rang));
line(linx22*cos(rang)+liny22*sin(rang),-liny22*cos(rang)+linx22*sin(rang));
line(linx23*cos(rang)-liny23*sin(rang),liny23*cos(rang)+linx23*sin(rang));
line(linx23*cos(rang)+liny23*sin(rang),-liny23*cos(rang)+linx23*sin(rang));
fill(xcoordsf*cos(rang)-ycoordsf*sin(rang),ycoordsf*cos(rang)+xcoordsf*sin(rang),'r');
fill(xcoordsg*cos(rang)-ycoordsg*sin(rang),ycoordsg*cos(rang)+xcoordsg*sin(rang),'k');
fill(xcoordsg*cos(rang)+ycoordsg*sin(rang),-ycoordsg*cos(rang)+xcoordsg*sin(rang),'k');
rang=rang+2*pi/nstatteeth;
end
line(rstatout*cos(linspace(0,2*pi)),rstatout*sin(linspace(0,2*pi)));
fill([rstatin*cos(linspace(0,2*pi))
ro*cos(linspace(0,2*pi))],[rstatin*sin(linspace(0,2*pi)) ro*sin(linspace(0,2*pi))],'k');
fill([ri*cos(linspace(0,2*pi)) ],[ri*sin(linspace(0,2*pi))],'w');


%%%%%%%%%%%%%%%%%%%%%%%%
%draw_side_Lundell.m%
%%%%%%%%%%%%%%%%%%%%%%%%
%draws sectional cut of Lundell
figure(3);
%subplot(122);

%sideview.m
%sectional view of machine
%clf reset;
axis square
axis off
axis([-drawsize drawsize -drawsize drawsize])
hold on;
samescale=1;
interstacklen=kLcoil*L;
stacklen=L/2;
innerrad=ri;
endturnwid=statendturnwid;
pp=p;
rottoprad=ro;
stattoprad=rstatin;
```

```
fill([-L/2 L/2 L/2 -L/2],[rstatin rstatin rstatout rstatout],'w')
fill([-L/2 L/2 L/2 -L/2],-[rstatin rstatin rstatout rstatout],'w')
sh=statendturnwid;
fill([-(L/2+sh) -L/2 -L/2 -1*(L/2+sh)],[rstatslotbot rstatslotbot (rstatin+h0+ht)
(rstatin+h0+ht)],'r')
fill([(L/2+sh) L/2 L/2 (L/2+sh)],[rstatslotbot rstatslotbot (rstatin+h0+ht)
(rstatin+h0+ht)],'r')
fill([-(L/2+sh) -L/2 -L/2 -1*(L/2+sh)],-[rstatslotbot rstatslotbot (rstatin+h0+ht)
(rstatin+h0+ht)],'r')
fill([(L/2+sh) L/2 L/2 (L/2+sh)],-[rstatslotbot rstatslotbot (rstatin+h0+ht)
(rstatin+h0+ht)],'r')
fill([-L/2 L/2 L/2 -L/2],[ro ro rstatin rstatin],'k')
fill([-L/2 L/2 L/2 -L/2],-[ro ro rstatin rstatin],'k')
fill(kLcoil*[-L/2 L/2 L/2 -L/2],[k2*R k2*R k1*R k1*R],'y')
fill(kLcoil*[-L/2 L/2 L/2 -L/2],-[k2*R k2*R k1*R k1*R],'y')
fill([-kLcoil*L/2 kLcoil*L/2 kLcoil*L/2 (kLcoil/2+ks)*L (kLcoil/2+ks)*L -(kLcoil/2+ks)*L
-(kLcoil/2+ks)*L L/2 L/2 -kLcoil*L/2],[k2*R k2*R kfpout*R kfpout*R ri ri ro ro kpeb*R
kfpout*R],'w');
if mod(p,2)==0
fill([-kLcoil*L/2 kLcoil*L/2 kLcoil*L/2 (kLcoil/2+ks)*L (kLcoil/2+ks)*L -(kLcoil/2+ks)*L
-(kLcoil/2+ks)*L L/2 L/2 -kLcoil*L/2],-[k2*R k2*R kfpout*R kfpout*R ri ri ro ro kpeb*R
kfpout*R],'w');
else
fill(-[kLcoil*L/2 kLcoil*L/2 kLcoil*L/2 (kLcoil/2+ks)*L (kLcoil/2+ks)*L -(kLcoil/2+ks)*L
-(kLcoil/2+ks)*L L/2 L/2 -kLcoil*L/2],-[k2*R k2*R kfpout*R kfpout*R ri ri ro ro kpeb*R
kfpout*R],'w');
end
fill([-(kLcoil/2+ks)*L (kLcoil/2+ks)*L (kLcoil/2+ks)*L -(kLcoil/2+ks)*L],[-ri -ri ri
ri],'w')
totallen=kLcoil*L+2*ks*L;
```

F.1.18 Draw Homopolar Inductor Alternator

```
%%%%%%%%%%%%%%%%
%draw_cs_HIA.m%
%%%%%%%%%%%%%%%%
%draws cross-section of homopolar inductor alternator

figure(4)
clf reset
drawcircles=0;
if drawcircles==0
subplot(121)
end
axis square
axis off
axis([-drawsize drawsize -drawsize drawsize])
hold on
rstatout=Rout;
fill(rstatout*cos(linspace(0,2*pi)),rstatout*sin(linspace(0,2*pi)),'w');
line(ri*cos(linspace(0,2*pi)),ri*sin(linspace(0,2*pi)));
x01=ro*cos(1/2*polefrac*2*pi/p);
y01=ro*sin(1/2*polefrac*2*pi/p);
x02=rsb*cos(1/2*polefrac*2*pi/p);
y02=rsb*sin(1/2*polefrac*2*pi/p);
rang=0;
linx1=linspace(x02,x01);
liny1=linspace(y02,y01);
for copy=1:p
line(ro*cos(linspace(-
1/2*polefrac*2*pi/p+rang,1/2*polefrac*2*pi/p+rang)),ro*sin(linspace(-
1/2*polefrac*2*pi/p+rang,1/2*polefrac*2*pi/p+rang)));
line(rsb*cos(linspace(1/2*polefrac*2*pi/p+rang,2*pi/(2*p)+rang)),
rsb*sin(linspace(1/2*polefrac*2*pi/p+rang,2*pi/(2*p)+rang)));
line(rsb*cos(linspace(-1/2*polefrac*2*pi/p+rang,-2*pi/(2*p)+rang)), rsb*sin(linspace(-
1/2*polefrac*2*pi/p+rang,-2*pi/(2*p)+rang)));
line(linx1*cos(rang)-liny1*sin(rang),liny1*cos(rang)+linx1*sin(rang));
line(linx1*cos(rang)+liny1*sin(rang),-liny1*cos(rang)+linx1*sin(rang));
if polefrac<1/2
```

```
radc=[rsb,ro,ro,rsb];
anglec=[1/2*polefrac*2*pi/p 1/2*polefrac*2*pi/p 1/2*2*pi/2/p 1/2*2*pi/2/p];
diff=1/2*2*pi/2/p-1/2*polefrac*2*pi/p;
fill(radc.*cos(anglec+rang),radc.*sin(anglec+rang),'k')
fill(radc.*cos(-anglec+rang),radc.*sin(-anglec+rang),'k')
fill(radc.*cos((anglec+diff)+rang),radc.*sin((anglec+diff)+rang),'k')
fill(radc.*cos(-(anglec+diff)+rang),radc.*sin(-(anglec+diff)+rang),'k')
end
rang=rang+2*pi/p;
end
if drawcircles==1
rr=(ro-rsb)/4;
[xa,ya,xb,yb,x3,y3]=connectlinearc(x01,y01,x02,y02,ro,rr);
figure(4)
line(x3(1)+rr*cos(linspace(0,2*pi)),y3(1)+rr*sin(linspace(0,2*pi)));
line(x3(1)+rr*cos(linspace(0,2*pi)),-y3(1)+rr*sin(linspace(0,2*pi)));
x03=xa(1);
y03=ya(1);
x04=xb(1);
y04=yb(1);

rr=(ro-rsb)/2;
[xa,ya,xb,yb,x3,y3]=connectlinearc(x02,y02,x01,y01,rsb,rr);
figure(4)
line(x3(9)+rr*cos(linspace(0,2*pi)),y3(9)+rr*sin(linspace(0,2*pi)));
line(x3(9)+rr*cos(linspace(0,2*pi)),-y3(9)+rr*sin(linspace(0,2*pi)));
x06=xa(13);
y06=ya(13);
x05=xb(9);
y05=yb(9);
end
ht=min(3/8*(2*pi/nstatteeth*rstatin-stattoothwid),stattoothwid/2);
h0=min(stattoothht/10,ht);

y24=stattoothwid/2;
alpha=asin(stattoothwid/2/rstatslotbot);
x24=rstatslotbot*cos(asin(alpha));
x23=x24-stattoothht+h0+ht;
y23=y24;
x22=x23-ht;
y22=y23+ht;
y21=y22;
x21=rstatin*cos(asin(y22/rstatin));
x25=rstatslotbot*cos(1/2*2*pi/nstatteeth);
y25=rstatslotbot*sin(1/2*2*pi/nstatteeth);
x26=rstatin*cos(1/2*2*pi/nstatteeth);
y26=rstatin*sin(1/2*2*pi/nstatteeth);
rang=0;
linx21=linspace(x22,x21);
liny21=linspace(y22,y21);
linx22=linspace(x23,x22);
liny22=linspace(y23,y22);
linx23=linspace(x24,x23);
liny23=linspace(y24,y23);
xcoordsf=[x23,rstatslotbot*cos(linspace(asin(alpha),2*pi/nstatteeth-
asin(alpha))),sqrt(x23^2+y23^2)*cos(linspace(2*pi/nstatteeth-
asin(y23/x23),asin(y23/x23)))];
ycoordsf=[y23,rstatslotbot*sin(linspace(asin(alpha),2*pi/nstatteeth-
asin(alpha))),sqrt(x23^2+y23^2)*sin(linspace(2*pi/nstatteeth-
asin(y23/x23),asin(y23/x23)))];
xcoordsg=[x21,x22,sqrt(x23^2+y23^2)*cos(linspace(asin(y23/x23),1/2*2*pi/nstatteeth)),x26]
;
ycoordsg=[y21,y22,sqrt(x23^2+y23^2)*sin(linspace(asin(y23/x23),1/2*2*pi/nstatteeth)),y26]
;
for copy=1:nstatteeth
line(rstatin*cos(linspace(-
asin(y21/rstatin)+rang,asin(y21/rstatin)+rang)),rstatin*sin(linspace(-
asin(y21/rstatin)+rang,asin(y21/rstatin)+rang)));
line(rstatslotbot*cos(linspace(asin(alpha)+rang,2*pi/2/nstatteeth+rang)),
rstatslotbot*sin(linspace(asin(alpha)+rang,2*pi/2/nstatteeth+rang)));
```

```
line(rstatslotbot*cos(linspace(-asin(alpha)+rang,-2*pi/2/nstatteeth+rang)),
rstatslotbot*sin(linspace(-asin(alpha)+rang,-2*pi/2/nstatteeth+rang)));
line(linx21*cos(rang)-liny21*sin(rang),liny21*cos(rang)+linx21*sin(rang));
line(linx21*cos(rang)+liny21*sin(rang),-liny21*cos(rang)+linx21*sin(rang));
line(linx22*cos(rang)-liny22*sin(rang),liny22*cos(rang)+linx22*sin(rang));
line(linx22*cos(rang)+liny22*sin(rang),-liny22*cos(rang)+linx22*sin(rang));
line(linx23*cos(rang)-liny23*sin(rang),liny23*cos(rang)+linx23*sin(rang));
line(linx23*cos(rang)+liny23*sin(rang),-liny23*cos(rang)+linx23*sin(rang));

fill(xcoordsf*cos(rang)-ycoordsf*sin(rang),ycoordsf*cos(rang)+xcoordsf*sin(rang),'r');
fill(xcoordsg*cos(rang)-ycoordsg*sin(rang),ycoordsg*cos(rang)+xcoordsg*sin(rang),'k');
fill(xcoordsg*cos(rang)+ycoordsg*sin(rang),-ycoordsg*cos(rang)+xcoordsg*sin(rang),'k');
rang=rang+2*pi/nstatteeth;
end
line(rstatout*cos(linspace(0,2*pi)),rstatout*sin(linspace(0,2*pi)));
fill([rstatin*cos(linspace(0,2*pi))
ro*cos(linspace(0,2*pi))],[rstatin*sin(linspace(0,2*pi)) ro*sin(linspace(0,2*pi))],'k');
fill([ri*cos(linspace(0,2*pi)) ],[ri*sin(linspace(0,2*pi))],'w');
%statbotrad=R*(1+kslotstat+kbi);
line(statbotrad*cos(linspace(0,2*pi)),statbotrad*sin(linspace(0,2*pi)));



%%%%%%%%%%%%%%%%
%draw_side_HIA.m%
%%%%%%%%%%%%%%%%
%draws sectional cut of homopolar inductor alternator

figure(4);
subplot(122);
%sideview.m
%sectional view of machine
%clf reset;
axis square
axis off
%imagesize=1000;
axis([-drawsize drawsize -drawsize drawsize])
hold on;
samescale=1;
interstacklen=kHcoil*L;
stacklen=L/2;
innerrad=ri;
endturnwid=statendturnwid;
pp=p;
rottoprad=ro;
stattoprad=rstatin;
rotslotbotrad=rsb;
outerrad=rstatout;
statslotbotrad=rstatslotbot;
halfshaftlen=(interstacklen+2*stacklen)/2;
halfinterstacklen=interstacklen/2;
fill([-halfshaftlen halfshaftlen halfshaftlen -halfshaftlen],[-outerrad -outerrad
outerrad outerrad],'k')
fill([-halfshaftlen halfshaftlen halfshaftlen -halfshaftlen],[-innerrad -innerrad
innerrad innerrad],'w')
fill([-halfshaftlen halfshaftlen halfshaftlen -halfinterstacklen -halfinterstacklen -
halfshaftlen],[innerrad innerrad rotslotbotrad rotslotbotrad rottoprad rottoprad],'w')
line(-ones(1,100)*halfshaftlen,linspace(rottoprad,stattoprad))
line(ones(1,100)*halfshaftlen,linspace(rotslotbotrad,stattoprad))
if (mod(pp,2)==0)
     fill([-halfshaftlen halfshaftlen halfshaftlen -halfinterstacklen -halfinterstacklen
-halfshaftlen],[-innerrad -innerrad -rotslotbotrad -rotslotbotrad -rottoprad -
rottoprad],'w')
     line(ones(1,100)*halfshaftlen,linspace(-rotslotbotrad,-stattoprad));
     line(-ones(1,100)*halfshaftlen,linspace(-rottoprad,-stattoprad));
else
     fill([-halfshaftlen halfinterstacklen halfinterstacklen halfshaftlen halfshaftlen -
halfshaftlen],[-rotslotbotrad -rotslotbotrad -rottoprad -rottoprad -innerrad -
innerrad],'w')
     line(-ones(1,100)*halfshaftlen,linspace(-rotslotbotrad,-stattoprad));
     line(ones(1,100)*halfshaftlen,linspace(-rottoprad,-stattoprad));
end
```

```
fill([halfinterstacklen halfshaftlen halfshaftlen halfinterstacklen],[stattoprad
stattoprad statbotrad statbotrad],'w')
fill([halfinterstacklen halfshaftlen halfshaftlen halfinterstacklen],[-stattoprad -
stattoprad -statbotrad -statbotrad],'w')
fill([-halfinterstacklen -halfshaftlen -halfshaftlen -halfinterstacklen],[stattoprad
stattoprad statbotrad statbotrad],'w')
fill([-halfinterstacklen -halfshaftlen -halfshaftlen -halfinterstacklen],[-stattoprad -
stattoprad -statbotrad -statbotrad],'w')
fill([-halfshaftlen halfshaftlen halfshaftlen -halfshaftlen],[statbotrad statbotrad
outerrad outerrad],'w')
fill([-halfshaftlen halfshaftlen halfshaftlen -halfshaftlen],[-statbotrad -statbotrad -
outerrad -outerrad],'w')
fill([-halfinterstacklen halfinterstacklen halfinterstacklen -
halfinterstacklen],[statslotbotrad statslotbotrad statbotrad statbotrad],'y')
fill([-halfinterstacklen halfinterstacklen halfinterstacklen -halfinterstacklen],[-
statslotbotrad -statslotbotrad -statbotrad -statbotrad],'y')
fill([-halfinterstacklen halfinterstacklen halfinterstacklen -
halfinterstacklen],[(stattoprad+h0+ht) (stattoprad+h0+ht) statslotbotrad
statslotbotrad],'r')
fill([-halfinterstacklen halfinterstacklen halfinterstacklen -halfinterstacklen],[-
(stattoprad+h0+ht) -(stattoprad+h0+ht) -statslotbotrad -statslotbotrad],'r')
fill([halfshaftlen halfshaftlen+endturnwid halfshaftlen+endturnwid
halfshaftlen],[(stattoprad+h0+ht) (stattoprad+h0+ht) statslotbotrad statslotbotrad],'r')
fill([-halfshaftlen -(halfshaftlen+endturnwid) -(halfshaftlen+endturnwid) -
halfshaftlen],[(stattoprad+h0+ht) (stattoprad+h0+ht) statslotbotrad statslotbotrad],'r')
fill([halfshaftlen halfshaftlen+endturnwid halfshaftlen+endturnwid halfshaftlen],[-
(stattoprad+h0+ht) -(stattoprad+h0+ht) -statslotbotrad -statslotbotrad],'r')
fill([-halfshaftlen -(halfshaftlen+endturnwid) -(halfshaftlen+endturnwid) -
halfshaftlen],[-(stattoprad+h0+ht) -(stattoprad+h0+ht) -statslotbotrad -
statslotbotrad],'r')
totallength=interstacklen+2*stacklen;
```

F.2 PCB Transformer Code
F.2.1 PCB Transformer Output Versus Frequency

```
%%%%%%%%%%%%%%%%%
%analyzepcbvsf.m%
%%%%%%%%%%%%%%%%%
%determines output performance of pcb transformer as frequency is varied
method=2;
%1 picks freq for you given current you want
%2 picks current given frequency you have
withC4=0;
useknownparams=1;
withrectifier=1;
wresonancecap=0;
type=12;
filtertype=2; %1= constant current %2=constant voltage
accuracy=1; %1=no diode; 2=with diode; 3=with diode and resistor
simplify=0;
halfbridge=0; %1=halfbridge, 0=fullbridge
finterest=112.36e3;
finterest=400e3;
plottype='r'; %y,m,c,r,g,b,w,k, .,o,x,+,*,s,d,v,^,<,>,p,h,-,:,-.,--
f=linspace(1e3,1e6,1000); %frequencies for evaluation
sigma=5.8e7;%4.45e7; %copper conductivity
inchtom=2.54/100; %inch to meter conversion factor
miltom=25.4e-6; %mil to meter conversion factor
Di=2.4385*inchtom; %outer diameter of bobbin
Do=3.4555*inchtom; %inner diameter of bobbin
Nfield=65; %number of field turns
wfoil=23e-3; %width of copper foil
tfoil=6.2*miltom; %thickness of copper foil
%Rinterest=Nfield*pi*(Do+Di)/2/sigma/wfoil/tfoil; %field winding resistance
Rinterest=.0902;
Ifieldreqd=18
Jpredict=Ifieldreqd/(wfoil*tfoil); %field winding current density
plotall=0;
plotnone=0;
diodedrop=0.35;%rectifier diode drop : schottky diodes
```

263

```
if useknownparams
C12=3.2630e-011; %calculated
n=4/2;
Lp=0.969e-6;
Lsec=0.307e-6;
Mps=(2.043e-6-(Lp+Lsec))/2;
a0=0.0494
a1=2.9861e-007
a2=-5.5736e-013
a3=6.6569e-019
a4=-2.7291e-025
b0=0.0321
b1=8.2500e-008
b2=-1.1362e-013
b3=1.1968e-019 ·
b4=-4.3914e-026
Rp=a0+a1*f+a2*(f.^2)+a3*(f.^3)+a4*(f.^4);
Rs=b0+b1*f+b2*(f.^2)+b3*(f.^3)+b4*(f.^4);
end
k=Mps/sqrt(Lp*Lsec); %coupling coefficient
Llkp=Lp-n*Mps; %primary leakage inductance
Llks=Lsec-(1/n)*Mps; %secondary leakage inductance
C1=0;
fresonantdesired=finterest;
Rinterest=0.0902
Rfield=Rinterest;
Vd=diodedrop;
if halfbridge
Vgainmagdes=(Ifdes*Rfield+2*diodedrop)/(14/2);
else
Vgainmagdes=(Ifdes*Rfield+2*diodedrop)/(14/1);
end
Mpsprime=n*Mps; %mutual inductance reflected to primary side
Rsprime=(n^2)*Rs; %secondary winding resistance reflected to primary side
Llksprime=(n^2)*Llks; %secondary leakage inductance reflected to primary side
Leq2=parimp([Llkp Mpsprime])+Llksprime; %simple circuit equivalent inductance value
Leq=Leq2/(n^2);
C12prime=C12/n;
if wresonancecap
Ceqdesired=1/Leq2/(2*pi*fresonantdesired)^2;
C2primedesired=Ceqdesired-C12prime;
C2=n^2*C2primedesired-(1-n)*C1;
else
C2=0;%1e-9;
end
C1=0;
if halfbridge
Vp=4/pi*(14/2); %half-bridge inverter
else
Vp=4/pi*(14/1); %full-bridge inverter
end
C1prime=C1+(n-1)/n*C12;
C2prime=1/(n^2)*C2+(1-n)/(n^2)*C12;
if simplify
    C12=0;
    C1=0;
    C2=0;
    C1prime=0;
    C2prime=0;
    C12prime=0;
    Rp=0*ones(1,size(f,2));
    Rs=0*ones(1,size(f,2));
    Rsprime=Rs*(n^2);
    end
%paper check
if withrectifier
    Rload=((pi^2)/8)*Rfield;
else
    Rload=Rfield;
end
omega=2*pi*f;
```

```
s=j*omega;
%paper formulas
X1=Rp+s*Llkp;
X2=Rsprime+s*Llksprime;
Y1=X2.*(1./X1+1./(s*Mpsprime))+1;
Y2=1./X2+s*C12prime+s*C2prime+1/((n^2)*Rload);
Y=-1./X2+Y1.*Y2;
A=(s*C12prime+X2./X1.*Y2)./Y;
Vgain=(1./X1+s.*C12prime.*Y1)./(n*Y);
Zin=1./(s*C12prime.*(1-n*Vgain)+(1-A)./X1+s*C1prime);
Vgainmag=sqrt((real(Vgain).^2)+imag(Vgain).^2);
Zinmag=sqrt((real(Zin).^2)+imag(Zin).^2);
Ceq=C2prime+C12prime;
sarray=s; %omega frequencies
C3prime=0;
V4=0;
ZC3prime=0;
C4=0;
%thesis formulas
for count=1:size(omega,2)
s=sarray(count);
why1=s*C1prime;
whyM=1/(s*Mpsprime);
if simplify
why2=0;
why12=0;
else
why2=s*C2prime;
why12=s*C12prime;
end
why11=1/(Rp(count)+s*Llkp);
whyl2=1/(Rsprime(count)+s*Llksprime);
why3=s*C3prime;
whyL=(1/(n^2)*Rload);
why3L=1/(ZC3prime+((n^2)*Rload));
why3L=1e6;
why4=s*C4;
%z1=1/why1;
zM=1/whyM;
if simplify | why2==0
z2=inf;
else
z2=1/why2;
end
if simplify | why12==0
z12=inf;
else
z12=1/why12;
end
z11=1/why11;
z12=1/whyl2;
whymatrix=[why11+why12+whyM -why12;-why12 why12+why12+why2];
gainvector=inv(whymatrix)*[why11; why12];
Voc=Vp*gainvector(2);
whymatrix2=[why11 why12;-why12 why12+why12+why2];
gainvector2=inv(whymatrix2)*[why11+why1;why12];
Voc2=Vp*gainvector2(2);
Zout(count)=parimp([ (parimp([z11 zM])+z12) z2 z12])/(n^2);
Lout(count)=imag(Zout(count))/omega(count);
Rout(count)=real(Zout(count));
Vocarray(count)=abs(Voc)/n;
end
if wresonancecap
resonantfreq=1/(2*pi*(sqrt(Leq*Ceq))); %no load
end
Pin=Vp^2*real(1./Zin);
Pout=((Vgainmag*Vp).^2)/Rload;
eff=(Vgainmag.^2)/Rload./real(1./Zin);
Vs=Vgainmag*Vp;
Is=Vs/Rload;
Vsourceold=Vp*Mpsprime/(Mpsprime+Llkp)/n;
```

```
Vsource=Vocarray;
if withrectifier
if filtertype==1
[VRfield,Ifield]=Voincclfun(Vsource,Vd,omega,Lout,Rfield,Rout,accuracy,type);
elseif filtertype==2
if accuracy==1
Ifield=2/pi./omega.*Vsource./Lout./sqrt(1+(8*Rfield/(pi^2)./omega./Lout).^2); %no diode
VRfield=Ifield*Rfield;
elseif accuracy==2
VRfield= 1./(64*Rfield^2.+omega.^2.*Lout.^2*pi^4).*(-
128*Vd*Rfield+2.*(64.*Vsource.^2*pi^2*Rfield^2.+omega.^2.*Lout.^2*pi^6.*Vsource.^2-
64.*omega.^2.*Lout.^2*pi^4*Vd^2).^(1/2)).*Rfield; %with diode
for count=1:size(VRfield)
if VRfield(count)<0
VRfield(count)=0;
end
end
Ifield=VRfield/Rfield;
elseif accuracy==3
VRfield=
1/2./(64*Rfield^2+16*Rfield*pi^2.*Rout+pi^4.*Rout.^2.+omega.^2.*Lout.^2*pi^4).*(-
256*Rfield*Vd-
32*Vd*pi^2.*Rout+4.*(64*Vsource.^2*pi^2*Rfield^2+16*Rfield*pi^4.*Rout.*Vsource.^2+pi^6.*R
out.^2.*Vsource.^2.+omega.^2.*Lout.^2*pi^6.*Vsource.^2-
64*omega.^2.*Lout.^2*pi^4*Vd^2).^(1/2))*Rfield; %with diode and source resistor
for count=1:size(VRfield)
if VRfield(count)<0
VRfield(count)=0;
end
end
Ifield=VRfield/Rfield;
end
end
else
VRfield=Vs;
Ifield=Is;
end
Pout2=(VRfield).^2/Rfield;
if plotall
figure(1)
hold on
if filtertype==1
    plot(f,Vocarray,':')
else
    plot(f,Vocarray)
end
xlabel('Frequency (hz)')
ylabel('Open circuit voltage (V)')
figure(2)
hold on
if filtertype==1
    plot(f,Lout,':')
else
    plot(f,Lout)
end
xlabel('Frequency (hz)')
ylabel('Impedance (ohms)')
figure(3)
hold on
if filtertype==1
    plot(f,Rout,':')
    else
    plot(f,Rout)
end
xlabel('Frequency (hz)')
ylabel('Rout (ohms)')
end
if ~plotnone
figure(4)
hold on
if filtertype==1
```

```
    plot(f,Ifield,':')
else
    plot(f,Ifield)
end
xlabel('Frequency (hz)')
ylabel('Current (A)')
figure(5)
hold on
if filtertype==1
    NIfield=Ifield.*Nfield;
    plot(f,NIfield,':')
else
    NIfield=Ifield.*Nfield;
    plot(f,NIfield)
end
('Frequency (hz)')
ylabel('Ampere turns')
end
if method==1
[fdifference,fdesindex]=min(abs(Ifield-Ifieldreqd));
elseif method==2
[fdifference,fdesindex]=min(abs(f-finterest));
end
secondaryvoltage=Vs(fdesindex)
outputvoltage=VRfield(fdesindex)
fieldcurrent=Ifield(fdesindex)
T=1/f(fdesindex);
if halfbridge
vm=(14/2);
else
vm=(14/1); %full-bridge
end
deltaim=vm*T/Mpsprime/4 %change in magnetizing current
if filtertype==1
primcurideal=(1/n)*fieldcurrent; %square wave amplitude
primcurpeak=deltaim+primcurideal
irmsmosfet=primcurideal*sqrt(1+(1/3)*((deltaim/primcurideal)^2))
elseif filtertype==2
primcurideal=(1/n)*fieldcurrent*pi/2; %sinusoidal amplitude
primcurpeak=sqrt((8/(pi^2)*deltaim)^2+primcurideal^2)
irmsmosfet=primcurpeak/sqrt(2)
end
fsw=f(fdesindex)
junctiontemp
pcbeff
legend('Capacitor filter','Inductor filter')
```

F.2.2 PCB Transformer Output Versus Frequency and Field Resistance

```
%%%%%%%%%%%%%%%%%%%%%%%
%analyzepcbvsfvsr.m%
%%%%%%%%%%%%%%%%%%%%%%%
%analyzes pcb output performance versus frequency and number of field turns
%now assuming constant current or constant voltage load and not oversimplified model used
before
%Rp and Rs varying with frequency as measured
method=1;
%1 picks freq for you given current you want
%2 picks current given frequency you have
withC4=0;
useknownparams=1;
withrectifier=1;
wresonancecap=0;
type=12;
halfbridge=0; %1=halfbridge, 0=fullbridge
filtertype=2; %1= constant current %2=constant voltage
modratm=1; %modify Rfield according to measurement
accuracy=1; %1=no diode; 2=with diode; 3=with diode and resistor
simplify=0;
fixturns=1;
fixfreq=0;
```

267

```
plottype='b'; %y,m,c,r,g,b,w,k,  .,o,x,+,*,s,d,v,^,<,>,p,h,-,:,-.,--
switchlosstype=1; %1=tim, 2=datasheet approx
f=linspace(10e3,1e6,82);
sigma=5.8e7;
inchtom=2.54/100;
miltom=25.4e-6;
Di=2.4385*inchtom;
Do=3.4555*inchtom;
Nfield=65;
wfoil=23e-3;
tfoil=6.2*miltom;
R5mil=65*pi*(Do+Di)/2/(wfoil*5*miltom)/sigma;
Rinterest=Nfield*pi*(Do+Di)/2/sigma/wfoil/tfoil;
Ifieldreqd=20;
Jpredict=Ifieldreqd/(wfoil*tfoil);
plotall=0;
plotnone=0;
diodedrop=0.35;%0.25; %0.7 default
Rdson=17.5e-3;
Ro=0.041825;
Ri=0.026095;
L=0.03022;
inchtom=2.54/100;
miltom=25.4e-6;
Di=2.4385*inchtom;
Do=3.4555*inchtom;
Ri=Di/2;
Ro=Do/2;
W=Ro-Ri;
L=23e-3;
tfoilkap=1*miltom; %insulation thickness
Nffarray=linspace(51,132,132-51+1);
numresistorval=size(Nffarray,2);
kpffarray=(W-tfoilkap*Nffarray)/W; %assuming no kapton in sides, single side
Rfieldarray=(Nffarray.^2)*pi*(Ro+Ri)/sigma./kpffarray/W/L;
if modratm
        Rfieldarray=Rfieldarray*.0902/.0661661; end
impliedcuthick=W./Nffarray-tfoilkap;

if useknownparams
C12=3.2630e-011; %calculated
n=4/2;
Lp=0.969e-6;
Lsec=0.307e-6;
Mps=(2.043e-6-(Lp+Lsec))/2;
a0=0.0494 %4:2
a1=2.9861e-007
a2=-5.5736e-013
a3=6.6569e-019
a4=-2.7291e-025
b0=0.0321
b1=8.2500e-008
b2=-1.1362e-013
b3=1.1968e-019
b4=-4.3914e-026
Rp=a0+a1*f+a2*(f.^2)+a3*(f.^3)+a4*(f.^4);
Rs=b0+b1*f+b2*(f.^2)+b3*(f.^3)+b4*(f.^4);
end
k=Mps/sqrt(Lp*Lsec);
Llkp=Lp-n*Mps;
Llks=Lsec-(1/n)*Mps;
C1=0;
fresonantdesired=finterest;
Rinterest=0.0902;
Rfield=Rinterest;
Vd=diodedrop;
Vgainmagdes=(Ifdes*Rfield+2*diodedrop)/(14/2);
Mpsprime=n*Mps;
Rsprime=(n^2)*Rs;
Llksprime=(n^2)*Llks;
for Rfieldindex=1:numresistorval
```

```
Rfield=Rfieldarray(Rfieldindex);
Leq2=parimp([Llkp Mpsprime])+Llksprime;
Leq=Leq2/(n^2);
C12prime=C12/n;
if wresonancecap
Ceqdesired=1/Leq2/(2*pi*fresonantdesired)^2;
C2primedesired=Ceqdesired-C12prime;
C2=n^2*C2primedesired-(1-n)*C1;
else
C2=0;
end
C1=0;
if halfbridge
Vp=4/pi*(14/2); else
    Vp=4/pi*(14/1);
end
C1prime=C1+(n-1)/n*C12;
C2prime=1/(n^2)*C2+(1-n)/(n^2)*C12;
if simplify
    C12=0;
    C1=0;
    C2=0;
    C1prime=0;
    C2prime=0;
    C12prime=0;
    Rp=0*ones(1,size(f,2));
    Rs=0*ones(1,size(f,2));
    Rsprime=Rs*(n^2);
    end
if withrectifier
    Rload=((pi^2)/8)*Rfield;
else
    Rload=Rfield;
    end
omega=2*pi*f;
s=j*omega;
X1=Rp+s*Llkp;
X2=Rsprime+s*Llksprime;
Y1=X2.*(1./X1+1./(s*Mpsprime))+1;
Y2=1./X2+s*C12prime+s*C2prime+1/((n^2)*Rload);
Y=-1./X2+Y1.*Y2;
A=(s*C12prime+X2./X1.*Y2)./Y;
Vgain=(1./X1+s.*C12prime.*Y1)./(n*Y);
Zin=1./(s*C12prime.*(1-n*Vgain)+(1-A)./X1+s*C1prime);
Vgainmag=sqrt((real(Vgain).^2)+imag(Vgain).^2);
Zinmag=sqrt((real(Zin).^2)+imag(Zin).^2);
Ceq=C2prime+C12prime;
sarray=s;
C3prime=0;
V4=0;
ZC3prime=0;
C4=0;
for count=1:size(omega,2)
s=sarray(count);
why1=s*C1prime;
whyM=1/(s*Mpsprime);
if simplify
why2=0;
why12=0;
else
why2=s*C2prime;
why12=s*C12prime;
end
why11=1/(Rp(count)+s*Llkp);
why12=1/(Rsprime(count)+s*Llksprime);
why3=s*C3prime;
whyL=(1/(n^2)*Rload);
why3L=1/(ZC3prime+((n^2)*Rload));
why3L=1e6;
why4=s*C4;
zM=1/whyM;
```

```
if simplify | why2==0
z2=inf;
else
z2=1/why2;
end
if simplify | why12==0
z12=inf;
else
z12=1/why12;
end
zl1=1/whyl1;
zl2=1/whyl2;
whymatrix=[whyl1+whyl2+whyM -whyl2;-whyl2 why12+whyl2+why2];
gainvector=inv(whymatrix)*[whyl1; whyl2];
Voc=Vp*gainvector(2);
Zout(count)=parimp([ (parimp([zl1 zM])+zl2) z2 z12])/(n^2);
Lout(count)=imag(Zout(count))/omega(count);
Rout(count)=real(Zout(count));
Vocarray(count)=abs(Voc)/n;
end
if wresonancecap
resonantfreq=1/(2*pi*(sqrt(Leq*Ceq))); %no load
end
Pin=Vp^2*real(1./Zin);
Pout=((Vgainmag*Vp).^2)/Rload;
eff=(Vgainmag.^2)/Rload./real(1./Zin);
Vs=Vgainmag*Vp;
Is=Vs/Rload;
Vsourceold=Vp*Mpsprime/(Mpsprime+Llkp)/n;
Vsource=Vocarray;
if withrectifier
if filtertype==1
[VRfield,Ifield]=Voincclfun(Vsource,Vd,omega,Lout,Rfield,Rout,accuracy,type);
elseif filtertype==2
if accuracy==1
Ifield=2/pi./omega.*Vsource./Lout./sqrt(1+(8*Rfield/(pi^2)./omega./Lout).^2); %no diode
VRfield=Ifield*Rfield;
elseif accuracy==2
VRfield= 1./(64*Rfield^2.+omega.^2.*Lout.^2*pi^4).*(-
128*Vd*Rfield+2.*(64.*Vsource.^2*pi^2*Rfield^2.+omega.^2.*Lout.^2*pi^6.*Vsource.^2-
64.*omega.^2.*Lout.^2*pi^4*Vd^2).^(1/2)).*Rfield; %with diode
for count=1:size(VRfield)
if VRfield(count)<0
VRfield(count)=0;
end
end
Ifield=VRfield/Rfield;
elseif accuracy==3
VRfield=
1/2./(64*Rfield^2+16*Rfield*pi^2.*Rout+pi^4.*Rout.^2.+omega.^2.*Lout.^2*pi^4).*(-
256*Rfield*Vd-
32*Vd*pi^2.*Rout+4.*(64*Vsource.^2*pi^2*Rfield^2+16*Rfield*pi^4.*Rout.*Vsource.^2+pi^6.*R
out.^2.*Vsource.^2.+omega.^2.*Lout.^2*pi^6.*Vsource.^2-
64*omega.^2.*Lout.^2*pi^4*Vd^2).^(1/2))*Rfield; %with diode and source resistor
for count=1:size(VRfield)
if VRfield(count)<0
VRfield(count)=0;
end
end
Ifield=VRfield/Rfield;
end
end
else
VRfield=Vs;
Ifield=Is;
end
Pout2=(VRfield).^2/Rfield;
pcbeffvect
VRfieldmatrix(Rfieldindex,:)=VRfield;
Ifieldmatrix(Rfieldindex,:)=Ifield;
NIfieldmatrix(Rfieldindex,:)=Nffarray(Rfieldindex)*Ifield;
```

```
Pout2matrix(Rfieldindex,:)=Pout2;
Irmsmosfetmatrix(Rfieldindex,:)=irmsmosfet;
if switchlosstype==1
    effmatrix(Rfieldindex,:)=eff;
    Iinputmatrix(Rfieldindex,:)=Pinput/14;
else
effmatrix(Rfieldindex,:)=eff2;
Iinputmatrix(Rfieldindex,:)=Pinput2/14;
end
end
if filtertype==1
Ifieldind=Ifieldmatrix;
NIfieldind=NIfieldmatrix;
effind=effmatrix;
Iinputind=Iinputmatrix;
Irmsmosfetind=Irmsmosfetmatrix;
elseif filtertype==2
Ifieldcap=Ifieldmatrix;
NIfieldcap=NIfieldmatrix;
effcap=effmatrix;
Iinputcap=Iinputmatrix;
Irmsmosfetcap=Irmsmosfetmatrix;
end
figure(41)
surfc(Rfieldarray,f,Ifieldmatrix')
xlabel('Resistor (ohms)')
ylabel('Frequency (Hz)')
zlabel('Current (A)')
view(160,30)
figure(42)
surfc(Rfieldarray,f,NIfieldmatrix')
xlabel('Resistor (ohms)')
ylabel('Frequency (Hz)')
zlabel('Ampere turns (A-turns)')
view(160,30)
figure(43)
surfc(Rfieldarray,f,effmatrix')
xlabel('Resistor (ohms)')
ylabel('Frequency (Hz)')
zlabel('Efficiency')
view(160,30)
figure(44)
surfc(Rfieldarray,f,14*Iinputmatrix')
xlabel('Resistor (ohms)')
ylabel('Frequency (Hz)')
zlabel('Input power (W)')
view(160,30)
figure(45)
surfc(Rfieldarray,f,Irmsmosfetmatrix')
xlabel('Resistor (ohms)')
ylabel('Frequency (Hz)')
zlabel('Primary rms current (A)')
view(160,30)
if fixturns
    numturns=65;
    [ndiff,nindex]=min(abs(numturns-Nffarray));
figure(21)
hold on
plot(f,Ifieldmatrix(nindex,:),plottype)
xlabel('Frequency (Hz)')
ylabel('Field current (A)')
title(Rfieldarray(nindex))
figure(22)
hold on
plot(f,NIfieldmatrix(nindex,:),plottype)
xlabel('Frequency (Hz)')
ylabel('Field ampere turns')
title(Rfieldarray(nindex))
figure(23)
hold on
plot(f,effmatrix(nindex,:),plottype)
```

```
xlabel('Frequency (Hz)')
ylabel('Efficiency')
title(Rfieldarray(nindex))
figure(24)
hold on
plot(f,14*Iinputmatrix(nindex,:),plottype)
xlabel('Frequency (Hz)')
ylabel('Input power (W)')
title(Rfieldarray(nindex))
figure(25)
hold on
plot(f,Irmsmosfetmatrix(nindex,:),plottype)
xlabel('Frequency (Hz)')
ylabel('Primary rms current')
title(Rfieldarray(nindex))
end
if fixfreq
[fdifference,fdesindex]=min(abs(f-finterest));
figure(31)
hold on
plot(Rfieldarray,Ifieldmatrix(fdesindex,:),plottype)
xlabel('Resistance (ohms)')
ylabel('Field current (A)')
title(finterest)
figure(32)
hold on
plot(Rfieldarray,NIfieldmatrix(fdesindex,:),plottype)
xlabel('Resistance (ohms)')
ylabel('Field ampere turns')
title(finterest)
figure(33)
hold on
plot(Rfieldarray,effmatrix(fdesindex,:),plottype)
xlabel('Resistance (ohms)')
ylabel('Efficiency')
title(finterest)
figure(34)
hold on
plot(Rfieldarray,Iinputmatrix(fdesindex,:),plottype)
xlabel('Resistance (ohms)')
ylabel('Input power (W)')
title(finterest)
figure(35)
hold on
plot(Rfieldarray,Irmsmosfetmatrix(fdesindex,:),plottype)
xlabel('Resistance (ohms)')
ylabel('Primary rms current')
title(finterest)
end
figure(21)
hold on
plot(f,ones(1,size(f,2))*3.6*332/65,'r')
figure(22)
hold on
plot(f,ones(1,size(f,2))*3.6*332,'r')
```

F.2.3 Efficiency Calculator

```
%%%%%%%%%%
%pcbeff.m%
%%%%%%%%%%
%calculations efficiency of PCB transformer output vs. freq
Pfield=fieldcurrent^2*Rfield %field losses
Pdiode=2*diodedrop*fieldcurrent %diode losses
if size(Rp,2)==1 & size(Rs,2)==1
Rprim=Rp; %primary winding resistance
Rsec=Rs; %secondary winding resistance
else
    Rprim=Rp(fdesindex);
    Rsec=Rs(fdesindex);
    end
```

272

```
if filtertype==1
    Isec=fieldcurrent; %secondary current
    Psec=(Isec^2)*Rsec %secndary losses
elseif filtertype==2
    Isec=pi/2*fieldcurrent
    Psec=0.5*(Isec^2)*Rsec
end
Pprim=(irmsmosfet^2)*Rprim %primary side losses
Pinverter=2*Ptot %inverter losses
Pinverter2=2*Ptot2;
Pinput= (Pfield+Pdiode+Psec+Pprim+Pinverter) %input power
Pinput2=(Pfield+Pdiode+Psec+Pprim+Pinverter2)
eff=Pfield/Pinput %efficiency
eff2=Pfield/Pinput2


%%%%%%%%%%%%%%
%pcbeffvect.m%
%%%%%%%%%%%%%%
%efficiency calculator
T=1./f;
if halfbridge
    vm=14/2;
else
    vm=14;
end
deltaim=vm*T/Mpsprime/4;
if filtertype==1
primcurideal=(1/n)*Ifield; %square wave amplitude
primcurpeak=deltaim+primcurideal; %primary current peak
irmsmosfet=primcurideal.*sqrt(1+(1/3).*((deltaim./primcurideal).^2));
elseif filtertype==2
primcurideal=(1/n).*Ifield*pi/2; %sinusoidal amplitude
primcurpeak=sqrt((8/(pi^2)*deltaim).^2+primcurideal.^2);
irmsmosfet=primcurpeak/sqrt(2); %irms current throguh mosfet
end
Pfield=Ifield.^2*Rfield;
Pdiode=2*diodedrop*Ifield;
if filtertype==1
    Isec=Ifield;
    Psec=(Isec.^2).*Rs;
elseif filtertype==2
    Isec=pi/2*Ifield;
    Psec=0.5*(Isec.^2).*Rs;
end
Pprim=(irmsmosfet.^2).*Rp;
Pinverter=2*Ptot;
Pinverter2=2*Ptot2;
Pinput= (Pfield+Pdiode+Psec+Pprim+Pinverter);
Pinput2=(Pfield+Pdiode+Psec+Pprim+Pinverter2);
eff=Pfield./Pinput;
eff2=Pfield./Pinput2;
```

F.2.4 Constant Current Load Output Current Calculator

```
%%%%%%%%%%%%%%
%Voincclfun.m%
%%%%%%%%%%%%%%

%function that determines output current given various parameters with constant current
load
function [VRfieldarray,Ifieldarray]=Voincclfun(Vs,Vd,omega,Leq,Rfield,Rs,accuracy,type)
%syms Vs Vo Vd omega Leq Rfield Rs lambda v
omegaarray=omega;
Rout=Rs;
Lout=Leq;
Vsource=Vs;
for count=1:size(omegaarray,2)
omega=omegaarray(count);
Rs=Rout(count);
Leq=Lout(count);
```

273

```
Vs=Vsource(count);

ftol=1e-3;
deltatol=1e-3;
h=0.001;
h1=0.0001;
h2=0.0001;


if accuracy==1
VRfield=2*Vs/pi./(1+(2*Vs/pi)*omega*Leq/Vs/Rfield);
Ifield=VRfield/Rfield;
end

if accuracy==2
type
count
ftol=1e-5;
deltatol=1e-5;
if Vs>2*Vd
lambda=asin(2*Vd/Vs);
%fo=inf;
%deltau=inf;
Ido=2*Vs/pi/(2*omega*Leq/pi+Rfield);
k1=Rfield*Vs/2/omega/Leq;
k2=Vs/pi;

oldcalc=0;
if oldcalc
uo=acos(1-2*omega*Leq*Ido/Vs);
uoinit=uo; %for comparison                             ..
while (1)
k1=Rfield*Vs/2/omega/Leq;
k2=Vs/pi;
fo=(k1-k2)*cos(lambda)-(k1+k2)*cos((uo)-lambda)+2*Vd;
fright=(k1-k2)*cos(lambda)-(k1+k2)*cos((uo+h)-lambda)+2*Vd;
fleft=(k1-k2)*cos(lambda)-(k1+k2)*cos((uo-h)-lambda)+2*Vd;

derivf=(fright-fleft)/(2*h);
deltau=-fo/derivf;

uo=uo+deltau;

if abs(fo)<ftol & abs(deltau)<deltatol | derivf==0
    break
end
end
end %of while

else
uo=acos(((k1-k2)*cos(lambda)+2*Vd)/(k1+k2))+lambda;
end

VRfield=1/pi*Vs*(cos(uo-lambda)+cos(lambda))-2*Vd;
Ifield=VRfield/Rfield;
if VRfield<0
    VRfield=0;
    Ifield=0;
    end
    else
VRfield=0;
Ifield=0;
end %of if Vs>2*Vd
end %of if accuracy==2

if accuracy==3
 type
 count
if Vs>2*Vd
lambdao=asin(2*Vd/Vs);
Ido=2*Vs/pi/(2*omega*Leq/pi+Rfield);
```

274

```
Vdo=Ido*Rfield;
uo=acos(1-2*omega*Leq*Ido/Vs);
lambdaoinit=lambdao;
uo=0;
lambdao=0;
uoinit=uo; %for comparison
D=0;
while (1)
B=(Vs/Rs*omega*sin(lambdao)-Vs/Leq*cos(lambdao)) /((omega^2)*Leq/Rs+Rs/Leq);
B2right=(Vs/Rs*omega*sin(lambdao+h2)-Vs/Leq*cos(lambdao+h2)) /((omega^2)*Leq/Rs+Rs/Leq);
B2left =(Vs/Rs*omega*sin(lambdao-h2)-Vs/Leq*cos(lambdao-h2)) /((omega^2)*Leq/Rs+Rs/Leq);
C=(Vs/Leq*sin(lambdao)-B*omega)*Leq/Rs;
C2right=(Vs/Leq*sin(lambdao+h2)-B2right*omega)*Leq/Rs;
C2left =(Vs/Leq*sin(lambdao-h2)-B2left *omega)*Leq/Rs;
E=sqrt(B^2+C^2);
E2right=sqrt(B2right^2+C2right^2);
E2left=sqrt(B2left^2+C2left^2);
x=atan(B/C);
x2right=atan(B2right/C2right);
x2left=atan(B2left/C2left);

fo1      =(1/pi*Vs*(cos(uo-lambdao)+cos(lambdao)) -2*Vd)/(Rfield+Rs*(pi-uo)/pi) *(1+exp(-
Rs/Leq*uo/omega))-(C+D)*exp(-Rs/Leq*uo/omega)+E*cos(uo-x)+D;
fo1right=(1/pi*Vs*(cos((uo+h1)-lambdao)+cos(lambdao))-2*Vd)/(Rfield+Rs*(pi-
(uo+h1)/pi))*(1+exp(-Rs/Leq*(uo+h1)/omega))-(C+D)*exp(-
Rs/Leq*(uo+h1)/omega)+E*cos((uo+h1)-x)+D;
fo1left =(1/pi*Vs*(cos((uo-h1)-lambdao)+cos(lambdao))-2*Vd)/(Rfield+Rs*(pi-(uo-
h1))/pi)*(1+exp(-Rs/Leq*(uo-h1)/omega))-(C+D)*exp(-Rs/Leq*(uo-h1)/omega)+E*cos((uo-h1)-
x)+D;
fo12right=(1/pi*Vs*(cos(uo-(lambdao+h2))+cos(lambdao+h2))-2*Vd)/(Rfield+Rs*(pi-
uo)/pi)*(1+exp(-Rs/Leq*uo/omega))-(C2right+D)*exp(-Rs/Leq*uo/omega)+E2right*cos(uo-x)+D;
fo12left =(1/pi*Vs*(cos(uo-(lambdao-h2))+cos(lambdao-h2))-2*Vd)/(Rfield+Rs*(pi-
uo)/pi)*(1+exp(-Rs/Leq*uo/omega))-(C2left+D)*exp(-Rs/Leq*uo/omega)+E2left*cos(uo-x)+D;
fo2      =Vs*sin(lambdao)-2*Vd-Rs*(1/pi*Vs*(cos(uo-lambdao)+cos(lambdao))-
2*Vd)/(Rfield+Rs*(pi-uo)/pi);
fo21right=Vs*sin(lambdao)-2*Vd-Rs*(1/pi*Vs*(cos((uo+h1)-lambdao)+cos(lambdao))-
2*Vd)/(Rfield+Rs*(pi-(uo+h1))/pi);
fo21left =Vs*sin(lambdao)-2*Vd-Rs*(1/pi*Vs*(cos((uo-h1)-lambdao)+cos(lambdao))-
2*Vd)/(Rfield+Rs*(pi-(uo-h1))/pi);
fo22right=Vs*sin(lambdao+h2)-2*Vd-Rs*(1/pi*Vs*(cos(uo-(lambdao+h2))+cos(lambdao+h2))-
2*Vd)/(Rfield+Rs*(pi-uo)/pi);
fo22left =Vs*sin(lambdao-h2)-2*Vd-Rs*(1/pi*Vs*(cos(uo-(lambdao-h2))+cos(lambdao-h2))-
2*Vd)/(Rfield+Rs*(pi-uo)/pi);
derivfo11=(fo1right-fo1left)/(2*h1);
derivfo12=(fo12right-fo12left)/(2*h2);
derivfo21=(fo21right-fo21left)/(2*h1);
derivfo22=(fo22right-fo22left)/(2*h2);
jac=[derivfo11 derivfo12;derivfo21 derivfo22];
xx=inv(jac)*[-fo1;-fo2];
deltau=xx(1);
deltalambda=xx(2);
uo=uo+deltau;
lambdao=lambdao+deltalambda;
if norm([fo1,fo2])<ftol & norm([deltau,deltalambda])<deltatol
   break
   end
end %of while
Ifield=(1/pi*Vs*(cos(uo-lambdao)+cos(lambdao))-2*Vd)/(Rfield+Rs*(pi-uo)/pi);
VRfield=Ifield*Rfield;
if Ifield<0
   VRfield=0;
   Ifield=0;
   end
else
Ifield=0;
VRfield=0;
end %of Vs>2*Vd
end %of if accuracy
VRfieldarray(count)=VRfield;
Ifieldarray(count)=Ifield;
end
```

F.2.5 PCB Transformer Parameter Calculator

```
%%%%%%%%%%%%%%%%%%
%pcbparamcalc.m%
%%%%%%%%%%%%%%%%%%
%calculates pcb transformer parameters
approx=1;
same=1; %if primary inductance equals secondary inductance
routmax=(0.02878+2*0.0145)/2;
innerrad=0.02878/2;
onemil=25.4e-6;
intom=0.0254;
mu0=4*pi*1e-7;
epsilon0=8.854e-12;
sigma=4.45e7;
D=0.2;
%4 ounce copper tracks derived from 2 ounce copper 4:2
wp=0.2/2*intom;
sp=wp+15*onemil;
hp=0.0027*2*intom; %h2
rip=0.02878/2+.0016;
ws=2*(0.2/2*intom)+1*(15*onemil);
ss=ws+15*onemil;
hs=0.0027*2*intom; %h1
ris=0.02878/2+.0016;
z=25*onemil;
Np=floor((routmax-rip)/sp); %number of turns on primary winding
Ns=floor((routmax-ris)/ss); %number of turns on secondary winding
end
routp=rip+Np*sp-(sp-wp);
routs=ris+Ns*sp-(ss-ws);
doutp=routp*2;
douts=routs*2;
zorg=z;
Mps=mutualindcalc(Np,rip,sp,wp,hp,Ns,ris,ss,ws,hs,z,approx);
Lp=selfindcalc(Np,rip,sp,wp,hp,approx);
if same==1
    Lsec=Lp;
else
    Lsec=selfindcalc(Ns,ris,ss,ws,hs,approx);
end
n=Np/Ns;
Mpsprime=n*Mps;
Llkp=Lp-n*Mps;
Llks=Lsec-(1/n)*Mps;
C12=epsilon0*pi*(min(rip+(Np-1)*sp+wp,ris+(Ns-1)*ss+ws))^2/zorg;

rsump=0;
rsums=0;
for icount=1:Np
    r1=rip+(icount-1)*sp;
    r2=rip+(icount-1)*sp+wp;
    r=sqrt(r1*r2);
    rsump=rsump+r;
end
lenp=2*pi*rsump;
for jcount=1:Ns
        a1=ris+(jcount-1)*ss;
        a2=ris+(jcount-1)*ss+ws;
        a=sqrt(a1*a2);
    rsums=rsums+a;
    end
lens=2*pi*rsums;
Rp=lenp/(sigma*wp*hp);
Rs=lens/(sigma*ws*hs);

%%%%%%%%%%%%%%%%%
%selfindcalc.m%
%%%%%%%%%%%%%%%%%
function Lp=selfindcalc(Np,rip,sp,wp,hp,approx)
```

```
k=linspace(1e-6,1e5,1000001); %9+8*integer
mu0=4*pi*1e-7;
Lp=0;
hs=hp;
for icount=1:Np
    r1=rip+(icount-1)*sp;
    r2=rip+(icount-1)*sp+wp;
    for jcount=1:Np
        a1=rip+(jcount-1)*sp;
        a2=rip+(jcount-1)*sp+wp;
    %Mps=Mps+mu0*pi/(hs*log(r2/r1)*hp*log(a2/a1))*int((besselj(0,k*r2)-
besselj(0,k*r1))*(besselj(0,k*a2)-besselj(0,k*a1))/(k^2)*(2/(k^2)*(cosh(k*(hs+hp)/2)-
cosh(k*(hs-hp)/2)))*exp(-k*abs(z)),k,0,inf);
        if approx==1
        r=sqrt(r1*r2);
        a=sqrt(a1*a2);
        rf1=r*(1+(hp^2)/(24*r^2))-sqrt(((wp^2)-(hp^2))/12);
        rf2=r*(1+(hp^2)/(24*r^2))+sqrt(((wp^2)-(hp^2))/12);
        af1=a*(1+(hp^2)/(24*a^2))-sqrt(((wp^2)-(hp^2))/12);
        af2=a*(1+(hp^2)/(24*a^2))+sqrt(((wp^2)-(hp^2))/12);

        if icount==jcount
            z=0.2235*(hp+wp);
            f=sqrt(4*a*r/(z^2+(a+r)^2));
    [K,E]=ellipke(f);
        Lpinc=mu0*sqrt(a*r)*2/f*((1-(f^2)/2)*K-E);
        else
            z=0;
            f=sqrt(4*af1*rf1/(z^2+(af1+rf1)^2));
            [K,E]=ellipke(f);
            Mrf1af1=mu0*sqrt(af1*rf1)*2/f*((1-(f^2)/2)*K-E);
            f=sqrt(4*af2*rf1/(z^2+(af2+rf1)^2));
                [K,E]=ellipke(f);
            Mrf1af2=mu0*sqrt(af2*rf1)*2/f*((1-(f^2)/2)*K-E);
                f=sqrt(4*af1*rf2/(z^2+(af1+rf2)^2));
                [K,E]=ellipke(f);
            Mrf2af1=mu0*sqrt(af1*rf2)*2/f*((1-(f^2)/2)*K-E);
            f=sqrt(4*af2*rf2/(z^2+(af2+rf2)^2));
                [K,E]=ellipke(f);
            Mrf2af2=mu0*sqrt(af2*rf2)*2/f*((1-(f^2)/2)*K-E);
        Lpinc=(Mrf1af1+Mrf1af2+Mrf2af1+Mrf2af2)/4;
        end
        Lp=Lp+Lpinc;
    else
        zself=0;

        integrand=mu0*pi/(hs*log(r2/r1)*hp*log(a2/a1))*(besselj(0,k*r2)-
besselj(0,k*r1)).*(besselj(0,k*a2)-besselj(0,k*a1))./(k.^2).*(2./(k.^2).*(cosh(k*hp)-
1)).*exp(-k*abs(zself));
        Lp=Lp+integratec(integrand,k);
    end

    end
end

%%%%%%%%%%%%%%%%%
%mutualindcalc.m%
%%%%%%%%%%%%%%%%%%
%calculates mutual inductance between two windings
function Mps=mutualindcalc(Np,rip,sp,wp,hp,Ns,ris,ss,ws,hs,z,approx)
k=linspace(1e-6,1e5,1000001);
mu0=4*pi*1e-7;
Mps=0;
for icount=1:Np
    r1=rip+(icount-1)*sp;
    r2=rip+(icount-1)*sp+wp;
    for jcount=1:Ns
        a1=ris+(jcount-1)*ss;
        a2=ris+(jcount-1)*ss+ws;
        if approx==1
        r=sqrt(r1*r2);
```

```
      a=sqrt(al*a2);
        f=sqrt(4*a*r/(z^2+(a+r)^2));
        [K,E]=ellipke(f);
        Mps=Mps+mu0*sqrt(a*r)*2/f*((1-(f^2)/2)*K-E);
          else
        integrand=mu0*pi/(hs*log(r2/r1)*hp*log(a2/a1))*(besselj(0,k*r2)-
besselj(0,k*r1)).*(besselj(0,k*a2)-
besselj(0,k*a1))./(k.^2).*(2./(k.^2).*(cosh(k*(hs+hp)/2)-cosh(k*(hs-hp)/2))).*exp(-
k*abs(z));
        Mps=Mps+integratec(integrand,k);
      end
    end
end


%%%%%%%%%%%%%%
%integratec.m%
%%%%%%%%%%%%%%
%integrator
function [integral]=integratec(u,k)
gridsize=k(2)-k(1);
%integrand=mu0*pi/(hs*log(r2/r1)*hp*log(a2/a1))*(besselj(0,k*r2)-
besselj(0,k*r1))*(besselj(0,k*a2)-besselj(0,k*a1))/(k^2)*(2/(k^2)*(cosh(k*(hs+hp)/2)-
cosh(k*(hs-hp)/2)))*exp(-k*abs(z))
integral=0;
accuracy=4;
if accuracy==1
    %k = number of pts=3+2*integer
    for count=1:(floor((size(k,2))/2))
    index=2*count;
    integral=integral+gridsize/3*(u(index+1)+4*u(index)+u(index-1));
end
elseif accuracy==2
    %k must have number of pts=5+4*integer
for count=1:(floor((size(k,2))/4))
    index=3+4*(count-1);
    integral=integral+2*gridsize/45*(7*u(index+2)+32*u(index+1)+12*u(index)+32*u(index-
1)+7*u(index-2));
end
elseif accuracy==3
    %k must have number of pts=7+6*integer
    for count=1:floor((size(k,2))/6)
    index=4+6*(count-1);

integral=integral+gridsize/140*(41*u(index+3)+216*u(index+2)+27*u(index+1)+272*u(index)+2
7*u(index-1)+216*u(index-2)+41*u(index-3));
end
elseif accuracy==4
    %k must have number of pts=9+8*k
for count=1:floor((size(k,2))/8)
    index=5+8*(count-1);
    integral=integral+4*gridsize/14175*(989*u(index+4)+5888*u(index+3)-
928*u(index+2)+10496*u(index+1)-4540*u(index)+10496*u(index-1)-928*u(index-
2)+5888*u(index-3)+989*u(index-4));
end

end
```

5815-54